SANDIA REPORT
SAND2015-2593
Unlimited Release
Printed March 2015

Structural Health and Prognostics Management for Offshore Wind Plants: Final Report of Sandia R&D Activities

D. Todd Griffith

Prepared by
Sandia National Laboratories
Albuquerque, New Mexico 87185 and Livermore, California 94550

Sandia National Laboratories is a multi-program laboratory managed and operated by Sandia Corporation, a wholly owned subsidiary of Lockheed Martin Corporation, for the U.S. Department of Energy's National Nuclear Security Administration under contract DE-AC04-94AL85000.

Issued by Sandia National Laboratories, operated for the United States Department of Energy by Sandia Corporation.

Available to DOE and DOE contractors from
U.S. Department of Energy
Office of Scientific and Technical Information
P.O. Box 62
Oak Ridge, TN 37831

Telephone: (865) 576-8401
Facsimile: (865) 576-5728
E-Mail: reports@osti.gov
Online ordering: http://www.osti.gov/scitech

Available to the public from
U.S. Department of Commerce
National Technical Information Service
5301 Shawnee Rd
Alexandria, VA 22312

Telephone: (800) 553-6847
Facsimile: (703) 605-6900
E-Mail: orders@ntis.gov
Online order: http://www.ntis.gov/search

SAND2015-2593
Unlimited Release
Printed March 2015

Structural Health and Prognostics Management for Offshore Wind Plants: Final Report of Sandia R&D Activities

D. Todd Griffith
Wind Energy Technologies Department
Sandia National Laboratories
P.O. Box 5800
Albuquerque, New Mexico 87185-MS1124

Abstract

This final report is a compilation of research efforts – funded by the US Department of Energy Wind and Water Power Technologies Office over a four-year period from FY11 through FY14. The goals of this research program were to develop and evaluate technical innovations with promise for maximizing revenues and reducing levelized cost of energy (LCOE) for offshore wind plants – more specifically the goals of the Structural Health and Prognostics Management (SHPM) program were to reduce O&M costs and increase energy capture through use of SHPM-based technologies. A technology roadmap was developed at the start of the project to guide the research efforts. This roadmap identified and outlined six major research thrust areas each having five stages of maturity. Research was conducted in each of these thrust areas, as documented throughout this report, although a major focus was on development of damage detection strategies for the most frequent blade damage conditions and damage mitigation and life-extension strategies via changes in turbine operations (smart loads management). The work summarized in this compilation report is the product of the work of many researchers. A summary of the major findings, status of the SHPM Technology Roadmap and recommendations for future work are also provided.

ACKNOWLEDGMENTS

This work was funded by the US Department of Energy Wind and Water Power Technologies Office.

This report includes the contributions of many people, as noted in the publications list of Chapter 1 and throughout the referenced materials. The original reports were co-authored and/or included contributions from the following individuals:

Sandia National Laboratories: Dr. Jonathan White, Mr. Brian Resor, Mr. Joshua Paquette

ATA Engineering, Inc: Dr. Nate Yoder, Dr. Rory Davis, Dr. Keith van der Walde, Mr. Tim Marinone

Purdue University/Vanderbilt University: Dr. Douglas Adams, Mr. Noah Myrent, Dr. Natalie Barrett, Mr. Joshua Kusnick, Dr. Nasir Bilal, Mr. Dave Koester

Georgia Tech: Dr. Phillip Richards, Dr. Dewey Hodges

Graduate students who completed a MS thesis or PhD dissertation funded by the SHPM program are:

MS Theses:
Joshua Kusnick, Purdue University (May 2012)
Noah Myrent, Purdue University (December 2013)

PhD Dissertation:
Phillip Richards, Georgia Tech University (December 2014)
Natalie Barrett, Purdue University (presently pursuing)

CONTENTS

(this page intentionally left blank)

CHAPTER 1. REPORT SUMMARY AND OUTLINE

This final report is a compilation of the research performed in the Sandia Structural Health and Prognostics Management (SHPM) program. The SHPM program focused on research to develop and evaluate technical innovations showing promise for maximizing plant revenues and reducing LCOE for offshore wind plants. More specifically the goals of the SHPM program were to reduce O&M costs and increase energy capture through use of SHPM-based technologies. This chapter provides an outline of the research conducted from 2011 to 2015.

This research addresses one of the key challenges facing the industry, that is, to develop reliable methods to detect damage in the rotor blades and to detect them early enough to impact operations and repair/maintenance decisions leading to reduced costs and increased revenues. Sandia addressed this challenge by performing research in the areas of structural health monitoring (SHM) and prognostics management. The principal motivations of this research are to reduce operations and maintenance (O&M) costs, improve wind-plant reliability, and reduce downtime. A particular focus, when considering siting in the offshore environment, is to mitigate the large rise in costs for offshore O&M due to access difficulty, weather, high sea states, etc. using structural health monitoring and prognostics management (as illustrated in Figure 1).

Figure 1. Illustration of Offshore Wind Accessibility Challenges (Weather, High Sea States and Remote Access) that Motivate the Need for Structural Health and Prognostics Management

With the overall goals to significantly reduce O&M costs and increase energy capture, the motivations behind this research were to develop and evaluate new strategies – robust and cost-effective SHPM strategies that can provide the following features (of varying complexity):

1. ensure operations in a desired (designed) safe state of health,
2. aid in planning of maintenance processes versus more costly unplanned servicing,
3. avoid catastrophic failures through advance warning, and/or
4. improve energy capture by avoiding unnecessary shutdown and increasing overall plant availability.

LCOE is affected in 3 principal ways through implementation of an SHPM monitoring system:

1. Increased capital costs for sensing and prognostics. These additional costs must be offset by the benefits of SHPM (in the following two areas, O&M and AEP) for cost-effectiveness:
2. Reduced operations and maintenance (O&M) costs via improved maintenance processes and improved maintenance planning, and also the benefit of
3. Increased energy capture (AEP) by minimization of downtime or planning of downtime when the wind resource (and revenue loss) is at a minimum,

as illustrated in Figure 2.

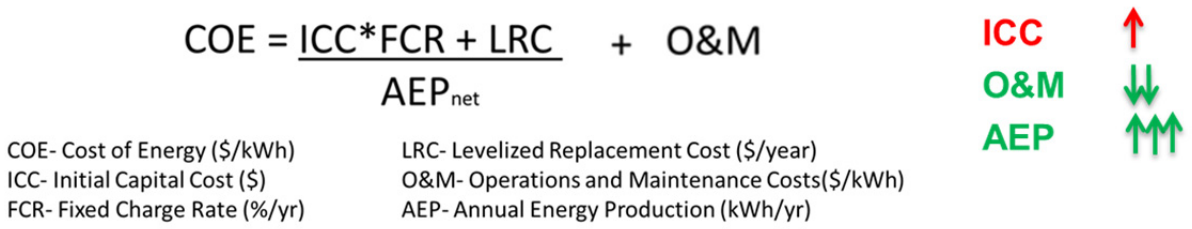

Figure 2. Illustration of SHPM Impacts on LCOE (Higher Capital Costs with Potential for Improvements in AEP and O&M Cost Reductions)

This report is organized into chapters according to the major topics of the research. The order of the topics is chronological, evolving from FY11 to FY14.

Chapter 2 provides a summary of the initial SHPM roadmap, developed in FY11. In this work, the broad context of the research scope was proposed. A key element described in this roadmap is a multi-scale approach to simulations of damage that is a broadly applicable tool for analysis of damaged turbines. A first case study of TE (trailing edge) disbond was performed to demonstrate the initial SHPM roadmap and illustrate the multi-scale simulation of damage approach.

Chapter 3 provides an updated and more comprehensive SHPM technology roadmap (refined in FY12 and FY13). The updated SHPM roadmap defines six major thrust areas of SHPM research along with five stages of maturity for each thrust area. This roadmap proposes a maturation path for each of these major thrust areas, that is, how each should be matured individually. The roadmap also proposes how these thrust areas can be vertically integrated to produce an SHPM "system" with the goal to mature the technology sufficiently to produce a 1st generation cost-effective SHPM system.

Chapter 4 documents additional case studies of damage detection (i.e. global operating sensitivity of damage) for the cases of rotor imbalance (aerodynamic imbalance and mass imbalance) and shear web (SW) disbond. Following the initial case study of TE disbond, these additional case studies were pursued to identify rotor response measurements (i.e. operating signatures) that are sensitive to these types of damage/fault conditions. Damage detection and damage characterization strategies were developed for both SW disbond and rotor imbalance

demonstrating that the multi-scale simulation approach is broadly applicable and useful for development of damage detection strategies. In addition, an O&M cost analysis was performed to provide an initial model for assessing the cost-benefits of SHPM.

Chapter 5 presents findings for local sensitivity of damage effects, as specified in the multi-scale simulation of damage approach. Here, the state of health or severity of damage (based on local sensitivity loads analysis) is addressed. In the initial study, as summarized in Chapter 2, fatigue load considerations were considered by investigating the impact of damage on remaining fatigue life. In the work summarized in Chapter 5, nonlinear analysis is introduced into the blade damage structural analysis in order to improve blade damage models. Also, additional load cases were investigated by performing buckling calculations for damaged blades to assess remaining life as determined by remaining buckling margins. Progressive damage analysis, a related topic, was considered in later work and is summarized in Chapter 7. In addition, Chapter 5 includes results for improved beam property estimation for damaged blades – a study was performed to evaluate nonlinear effects in the damage modeling approach for beam property estimation. Linear and nonlinear solutions for modeling the damage are examined and the estimated damaged-blade beam properties (which are used in turbine aero-elastic simulations of damaged turbines) are compared.

Chapter 6 presents the results of studies to evaluate the robustness of the operational damage detection strategies that were developed for rotor imbalance and SW disbond (in Chapter 4). While the damage detection strategies showed promise for simple, uniform inflow conditions in the initial studies, these follow-on studies conducted in FY13 were designed to test the robustness of the damage detection strategies to realistic and variable inflow conditions. Inflow variability studies with a probability of detection (POD) analysis were conducted to evaluate and quantify the robustness of the developed damage detection strategies under these realistic and variable inflow conditions.

In Chapter 7, additional elements of the SHPM technology roadmap of Chapter 3 were addressed in the area of operations decisions – these include damage mitigation and prognostics management. Damage mitigation (e.g. mitigation of damage initiation or damage growth) was considered through a smart loads management approach (controls). A progressive damage model is applied and validated for blade disbonds in the trailing edge and shear web. The impact of derating was quantified by comparing strain energy release rates for normal operation and derated operation. Damage-tolerant design is also considered.

Chapter 8 covers economics considerations for SHPM; focused on impacts of derating on improving energy capture (or AEP, Annual Energy Production). The variation of AEP with several variables (i.e. seasonal variations in wind resource, derating type, derating level, and site characteristics) is quantified. The analysis is useful to understand the opportunities for increased AEP and the overall economics of derating including the most suitable derating strategy and best derating level as well as the best derating time.

Chapter 9 is the concluding chapter and includes a summary of the major findings of the Sandia SHPM research program. A current status of SHPM in reference to the updated SHPM roadmap (Chapter 3) is also provided along with near-term and longer-term recommendations for future

work in each thrust area of the roadmap. In addition, a high-level list of future work recommendations is summarized.

Here, a summary of publications from the Sandia SHPM program (from FY11 to FY14) is provided. These reports/papers are the major sources for Chapters 2 through Chapter 8 of this final report.

Publications List

1. Griffith, D.T., Yoder, N., Resor, B.R., White, J., Paquette, J., Ogilvie, A., and Peters, V., "Prognostic Control to Enhance Offshore Wind Turbine Operations and Maintenance Strategies," Proceedings of the European Wind Energy Conference Annual Event (Scientific Track), April 16-19, 2012, Copenhagen, Denmark.

2. Griffith, D.T., Yoder, N.C., Resor, B.R., White, J.R., and Paquette, J.A., "Structural Health and Prognostics Management for Offshore Wind Turbines: An Initial Roadmap," Sandia National Laboratories Technical Report, December 2012, SAND2012-10109.

3. Myrent, N., Kusnick, J., Barrett, N., Adams, D., and Griffith, D.T., "Structural Health and Prognostics Management for Offshore Wind Turbines: Case Studies of Rotor Fault and Blade Damage with Initial O&M Cost Modeling," Sandia National Laboratories Technical Report, April 2013, SAND2013-2735.

4. Myrent, N.J., Kusnick, J.F., Adams, D.E., and Griffith, D.T., "Pitch Error and Shear Web Disbond Detection on Wind Turbine Blades for Offshore Structural Health and Prognostics Management," 54th AIAA/ASME/ASCE/AHS/ASC Structures, Structural Dynamics, and Materials Conference, April 8-11, 2013, Boston, MA, USA, AIAA-2013-1695.

5. Griffith, D.T., Yoder, N.C., Resor, B.R., White, J.R., and Paquette, J.A., "Structural Health and Prognostics Management for the Enhancement of Offshore Wind Turbine Operations and Maintenance Strategies," Wiley Journal of Wind Energy, September 2013.

6. Myrent, N., Griffith, D.T., et al, "Aerodynamic Sensitivity Analysis of Rotor Imbalance and Shear Web Disbond Detection Strategies for Offshore Structural Health Prognostics Management of Wind Turbine Blades," 32nd ASME Wind Energy Symposium, National Harbor, MD, USA, January 2014.

7. Kusnick, J., Adams, D., and Griffith, D.T., "Wind Turbine Rotor Imbalance Detection Using Nacelle and Blade Measurements," Wind Energy, Wiley, January 2014, DOI: 10.1002/we.1696.

8. Richards, P.W., Griffith, D.T, and Hodges, D.H., “Structural Health and Prognostic Management: Operating Strategies and Design Recommendations for Mitigating Local Damage Effects in Offshore Turbine Blades," 70th American Helicopter Society Annual Forum & Technology Display, May 20-22, 2014, Montreal, Quebec, Canada.

9. Richards, P.W., Griffith, D.T., and Hodges, D.H., “High-fidelity Modeling of Local Effects of Damage for Derated Offshore Wind Turbines,” Science of Making Torque from Wind Conference, June 18-20, 2014, Lyngby, Denmark.

10. Myrent, N.J, Barrett, N.C., Adams, D.E., and Griffith, D.T., “Structural Health and Prognostics Management of Offshore Wind Turbines: Sensitivity Analysis of Rotor Fault and Blade Damage with O&M Cost Modeling,” Sandia National Laboratories Technical Report, July 2014, SAND2014-15588.

11. Myrent, N, Adams, D., Griffith, D.T., “Wind turbine blade shear web disbond detection using rotor blade operational sensing and data analysis,” Philosophical Transactions of the Royal Society A, DOI: 10.1098/rsta.2014.0345 Published 12 January 2015.

(this page intentionally left blank)

CHAPTER 2. THE INITIAL ROADMAP FOR STRUCTURAL HEALTH AND PROGNOSTICS MANAGEMENT – FY11

The initial SHPM roadmap[1] is presented in this chapter. Highlights include:

- The multi-scale approach to simulation of damage is introduced.
- A high-fidelity 5MW blade model is developed and utilized for damage sensitivity studies for the case of trailing edge (TE) disbonding.
- Prognostics concepts are outlined.

[1] Sandia Technical Report: SAND2012-10109

SAND2012-10109
Unlimited Release
Printed December 2012

Structural Health and Prognostics Management for Offshore Wind Turbines: An Initial Roadmap

D. Todd Griffith, Brian R. Resor, Jonathan R. White, Joshua A. Paquette
Wind Energy Technology Department
Sandia National Laboratories
P.O. Box 5800
Albuquerque, New Mexico 87185-MS1124

Nathanael C. Yoder
ATA Engineering
11995 El Camino Real, Suite 200
San Diego, CA 92130

Abstract

Operations and maintenance costs for offshore wind plants are expected to be significantly higher than the current costs for onshore plants. One way in which these costs may be able to be reduced is through the use of a structural health and prognostic management system as part of a condition based maintenance paradigm with smart load management. To facilitate the creation of such a system a multiscale modeling approach has been developed to identify how the underlying physics of the system are affected by the presence of damage and how these changes manifest themselves in the operational response of a full turbine. The developed methodology was used to investigate the effects of a candidate blade damage feature, a trailing edge disbond, on a 5-MW offshore wind turbine and the measurements that demonstrated the highest sensitivity to the damage were the local pitching moments around the disbond. The multiscale method demonstrated that these changes were caused by a local decrease in the blade's torsional stiffness due to the disbond, which also resulted in changes in the blade's local strain field. Full turbine simulations were also used to demonstrate that derating the turbine power by as little as 5% could extend the fatigue life of a blade by as much as a factor of 3. The integration of the health monitoring information, conceptual repair cost versus damage size information, and this load management methodology provides an *initial roadmap* for reducing operations and maintenance costs for offshore wind farms while increasing turbine availability and overall profit.

CONTENTS

FIGURES

TABLES

NOMENCLATURE

BPE	Beam Property Extraction
CBM	condition based maintenance
FE	finite element
kWh	kilowatt-hour
LP	low pressure
MW	Megawatt
NREL	National Renewable Energy Laboratory
NuMAD	Numerical Manufacturing and Design Tool
O&M	operations and maintenance
RMS	root mean square
SHPM	structural health and prognostics management
SNL	Sandia National Laboratories
TE	trailing edge
UD	uni-directional

EXECUTIVE SUMMARY

Offshore wind energy could potentially play a significant role in helping the U.S. obtain an energy portfolio composed of clean, renewable and diversified resources. One current obstacle to the utilization of offshore wind energy is that most projections put the operations and maintenance (O&M) costs of offshore wind farms between 2 to 5 times the current average O&M costs for onshore wind farms [1]. One way in which those costs may be reduced is through a simple yet effective structural health monitoring system as part of an overall condition based maintenance paradigm. A successful health monitoring system would be able to reduce or eliminate unplanned or unnecessary maintenance as well as reducing logistic lead times and optimizing supply chain management through the use of prognostics (predictive estimates of damage).

A methodology has been created to aid in the development and optimization of a structural health and prognostics management (SHPM) system for wind turbine blades using physics-based simulations. The developed scheme is a multiscale modeling and simulation approach that propagates the effects of damage from high fidelity local simulations to full turbine simulations using reduced order models as illustrated in Figure 1. This technique can be used as an initial roadmap for the development of future health monitoring systems because it allows for the investigation of the effects of damage on both local and global scales. Globally, the operational responses of the full turbine models can be analyzed for the development of health monitoring algorithms and identification of the optimal measurement types, locations, and directions. The loads from these full turbine simulations can then be applied to high fidelity models in order to investigate the localized effects of damage.

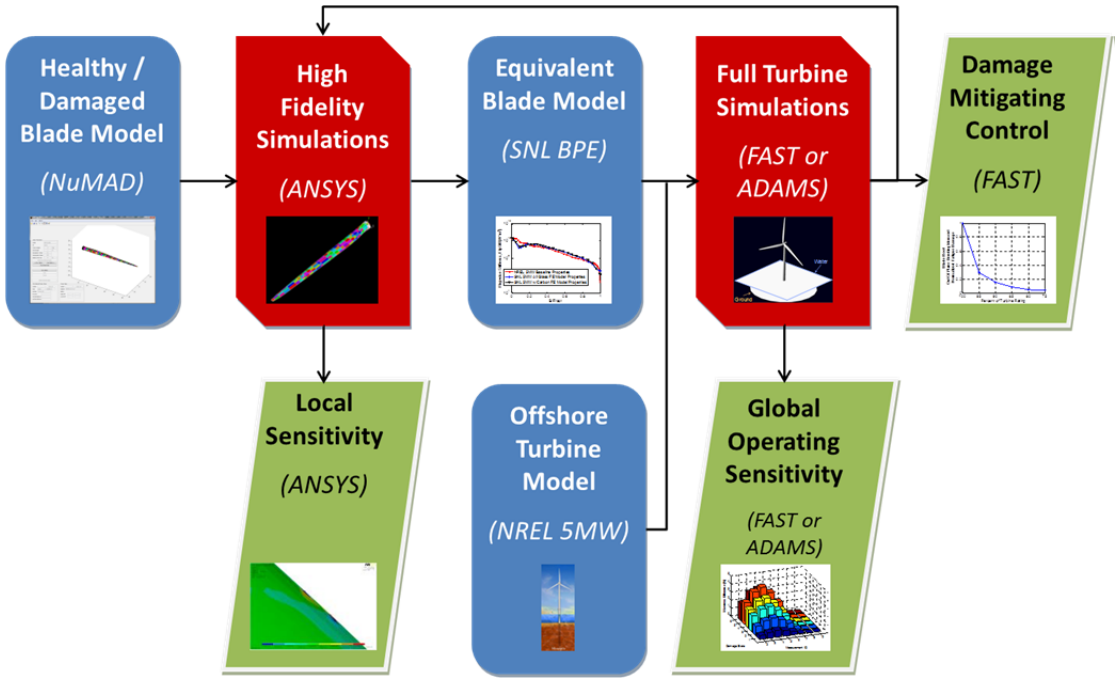

Figure 1. The multiscale modeling and simulation methodology designed to aid in the development and optimization of health monitoring systems for wind turbine blades.

As a representative example of how the developed methodology could be used to evaluate health monitoring systems, the effects of a trailing edge (TE) disbond on a 5-MW offshore wind turbine were investigated. Local analyses indicated that the TE disbond resulted in a local decrease in the torsional stiffness and change in strain field of the blade around the disbond, as shown by certain mode shapes such as the one in Figure 2. In global simulations (full turbine), the damage was most apparent in the sensitivity of the local per-revolution pitching moment of the damage blade around the disbond location (Figure 3). **The simulation results, clearly illustrated the benefit of the multiscale modeling approach and the utility of local strain measurements around the damage location for detection of TE disbonds.**

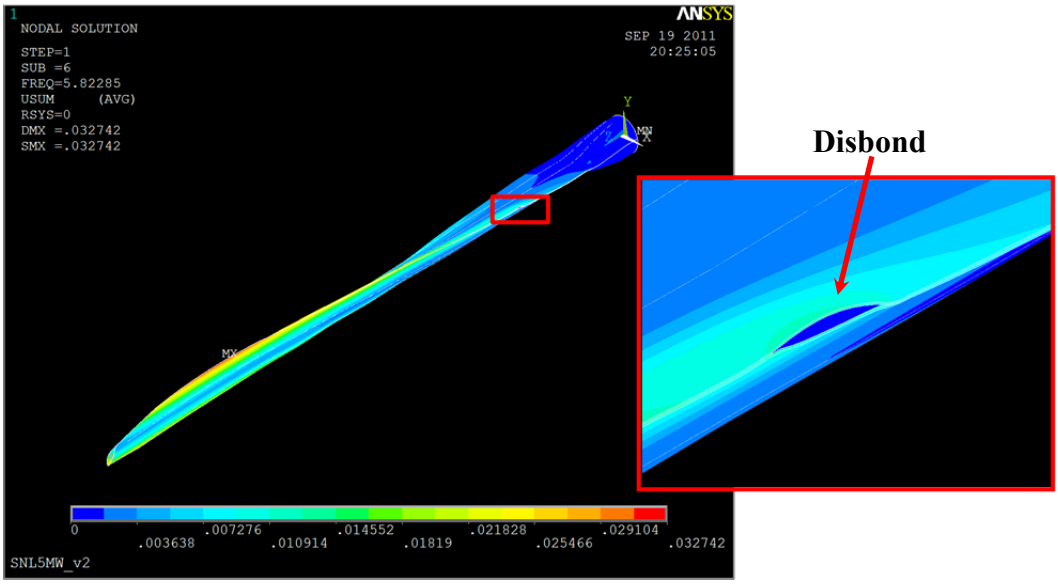

Figure 2. The TE separation in the first torsional mode shape of a damaged blade.

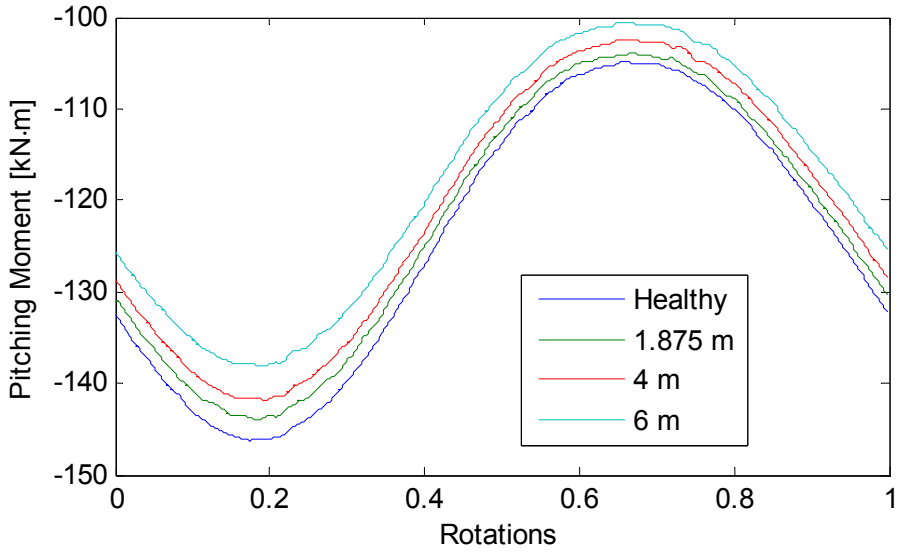

Figure 3. The increase in the once per-revolution local pitching moment of the healthy blade and blades with a disbond that was 1.875, 4 or 6 meters in length.

In addition to significant improvement in O&M costs of wind turbines, a structural health and prognostics monitoring system can be used as an integral component of health-driven wind turbine control. Consequently, damage mitigating control methodologies were investigated for smart turbine load management. **These initial simulations found that derating a turbine power production by as little as 5% resulted in a reduction in the equivalent loading by 10% and a blade fatigue life extension of 300%, as shown in Figure 4.** Therefore, if the health of a turbine is known, the power production of that turbine could be derated slightly to avoid costly unscheduled repairs and coordinate the lower-cost scheduled repair of many turbines. While further research into the optimal damage mitigating control methodologies is needed, it is evident that significant extensions of life can be achieved through small and simple changes in the turbine's operation. Furthermore, these load management strategies could prove especially beneficial for offshore turbines where maintenance may be limited by the weather and the increased possibility of servicing multiple turbines during a single visit to the wind plant may result in significantly reduced offshore O&M costs.

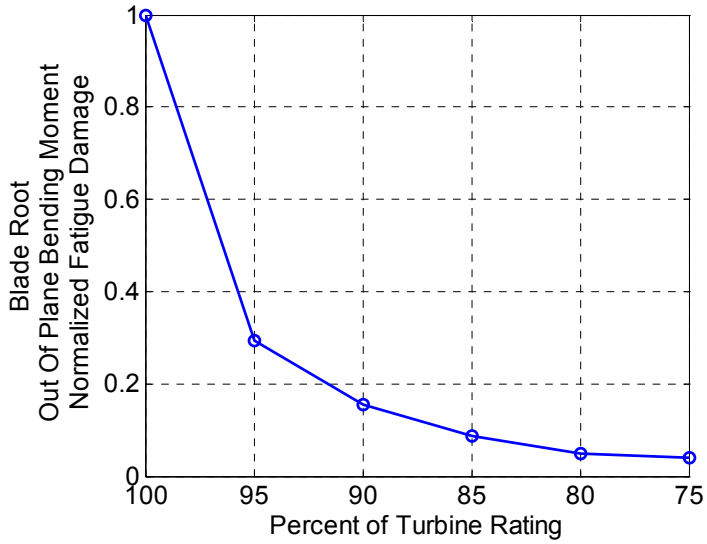

Figure 4. Normalized fatigue damage due as a function of turbine rating.

1. INTRODUCTION

Offshore wind energy in the United States is an untapped energy resource that could play a pivotal role in helping the U.S. obtain an energy portfolio composed of clean, renewable and diversified resources. Some of the drivers for the utilization of offshore wind include the proximity of the offshore resources to population centers and the potential for higher capacity factors due to higher resource winds [1, 2]. Because of these and other potential benefits of offshore wind, the Offshore Wind Innovation and Demonstration initiative has developed an ambitious goal of deploying 10 GW of offshore capacity by 2020 at a cost of energy of only $0.10/ kWh [3].

1.1. Drivers for Offshore SHPM

As of June 2011, while nine offshore projects totaling over 2 GW of capacity were in various stages of the permitting and development process, no offshore wind energy projects had been installed in the United States [4]. Part of the reason for this lack of development is that operations and maintenance (O&M) costs are expected to be significantly higher for offshore wind turbines than onshore wind turbines. Recent projections of O&M costs have ranged between $11 and $66 U.S. dollars per megawatt-hour with the majority of estimates being between 2 to 5 times the cost of onshore O&M [1]. These higher O&M costs represent a larger overall proportion of the cost of energy than for onshore turbines even when the large initial investment required for the installation of offshore turbines is included [5]. One of the reasons that O&M costs are likely to be higher offshore than onshore is that the offshore environment will bring with it increased loading which is relatively uncharacterized due to the lack of existing offshore installations. Offshore turbines will also have to be built to withstand the environmental harshness of the offshore environment. Lastly, access to the turbines will be difficult, costly, and occasionally may not be possible due to high sea states [1,6].

1.2. SHPM Benefits

One potential way in which these higher O&M costs could be addressed is through the use of a structural health and prognostics management (SHPM) system as part of a condition based maintenance (CBM) paradigm [6-12]. By continuously monitoring the health, or condition, of structural components in each wind turbine from land, required maintenance actions can be scheduled ahead of time and performed when they are needed rather than on a preset schedule or only after failure has already occurred. The benefits of a CBM strategy are expected to include less regular maintenance, the reduction or avoidance of unscheduled maintenance and improved supply chain management [6, 9-11].

Furthermore, because wind turbines are active systems, monitoring the health of wind turbine components allows turbines to be operated based on their health so that smart turbine load management strategies can be used to optimize the profit of the entire wind plant. For example, if a turbine blade becomes damaged and that damage is detected at an early stage by the SHPM system, the turbine could be derated so that smaller less costly repairs could be performed on the turbine. While this action would reduce the amount of power generated by the turbine in the

short-term, it may allow for less extensive maintenance actions to be performed, extend the overall life of the turbine, and allow for multiple turbines to be serviced during the same visit to the plant in order to maximize the overall profit of the wind power plant. In addition, the SHPM system could provide information to avoid catastrophic failures by alerting operators to the presence of damage before it reaches dangerous levels.

2. MULTISCALE SIMULATION APPROACH

To facilitate the investigation of SHPM systems for wind turbine blades using operational responses, a multiscale modeling approach was developed that propagates the effects of damage from high fidelity local simulations to full turbine simulations using reduced order models. A simulation campaign was then performed to identify operational response measurements that are sensitive to a representative form of damage. These simulations were an essential first step in identifying promising measurements for use in the operational monitoring of offshore wind turbines because of the scarcity of data from offshore wind turbines. In addition, simulations provide the unique ability to cost effectively investigate the sensitivity of many different potential measurements and measurement locations along with many types of blade or turbine damage while eliminating variability from sources other than damage.

In order to accurately capture the effects of damage on an offshore wind turbine's response a multiscale modeling approach was used. The simulation approach used high fidelity blade and damage models to model the influence of damage on the blade. This model was then reduced to an equivalent blade model of sufficient resolution to capture the influence of the damage while still being able to be integrated into simulations of a full offshore wind turbine. In addition to the analysis of the results from these full turbine simulations, the equivalent loads from these simulations can be fed back into the high fidelity model so that localized sensitivity measures can be obtained. The overall approach is shown in flowchart form in Figure 5. As an extension of this work even more accurate and refined damage modeling methodologies could be used to create the damage blade models or model the propagation of damage.

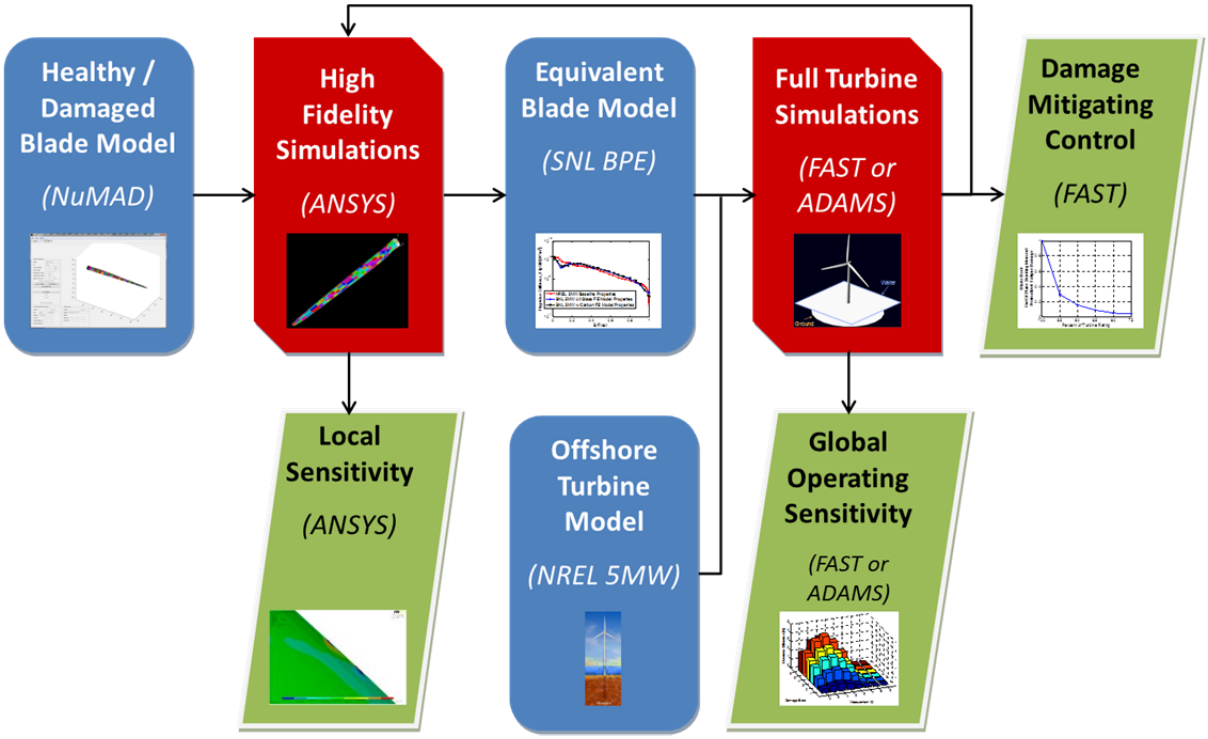

Figure 5. Developed simulation methodology for the identification of operational response measurements that are the most sensitive to damage.

In order to perform the desired simulations a variety of different software packages had to be integrated. The software packages that were used to obtain the results in this report are indicated in parenthesis in the Figure 5 flowchart. Sandia National Laboratories' (SNL's) Numerical Manufacturing and Design Tool (NuMAD) software was used to create a high fidelity blade model in the commercial finite element software package ANSYS. A trailing edge (TE) disbond damage feature was then introduced into the model and equivalent beam properties were extracted using SNL's Beam Property Extraction (BPE) software. The reduced order models were then integrated into a full turbine model for simulations of the damaged turbine in either FAST [13] or MSC.ADAMS [14]. Results from each stage of this modeling process were then used to assess the influence of the damage on the response of the blade and the turbine as a whole and determine a subset of measurements that could prove beneficial for future SHPM investigations. Global operating sensitivity to damage was calculated using either the FAST or MSC.ADAMS turbine simulations. Aerodynamic loads from the full turbine simulations were fed back to the high fidelity simulation to quantify the localized damage sensitivity.

Even if a SHPM system proves effective in detecting damage, in order to utilize the information most effectively, the cost of repairing the damage should be taken into account in the CBM framework. This allows the health information to not just be used for the scheduling and optimization of the maintenance procedures, but to also be used to optimize the operation of the slightly damaged turbines. By propagating aerodynamic loads from full turbine simulations back into local high fidelity simulations it was demonstrated that significant extensions in the fatigue life of a blade could be achieved by derating a turbine's power production by as little as 5%. Therefore, using smart turbine load management strategies with damage mitigating control could allow for the productive life of blades to be extended while slowing the propagation of damage until the appropriate maintenance can be performed in the most cost effective manner.

This report will attempt to address the integration of SHPM into the O&M process for wind power plants in several ways. First a multiscale simulation based methodology that can be used to determine the measurement channels that are the most sensitive to a representative form of damage in a cost-effective manner has been developed and can be extended to investigate the application of other potential health monitoring methods. Secondly, the dependence of repair costs on damage size has been recognized through illustration of a conceptual model. The utility of integrating the knowledge of these costs with damage state of the turbine can be utilized not just to perform more cost-effective CBM but also to operate individual turbines to extend their life and maximize overall plant profit.

3. FIVE MEGAWATT OFFSHORE TURBINE MODEL DEVELOPMENT

In order to investigate the potential of using operational measurements for the SHPM of offshore wind turbines a model of a representative offshore turbine was needed. This section will describe the overall turbine model that was used in this simulation study and then move on to detail the development of the high fidelity wind turbine blade model. Next, the damage modeling methodology used in this study and the development of reduced order blade models from the finite element models will be discussed.

3.1. Five Megawatt Turbine Model Description

A representative utility-scale multimegawatt turbine model known as the National Renewable Energy Laboratory (NREL) offshore 5-MW baseline wind turbine was developed by NREL in order to support concept studies aimed at assessing offshore wind technology [15]. The model is used as a reference by research teams throughout the world to standardize baseline offshore wind turbine specifications and to quantify the benefits of advanced land- and sea-based wind energy technologies. The wind turbine is a conventional three-bladed upwind variable-speed variable blade-pitch-to-feather-controlled turbine. The model was created using broad design information from published documents of turbine manufacturers, with a heavy emphasis on the REpower 5-MW machine. Detailed data was unavailable so publicly available properties from the conceptual models in the WindPACT, RECOFF, and DOWEC projects were used to create the 5-MW model. The specifications of the NREL offshore 5-MW baseline wind turbine include aerodynamic, structural, and control-system properties. Table 1 lists the basic specifications of the 5-MW turbine model and an image of the MSC.ADAMS model of the offshore wind turbine is shown in Figure 6.

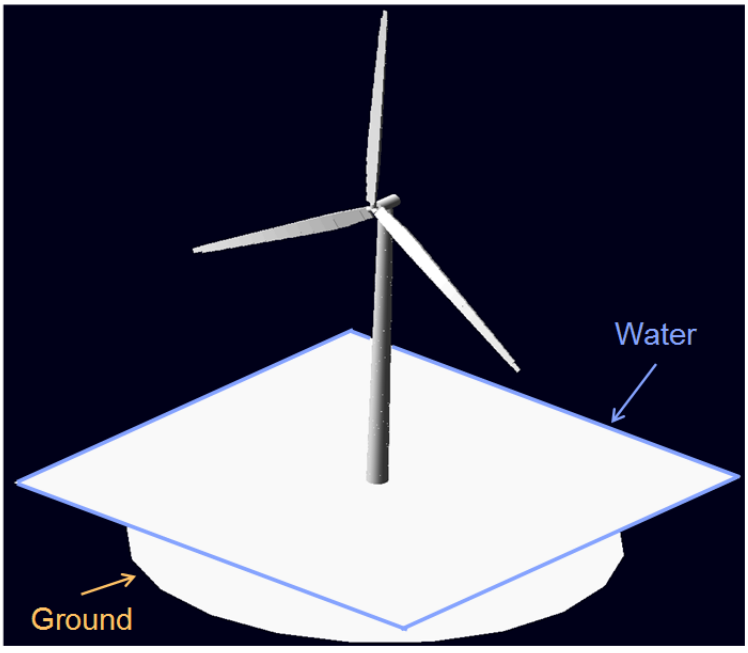

Figure 6. An image of the offshore 5-MW wind turbine model in MSC.ADAMS.

Table 1. Gross properties of the NREL 5-MW baseline wind turbine.

Property	Value
Rating	5 MW
Rotor Orientation, Configuration	Upwind, 3 Blades
Control	Variable Speed, Collective Pitch
Drivetrain	High Speed, Multiple-Stage Gearbox
Rotor, Hub Diameter	126 m, 3 m
Hub Height	90 m
Cut-In, Rated, Cut-Out Wind Speed	3 m/s, 11.4 m/s, 25 m/s
Cut-In, Rated Rotor Speed	6.9 rpm, 12.1 rpm
Rated Tip Speed	80 m/s
Overhang, Shaft Tilt, Precone	5 m, 5º, 2.5º
Rotor Mass	110,000 kg
Nacelle Mass	240,000 kg
Tower Mass	347,460 kg
Water Depth	20 m
Wave Model	JONSWAP/Pierson-Moskowitz Spectrum
Significant Wave Height	6 m
Platform	Fixed-Bottom Monopile

To obtain a blade model that could be used as part of full turbine simulations, Sandia's NuMAD software was used to design a detailed composite layup. NuMAD allowed complex blade models to be integrated with damage models in ANSYS after which the effective beam properties of the damaged blade could be obtained using the SNL BPE software. The following sections detail the development of the 5-MW blade model and the damage modeling methodology used to model a TE disbond.

3.2. Five Megawatt Blade Model Development

The publicly available NREL 5-MW turbine aeroelastic model and associated report do not contain detailed information about the blade design, i.e. material selection and material placement, airfoil shapes and shear webs. The publicly available model only contains a desired distribution of effective cross sectional properties for a blade. However, a detailed computer model of the blade is needed in order to perform analyses to support structural health monitoring research on a system of this size. Sandia's NuMAD software was used to create the detailed blade model for the current work. NuMAD is a preprocessor for ANSYS, a commercially available finite element (FE) analysis software package. NuMAD translates material properties, material locations, airfoil shapes and shear web locations into a large degree-of-freedom ANSYS FE model composed of shell elements. ANSYS is used to solve the model's response to input forces that are representative of aerodynamic loads on the blade. Calculation of localized strains, blade panel buckling response and general blade deformation are all important analyses that can be performed in ANSYS.

The blade model developed for this work used existing blade geometry data from the DOWEC study and composite layup information from the UpWind program in a preliminary 5-MW

baseline blade model. The preliminary all-glass composite layup (a modified version of UpWind) produced a blade that is too heavy compared to the blade weight specified for the 5-MW turbine in the NREL report [15]. Weight reduction of the initial blade was achieved through the use of carbon fiber spar caps, which at the same time enabled preservation of the specified distribution of blade stiffness. Material properties for uni-directional (UD) carbon fiber (Newport 307) were obtained from the Sandia-MSU Materials Database [16] and used for the carbon spar caps. Figure 7 illustrates the distribution of material layers along the span of the blade.

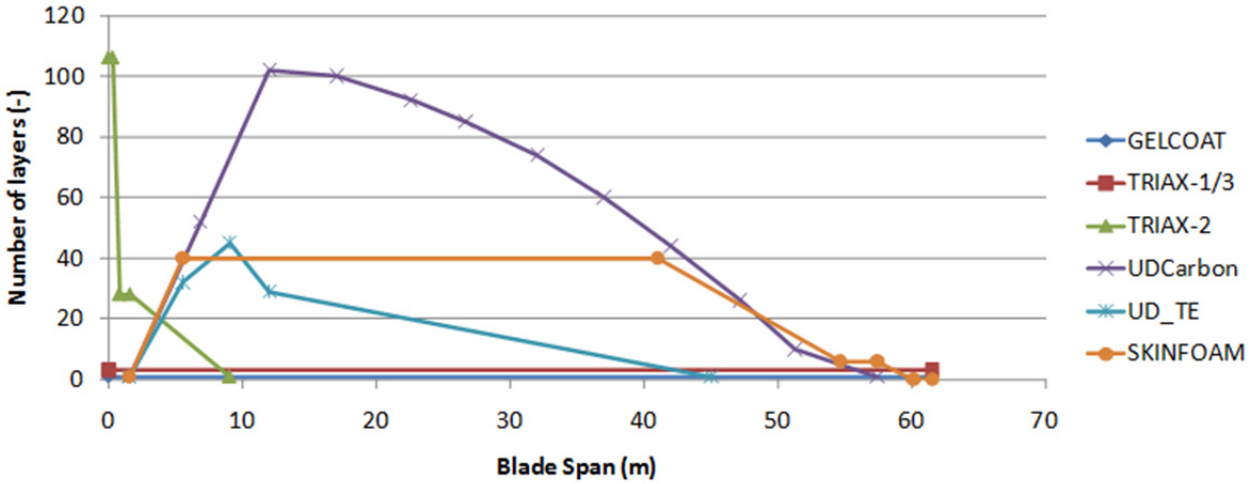

Figure 7. Distribution of layers along the span of the blade model.

The TU-Delft family of airfoils was used for the majority of this blade. NACA 64-series airfoils were used in the final one-third blade span. No transition airfoils were reported between the root circle and airfoil at maximum chord. Intermediate airfoil shapes were developed as part of this work using a technique that preserves the blending of camber lines while also preserving a smooth blade thickness profile. Figure 8 shows a picture of the completed finite element model in ANSYS.

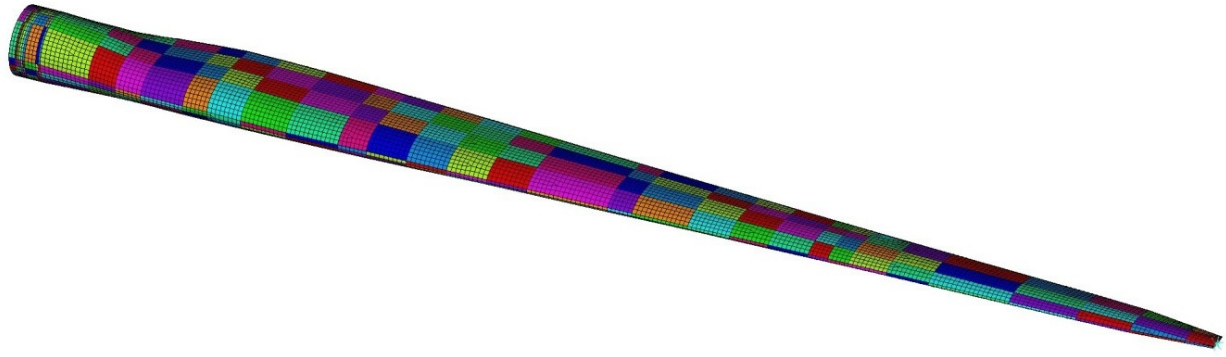

Figure 8. Overview of the ANSYS finite element mesh for the 5-MW blade model.

The Sandia Beam Property Extraction (BPE) tool was used to determine the equivalent beam property distributions for this blade model. The BPE tool is discussed in more detail in Section

3.3 of this report. Figure 9 shows three different curves representing beam properties: first, the specified properties taken directly from the NREL 5-MW aeroelastic system model, second, the properties computed using the preliminary all-glass blade model, and third, the properties computed using the blade model with carbon fiber spar caps. Figure 9 (a) shows the discrepancy between the NREL 5-MW specified mass distribution and the mass distribution achieved using fiberglass alone. It also shows the greatly decreased mass distribution achieved by replacing the fiberglass spar cap with the appropriate number of layers of unidirectional carbon fiber. The three remaining plots in Figure 9 ((b)-(d)) show the variations in the blade's stiffness parameters along the span of the blade while Table 2 shows the computed blade mass for each of the three scenarios. The inclusion of the carbon spar cap in the SNL 5MW blade resulted in good agreement with the mass and stiffness properties of the NREL 5MW baseline.

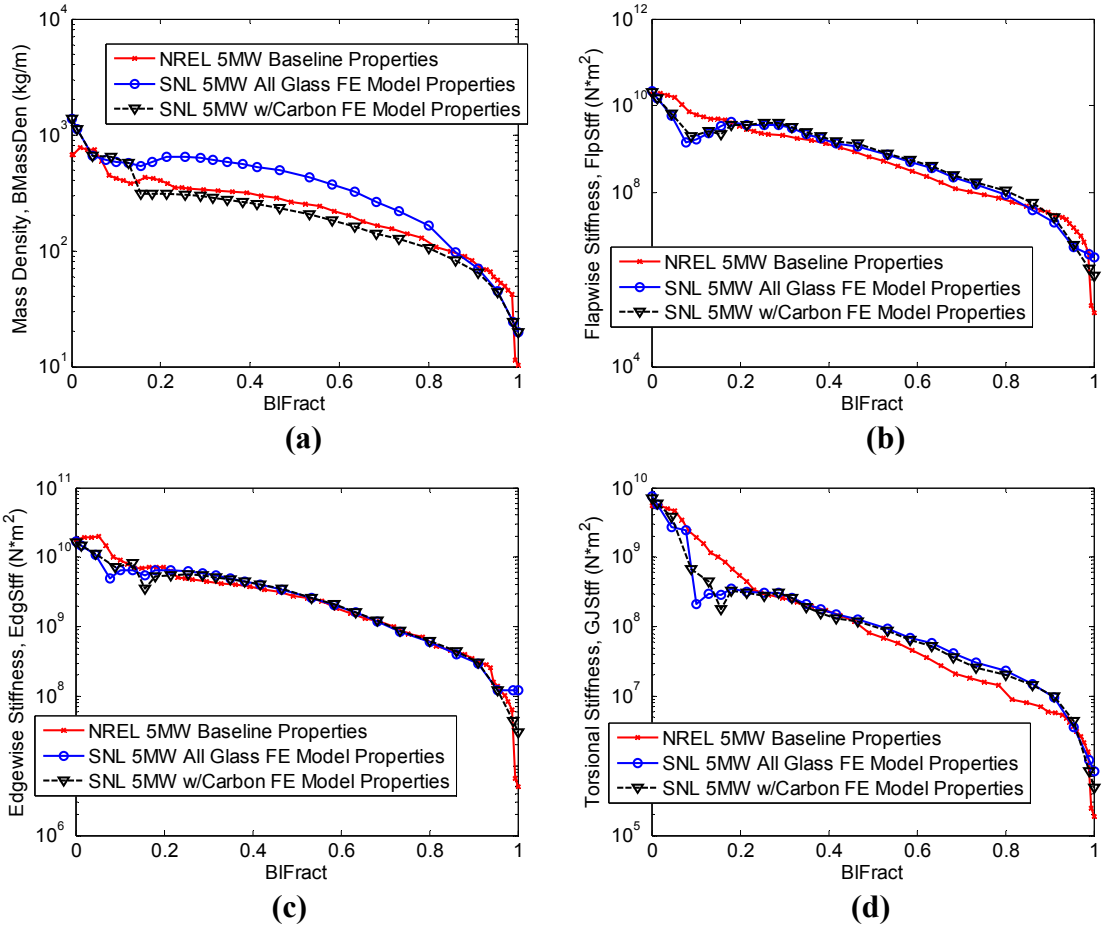

Figure 9. Blade properties as calculated by BPE including the (a) mass density, (b) flap-wise stiffness, (c) edge-wise stiffness, and (d) torsional stiffness along the span of the blade.

Table 2. Summary of estimated mass for each version of the model.

Specified weight of NREL 5-MW Blade	17,740 kg
Fiberglass Blade Model Weight	25,630 kg
Weight of Blade Model With Carbon Spar Caps	16,381 kg

3.3. Equivalent Beam Property Extraction (BPE)

Blades are complex structural items with span-wise varying shapes, many layers of fiber and resin composite material, sandwich structures and, typically, one or more shear webs (Figure 10). The current approach for wind turbine aeroelastic simulation requires the simplification of this complex wind turbine blade structure into a beam model. Equivalent beam properties of the blade are determined at a discrete number of locations along the span of the blade in order to create a model consisting of several beam elements.

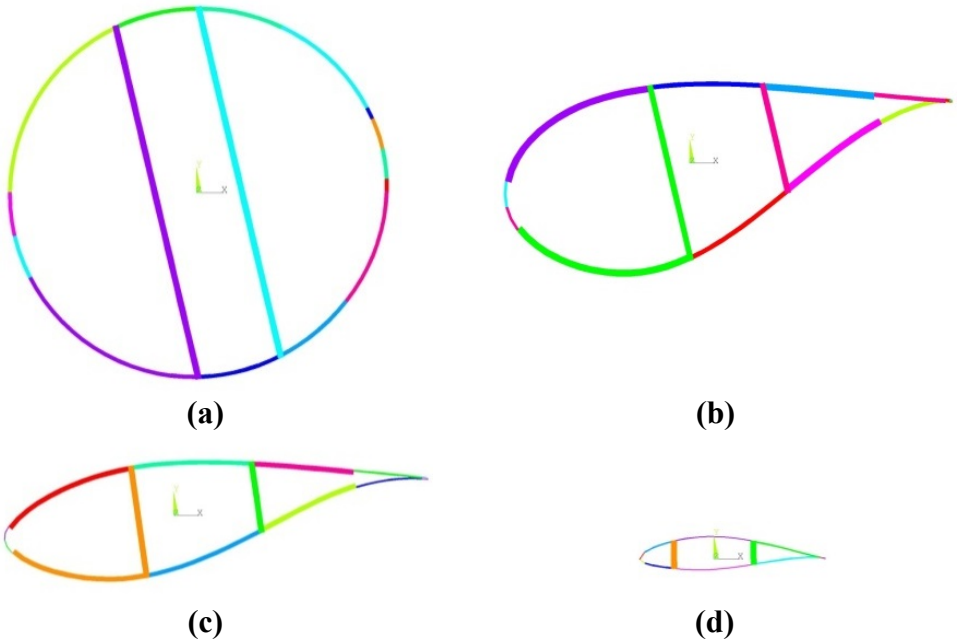

Figure 10. Blade cross section shapes for the SNL 5-MW blade model. Colors correspond to different composite layup regions: (a) root, (b) max chord, (c) mid-span and (d) tip.

Currently there are multiple tools and approaches available to the wind industry that will aid the designer in converting complex blade laminate and structural geometry information into equivalent beam properties for aeroelastic simulations. A common approach is to calculate properties for the Euler-Bernoulli beam based on material properties and skin geometry of each two-dimensional section. The properties at each two-dimensional section are independent of adjacent sections. Simple examples include the following. In addition, warping functions for torsion must be calculated.

$$EI\_flap = \iint E(x,y)x^2 dxdy\,, \tag{1}$$

$$EI\_edge = \iint E(x,y)y^2 dxdy\,, \tag{2}$$

$$GJ = \iint G(x,y)(x^2+y^2)dxdy \quad \text{and} \tag{3}$$

$$EA = \iint E(x,y)dxdy \tag{4}$$

A more involved approach uses a three-dimensional finite element model of the blade and analyzes the deflection of selected nodes in response to applied loads, as seen in Figure 11. Effective properties for Timoshenko beam elements are then determined by analyzing the relative displacements for each pair of adjacent sections. This approach can include effects that are difficult to include in a two-dimensional approach, such as axial warping in torsion and cross-sectional deformation in bending.

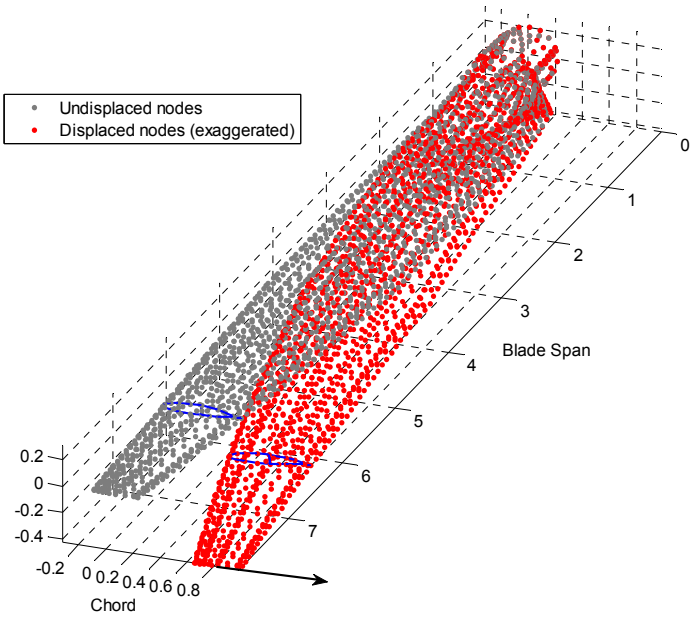

Figure 11. Finite element nodes: single point edgewise load at the blade tip. A set of finite element nodes representing a blade section is highlighted in blue.

SNL BPE is a code and a technique to extract equivalent beam properties from a wind turbine blade finite element model [17]. The method is based on applying loads in each of the six degrees of freedom at the tip of the three-dimensional blade model then processing the resulting nodal displacements to generate the 6×6 Timoshenko stiffness matrices for the specified beam discretization. The method; therefore, includes three-dimensional effects such as shear and warping. It also captures effects arising from nearby boundary conditions and non-uniform blade geometry. Calculation of the section properties are demonstrated in a series of validation examples in Malcolm and Laird [17-20]. BPE accommodates blades with curvature in one or both directions and has the ability to identify the center of mass, elastic center, principal directions, shear center and off-axis coupling terms. More discussion of BPE theory and application can be found in references by Laird et.al. [21] and Resor [22, 23].

To improve the overall performance of BPE several small changes were made to the BPE process for its application in this work. The first change was the application of more than six load cases to the ANSYS model. By applying more than six linearly independent sets of loads, the inversion process to determine the equivalent stiffness matrices was overdetermined and the numerical conditioning of the inverse problem was improved. The second change was the incorporation of the beam elements' physical properties directly into the inversion process used to calculate the resulting stiffness matrices. Based on the physical characteristics of the beam elements, each section should have a symmetric positive-definite stiffness matrix. However,

neither the symmetry nor the positive definitiveness of the estimated stiffness matrix is guaranteed through the use of the previously utilized linear least squares inversion. To address this problem, a method that had been developed specifically to determine symmetric positive-definite matrices [24] was used to calculate the resulting 6x6 beam element stiffness matrices for the applied forces and resulting displacements.

The detailed blade model (SNL 5MW) developed for this study is a useful tool for evaluation of local changes in blade structural response for various applied loads. The current work has focused on developing a model that could be used for these initial SHPM scoping studies to direct future work. While the current model is fairly mature, it will also benefit from additional refinements in the future. First, the outboard upper surface (low pressure, LP, surface) spar cap is rather thin and buckles under applied load. This can be dealt with by 1) tapering the width of the spar cap so that it's narrower outboard, 2) adding a foam layer in the LP spar cap to increase thickness and buckling resistance, or 3) adding more layers of UD carbon outboard in the spar cap. This blade design should be evaluated in detail with respect to all certification design load cases. As is, there are certain localized strains that exceed allowed levels under applied load as well as buckling load factors that are low. Both of these issues can be solved with a deeper assessment and redesign of material placement and transition of cross section shapes. Even with the future work desired on this blade model, it is adequate for the SHPM investigation described in the remainder of the report.

3.4. Damage Modeling Methodology

To model the presence of a TE (trailing edge) disbond on a wind turbine blade, the NuMAD software was modified so that nodes on the blade TE were split into two different nodes (i.e. TE nodes were unequivalenced). This effectively split the blade model at the TE in a similar way to how the blade is physically constructed by bonding two separate clam shells together. To simulate a healthy TE bond, the top and bottom TE nodes were connected using constraint equations in all six degrees of freedom. In the area of the blade in which the TE disbond existed the constraints were removed so that there was no connection between the top and bottom of the blade. Figure 12 shows an example of the influence of this disbond on the blade's dynamics where the separation of the 1.25 meter long disbond extending from max chord outboard is readily apparent in the first torsional mode shape of the cantilevered blade. While the separation of the TE is clearly visible in the mode shape, it resulted in a decrease in natural frequency of less than 0.01 Hz.

While this modeling methodology effectively models a disbond in which the two sides do not come into contact, it fails to take into account the possible interaction of the top and bottom surfaces of the disbond. For large disbonds in which interaction between the top and bottom of the blade may have a significant influence, the relative decrease in stiffness due to the disbond is likely over-estimated because the added stiffness due to the interaction of the two sides of the disbond is not taken into account. Modeling the interaction between the two surfaces could be achieved using nonlinear surface contact constraints on both sides of the blade but this was not accomplished during this initial investigation and remains as future work.

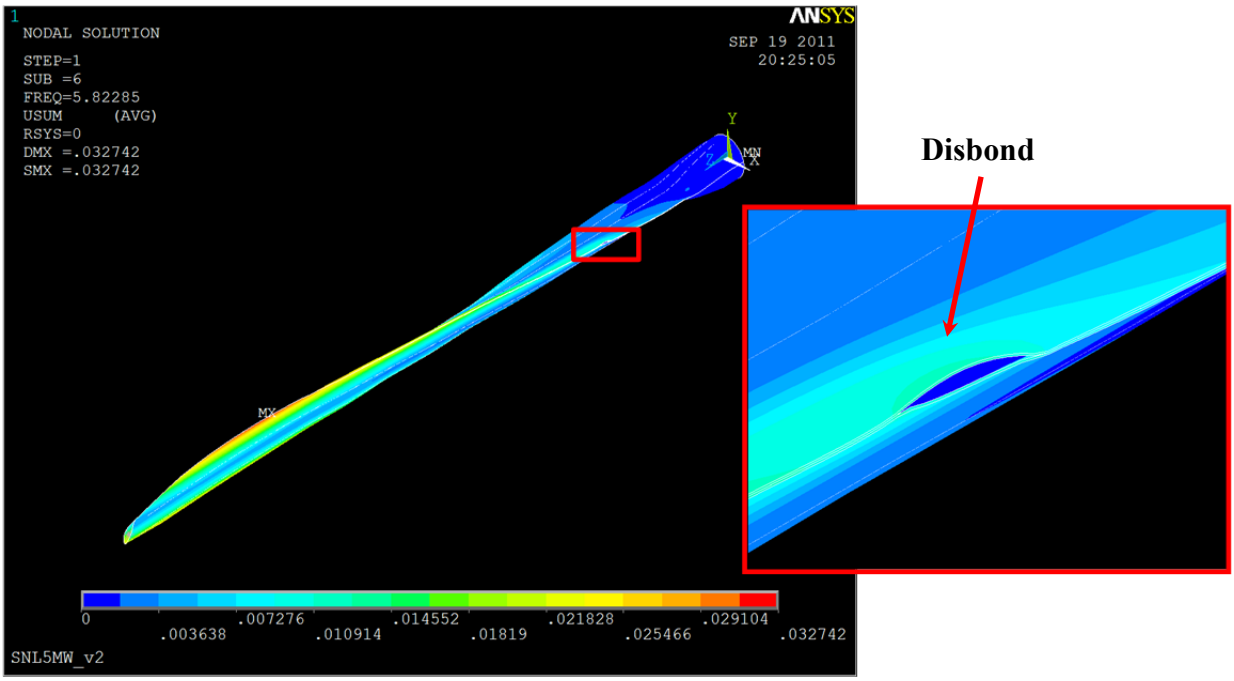

Figure 12. An image of the first torsional mode shape of a cantilevered blade with a disbond extending 1.25 m from max chord toward the tip of the blade.

4. DAMAGE SENSITIVITY STUDY

In this chapter the developed multiscale modeling methodology is demonstrated through an investigation into the sensitivity of a wide range of potential operational measurements to the presence of a TE disbond. This damage feature was chosen because it is commonly seen in the field [25]. For this initial investigation, all of the disbonds were assumed to have initiated at max chord of the blade (14.35 meters along the span from the root) and propagated outboard toward the tip of the blade.

This chapter begins with an explanation of the results obtained from the reduced order equivalent blade models of the damaged blades that were produced using SNL's BPE technique (Section 3.3) and the physical insight that these results give on the physical effects of the TE disbond. Next a brief example of a local sensitivity analysis that uses the loads from the full turbine simulations is presented that demonstrates the localized nature of the changes in the blade's strain field due to damage. The chapter then concludes with an in depth review of the global sensitivity analysis. The data features that were used to quantify the sensitivity of the operational measurements are presented first and then the results from full turbine aeroelastic simulations in FAST [13] and ADAMS [14] are presented. While, the results from the FAST simulations showed only very slight changes in the operational response of the turbine the ADAMS simulations resulted in far more significant changes. This difference is believed to be due to the fact that ADAMS takes into account the torsional flexibility of the blades while FAST does not.

4.1. BPE Five Megawatt Sensitivity Analysis

The creation of a reduced order model for use in full turbine simulations offered the ability to investigate the physical manifestation of the TE disbond on the blade stiffness parameters. To determine which of the span-wise stiffness values calculated using BPE were the most sensitive to the presence of the TE disbond, a series of 37 different blade models were created with disbonds that extended up to 6 meters outboard from max chord. For each of these blade models the equivalent beam stiffness values were extracted using BPE at 23 locations along the span of the blade.

4.1.1. *BPE Convergence Analysis*

The first step in the extraction of equivalent beam parameters was to perform a convergence analysis to determine an appropriate mesh seed size in ANSYS to ensure that the parameters extracted using BPE were from a sufficiently converged model. This analysis was performed by calculating the average absolute percent difference in the extracted BPE stiffness values between each candidate seed size and the reference results that were obtained from a mesh seed size that was 1.8% of maximum chord (0.08 m). By calculating the average absolute percent difference of the changes in the estimated EI, EA, and GJ values, changes in all of the estimated stiffness values could be combined into a single convergence metric. The resulting mean absolute percent difference as a function of mesh seed size can be seen in Figure 13 where the mesh seed size is plotted on a log scale. Based on this analysis a mesh seed size of 0.125 m was chosen for future analyses and is highlighted in Figure 13.

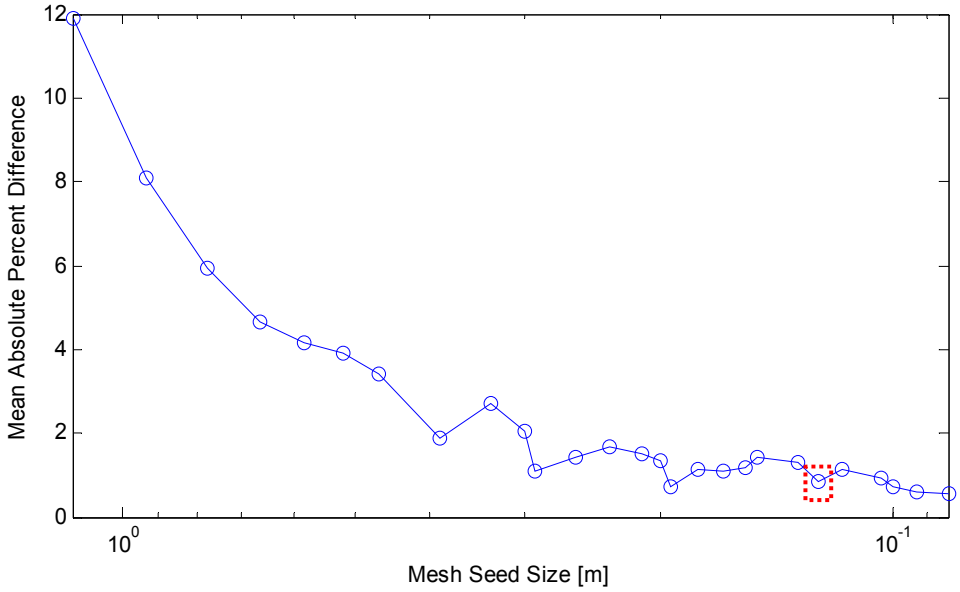

Figure 13. The mean absolute percent difference in the extracted BPE stiffness values as a function of ANSYS mesh seed size.

4.1.2. *BPE Trailing Edge Disbond Sensitivity*

The sensitivity of the estimated reduced order stiffness values to the TE disbond was quantified by calculating the percent decrease in each of the stiffness values for all of the sections in the reduced order model. The flap-wise and edge-wise bending stiffness values were almost completely unaffected by the presence of the disbond as can be seen from Figure 14. In these plots the percentage decrease in the stiffness of each element is represented by the height and color of the vertical bar where the location of the element and the length of the disbond corresponding to the change are shown on the x-axis and y-axis respectively.

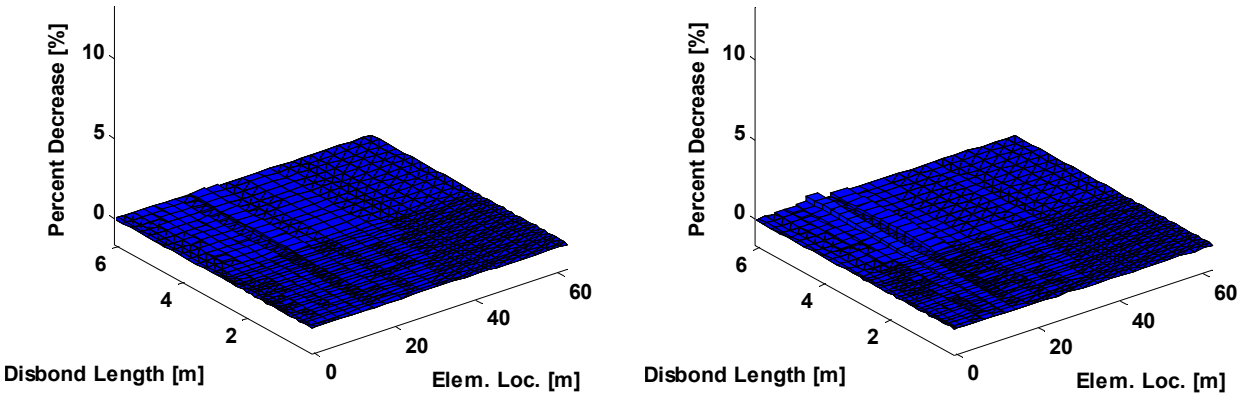

Figure 14. The percent decreases in the flap-wise (left) and edge-wise (right) stiffness values for segments spaced along the length of the blade and varying length disbonds.

The axial stiffness values extracted by BPE decrease slightly with the presence of fairly large TE disbonds as shown in Figure 15. For the 6 meter disbond a percentage decrease of 1.8% was seen in the blade section that was just at the outboard end of the disbond. This decrease may

have been due to changes in the three-dimensional warping and shear deformations of the blade that were caused by the presence of the disbond.

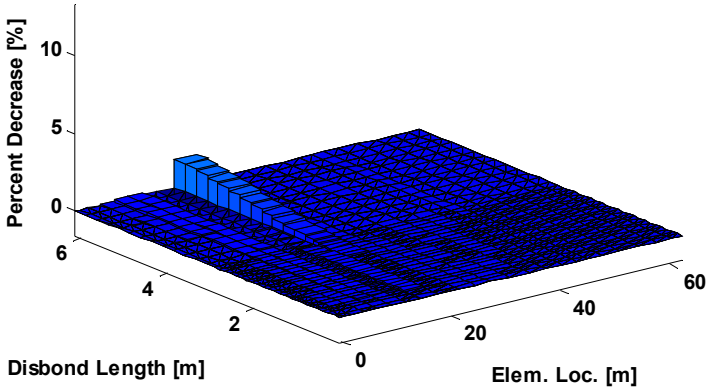

Figure 15. The percent decrease in the equivalent axial stiffness calculated by BPE due to a TE disbond.

The disbond had by far the largest effect; however, on the torsional stiffness of the blade sections near the damage as can be seen in Figure 16. In this plot percent decreases of over 13% were seen in the blade sections due to the 6 meter disbond while a 0.625 meter long disbond caused decreases of up to 0.9%. Another pertinent feature of the changes due to damage was that the decreases in the stiffness values were highly localized to the regions in which the disbond was present. The reduction of the reduced order model's torsional stiffness due to the disbond gives physical insight into the problem and suggests that the blade's torsional properties are heavily influenced by the TE disbond.

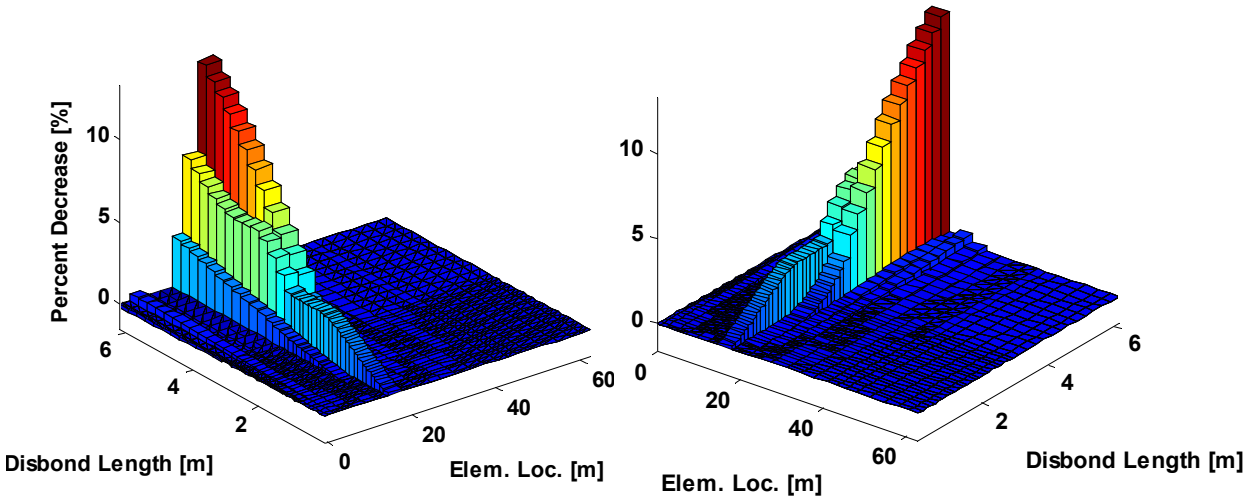

Figure 16. The percent decrease in the equivalent torsional stiffness of each section due to a TE disbond. Two different views of the same plot are shown to demonstrate the localization of the stiffness changes in the damaged sections of the blade.

4.2. **ANSYS Strain Field Results (Local Sensitivity)**

Aerodynamic loads from the full system aeroelastic simulation can be translated to a set of equivalent forces for application to finite element nodes as a distributed load in the detailed blade model. Figure 17 shows the 5-MW blade model with force vectors representing the steady aerodynamic load for normal operation at 11 m/s, near rated wind speed.

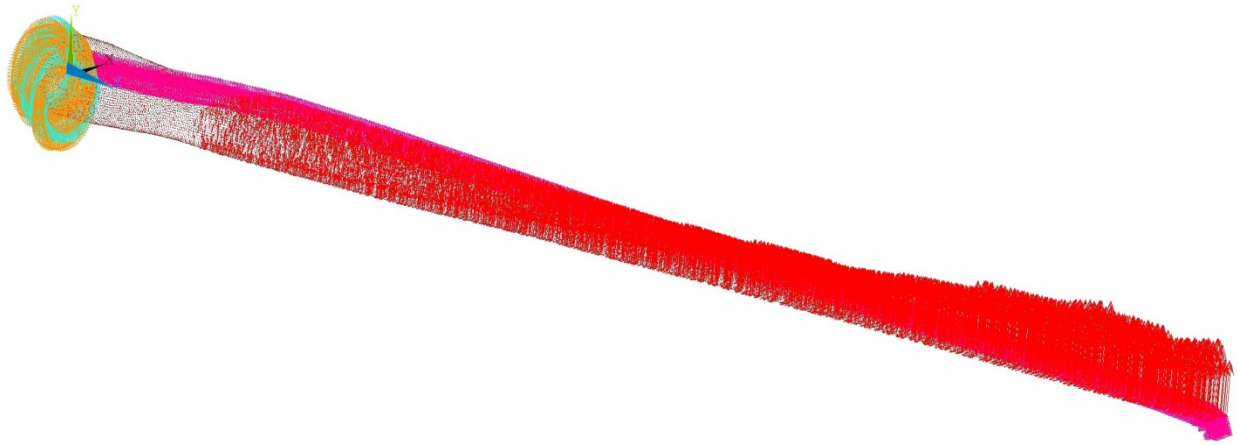

Figure 17. Force vectors representing aerodynamic load applied to the 5-MW blade finite element model.

A 0.625 meter long TE disbond, representing just over 1% of blade span, has been modeled in the detailed blade model. The response of the blade structure to the applied aerodynamic forces was computed for both the healthy and damaged blades and localized strains were determined in each element for both scenarios. The difference in strains for each element can be computed in order to see the effects of the damage on the overall blade strain distribution. The difference in blade longitudinal strain (along the span of the blade) between the healthy and unhealthy conditions is shown in Figure 18. The vast majority of the blade does not experience a change in strain due to this magnitude of damage, seen as the color green. Near the disbond at the TE there is evidence of a redistribution of strains, on the order of 50-150 microstrain. While a change in strain of this magnitude could be detected by a strain based health monitoring system, the sensors would clearly have to be located close the location of damage. Furthermore, data normalization procedures would be needed in order to account for variations in the operating temperature, turbine speed, and variations in the aerodynamic forces that naturally occur during turbine operation.

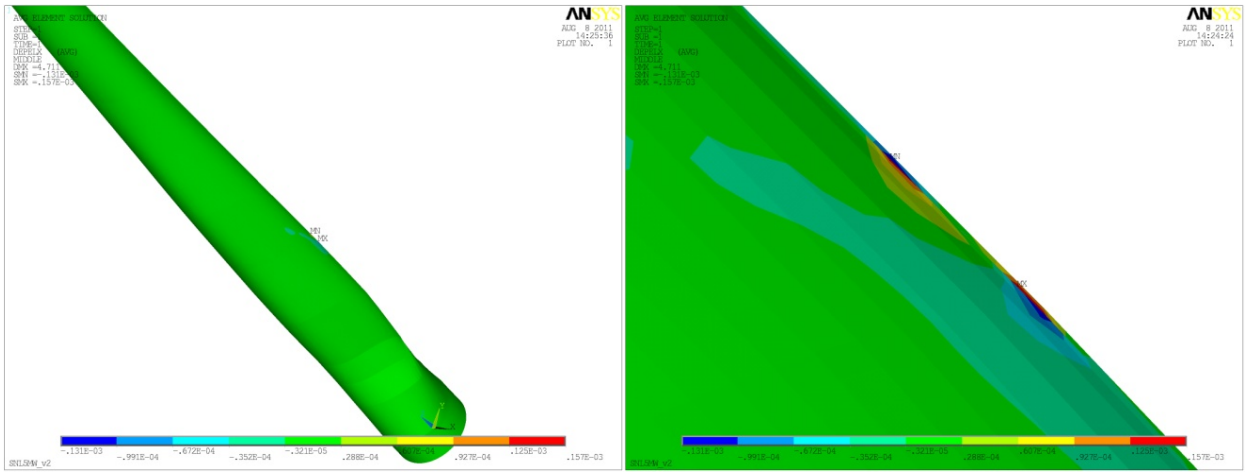

Figure 18. Graphical depiction of the magnitude of change in longitudinal strain resulting from the presence of a 0.625m long TE disbond located slightly outboard of maximum chord.

This example has briefly shown the potential for the use of aeroelastic models in computing blade loads, application of loads to the detailed blade model, and analysis of the blade structural response for effects of one type of blade damage. Additional types of damage can be represented in the blade finite element model and evaluated using this process.

4.3. Operational Response Results (Global Sensitivity)

Due to the large potential benefits of SHPM a large amount of research in the damage detection and structural health monitoring for wind turbines has been performed in recent years [10, 26-28]. To a large extent the prior work has focused on the application of specific methods or methodologies to a series of different potential problems. Rather than taking this approach to the problem of monitoring the health of offshore wind turbines using operational response measurements, this work approached the problem more generally by using full turbine simulations and simple time domain methods to identify which responses are the most sensitive to the presence of damage. This approach was selected because if the response measurement that is used by SHPM system is unaffected by the presence of damage, damage will not be able to be detected regardless of the sophistication of the damage detection methodology that is used.

To identify the effects of a TE disbond on the operational response characteristics of an offshore wind turbine, both FAST and ADAMS models of the turbine described in Section 3.1 were used in conjunction with seven different blade models. These blade models were developed using the NuMAD and BPE process that was described in Section 3.3. The seven different blade models used in these simulations included one healthy blade model as well as models that included disbonds with length 0.625, 1.25, 1.875, 2.5, 4 and 6 meters. These lengths corresponded to disbonds ranging from approximately 1-10% of the total length of the blade and were a subset of the blade models used in the BPE sensitivity study described in Section 4.1. In the full turbine simulations only a single blade (blade 1) was damaged by changing the reduced order blade model while the two other blades were modeled using the healthy blade model in all of the simulations.

Because the goal of this investigation was not the development of damage detection algorithms but rather the determination of the sensitivity of different measurements to damage; all of the input parameters to the model were kept consistent between the data sets other than the model for the damaged blade. By keeping all of the simulation parameters other than a single blade file constant the sensitivity analysis could be simplified considerably because the changes in the model's output should only be due to the TE disbond. Consequently, the same input wind data file with a mean wind speed of 11.4 m/s and IEC turbulence characteristic A (generated using TurbSim [29]) and selected for all of the simulations.

This section proceeds with an explanation of the data features that were used to quantify the sensitivity of the operational responses. The section then continues with the application of those measures to results from simulations performed in either FAST or ADAMS. Both simulation platforms were investigated because while FAST is able to perform full turbine aeroelastic simulations very efficiently it does not model either the longitudinal or torsional degrees of freedom of the blades. ADAMS simulations, on the other hand, require far more computational time than FAST, but are generally more refined and model both the longitudinal and torsional mass and stiffness characteristics of the blade. Therefore, the ADAMS simulations may be able to more accurately simulate the relatively small and localized changes in the torsional stiffness of the blades due to a TE disbond.

4.3.1. *Rotational Resampling and Synchronous Averaging*

In addition to analyzing the output responses of the simulations directly, data normalization through rotational resampling and synchronous averaging was also investigated. This process was performed in order to focus the sensitivity analysis on differences in the turbine's response due to the damaged blade rather than slight differences in the start-up of the turbine. Rotationally resampling is the process of interpolating data so that rather than having data points that are spaced equally in time, the acquired data points are spaced equally with respect to the rotor position (or azimuth angle) and occur at the same rotor position during each rotation.

Once the time histories were resampled, the average responses over an integer number of rotations of the turbine were calculated using synchronous averaging. In synchronous averaging blocks of data are averaged together in which each data point coincides with the same rotor position. This a common practice in the health monitoring of rotating machinery because responses that are repeated every rotation of the system constructively interfere, while random noise and transient events destructively interfere and their influence is minimized. Another benefit of time synchronous averaging using an integer number of rotations of the turbine is that it results in a signal that is nearly periodic. The periodic nature of the synchronously averaged signal reduces the amount of leakage if the signal is transferred into the frequency domain using the Fourier Transform.

However, once the rotational resampling and synchronous averaging procedures have been performed, the response measurements still must be post-processed to obtain a single data feature so that the sensitivity of each channel to the disbond can be quantified. Some sensitivity measures that were applied to the rotational resampled and synchronously averaged data or the raw time histories will now be discussed.

4.3.2. *Sensitivity Measures Investigated*

The sensitivity of a function is generally defined as the partial derivative of that function with respect to the variable of interest. In this case, however, the sensitivity of a response time history with respect to a change in a model must be computed, which is slightly more involved because it requires the condensation of the changes in the time history into a single data feature. Nonetheless several key aspects of how to define the sensitivity of a measurement can be derived from its definition for a function. The first, and most obvious, is that the measured response should change when the variable of interest is changed. For the present simulations this means that the time histories from the damaged model must be different in some way from the time histories generated by the healthy model. Secondly, the change in the time history should be in some way correlated to changes in the length of the disbond. Therefore; in the following analyses, channels will be defined as sensitive to the presence of the TE disbond if they are changed by the presence of the disbond and the change tends to increase as the size of the disbond increases. Furthermore, because the focus of this analysis was on the physics-based determination of the measurements that were the most sensitive to damage, only simple time based damage features have been investigated.

4.3.2.1. Statistical Moments

The first data feature that was used to assess the sensitivity of operational response measurements to the disbond were the statistical moments of the data. This data feature was only extracted from the raw time histories. These parameters were tracked because changes in the moments are correlated to changes in the underlying distribution of the data which may be caused by damage. The investigated moments included the mean, variance, skewness and kurtosis of the data. While the mean and variance of the data are well known measures of the expected value of the data and the spread of the data respectively, the skewness and kurtosis are less well known statistical moments that can be used to help describe the shape of the distribution.

The sample skewness [30] is an estimate of third standardized moment of a distribution and is defined as,

$$\hat{\tau} = \frac{\frac{1}{n}\sum_{i=1}^{n}\left(x[i]-\bar{x}\right)^3}{\left(\frac{1}{n}\sum_{i=1}^{n}\left(x[i]-\bar{x}\right)^2\right)^{3/2}} \tag{5}$$

where i is the index of the time point, n is the total number of data points and $\bar{x}$ is the sample mean of the data. The skewness is a measure of the asymmetry of a distribution where a positive skewness value indicates that there are relatively few values that are larger than the mean but those large values are relatively far away from the mean.

The sample kurtosis [30] is an estimate of the fourth standardized moment of a distribution and is defined as,

$$\hat{\kappa} = \frac{\frac{1}{n}\sum_{i=1}^{n}\left(x[i]-\bar{x}\right)^4}{\left(\frac{1}{n}\sum_{i=1}^{n}\left(x[i]-\bar{x}\right)^2\right)^2} \tag{6}$$

again where n is the number of data points and $\bar{x}$ is the sample mean of the data. Large values of kurtosis indicate that while a significant portion of the data is in a relatively narrow range there are also several large outliers. Therefore, the kurtosis can also be thought of as a representation of the "peakedness" of a distribution. Kurtosis is a widely used damage detection measure in the field of rotating machinery [31].

4.3.2.2. Standardized RMS Difference

Due to the fact that the only variation between the models was the presence of the TE disbond, the sensitivity of the model's responses could theoretically be calculated by directly calculating the differences between the healthy and damaged response time histories. To gauge the difference in the responses the root mean square (RMS) of the difference between the healthy time histories and the damaged time history was computed for each channel. However, if the magnitude of the signal itself is not taken into account in this investigation, the magnitude and the units of the response will influence the results. Therefore to normalize the data and create a unitless measure of sensitivity, the RMS differences were standardized by dividing the difference for each channel by the standard deviation of that data from the healthy blade. This sensitivity metric can be written for the j^{th} test as:

$$\Delta_j^{RMS} = \frac{\sqrt{\frac{1}{n}\sum_{i=1}^{n}\left(x_j[i]-x_0[i]\right)^2}}{\sqrt{\frac{1}{n}\sum_{i=1}^{n}\left(x_0[i]-\bar{x}_0\right)^2}} \tag{7}$$

where i is the index of the time point, the subscript represents the test the data is from with 0 indicating the healthy data, n is the total number of time points and $\bar{x}_0$ is the mean of the healthy data. While this process would not work for data that was a constant throughout the healthy simulation, all of the data of interest in this investigation was dynamic data.

Despite the straightforward nature of applying this approach to the raw time histories, a small difference early in the simulation can lead to a phasing differences between simulations that propagate throughout the entire duration and leads to anomalous indications of damage sensitivity. Because of these phasing issues, this data feature may be more useful when applied to the rotationally resampled and synchronously averaged data where any phasing differences were compensated for using the resampling procedure.

4.3.2.3. Maximum Standardized Mean Difference

In addition to facilitating synchronous averaging, rotationally resampling the data allows the changes in the response data at a given rotor position to be investigated. Therefore, to create this damage sensitivity metric rather than synchronously averaging the rotationally resampled data to obtain the average waveforms (as was the case when the standardized RMS analysis described above was applied to the synchronously averaged data) the distribution of the resampled data at a given rotation angle was analyzed. The damage sensitivity metric that was used in this work was the difference between the synchronously averaged waveforms divided by the standard deviation of the healthy data at each rotor position. This measure of sensitivity will be referred to as the maximum standardized mean difference and can be expressed for the j^{th} test as:

$$\Delta_j^{MAX} = \max_\theta \left(\frac{\bar{r}_j[\theta] - \bar{r}_0[\theta]}{\sqrt{\frac{1}{n_r}\sum_{i=1}^{n_r}\left(r_{0,i}[\theta] - \bar{r}_0[\theta]\right)^2}} \right) \tag{8}$$

where $\bar{r}_j[\theta]$ is the synchronously averaged data for the j^{th} test at the rotation angle (azimuth position) θ, $r_{0,i}[\theta]$ indicates the data from the healthy turbine during the i^{th} rotation, n_r is the total number of rotations in the healthy data set, and $\max_\theta$ indicates that the maximum is taken across all rotation angles. This sensitivity measure was chosen because it emphasizes differences in responses that are relatively consistent for a healthy turbine but changes due to the presence of damage.

4.3.3. *FAST Simulations*

Due to the desire to investigate the sensitivity of a wide range of different measurements to the TE disbond, 199 different response outputs were obtained from FAST. More outputs would have been investigated but at the time the study was performed FAST had a limit of 200 output parameters for a single test. A variety of different measurements were obtained on the turbine's rotor including the local accelerations and moments in three directions on blades 1 and 2 at the nine locations spaced along the span of which are shown in Figure 19. The same measurements from blade 3 were not acquired because they were assumed to be similar to those from blade 2 (also simulated as an undamaged blade) and were therefore not included in the analysis so that alternative measurements could be investigated. A variety of measurements that were not on the rotor were also acquired including the local tower accelerations and loads at 4 different locations on the tower. A variety of measurements from the turbine's drive train were also measured including the nacelle IMU translations and rotations, the generator speed, power and torque, as well as a variety of forces and moments from the low speed shaft.

The first response sensitivity metric that was applied to the FAST data were changes in the statistical moments of the response data. The mean, standard deviation, skewness and kurtosis for each of the 199 channels were calculated. Because the magnitude of the statistical moments can vary depending on the units of the underlying data, in order to compare the sensitivity of

multiple channels of data which may have different units, the percent change in each of the moments was also calculated.

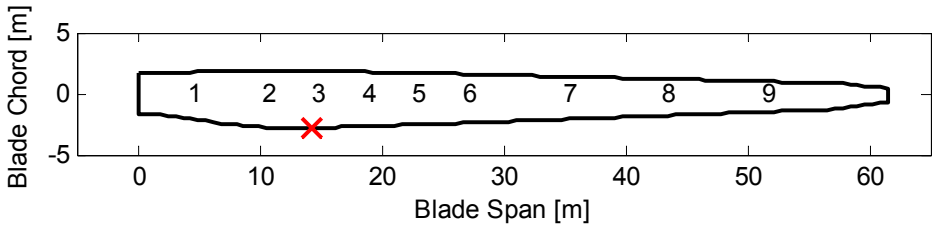

Figure 19. The locations of the local acceleration and moment measurements along the length of the blade. All of the investigated disbonds extend outboard from max chord which is indicated with a red "X".

Despite the fact that the mean of the responses were relatively unaffected by the presence of damage, several channels did show some slight changes in their mean values due to the damage. Some of the measurements that had small (<1%) changes in the mean of the data were the pitching moments on the damaged blade which progressively decreased with an increase in the length of the disbond. However, the mean of the low speed rotating shaft shear force that was directed perpendicularly to the length of the shaft changed the most in a relative sense and was correlated with the damage state. A bar chart showing the mean of this measurement channel for the healthy blade (damage state 0) all of the investigated disbond lengths (damage states 1-6) is shown in Figure 20 and the slight increase in the mean with the increasing length of the disbond is evident.

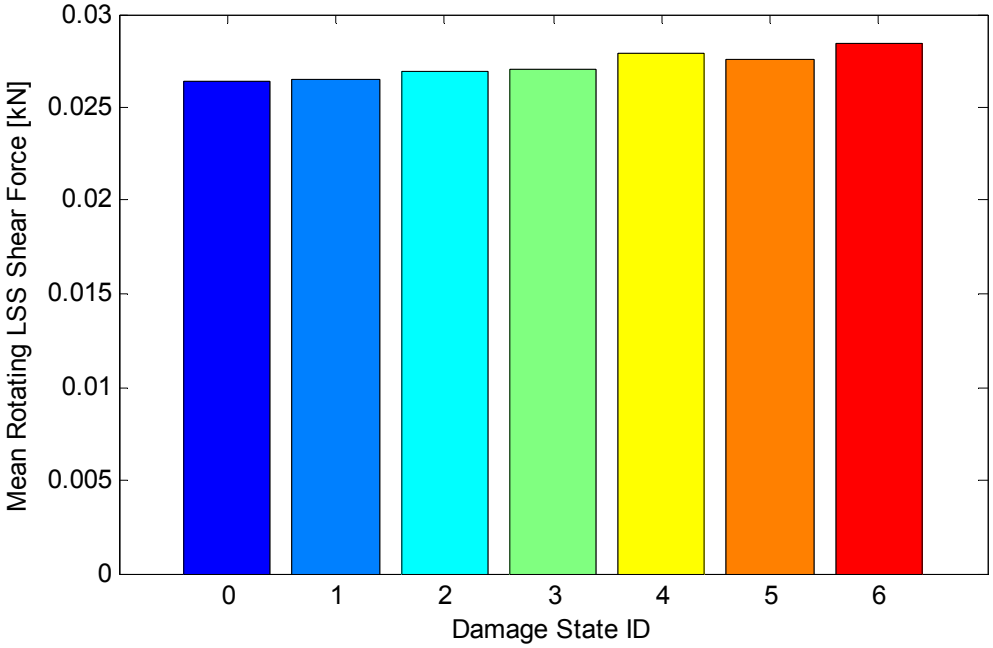

Figure 20. The mean rotating shear force in the low speed shaft for 7 turbine models. The damage states from 0 to 6 are the healthy blade and the blades with a 0.625, 1.25, 1.875, 2.5, 4, and 6 meter long disbond respectively.

While the largest percentage change in the mean of the data was not on the rotor, changes in the higher moments of the data that were correlated with the size of the disbond largely occurred in the measurements on the blade. The data that registered the largest and most consistent percent changes were the local pitching moments on the damaged blade near the damage location. The absolute percentage changes for the skewness of the pitching moments along the blade are shown in Figure 21 while the absolute percentage changes in the kurtosis of the data are shown in Figure 22. The z-axis on these plots indicates the absolute percentage change in the data while the x-axis indicates the measurement location ID (see Figure 19 for the locations) and the y-axis is the damage state. The large erratic absolute percent differences in the skewness for measurement location 1 are believed to be due to that fact that the skewness of the response near the blade root was almost zero and therefore the relatively small changes were magnified disproportionately. Note that the scale on the vertical axis of these two plots are different and that the most significant change on the statistical moments on the blade that was correlated with the damage state of the structure was the change in the skewness of the pitching moments near the location of the disbond.

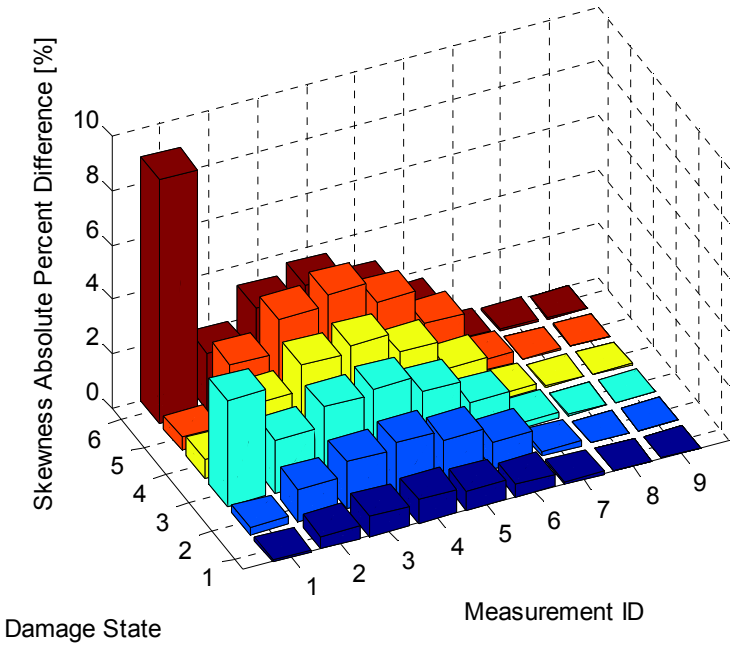

Figure 21. The absolute percent change in the skewness of the pitching moments along the length of the blade for the 6 different damage states. The damage states 1 through 6 correspond to disbonds of length 0.625, 1.25, 1.875, 2.5, 4, and 6 meters respectively.

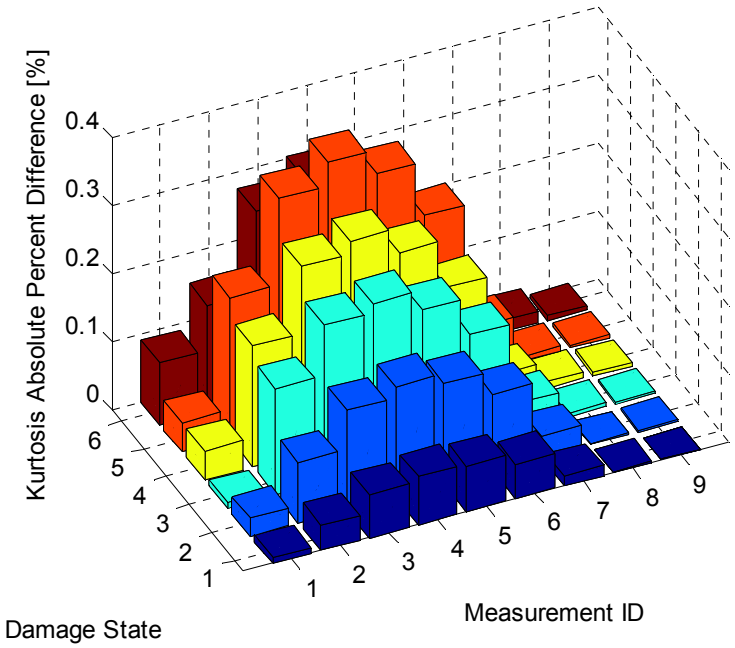

Figure 22. The absolute percent change in the kurtosis of the pitching moments along the length of the blade for the 6 different damage states. The damage states 1 through 6 correspond to disbonds of length 0.625, 1.25, 1.875, 2.5, 4, and 6 meters respectively.

When the standardized RMS difference methodology was applied directly to the FAST output data the data channel with the largest difference was found to be the azimuth, or rotor position. While this may be due to a change in the blade model, the second largest standardized difference was due to smallest (0.625 meter) disbond. Therefore, it is believed that this difference is due to slight changes in the response of the turbine during start-up which resulted in a slight shift in the position of the turbine.

When the standardized RMS difference (Section 4.3.2.2) was performed after the data had been rotationally resampled and synchronously averaged (Section 4.3.1) using a single rotation of the turbine, the data channels with the largest standardized sensitivity to the damage are the accelerations along the damaged blade in the edge-wise direction. A contour plot showing the magnitude of the standardized RMS difference for all nine of the edge-wise accelerations and each of the damage conditions is shown in Figure 23. Note that the largest absolute RMS differences do not occur for the most severe damage level but rather come about due to the 4 meter long disbond, which was also the case for skewness and kurtosis. For the majority of the locations and disbond lengths investigated, however, the differences in the time history increase as the length of the disbond increases and the most sensitive accelerometers are those near the location of the disbond. However, these differences are a product of very small differences in the response time histories as can be seen by a plot of the time history corresponding to the edge-wise accelerations measurements at 36.35 meters (Figure 24). This relatively small changes in the accelerations suggests that while some differences are observable in the overall average accelerations these changes would most likely be exceedingly difficult to detect in a real-world situation assuming that the FAST simulations accurately model the effects of the TE disbond on the turbine's responses.

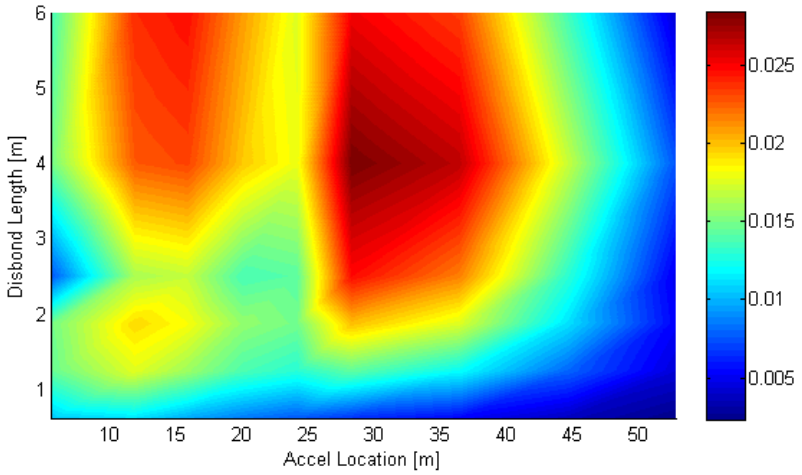

Figure 23. The standardized RMS difference in the edge-wise accelerations of the damage blade. The x-axis shows how the difference changes along the length of the blade while the y-axis shows how the difference is influenced by the length of the disbond.

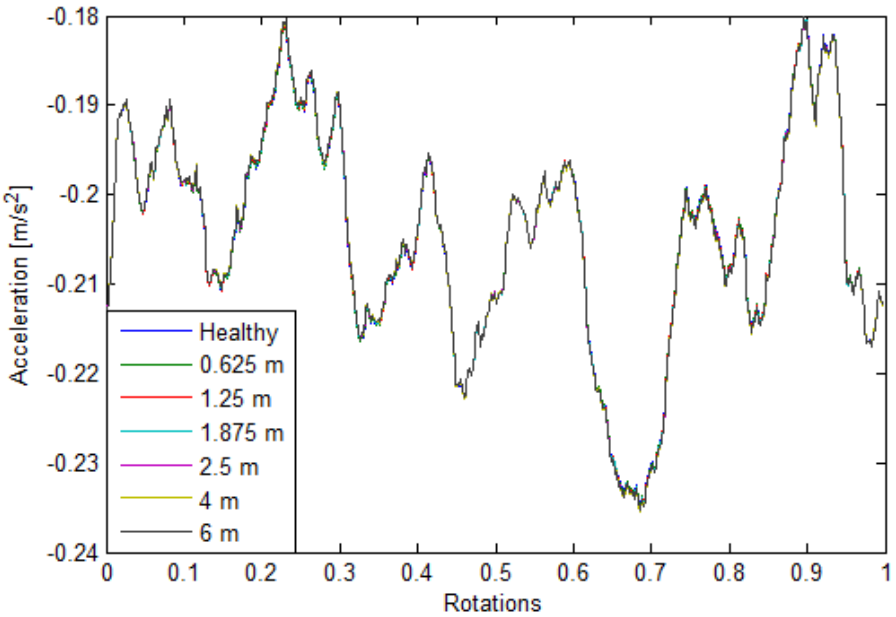

Figure 24. The average edge-wise accelerations at 36.35 meters for all 7 of the FAST models. Only very small differences between the responses are evident.

Using the maximum standardized mean difference the response channel with the largest sensitivity to damage was the local pitching moment on the damaged blade. A surface plot of the magnitude of the maximum standardized mean difference for all nine of the measurement locations where the local pitch moment of the blade was measured for each of the 6 different damage conditions is shown in Figure 25. Note that once again the largest differences do not occur for the most severe damage level but rather are seen for the 4 meter long disbond. Figure 26, however, shows that while the localized differences may increase with damage only very small differences are actually present in the time histories which once again suggests that

detecting these changes in the presence of variable loading or environmental factors would be very difficult.

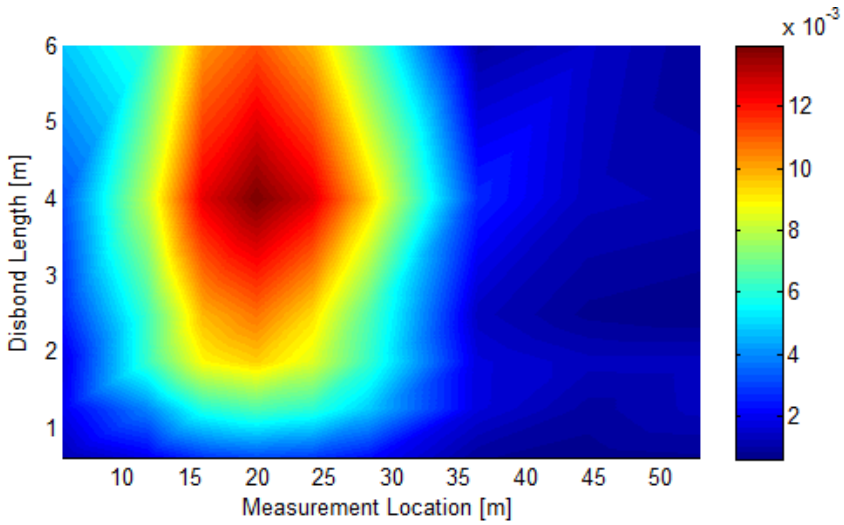

Figure 25. The maximum standardized mean difference in the damage blade's pitching moments. The x-axis shows how the difference changes along the length of the blade while the y-axis shows how the difference is influenced by the length of the disbond.

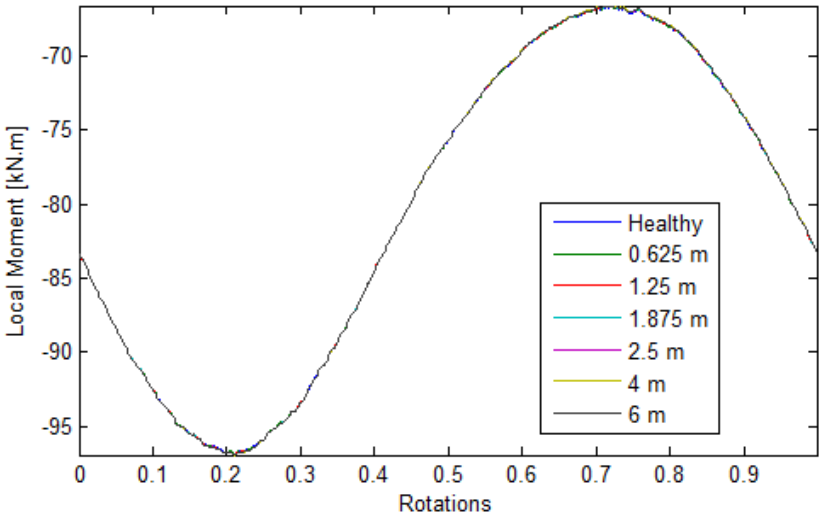

Figure 26. The average pitching moment at 20 meters for all 7 of the offshore FAST models. Only very small differences between the responses are evident.

While several different methods have been applied to the results of FAST simulation to determine operational responses that are sensitive to the presence of a TE disbond no significant changes in the turbine's response due to the disbond were found. However, the FAST simulations may not be appropriate for an investigation of the effects of a TE disbond because the blade's torsional degrees of freedom are not modeled in FAST. This is especially significant because the BPE sensitivity analysis found that the torsional stiffness of the blade was significantly affected by the presence of the TE disbond while the edge-wise and flap-wise degrees of freedom were relatively unaffected. Therefore, the operational sensitivity analysis was also conducted using an ADAMS model as detailed in the next section.

4.3.4. *ADAMS Simulation Results*

Because the blade's torsional degrees of freedom could not be modeled in the FAST simulations, the FAST preprocessor was used to create an ADAMS model of the offshore 5-MW turbine which allows both the pitching and span-wise flexibility of the blade to be included in the model. As with the FAST simulations, 30 seconds of start-up data at the beginning of each simulation was discarded and the remaining hour of response data was acquired and analyzed. Furthermore, because ADAMS has no limit on the number of requested outputs a much larger candidate set of output responses could be investigated. A total of 1,007 different responses were recorded using a 100 Hz sampling rate for each of the simulations and all of the responses were analyzed to determine their sensitivity. These included the translational and rotational accelerations of all 17 lumped masses for each blade as well as the local forces and moments in each direction. Because of the limitations of the FAST post processing scripts, a new set of requests were added to the generated ADAMS models in order to obtain the equivalent responses directly from ADAMS. The locations of the response measurements along the span of the blade are shown in Figure 27. The translational and rotational forces and accelerations were also recorded at 21 evenly spaced locations along the height of the tower. A variety of other generator, nacelle, and other measurements were recorded and the most sensitive measurements will be described. Each of the simulations took over 8 hours to run on a Dell laptop with two Intel Core2 Duo x64 2.6 GHz processors, 8 GB of RAM, and a 7200 RPM 500 GB hard drive.

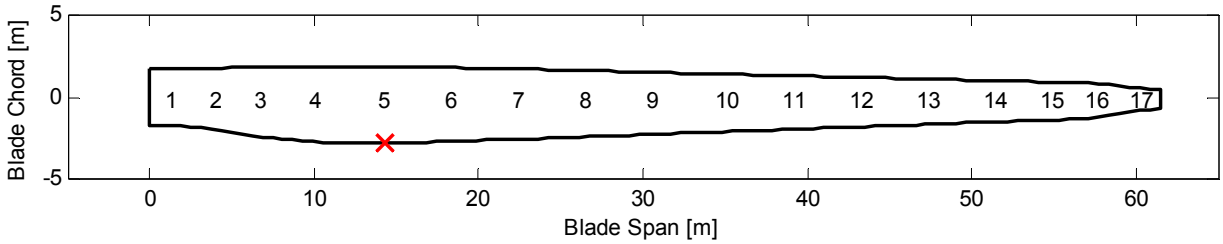

Figure 27. The 17 measurement locations on each of the blades used for the ADAMS models. All of the investigated disbonds extend outboard from max chord which is indicated with a red "X".

The preliminary step in this analysis was to determine an appropriate step size for the simulation methodology investigated. Based on work by White [32] the integrator selected for this analysis was the SI2 GSTIFF integration method. While this integrator was found to reduce the number of spurious peaks in the acquired acceleration signals, in this work it was not able to eliminate them using the integrator time step that was used in the FAST simulations. Therefore a convergence analysis was performed based on the maximum integrator step size used for the SI2 integration method. To create a dimensionless convergence metric the RMS difference between the time histories from the smallest step size (1E-4 seconds) and each candidate step size was calculated. However, in order to ensure that the responses with different units were accounted for equally, the difference of each response was normalized by the reference responses' standard deviations and the mean of these values across all of the channels was used as the convergence criteria and is shown in Figure 28. Based on this analysis, a step size of 1E-3 seconds was chosen because it appeared to reduce discontinuities in the time acceleration time histories and was a good compromise between accuracy and computation time.

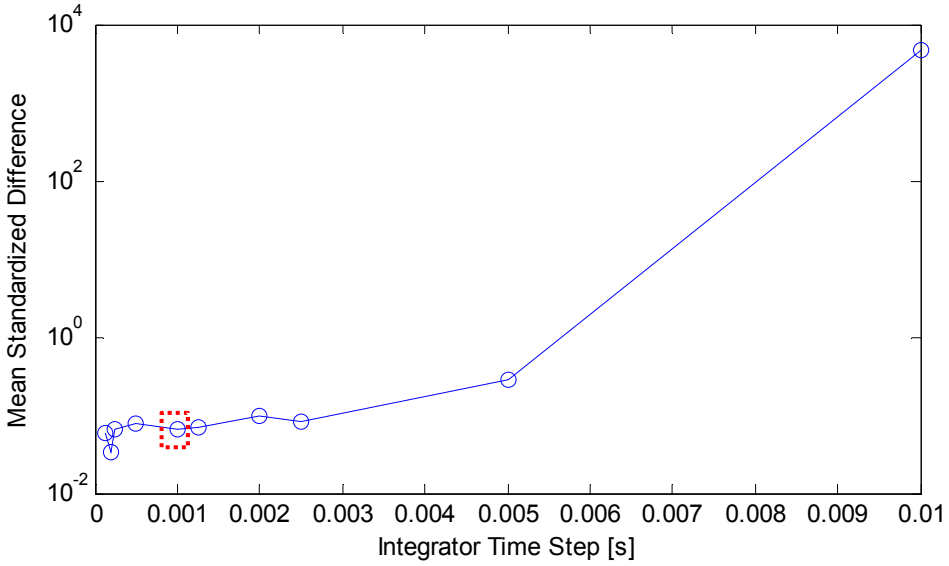

Figure 28. The convergence metric used to evaluate the integrator step size used in the ADAMS simulations.

The statistical moments of the responses from the ADAMS simulations of the offshore turbine showed significant percent changes but the majority of them did not exhibit consistent trends with respect to the length of the disbond. The cause of these inconsistent trends is currently unknown and due to the issues previously encountered with discontinuous accelerations, displacement and velocity measurements will be investigated in future simulations. The standardized RMS differences of the time histories were also investigated but as with the moments, the majority of the differences did not appear to correlate well with the extent of the damage.

However, the statistical moments of the pitching moments on the damage blade were well correlated with the presence and extent of the TE disbond and displayed significant percent changes in some cases. Figure 29 contains a three dimensional bar chart of the absolute percent different in the mean of the pitching moments along the span of the damaged blade due to the six different disbond lengths investigated. Note that two views of the plot are shown in the figure in order to demonstrate the span-wise variations in the changes. The mean pitching moments on the element centered at 15.85 meters down the span of the damaged blade changed up to 4% due to the disbond and in general the changes in the mean seem to generally increase with increasing length disbonds. These changes are over four times larger than those seen in the FAST simulations which is believed to be due to the fact that ADAMS takes into account the torsional flexibility of the blades while FAST does not.

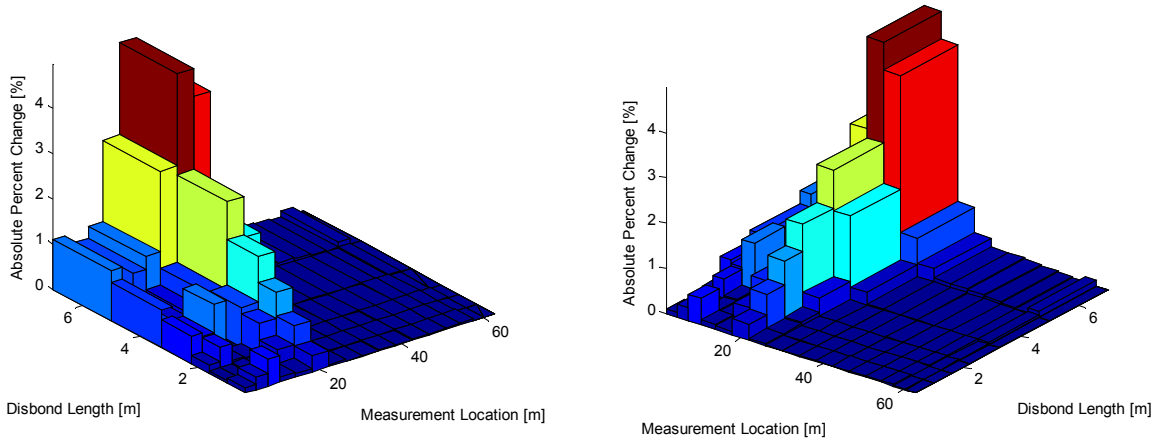

Figure 29. Two views of the absolute percent change in the mean of the pitching moments along the span of the damaged blade due to TE disbonds between 0.625 and 6 meters.

In addition to changes in the mean, the changes in the standard deviation, skewness, and kurtosis of the damaged blade's pitching moments were also well correlated with the size of the disbond. The changes in the standard deviation of the pitching moments are shown in Figure 30 and show even larger percent changes due to the disbond than did the mean of the data with changes of up to 20% for the 6 meter disbond. While the changes in the mean of the data also occurred near the root of the blade the differences in the standard deviation of the pitching moment were highly localized around the damage location.

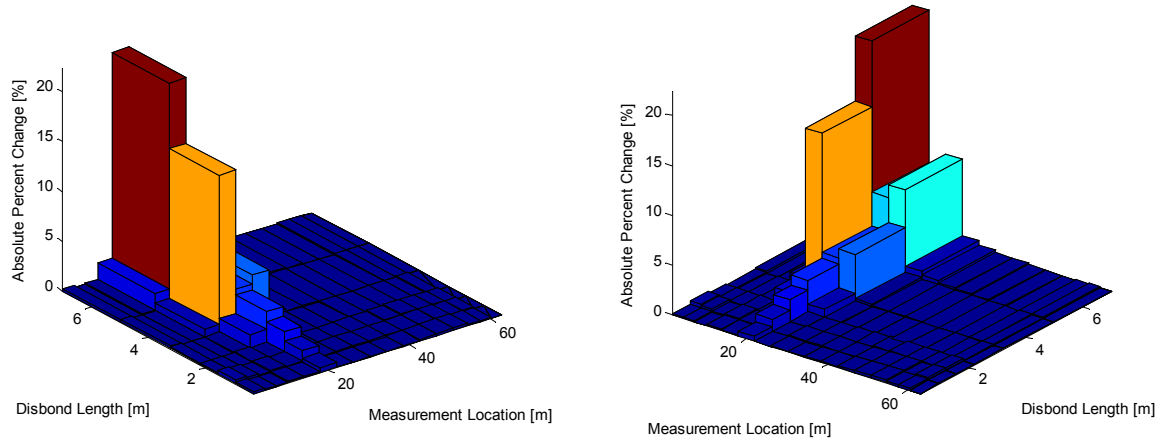

Figure 30. Two views of the absolute percent change in the standard deviation of the pitching moments along the span of the damaged blade due to TE disbonds between 0.625 and 6 meters.

The percent changes in the skewness of the data (Figure 31) were over 300% and were even more localized than the changes in the standard deviation. However, it should be noted that the healthy skewness values were fairly small which resulted in exaggerated percent differences. Changes in the kurtosis of the data were also localized around the damage location but only exhibited percent differences that were slightly larger than 10% as can be seen in Figure 32. *The consistent changes in all four of the statistical moments investigated shows that the pitching*

moments around the damage location are highly influenced by the TE disbond and should be included in an SHPM system designed to detect this form of damage.

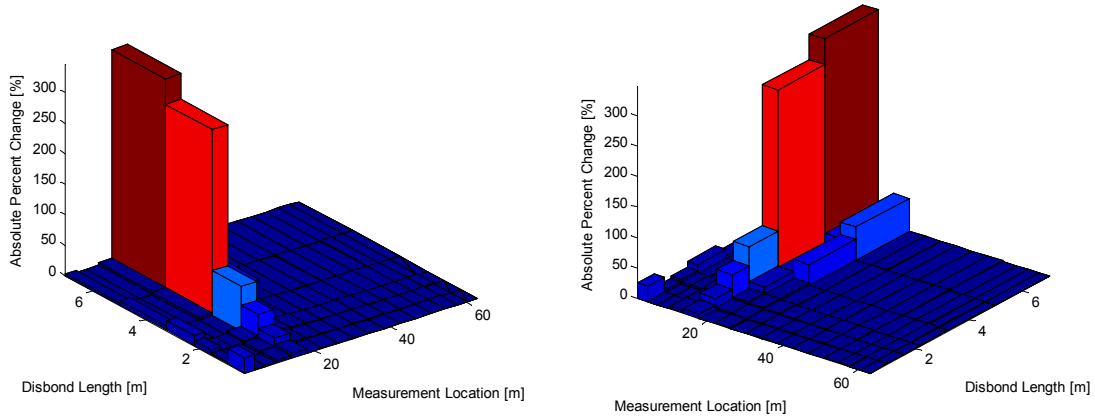

Figure 31. Two views of the absolute percent change in the skewness of the pitching moments along the span of the damaged blade due to TE disbonds between 0.625 and 6 meters.

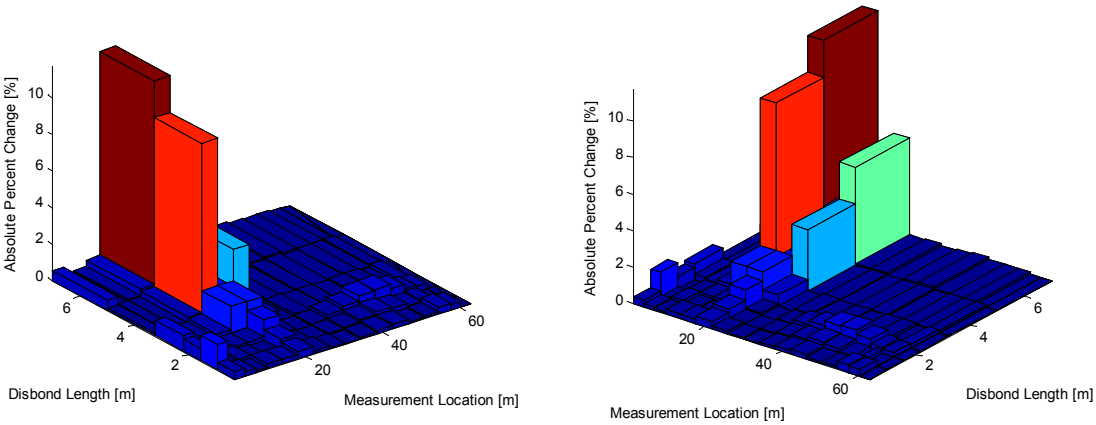

Figure 32. Two views of the absolute percent change in the kurtosis of the pitching moments along the span of the damaged blade due to TE disbonds between 0.625 and 6 meters.

To focus the sensitivity analysis on the operational response of the turbine, the rotational resampling and synchronous averaging technique described in Section 4.3.1 was performed on the ADAMS response measurements. When the standardized RMS difference (Section 4.3.2.2) of the average waveforms was utilized to determine the influence of the disbond on the models' responses, the responses with the largest changes between simulations were not correlated with the size of the disbond in the model. However, out of the channels of data whose standardized RMS difference was correlated with the disbond size, the pitching moments in the damage blade demonstrated by far the most significant differences. The RMS difference in the average waveforms generated from the pitching moments on the damaged blade are shown in Figure 33. RMS differences of over 9 kN•m were seen due to the 6 meter disbond, consistently increased with the length of the disbond, and were once again well localized around the location of the damage.

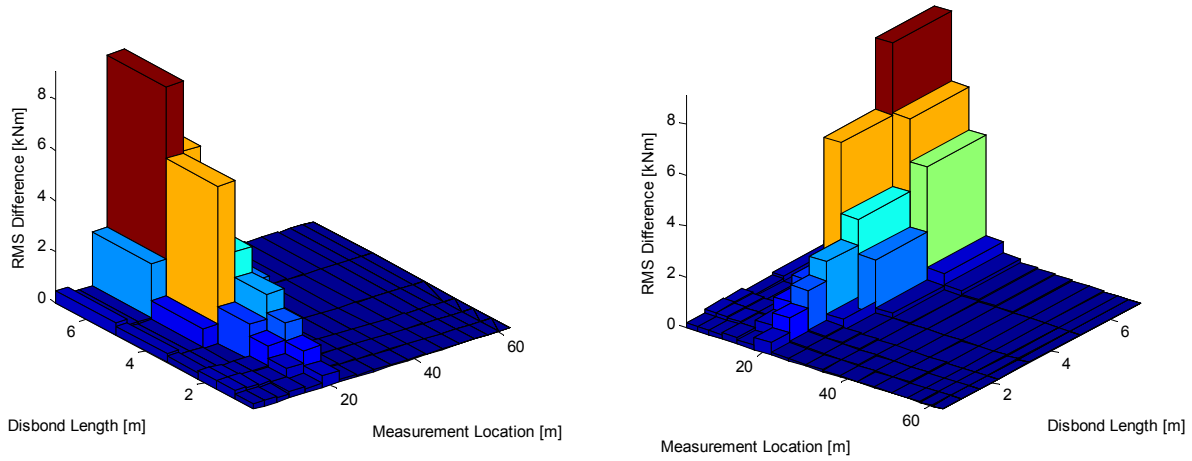

Figure 33. Two views of the RMS differences in the average pitching moments along the span of the damaged blade due to TE disbonds between 0.625 and 6 meters.

When the sensitivity of the rotationally resampled time histories was quantified using the standardized mean difference at different rotation angles (Section 4.3.2.3), the most sensitive measurements were once again found to be the pitching moment near the location of the disbond. A set of three dimensional bar charts (Figure 34) shows that the maximum standardized mean difference shows changes due to damage beginning with the 0.625 m disbond and that these differences increase as the length of the disbond increases. In this case the largest difference between the average waveforms is over 0.6 times the standard deviation of the healthy data. This maximum difference occurs in the blade section centered around 15.85 meters when the turbine is approximately 1/4 of the way through its rotation, as can be seen in Figure 35. Figure 35 also demonstrates, however, that relatively small changes are seen in this time history due to smaller length disbonds. However, the pitching moments in the next outboard section (centered around 19.95 meters) show differences even for the smallest disbond and these differences increase relatively consistently as the length of the disbond grows (Figure 36).

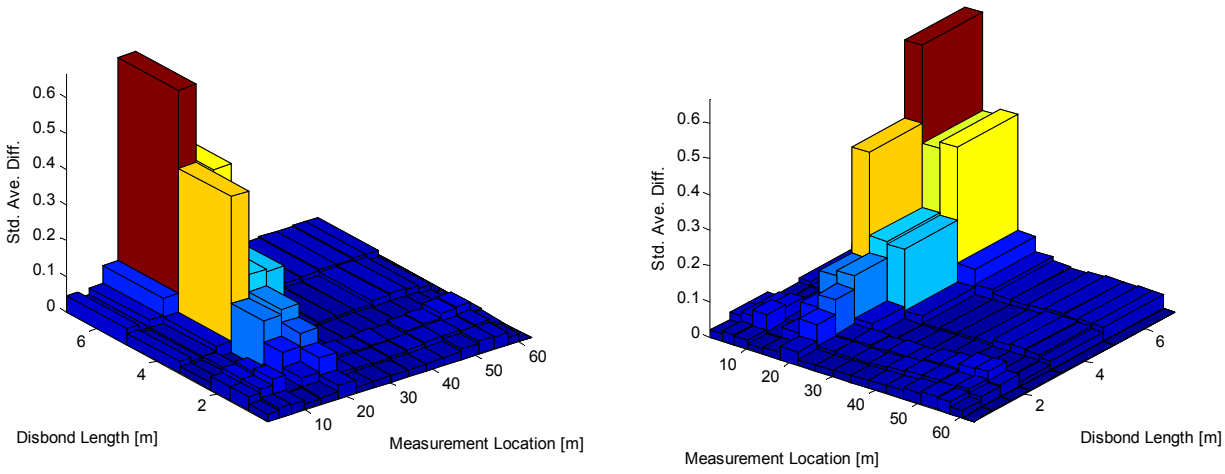

Figure 34. Two views of the maximum standardized mean difference in the pitching moments along the span of the damaged blade due to TE disbonds.

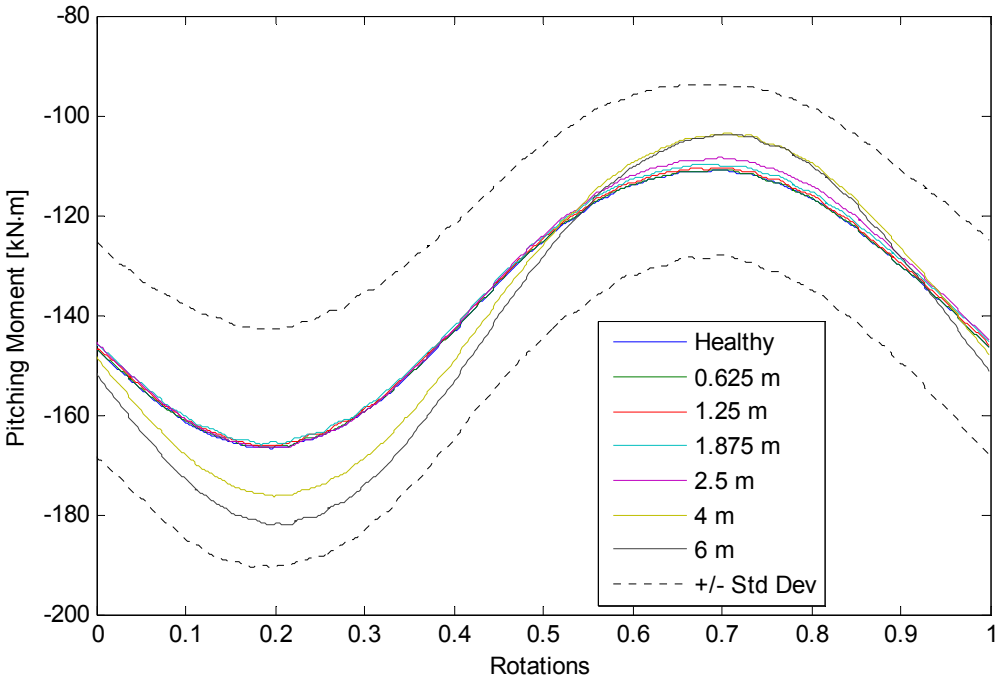

Figure 35. The average net pitching moment during one rotation of the turbine for a section centered around 15.85 m down the span of the damaged blade for all disbond lengths. The dotted lines are the healthy average pitching moment plus and minus one standard deviation.

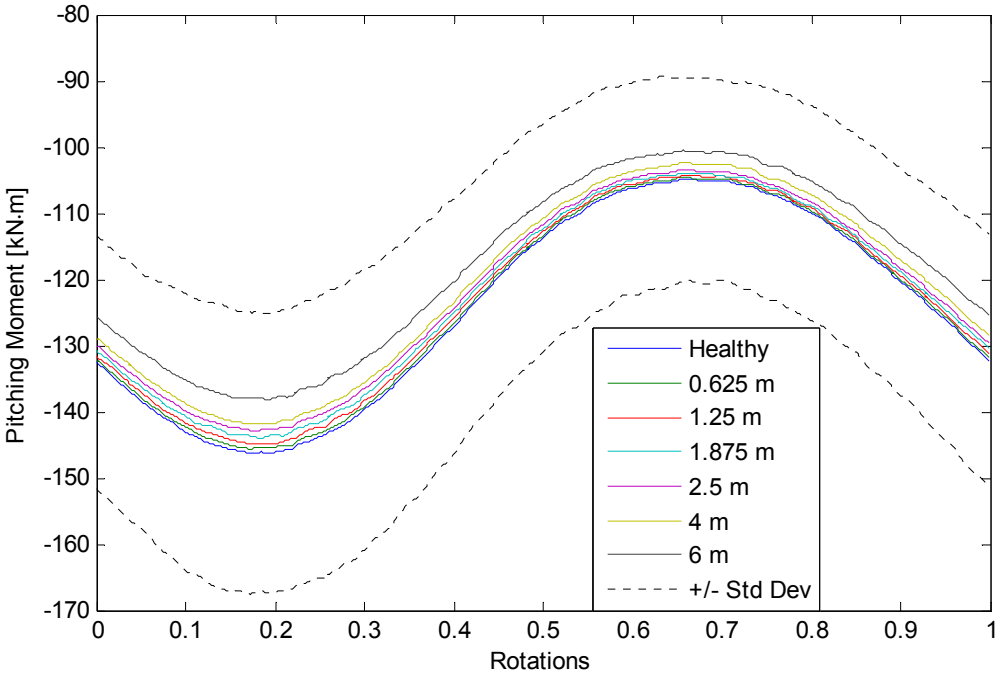

Figure 36. The average net pitching moment during one rotation of the turbine for a section centered around 19.95 m down the span of the damaged blade for all disbond lengths. The dotted lines are the healthy average pitching moment plus and minus one standard deviation.

Rather than simply taking the maximum standardized mean difference of the data, an alternative way to investigate the differences in the averaged data is to estimate the distribution of the data at a given rotation angle and quantify differences between the two distributions. In order to estimate the probability density function of the data, a Gaussian kernel density estimator [33] was used. An example of the changes in the estimated distributions due to damage is shown in Figure 37 which contains the probability density estimators of local pitching moment at 15.85 meters when the turbine is a quarter of the way through its rotation. The estimated distribution clearly changes for the larger damage levels as both the center and the spread of the distribution is significantly altered when the disbond is 4 or 6 meters in length.

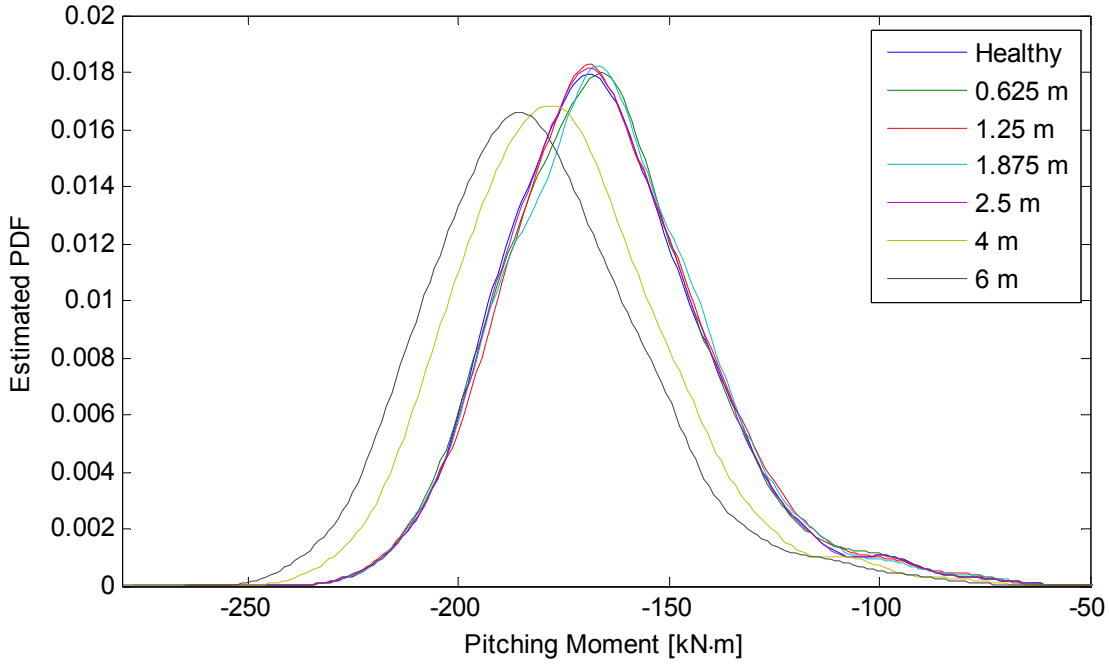

Figure 37. The probability density estimates generated using the local pitching moment one quarter of the way through a turbine rotation in the section of the damaged blade centered at 15.85 meters and all disbond lengths.

One way in which the significance of the differences between the distributions can be investigated quantitatively is using a two-sample t-test which tests the null hypothesis that two sets of independent random samples from normal distributions have equal means but unknown and possibly unequal variances. The tests were performed using the Matlab® Statistics Toolbox and the results generated from the pitching moments at 0.25 rotations from the blade section centered at 15.85 m are shown in Table 3. These data shows that the only disbond lengths for which the probability of the two distributions having the same mean was less than 5% were the 4 and 6 meter long disbonds. However, based on the data from the hour of averages the probability of either of these damage cases being from the healthy distribution is less than 4E-12%. Lastly, the 95% confidence interval on the difference between the healthy data and the data from the blade with the 4 meter disbond was between 7.34 and 12.4 kN•m while for the 6 meter long disbond that difference increased to between 13.3 and 18.5 kN•m. While the underlying data used for these tests is non-normal (as is clear through the extended right tail of the distribution) these very low probabilities and large differences in the mean indicate the significance of this change.

Table 3. The results of the two-sample t-tests using the pitching moment at 15.85 down the span of the damaged blade comparing the data from the healthy blade to the data from each of the disbond lengths.

Disbond Size	Reject Hypothesis	P-Value of Test	95% Difference Confidence Interval
0.625	No	0.88	-2.70 to 2.31
1.25	No	0.58	-3.22 to 1.79
1.875	No	0.52	-3.32 to 1.69
2.5	No	0.99	-2.51 to 2.47
4	Yes	4E-14	7.34 to 12.4
6	Yes	4E-32	13.3 to 18.5

While the pitching moments from the section centered at 15.85 meters changed significantly for the 4 meter and 6 meter long disbonds, they were unable to statistically differentiate other damage states from the response of the healthy blade. When the probability density estimates were generated from the pitching moments of the blade section centered at 19.95 meters; however, smaller but more consistent changes were evident as shown in Figure 38. To investigate the significance of these changes two-sample t-tests were then performed as described in the previous paragraph. While the hypothesis of significantly different means cannot be rejected with 95% confidence for the 0.625 and 1.25 meter long disbonds the t-test indicates significantly different means for all of the larger disbonds as shown in Table 4.

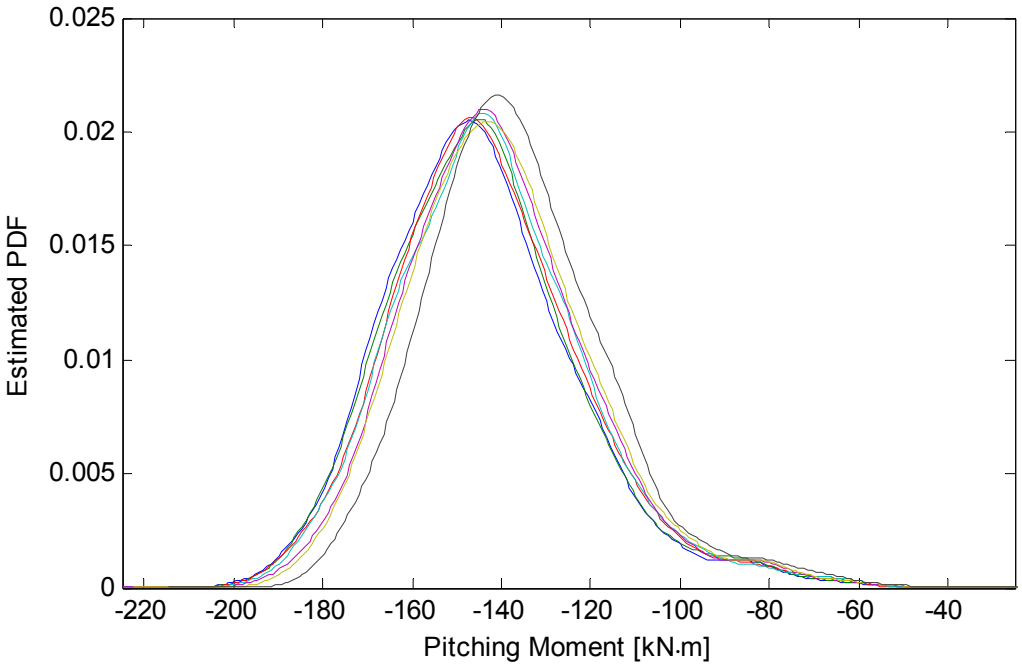

Figure 38. The probability density estimates generated using the local pitching moment one quarter of the way through a turbine rotation in the section of the damaged blade centered at 19.95 meters and all disbond lengths.

Table 4. The results of the two-sample t-tests using the pitching moment at 19.95 down the span of the damaged blade comparing the data from the healthy blade to the data from each of the disbond lengths.

Disbond Size	Reject Hypothesis	P-Value of Test	95% Difference Confidence Interval
0.625	No	0.59	-2.84 to 1.61
1.25	No	0.18	-3.74 to 0.69
1.875	Yes	0.046	-4.48 to -0.0445
2.5	Yes	0.0027	-5.57 to -1.17
4	Yes	1.19E-4	-6.52 to -2.12
6	Yes	2.37E-12	-10.0 to -5.66

Using a variety of different methods the sensitivity of the local pitching moments around the damage location to the presence of a TE disbond has been demonstrated and consequently these measurements would be advantageous to have in any SHPM designed to detect the presence of these disbonds. While in this case no off-rotor responses showed significant sensitivity to damage, other types of damage that have a larger effect on the underlying strength of the blades may impact these measurements more significantly and therefore the influence other commonly seen damage mechanisms should be investigated in the future. Furthermore, this example has illustrated the utility of the developed multiscale modeling methodology in the identification of measurements that are sensitive to a particular form of damage and the construction of an SHPM system.

5. OPERATIONS AND MAINTENANCE OF A SMART OFFSHORE WIND FARM

5.1. Progressive Damage and Cost Function Model

To effectively integrate an SHPM system into the overall O&M strategy for an offshore wind energy plant the repair costs associated with damage should be characterized. While some investigations of CBM implementations [34, 35] use a constant repair cost for each component, a the likely repair cost versus damage size function is expected to be more similar to a piecewise function where different types of repairs have different costs associated with them. Such a curve is shown for blade repairs in Figure 39 and will be employed in future cost-benefit analysis for structural health monitoring. There are four distinct regions of the cost model:

1. Small defects which do not need to be repaired
2. Moderate defects which can be repaired up-tower
3. Large defects which require the blade to be removed
4. Very large defects which require blade removal and replacement

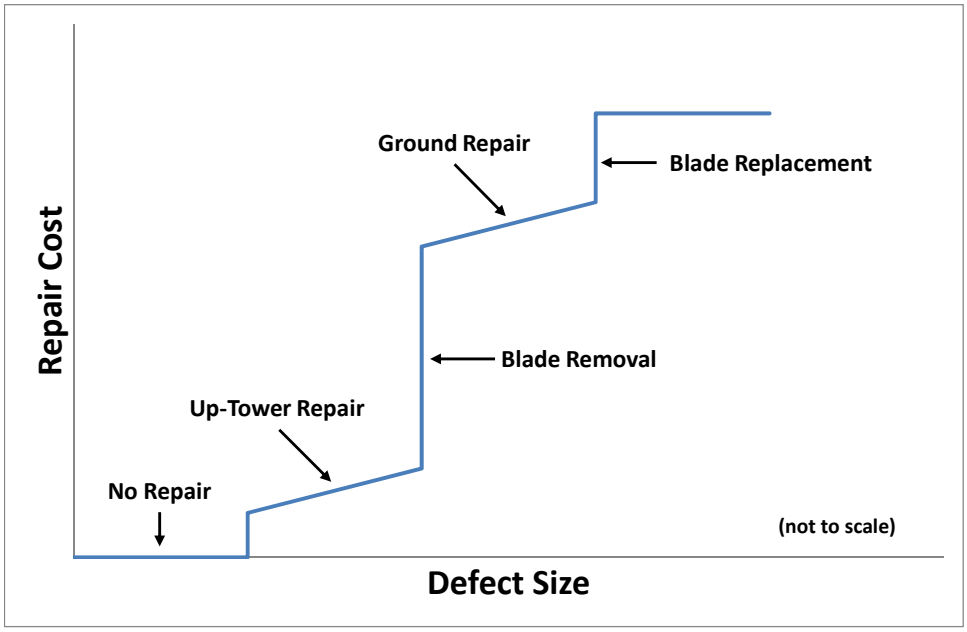

Figure 39. Example defect-cost model demonstrating the piecewise nature of defect size versus repair cost.

The exact numbers for this model have not been determined to date, nor has the relationship between repair cost and such factors as defect location, blade size, etc. However, the impact of this cost model in the SHPM cost-benefit analysis would be to show that knowledge of the damage state and the expected future loads would allow an intelligent controller to limit damage growth and keep it within the lower cost regions of the above curve until the repairs can be made. Furthermore, if a damage mitigating control strategy can be developed the turbine could continue to produce revenue even in this degraded state.

5.2. **Mitigation of Damage Growth by Turbine Derating**

Next we consider a simple example to evaluate the potential of mitigating wind turbine blade damage by derating the turbine. The presence of a disbond, a crack, or similar damage in the blade can cause a stress concentration which, if high enough, will become the dominant failure point in the blade structure. Due to the cyclic nature of wind blade loads, with time the higher stresses near the crack will exceed allowable levels and will lead to more rapid damage propagation.

5.2.1. *Stress Increase Due To Blade Damage*

A very simplified example is shown here in order to demonstrate the concept of stress amplification resulting from the presence of blade damage, in this case a simple crack. If one assumes that a crack is present in the blade such that the crack has an elliptical shape, is oriented perpendicular to applied stress, and is a relatively long crack with small crack tip radius of curvature, then the stress concentration factor associated with the crack is represented by Equation (9)

$$K_t = \frac{\sigma_{\max}}{\sigma} = 2\left(\frac{a}{\rho}\right)^{1/2} \tag{9}$$

where ρ is the crack tip radius of curvature and a is the half length of internal crack.

Making some assumptions about the crack tip radius, one can get a basic sense of the trends and magnitude of stress concentration factors associated with the damage. The stress concentration factor is highly dependent on the crack tip geometry and increases most rapidly for smaller crack lengths as seen in Figure 40. This trend highlights the importance of detecting cracks at early stages.

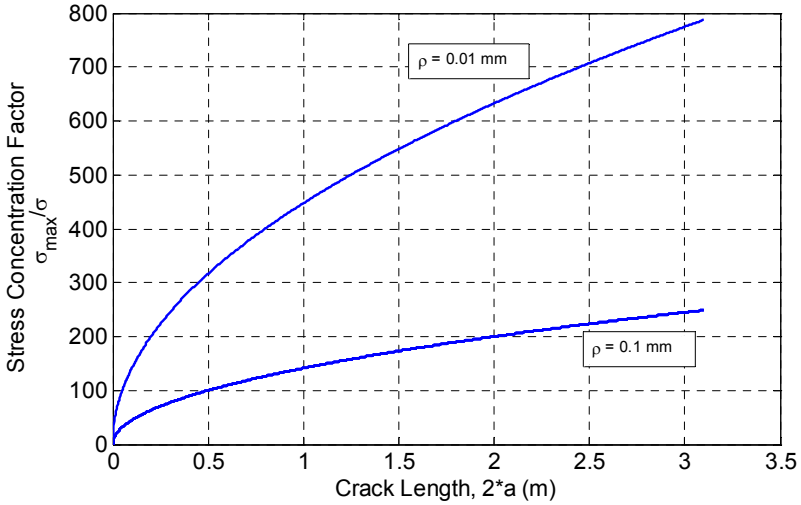

Figure 40. Stress concentration factors, K_t, as a function of crack length; shown for two different crack tip radii, rho.

5.2.2. *Fatigue Life Considerations*

An important blade design driver is fatigue life. The fatigue life of wind blade materials can be estimated using Miner's Rule which has the form:

$$Damage = \sum_i \frac{n_i}{N_F(\gamma_f \gamma_m S_i)} \leq 1.0 \tag{10}$$

where γ_f and γ_m are partial factors of safety for loads and materials, respectively; specified by design standards, n_i is the number of cycles at cyclic stress level S_i, N_F is the number of cycles to failure at the given stress level, and the material is said to have failed when the Damage summation exceeds unity.

The number of cycles to failure, N_F, depends on material properties derived from fatigue testing and can be modeled using a wide variety of different methods. One such model is the simple two parameter model for fatigue damage which can be written as:

$$N_F = \left(\frac{1}{C} S\right)^{-b} \tag{11}$$

While more elegant, multi-parameter fatigue life models may be easily inserted for N_F at this point in the analysis process, the simple two parameter model was used in this investigation to gain an initial understanding of the problem.

The damage computed using Miner's Rule can be linearly extrapolated to unity in order to arrive at an estimated fatigue life span of a material. Similarly, the damage for two different stress states can be compared in order to arrive at an estimate of the relative change in fatigue life. Consider the simple example of a 0.5m crack with 0.1mm crack tip radius. Equation (9) and Figure 40 would indicate a stress amplitude increase by a factor of 100 in the material nearest the crack. The ratio of fatigue damage for the blade with the crack and the healthy blade is an indicator of the expected change in fatigue lifetime. The proportional increase in the amount of damage due to the crack can be computed by using equation (11) to determine the number of cycles to failure and simplifying equation (10):

$$\frac{Damage_{cracked}}{Damage_{healthy}} = \frac{\left(\sum_i \frac{C^{-b} n_i}{S_{cracked}^{-b}}\right)}{\left(\sum_i \frac{C^{-b} n_i}{S_{healthy}^{-b}}\right)} = \left(\frac{S_{cracked}}{S_{healthy}}\right)^b = K_t^{\,b} \approx 100^{12} = 1 \cdot 10^{24} \tag{12}$$

This magnitude of increase in fatigue damage would equate to an enormous decrease in fatigue lifetime for the material near the crack. In reality, this causes failure of the material and thus

growth of the crack. An important question is whether the crack growth accelerates toward complete failure or slows toward a steady state. The hope is that the SHPM system will be able to detect and estimate the size of damage so that the turbine can be controlled to mitigate damage growth and prevent catastrophic failure.

5.2.3. *Structural Impacts of Turbine De-Rating*

If the structural loads in the blade can be reduced in the presence of damage, then the propagation of damage can be slowed. One means to reduce loads in the blade is to reduce the energy capture of the turbine, i.e. to derate the turbine. With derating, the turbine experiences lower aerodynamic and structural loads. The result is a decrease in production, but it may be more advantageous to sacrifice some production capacity in the near term in favor of greater benefits in the long term as will be explained in Section 5.3.

Figure 41 shows a simulated distribution of fatigue damage for the 5-MW turbine. Each data point on the curve is computed using Equation (10) above. Stress cycles are found using rainflow counting of time waveform simulation data using Crunch [36] on data generated from aeroelastic simulations that were performed using FAST. The fatigue damage was calculated based on a Rayleigh wind distribution with average wind speed of 10 m/s, representative of an IEC Class I site. The data clearly show that maximum fatigue damage occurs as the turbine is operating in wind speeds that are slightly above 12m/s, the rated wind speed for this machine.

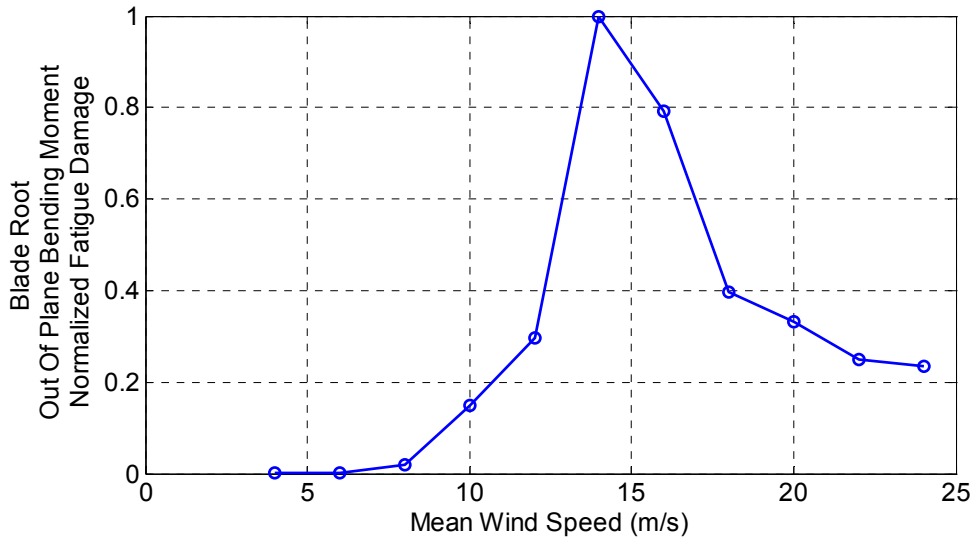

Figure 41. Fatigue damage distribution at operational wind speeds; blade root bending moment.

In the presence of damage, it could be beneficial to reduce the turbine loads in the vicinity of the peak in Figure 41 to slow the growth of the damage. This may be done through derating the turbine. Derating the turbine can be achieved through multiple methods, and a small subset of the possible methods is shown in Figure 42 where the control law is varied based on the wind speed region in which the turbine is operating. Mode 1 represents a decrease in the allowable rotor torque in Region 3 and unmodified operation in Region 2. Mode 2 represents a decrease in

allowable rotor torque in Region 3 as well as a decrease in rotor torque in Region 2, which may achieved through feathering the blades in Region 2. Mode 3 represents an entirely new approach where low and high wind speed operation and energy capture remain unaffected. In Mode 3 the turbine is derated only in the vicinity of the Region 2.5 transition, thus affecting only the highest operational fatigue loads. Design and implementation of Mode 2, Mode 3 and other more advanced prognostic control actions is an area for future research.

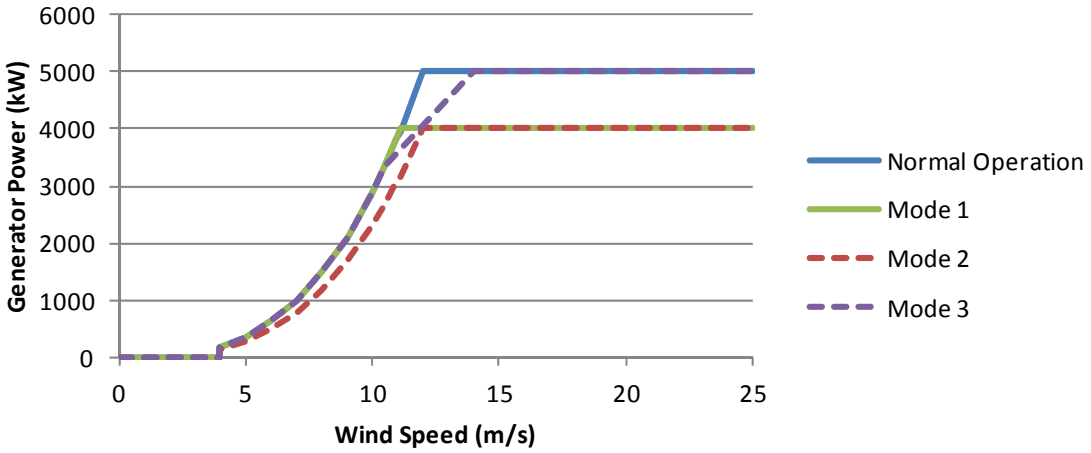

Figure 42. Illustration of various turbine derating schemes; curves for Modes 1, 2 and 3 illustrate 80% turbine rating.

It is helpful to analyze the effect of derating a turbine on the cyclic fatigue loads that are encountered on the blade. Figure 43 (a) shows the change in equivalent cyclic load experienced by the blade as a function of turbine rating. Figure 43 (b) shows the change in actual fatigue damage (inversely related to fatigue life) as a function of turbine rating when the Mode 1 derating method was used. Again, the data points in these simulations were generated by FAST and Crunch, using the fatigue analysis process described previously in this report. Derating to 95% leads to a reduction in cyclic loads to levels that are 90% of the rated levels. In addition, it leads to fatigue damage that is 30% of what was incurred at the rated level. Such a decrease in fatigue damage is equivalent to an increase in the fatigue life of the blade by a factor of more than three. The decrease in blade stress resulting from derating will help offset the stress concentrations that arise due to the presence of damage as shown in Figure 40. More significant derating leads to more impressive extension of expected fatigue life. Clearly, an optimization of turbine energy capture versus maintenance costs is required and will provide more understanding regarding an appropriate level of turbine load reductions in place of immediate blade maintenance.

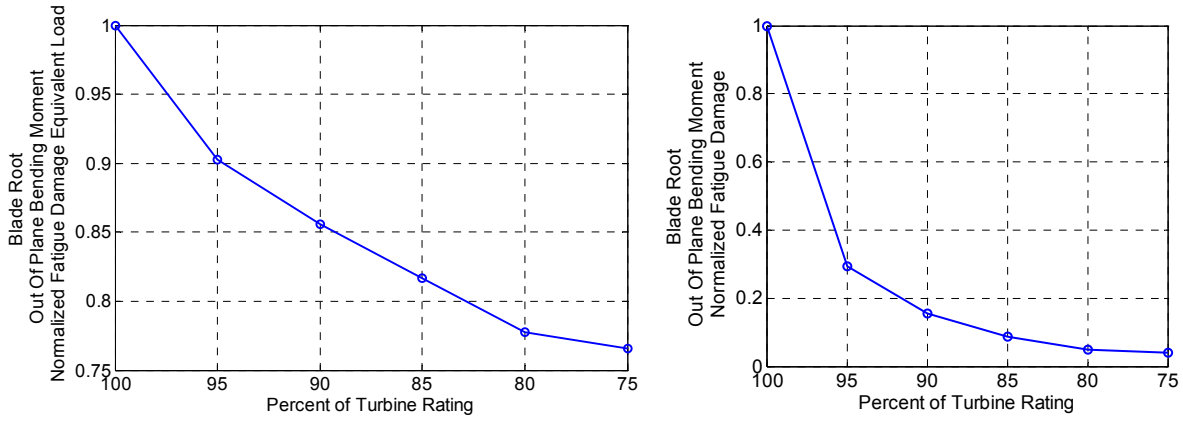

Figure 43. Decrease in (a) normalized cyclic load amplitude and (b) normalized fatigue damage as a function of turbine rating; simulations performed in 11 m/s average wind speed.

5.3. The Use of SHPM and Load Management for O&M

Many of the traditional analyses [7-12] of the benefits of SHPM systems into wind plant O&M take a passive view of the wind farm. This means that knowledge of the damage state of the turbine simply results in optimization of the maintenance of the turbines rather than changes in how the wind farm is operated. However, due to the difficulty of access associated with offshore wind turbines it may not always be desired, or possible, to repair a turbine as soon as a detectable amount of damage is present.

The decrease in loads and fatigue damage that can be achieved by derating a turbine (Section 5.2) demonstrates the feasibility of extending the life of a given turbine at the cost of a small percentage decrease in revenue. One of the benefits of this methodology is that for a single turbine even if maintenance cannot be performed when damage is detected, the turbine can be derated slightly so that it still generates revenue but does not accumulate large amounts of additional damage. This could potentially reduce the associated repair costs significantly if the transition between two different types of repairs can be avoided (see Section 5.1). A second benefit to the derating process that is especially relevant for offshore wind plants is that it this life extension methodology increases the possibility of servicing multiple turbines during a single visit to the offshore wind plant. Smart turbine load management, therefore enables the turbine operator to affect the progression of damage in a turbine so that the timing of operations and maintenance procedures can be optimized for the entire wind farm. Once quantitative damage size versus repair costs functions (Figure 39) have been determined, further simulations of an entire offshore wind plant could be used to quantitatively evaluate the cost reductions possible with a SHPM system and load management methodology.

6. CONCLUSIONS

This report provides an initial roadmap for integration of structural health and prognostics management (SHPM) into the O&M process for offshore wind plants. The key aspects of the work include (1) development of a multiscale modeling and simulation methodology to analyze the effects of damage in damaged operating turbines, (2) demonstration of this multiscale approach to perform sensitivity of damage studies for a candidate blade damage mechanism, (3) development of an initial conceptual damage and cost model for blade repair, and (4) identification and evaluation of smart turbine loads management (control) strategies based on SHPM for offshore wind plants.

A multiscale simulation methodology was developed for the investigation and development of SHPM methods for offshore wind turbine blades. The method relies on the propagation of damage from high fidelity component-level models to reduced order models that can be used in full turbine simulations so that the changes in the turbine's operational responses due to damage can be examined. These full turbine simulations can also be used to estimate the loads on individual components, such as turbine blades, and then be propagated back into to the high fidelity model to allow for further local analyses of the effects of damage to be conducted. By investigating the effects of damage on multiple scales, the developed methodology takes advantage of available software to investigate the underlying physical consequences of damage on both a local and global level. These simulations can then be used for many purposes including identification of global operational responses that are most sensitive to the damage (e.g. to evaluate sensing and detection options) and analysis of local effects of damage in the high-fidelity model (e.g. to estimate the remaining life or extent of the damage in the structure).

This report has demonstrated the application of the developed simulation-based methodology to perform a sensitivity of damage study of operational response measurements for the case of a TE (trailing edge) disbond on an offshore 5-MW wind turbine. A 61.5 meter blade model with a carbon fiber composite spar cap was developed using SNL's NuMAD software. The blade was then exported to ANSYS where the TE disbond was simulated by splitting the TE in half and constraining the bottom and top nodes to one another in the healthy portions of the blade. Reduced order models of the damaged blades were then created using SNL's BPE software. The analysis of these reduced order models demonstrated that the TE disbonds decreased the torsional stiffness of the blade around the disbond but did not significantly affect the blade's mass or stiffness in other directions. These reduced order blade models with varying levels of damage were included as part of a model of a 5-MW offshore turbine on a fixed monopole in 20 meters of water. The operational response of seven offshore turbine models with varying levels of damage was then simulated in both FAST and MSC.ADAMS. The operational responses were studied to quantify the sensitivity of the operational response to the TE disbonds. The sensitivities of the numerous operational responses (e.g. accelerations, moments) were quantified using measures that included analysis of statistical moments and standardized RMS difference. FAST simulations were found to be inadequate for modeling the effects of a TE disbond due to the fact that the torsional stiffness of the blades is not taken into account in FAST. However, from the ADAMS simulations it was apparent that the measurements which were the most sensitive to the presence and extent of the TE disbond were the pitching moments near the location of damage. The aerodynamic loads from the FAST simulations were calculated and

applied to the high fidelity ANSYS model, which also demonstrated that changes in the blade's strain field were localized around the edges of the disbond.

To examine how the structural health of each turbine could be used to optimize the operation and maintenance practices of an offshore wind plant, a qualitative damage size versus repair cost function for wind turbine blades was investigated. Additionally, smart load management (control) strategies were identified and simulations demonstrated that derating a turbine could be used to effectively decrease loads and significantly extend the fatigue life of a turbine while reducing the generated power by only a small percentage. The combination of the repair cost information along and the structural health of each turbine can be utilized in the optimization of damage mitigating control strategies to reduce the operations and maintenance costs associated with running an offshore wind energy plant.

7. FUTURE WORK

Rather than functioning as an in-depth investigation of all the possible areas of research in the SHPM of offshore wind turbines, this report has attempted to provide an initial "roadmap" into how the SHPM problem can be approached using a physics-based multiscale modeling and simulation methodology. As a consequence of this approach, there are a number of areas in which this initial report has only briefly touched on and are in need of further investigation.

In future work, this effort will be expanded to a more comprehensive system model in which the economics of power production and maintenance, sensitivity analyses of damages, and smart turbine load management (controls) will be analyzed to ensure the optimal operations strategy that balances maintenance processes with revenue production of the complete wind farm. This effort will consider cost-benefit trade-offs for traditional SCADA data streams as well as novel sensor or condition based monitoring system additions to traditional SCADA. In an additional avenue, SCADA data streams are likely to provide much more information than is the current practice because additional data mining and signal processing is possible.

Additional blade damage mechanisms in addition to TE disbond will be analyzed via similar sensitivity of damage studies to determine damage signatures that are potentially unique for different types of damage experienced in utility-scale wind turbine blades. The local analysis of the high-fidelity blade model will also include additional structural analyses beyond fatigue analysis. IEC standards for simulations will be used to establish critical damage sizes for these types of damage by determining the size of damage when the turbine no longer complies with certification requirements. A more complete model of the economics of integrating a SHPM system into offshore wind plants is required.

Another area that necessitates further investigation is the adequacy of the simple damage model used to model the TE disbond in this report. For example, the impact of the nonlinear surface contact in areas that have disbonds remains an area for future investigation. Such an exploration would include what effects the use of nonlinear contact constraints have on the equivalent stiffness values calculated by BPE, as well as the possible use of a nonlinear stiffness matrix in the damaged area in the full turbine simulations. The local strain sensitivity analysis should also be verified through a convergence analysis and ideally the model would be validated through the correlation with experimental strain measurements.

Based on the promising results from this study, another area that deserves further investigation is smart turbine loads management - the development of prognostic control and derating schemes. For example, results using Mode 2 and Mode 3 (as described in this report) or other more advanced derating schemes could be investigated and optimized. Furthermore, prognostic control algorithms that are based off mitigating damage growth or failures associated with the principal blade design drivers such as ultimate strength, deflection, and buckling should be investigated in addition to the fatigue analysis in this report.

Finally, the success of different damage detection algorithms for detecting various types and locations of damage remains future work. While this document focused solely on the use of time domain methods for the quantification of damage sensitivity, the developed multiscale

simulation methodology opens the doors for a wide variety of operational monitoring and damage detection methods to be investigated. However, as part of these investigations the influence of a wide amount of different parameters such as environmental changes and the impact of variable wind loadings would have to be investigated. Again, a more complete model of the economics of integrating a SHPM system into offshore wind plants is required along with evaluations of SHPM system performance.

These planned activities will provide a foundation for the future long-term research program aimed to support the needs of the offshore wind industry. The current activities can provide a starting point for moving from these FY11 simulation-based studies at Sandia to laboratory and field testing demonstration projects. Such testing can provide a deeper knowledge base regarding application and implementation of health monitoring to wind turbines, a database for evaluation of damage detection and sensing methods, and a means to evaluate how turbine-turbine interactions affect the methodologies.

8. REFERENCES

1. A.C. Levitt, W. Kempton, A.P. Smith, W. Musial and J. Firestone, "Pricing offshore wind power." *Energy Policy* (In Press) 2011.
2. W. Musial and B. Ram, *Large-Scale Offshore Wind Energy for the United State: Assessment of Opportunities and Barriers*, NREL Report No. TP-500-49229, Golden, CO, September 2010.
3. U.S. Department of Energy, *A National Offshore Wind Strategy: Creating an Offshore Wind Energy Industry in the United States,* Washington: Wind & Hydropower Technologies Program Report No. 5040, February 2011.
4. R. Wiser and M. Bolinger, *2010 Wind Technologies Market Report*, Lawrence Berkeley National Laboratory: Lawrence Berkeley National Laboratory. LBNL Paper LBNL-4820E, June 2011.
5. B. Snyder and M.J. Kaiser, "Ecological and economic cost-benefit analysis of offshore wind energy." *Renewable Energy* 34(6), pp. 1567-1578, 2009.
6. Y. Amirat, M.E.H Benbouzid, B. Bensaker, and R. Wamkeue, "Condition monitoring and fault diagnosis in wind energy conversion systems: a review." In *Proceedings 2007 IEEE International Electric Machines and Drives Conference*, Vol 2., pp. 1434-1439, 2007.
7. G. van Bussel, A.R. Henderson, C.A. Morgan, B. Smith, R. Barthelmie, K. Argyriadis, A. Arena, G. Niklasson, and E. Peltola, "State of the Art and Technology Trends for Offshore Wind Energy: Operation and Maintenance Issues," *Offshore Wind Energy EWEA Special Topic Conference*, Brussels, Belgium, December 2001.
8. L.W.M.M. Rademakers, H. Braam, M.B. Zaaiger, and G.J.W. van Bussel, "Assessment and optimisation of operation and maintenance of offshore wind turbines," in *Proceedings of the European Wind Energy Conference*, Madrid, Span, June 2003.
9. J. Nilsson and L. Bertling, "Maintenance management of wind power systems using condition monitoring systems – Life cycle cost analaysis for two case studies," *IEEE Transactions on Energy Conversion* 22(1), pp. 223-229, 2007.
10. C.C. Ciang, J.R. Lee, and H.J. Bang, "Structural health monitoring for a wind turbine system: a review of damage detection methods." *Measurement Science and Technology* 19(12), pp. 1-20, 2008.
11. F. Besnard, K. Fischer, and L. Bertling, "Reliability-centred asset maintenance – A step towards enhanced reliability availability and profitability of wind power plants" in *2010 IEEE PES Innovative Smart Grid Technologies Conference Europe (ISGT Europe)*, 2010.
12. Z. Hameed, S.H. Ahn, and Y.M. Cho, "Practical aspects of a condition monitoring system for a wind turbine with emphasis on its design, system architecture, testing and installation," *Renewable Energy*, 35(5), pp. 879-894, May 2010.
13. NWTC Design Codes (FAST by Jason Jonkman, Ph.D.). http://wind.nrel.gov/designcodes/simulators/fast/. Last modified 05-November-2010; accessed 05-November-2010.
14. R.R. Ryan, ADAMS – Multibody System Analysis Software, Multibody Systems Handbook. Berlin: Springer-Verlag, 1990.
15. J. Jonkman, S. Butterfield, W. Musial, and G. Scott, "Definition of a 5-MW Reference Wind Turbine for Offshore System Development," NREL/TP-500-38060, Golden, CO: National Renewable Energy Laboratory, February 2009.

16. Reference, MSU Database: MD-P2B; [±45/(0)4C]S; 55%vf; EP; Newport NB307; carbon prepreg; 85% Uni; 15% DB.
17. D.J. Malcolm and D.L. Laird, "Extraction of Equivalent Beam Properties from Blade Models." *Wind Energy*, 2007, 10, 135-137.
18. D.J. Malcolm and D.L. Laird, "Identification and Use of Blade Physical Properties," *AIAA 43rd Aerospace Sciences Meeting and Exhibit*, 2005.
19. D.J. Malcolm and D.L. Laird, "Modeling of Blades as Equivalent Beams for Aeroelastic Analysis," *AIAA 41st Aerospace Sciences Meeting and Exhibit*, 2003.
20. D.J. Malcolm and D.L. Laird, "Identification and Use of Blade Physical Properties," *AIAA 43rd Aerospace Sciences Meeting and Exhibit*, 2005
21. D.L. Laird, F.C. Montoya, and D. Malcolm, "Finite Element Modeling of Wind Turbine Blades." 43rd AIAA Aerospace Sciences Meeting and Exhibit, 2005, 9-17.
22. B. Resor, J. Paquette, D. Laird, and D.T. Griffith, "An Evaluation of Wind Turbine Blade Cross Section Analysis Techniques." 51st AIAA Structures, Structural Dynamics, and Materials Conference, 2010.
23. B. Resor and J. Paquette, "Uncertainties in Prediction of Wind Turbine Blade Flutter." 52nd AIAA/ ASME/ ASCE/ AHS/ ASC Structures, Structural Dynamics and Materials Conference, 2011.
24. Y. Chen and J.E. McInroy, "Estimation of Symmetric Positive-Definite Matrices from Imperfect Measurements," *IEEE Transactions on Automatic Control*, 47(10), pp. 1721-1725, 2002.
25. Jensen, F.M, "Failures in Trailing Edge Bondlines of Wind Turbine Blades," in *Proceedings of the 32nd Risoe International Symposium on Materials Science*, Roskilde, Denmark, 2011.
26. D.E. Adams, J.R. White, M. Rumsey, and C. Farrar, "Structural health monitoring of wind turbines: method and application to a HAWT," *Wind Energy*, 14(4), pp. 603-623, 2011.
27. M.A. Rumsey and J.A. Paquette, "Structural health monitoring of wind turbine blades, " in *Proceedings of SPIE Smart Structures and Materials & Nondestructive Evaluation and Health Monitoring,* San Diego, CA, March 2008.
28. A. Ghoshal, M.J. Sundaresan, M.J. Schulz, and P.F. Pai, "Structural health monitoring techniques for wind turbine blades," *Journal of Wind Engineering and Industrial Aerodynamics,* 85(3), pp. 309-324, 2000.
29. B.J. Jonkman and M.L. Buhl. *TurbSim user's guide [electronic resource]*. National Renewable Energy Laboratory, Golden, CO., 2006.
30. J. Bai and S. Ng, "Tests for Skewness, Kurtosis, and Normality for Time Series Data," *Journal of Business and Economic Statistics* 23(1), pp. 49-60, 2005.
31. C.R. Farrar and T.A. Duffey, "Vibration-Based Damage detection in Rotating Machinery." *Key Engineering Materials* Vols. 167-168, pp. 224-235, 1999.
32. J.R. White. "Operational Monitoring of Horizontal Axis Wind Turbines with Inertial Measurements," Doctoral Dissertation Purdue University (2010).
33. Z.I. Botev, J.F. Grotowski, and D.P. Kroese, "Kernel Density Estimation Via Diffusion." *The Annals of Statistics*, 38(5), pp. 2916-2957, 2010.
34. D. McMillan and G.W Ault, "Towards Quantification of Condition Monitoring benefit for Wind Turbine Generators," in *Proceedings European Wind Energy Conference*, Milan, pp. 112-116, May 2007.

35. D. McMillan and G.W. Ault, “Condition monitoring benefit for onshore wind turbines: sensitivity to operational parameters,” *IET Renewable Power Generation*, 2(1), pp. 60-72, March 2008.
36. NWTC Design Codes (Crunch by Marshall Buhl) Last modified 01-April-2008; accessed 01-April-2008.

(this page intentionally left blank)

CHAPTER 3. AN UPDATED SHPM TECHNOLOGY ROADMAP – FY12/FY13

An updated SHPM technology roadmap is presented in this chapter. This roadmap defines core technology development needs, outlines prognostics management concepts & their economics implications, and identifies the data & information that is needed for SHPM technology validation and cost analyses. The highlights include:

- Identification of 6 major thrust areas for SHPM research and development
- Detailed descriptions of the major thrust areas, including stages of maturity for each thrust area, are defined
- A description of vertical integration of these thrust areas into for a working SHPM "system" is provided

A Technology Roadmap for Structural Health and Prognostics Management Applied to Offshore Wind Plants

In fulfillment of FY13/Q2 Milestone for Offshore Project WE 5.1.1: "Prepare updated roadmap document outlining performance and economics of the SHM/PM applied to offshore wind plants."

D. Todd Griffith
Wind Energy Technology Department
Sandia National Laboratories

Contents

Figures

Tables

A Technology Roadmap for Structural Health and Prognostics Management Applied to Offshore Wind Plants

D. Todd Griffith
Sandia National Laboratories

Background

Although research in the fields of structural health monitoring and prognostics management are fairly rich in general, research in application to wind turbine rotor blades in either field is somewhat limited. Furthermore, the integration of these two disciplines to produce a cost-effective condition-based monitoring system for wind turbine rotors is non-existent.

In this section, a brief overview of recent work at Sandia is presented.

Sandia has had an active program for several years to investigate sensored blades with several blade-build and field testing demonstration projects (e.g. "Sensor Blade"). Blades for utility-scale wind turbines typically have no sensors in the blades, but if they do the sensors are limited to strain gauges in the blade root. The Sandia research involved embedding sensors along the entire blade span, which included acceleration, strain, and temperature sensors. The proposed applications for this "enhanced" blade sensing capability include structural health monitoring and active control of the rotor. The Sandia "Sensor Blade" work demonstrated the feasibility of manufacturing sensors into the blade, which is an important first step for evaluation and implementation of the conceived monitoring and control applications – such as SHPM (structural health and prognostics management) which is the focus of the present study.

Reference 1 provides an initial roadmap developed by Sandia National Laboratories for combining structural health monitoring and prognostics assets into a SHPM (structural health and prognostics management) system with application to wind turbine rotor blades. The key element established in this initial roadmap, the so-called multi-scale damage modeling and simulation methodology, addresses both how damage is modeled at multiple resolutions of the model and also the resulting manifestation (or effects) of damage in both the global operating dynamic response and localized effects related to remaining life. The intent of this multi-scale approach is to combine structural health monitoring and prognostic management so as to bridge the gap between being able to detect and characterize the presence of damage and then being able to make revenue-optimizing operations and maintenance decisions.

Reference 2 is a follow-on study to the initial work and details a set of additional case studies of rotor faults and damage as well as an initial cost analysis for SHPM. In the initial study, trailing edge disbond of the blade was examined. In Reference 2 rotor imbalance (including pitch error aerodynamic imbalance and mass imbalance) and shear web disbond were examined. Sensitivity of damage studies were performed and detection strategies using blade and non-blade sensors were developed. The initial SHPM cost analysis was defined and demonstrated.

Sandia's Initial Roadmap and Results for SHPM Applied to Wind Plants

In this section, the initial roadmap and results for SHPM applied to Wind Plants is presented in more detail. The first four sections describe key individual technical thrust areas of the research and the fifth and final section describes the initial integration of these technical thrusts for end to end evaluation of the performance and economics of SHPM.

Multi-scale Simulation of Damage Approach

A key element of this SHPM approach involves the multi-scale damage modeling and simulation methodology, as shown in Figure 1. The blue blocks indicate modeling steps for either the blade or turbine. Red blocks indicate simulations using these models. The green blocks indicate analysis stages and decision points in the process including the results of the two sensitivity analyses and the prognostic (damage mitigating) control decisions. Note that after the "Full Turbine Simulations" step the aerodynamic loads information is passed back to the "High Fidelity Simulations" step in order to perform the "Local Sensitivity" analysis step.

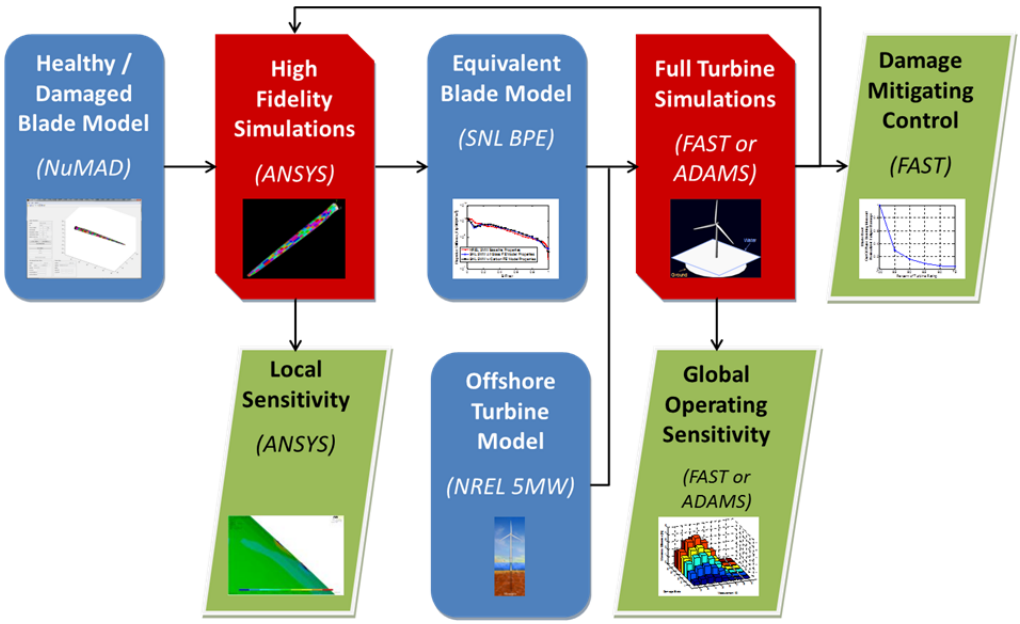

Figure 1. The multi-scale damage modeling and simulation methodology designed to aid in the development and optimization of health monitoring systems for wind turbine blades.

Global Operating Sensitivity to Damage: Operating Response

The operating response from the "Full Turbine Simulations" step provides what are essentially virtual sensor measurements for the as-modeled damaged rotor blade(s). These virtual sensor measurements are analyzed to evaluate viable sensing options to detect the as-modeled damage including sensor types, sensor locations, and required sensor characteristics – tailored to the unique dynamics of the wind turbine rotor. Viable damage detection strategies are also developed based on analysis of the global operating sensitivity. A large number of case studies can be examined in this framework by varying; for example, the type of damage, the location of the damage within the blade, and the extent of the damage (all of which are performed in the first step "Healthy/Damaged Blade Model").

Reference 1 presented an initial case study of rotor damage, a trailing edge disbond. The subsequent work considers additional case studies demonstrating the sensitivity of damage in the operating response to rotor imbalance and shear web disbonds.

Local Sensitivity to Damage: Blade State of Health

In order to make profitable decisions regarding operations and maintenance, the blade state of health must be estimated. While analysis of the global operating response is important to estimate the blade state of health, additional information is needed to fully understand the state of health and the significance of the current state of health with respect to operations and maintenance decisions. This knowledge is needed to understand if the damage could result in a catastrophic failure of the rotor or to better understand under what loading conditions the damage may grow in extent. The approach proposed in this work is to perform a complete set of loads calculations based on the international blade design standards (IEC and GL) for the as-modeled damaged blade to determine if the required margins on the partial safety factors are violated for the key blade design conditions (ultimate strength, tip-tower clearance, fatigue life, and buckling capacity) in the presence of the damage.

As an initial demonstration of the "Local Sensitivity" analysis, Reference 1 presented a study of the effect of a trailing edge disbond on the blade fatigue life and also the localized strain effects due to this type of damage. The subsequent work looks at localized strain, deflection, and buckling, although additional work is ongoing to further demonstrate this element of the methodology.

Prognostic (Damage Mitigating) Controls

Initial conceptual control strategies including derating were proposed in Reference 1. These concepts are indicated as Modes 1, 2, and 3 in Figure 2. The fundamental idea behind these control strategies is to reduce the loads on the rotor to avoid damage growth or catastrophic failure. Of course, the economics of derating strategies must be considered with respect to AEP, maintenance planning, and repair/replacement costs. Integration across all the technical thrust areas provide for this economics analysis – see Section 2.5.

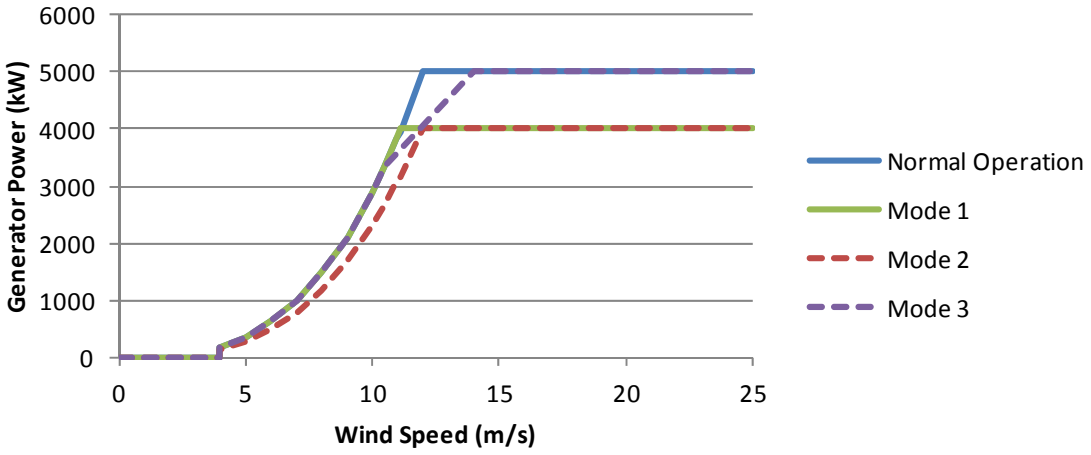

Figure 2. Illustration of a Few Prognostic Control Strategies Using Power Curves

Maintenance Process and States of Health Definitions

A conceptual model to define blade states of health and their associated repair/replacement costs has been developed (Reference 1). This approach has been utilized in the state-based SHPM cost model development. Initial cost data has been identified for these repair/replacement costs; however, refined estimates for these costs from industry-based studies are needed to improve the economics analysis.

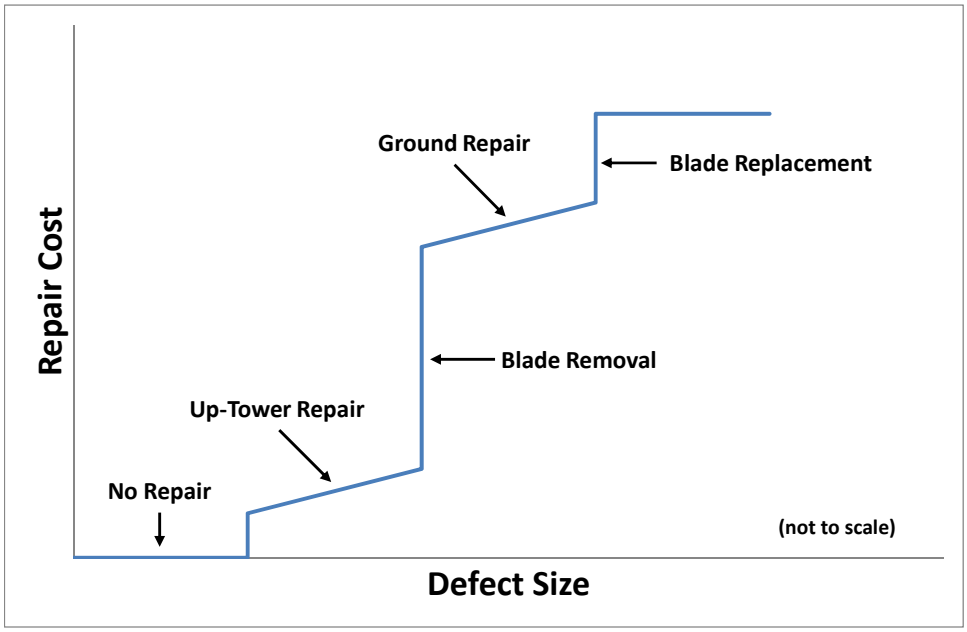

Figure 3. States of Health Concept and Cost Dependence (Four States: No Repair, Up-Tower, Ground, and Replacement).

SHPM Cost Model

Preliminary cost models compatible with the SHPM performance assessment were presented in Reference 2. These cost models offer potential for design of SHPM systems and can guide the optimal operations (control) and maintenance processes during operation of a wind farm. The conceptual flowchart for the initial state-of-health based approach is presented in Figure 4. This approach has been exercised to investigate sensitivities of the cost model output to input variables.

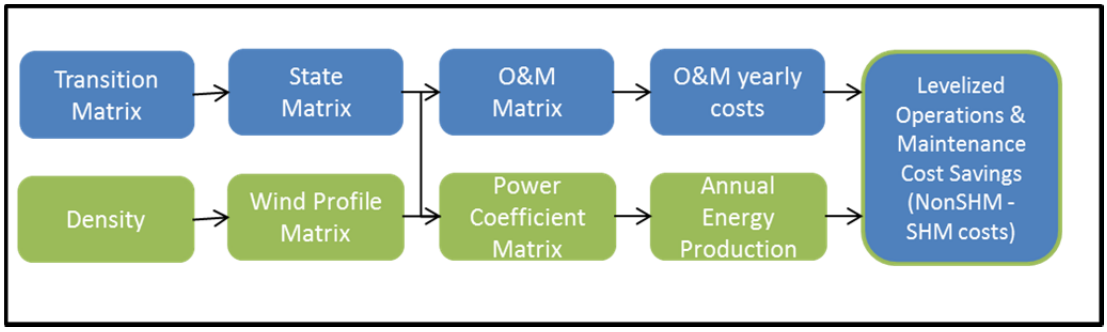

Figure 4. SHPM State-of-Health Based Cost Model Flowchart

Initial Integration of SHPM Technical Thrust Modules

An initial integration of the key elements described in Sections 2.1, 2.2, 2.3 and 2.4 was documented in Reference 2. The overall approach here is to integrate from end to end (1) the simulation of damage methodology, (2) damage sensitivity analysis, and (3) SHPM cost analysis. These three elements are shown in the left, middle, and right blocks of Figure 5, respectively.

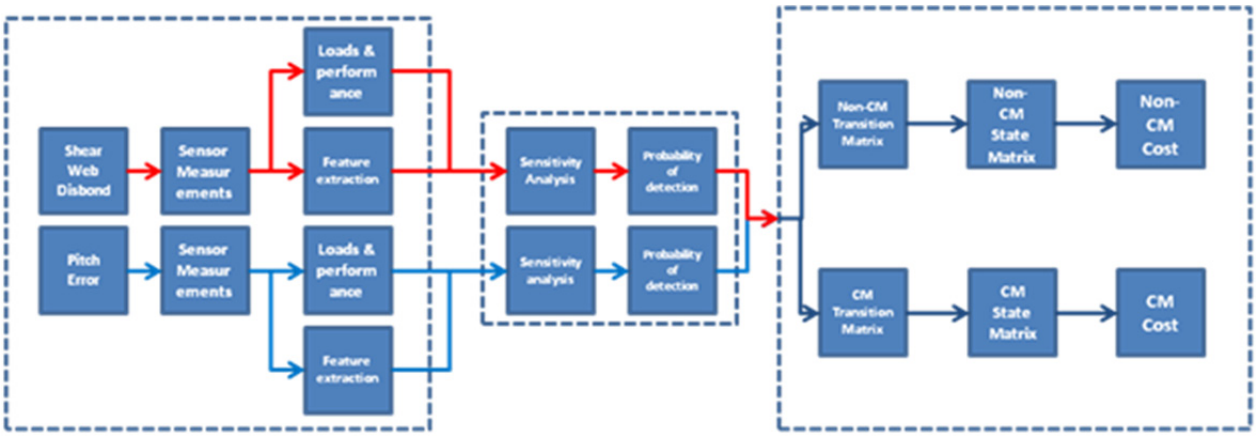

Figure 5. Overall approach for projecting COE benefits based on damage/fault detection strategies (Left Block: Operational Simulation of Damage (see Figure 1); Middle Block: Damage Sensitivity Analysis and Detection Evaluation; Right Block: Cost Analysis)

In an actual implementation of SHPM, the left-most block of simulations would be replaced by an actual operating response data stream. The purely simulation-based approach is used in the design phase to determine the most cost-effective hardware/sensor needs and associated operations and maintenance processes with the opportunity to analyze a large number of operating scenarios. For an operational implementation of SHPM, information from the right-most cost analysis block would feedback to the turbine operator or control system to aid in decision making.

Research Blocks in the Updated Technical Roadmap for SHPM Applied to Wind Plants

This section outlines the research thrusts that are required in this plan for *development of the 1st generation cost-effective SHPM system for wind turbine rotors*.

Thrust 1: Identify the critical/relevant damage features
Thrust 2: Model and characterize the damage features
- ***Thrust 2a:*** Effects of damage on operational response (Global Sensitivity)
- ***Thrust 2b:*** Effects of damage on blade state of health (Local Sensitivity)

Thrust 3: Economics analysis: Cost modeling for the SHPM process
Thrust 4: Operations decisions: SHPM prognostic control actions
Thrust 5: Operations decisions: SHPM maintenance actions

A high-level description of these thrust areas is provided in this section. A detailed roadmap for each of these areas is presented in the next section.

Thrust 1, Identify the critical/relevant damage features
In this Thrust Area, we identify the common, highly-relevant damage features for the studies. These damage features are ranked based on impact on revenue loss (consequence of failure, frequency of occurrence, downtime, replacement costs, etc.). Additional maturity is gained through assessment of the collective effects of these damage features on revenue losses.

Thrust 2, Model and characterize the damage features
In Thrust Area 2, modeling and characterizing the damage features (identified in Thrust Area 1) is done using the developed multi-scale simulation of damage approach (see Figure 1). The two key parts (or scales) of this approach are sensitivity analysis of the operating response (global) and sensitivity analysis of the blade state of health (local). The maturity plan for each of these modeling efforts involves refining the fidelity of damage modeling and moving toward data collection for validation of these models.

Thrust 2a, Effects of damage on operational response (Global Sensitivity)
This thrust area focuses on the effects of damage in the operating response. This is where sensor and condition monitoring systems are evaluated and designed as viable options to detect and characterize state of health.

Thrust 2b, Effects of damage on blade state of health (Local Sensitivity)
This thrust area focuses on effects of damage on blade state of health (i.e. blade remaining life). The proposed approach is to use loads analysis defined in blade design standards to evaluate performance margins of the principal design drivers (ultimate strains, tip-tower clearance, fatigue life, and buckling capacity) in the presence of damage. This evaluation will determine if blade remaining life has been diminished from the healthy design state to require shutdown, reduced loads management, or maintenance actions.

Thrust 3, Economics analysis: Cost modeling for the SHPM process
An economics analysis compatible with the other thrust areas is needed for development in Thrust Area 3. The maturity plan includes develop of initial cost models for SHPM moving to refined cost models and then integration and end to end demonstration with the other modules. The cost analysis should be flexible enough to be useful for design analysis as well as real-time economics decision-making.

Thrust 4, Operations decisions: SHPM prognostic control actions
This Thrust Area involves potential revenue-optimizing control actions based on smart loads management strategies using a SHPM system. These prognostic control actions can include shutdown to prevent catastrophic failure or derating strategies that avoid shutdown so to produce revenue until proper maintenance can be executed (based on component availability, weather, sea states, etc.).

Thrust 5, Operations decisions: SHPM maintenance actions
This Thrust Area involves new maintenance processes that are enabled by a SHPM system. One focus is to enable predictive or planned maintenance at lower costs versus conventional unplanned or reactive maintenance when using a cost-effective SHPM system.

An Updated Technical Roadmap for SHPM Applied to Wind Plants

This initial (version 1.0) of the Technical Roadmap for SHPM applied to wind plants is described in Table 1. The table is divided by major thrust area, as discussed in the previous section. There are 6 major Thrust Areas with 5 Stages of maturity for each thrust area. Descriptions for levels of maturity for each thrust area are provided for Stages 1 to 5 in the table.

The text in the table is color coded to indicate the status of the research in the context of the Sandia work (as of March 2013). Green indicates mature/completed work, blue is current focus areas, maroon is anticipated near-term next steps, and black is longer-term future work.

Technology integration is important in gathering the information and tools developed across the thrust areas to evaluate "system-level" SHPM performance, economics, and the associated trade-offs. Vertical integration across a single stage is not necessarily implied in this roadmap as the technical integration and their evaluation phases can take place by integrating across different stages as each of the thrust areas is matured.

Table 1. SHPM Technical Maturity Roadmap – Version 1.0
(Key: mature/completed, current, near-term future, longer-term future) As of March 2013

		Stage 1	Stage 2	Stage 3	Stage 4	Stage 5
Thrust Area 1	**Identify Relevant Damage Features**	• Identify single damage feature #1 • Define criterion for selection: rank based on impact on revenue	• Identify additional important rotor damage features	• Quantify and validate collective effects of these features on revenue loss	• Implement approach for experimental simulation of damage	• Identify and demonstrate the method for non-blade components (e.g. tower)
Thrust Area 2(a)	**Model and Characterize Damage Features: *Global Operating Sensitivity***	• Develop methodology to model and simulate damage globally • Identify sensor needs for blade and non-blade sensing for feature #1 • Identify detection strategy for feature #1	• ID sensor needs for multiple features (blade and non-blade) • ID detection strategies for additional features (blade and non-blade) • Comprehensive survey of industry sensor products (turbine and general)	• Mature detection robustness to uncertainties and multiple simultaneous damage features • Mature the damage model (linear versus nonlinear models) of operating sensitivity	• Mature the damage model (progressive damage model) for operating sensitivity • Laboratory demonstration of detection strategies	• Demonstrate detection in field tests on utility-scale rotor
Thrust Area 2(b)	**Model and Characterize Damage Features: *Local Damage Effects***	• Develop methodology to model and simulate damage locally • Develop a plan to quantify the blade state of health • Perform targeted load case analysis	• Perform complete set of load case analyses to quantify damage effects on state of health tied to IEC/GL blade design standards	• Mature the damage modeling (linear versus nonlinear models) for buckling and strain calculations	• Mature the damage model (progressive damage model) for effect on local sensitivity	• Demonstrate localized damage effects and their progression in full-scale blade test
Thrust Area 3	**SHPM Economics Analysis**	• Initial cost model defined for SHPM system assessment (ID inputs/outputs)	• Refine the fidelity of the SHPM cost model • Perform input/output sensitivity studies	• Integrate with simulations in Thrust Areas 2(a) and 2(b) in end to end case study of SHPM system cost and performance	• Field demonstration project to validate SHPM system model performance and economics	• Distribute validated SHPM cost and decision tools to industry
Thrust Area 4	**SHPM Operations Decisions: Controls**	• Define conceptual prognostic (damage mitigating) control modes	• Refined loads management strategy to avoid catastrophic failure/total loss	• Refined loads management strategy to maximize revenue; to mitigate damage growth	• Model and test/validate the impact of upstream turbine(s) wake on downstream SHPM	• Field demo of prognostic control in utility-scale rotor
Thrust Area 5	**SHPM Operations Decisions: Maintenance**	• Define conceptual maintenance states for blade SHPM • ID the information needed from sensor/SHM system for maintenance decisions	• Refine/expand model to include other information (vessels, weather, etc.) • Refine the blade repair/replacement cost information • Exercise SHPM cost model with new inputs	• Review loads management strategies in the context of optimal maintenance planning	• End to end simulations that demonstrate the effect of SHPM system on maintenance process economics	• Field test validation of SHPM-based maintenance operations for utility-scale wind farm

Technology Integrat

Technology Thrust Maturation Path

Motivation, Vision, Proof of Concept & Missing Required Data

Motivation

The principal motivation of this work is to reduce O&M costs for wind plants. In particular, the focus is to mitigate the large rise in costs for offshore O&M that arise due to difficulty of access, weather & high sea states, etc. In addition, this work is motivated by the opportunity to increase offshore turbine availability and maximize AEP enabled by improved SHPM-based decision making.

Vision of this Roadmap Document

The goal in formulating the plan communicated in this document is to identify the technical research blocks along with their maturation path needed to *develop the 1st generation cost-effective SHPM system for wind turbine rotors*. This plan also articulates the status of the on-going research at Sandia that is contributing to realizing this vision.

Proof of Concept and Missing Required Data

The initial proof of concept for these ideas is through a comprehensive and rigorous modeling and simulation campaign. Technology integration across the major thrust areas and end to end simulation of performance and economics of SHPM will be documented and shared with industry at various stages of the project development. These early efforts have been documented and used to seek industry backing and feedback to lead to data collection from laboratory and field demonstrations to validate the concepts and integrate across all thrust areas.

Required Data:

- Refined repair/replacement costs for blades (and other components)
- Sensor costs (initial capital equipment)
- O&M process costs (vessels, distance to port, etc.)
- Industry survey of downtime revenue losses
- Laboratory and field testing rotor response data for damaged rotor

Specific (near-term) opportunities:

- Lab-scale Testing: Utilize partnership with university and existing laboratory wind turbine testing rig
- Field Testing: Industrial partners including turbine manufacturer, owner/operator, and sensor/CBM companies for data sharing opportunities

References

1. D.T. Griffith, N. Yoder, B. Resor, J. White, and J. Paquette, "Structural Health and Prognostics Management for Offshore Wind Turbines: An Initial Roadmap," Sandia National Laboratories Technical Report, SAND2012-10109, Sandia National Laboratories; Albuquerque, NM, Printed December 2012.
2. N.J. Myrent, J.F. Kusnick, N.C. Barrett, D.E. Adams, and D.T. Griffith, "Structural Health and Prognostics Management for Offshore Wind Turbines: Case Studies of Rotor Fault and Blade Damage with Initial O&M Cost Modeling," Sandia National Laboratories Technical Report, SAND 2013-2735, Albuquerque, NM, Printed April 2013.

CHAPTER 4. ADDITIONAL CASE STUDIES OF GLOBAL OPERATING SENSITIVITY OF DAMAGE – FY12/FY13

In this chapter, the focus is development of damage detection strategies using the multi-scale simulation of damage methodology. Additional case studies are presented for shear web disbond blade damage and rotor imbalance[2]. The highlights of this chapter include:

- Development of damage detection and damage prognosis strategies:
  - for shear web disbond, and
  - for rotor imbalance (including both aerodynamic and mass imbalance)
- Comparison of damage detection strategies for the cases of using blade sensors and only non-blade sensors, which is a performance and cost tradeoff
- Quantification of the impacts of imbalance on increased loads
- Initial O&M cost analysis is performed in order to examine how cost-benefit analysis can be performed.

[2] Sandia Technical Report: SAND2013-2735.

SAND2013-2735
Unlimited Release
Printed April 2013

Structural Health and Prognostics Management for Offshore Wind Turbines: Case Studies of Rotor Fault and Blade Damage with Initial O&M Cost Modeling

Noah J. Myrent, Joshua F. Kusnick, Natalie C. Barrett, and Douglas E. Adams,
Purdue Center for Systems Integrity
1500 Kepner Dr.
Lafayette, IN 47905

D. Todd Griffith
Wind Energy Technology Department
Sandia National Laboratories
P.O. Box 5800
Albuquerque, New Mexico 87185-MS1124

Abstract

Operations and maintenance costs for offshore wind plants are significantly higher than the current costs for land-based (onshore) wind plants. One way to reduce these costs would be to implement a structural health and prognostic management (SHPM) system as part of a condition based maintenance paradigm with smart load management and utilize a state-based cost model to assess the economics associated with use of the SHPM system. To facilitate the development of such a system a multi-scale modeling approach developed in prior work is used to identify how the underlying physics of the system are affected by the presence of damage and faults, and how these changes manifest themselves in the operational response of a full turbine. This methodology was used to investigate two case studies: (1) the effects of rotor imbalance due to pitch error (aerodynamic imbalance) and mass imbalance and (2) disbond of the shear web; both on a 5-MW offshore wind turbine in the present report. Based on simulations of damage in the turbine model, the operational measurements that demonstrated the highest sensitivity to the damage/faults were the blade tip accelerations and local pitching moments for both imbalance and shear web disbond. The initial cost model provided a great deal of insight into the estimated savings in operations and maintenance costs due to the implementation of an effective SHPM system. The integration of the health monitoring information and O&M cost versus damage/fault severity information provides the initial steps to identify processes to reduce operations and maintenance costs for an offshore wind farm while increasing turbine availability, revenue, and overall profit.

CONTENTS

FIGURES

TABLES

NOMENCLATURE

AEP	annual energy production
BEM	Blade Element Momentum
BPE	Beam Property Extraction
CBM	condition based maintenance
COE	cost of energy
dB	decibel
DOE	Department of Energy
DOWEC	Dutch Offshore Wind Energy Converter Project
FAST	Fatigue, Aerodynamics, Structures, and Turbulence
FCR	fixed charge rate
FEA	Finite Element Analysis
HAWT	horizontal axis wind turbine
ICC	initial capital cost
LRC	levelized replacement cost
LSS	low speed shaft
NREL	National Renewable Energy Laboratory
NuMAD	Numerical Manufacturing and Design Tool
NWTC	National Wind Technology Center
O&M	operations and maintenance
POMDP	Partially Observed Markov Decision Process
PS	power spectrum
RMS	root mean square
SHPM	structural health prognostics management
SNL	Sandia National Laboratories
SW	shear web
TE	trailing edge
TSA	time synchronous average

EXECUTIVE SUMMARY

Offshore wind energy could potentially play a significant role in helping the U.S. obtain an energy portfolio composed of clean, renewable and diversified resources. One current obstacle to the utilization of offshore wind energy is that most projections put the operations and maintenance (O&M) costs of offshore wind farms between 2 to 5 times the current average O&M costs for onshore wind farms [1]. One way in which those costs may be reduced is through the use of a simple yet effective structural health monitoring system as part of an overall condition based maintenance paradigm. A successful health monitoring system would be able to prevent catastrophic failures, reduce or eliminate unplanned or unnecessary maintenance, and as well reduce logistic lead times and optimize supply chain management through the use of prognostics. In addition to the use of prognostics management for maintenance process improvement, potential exists to also use prognostics to increase energy capture through smart loads management; for example, by derating the turbine so that damage growth is mitigated while revenue production continues until maintenance can be performed.

A methodology has been created to aid in the development, evaluation, and optimization of a structural health and prognostics management (SHPM) system for wind turbines using physics-based simulations and state-space cost modeling. The developed scheme is a multi-scale modeling and simulation approach that propagates the effects of damage from high fidelity local simulations to full turbine simulations using reduced order models as illustrated in Figure 1. Fault and damage detection algorithms have been developed which provide information that feeds into a cost model to compare the cost of energy (COE) between a wind farm that would use a SHPM system to optimize the maintenance schedule and a wind farm which would not use such a system. Figure 2 shows the overall approach to utilizing SHM for optimizing O&M costs and Figure 3 shows the cost model flowchart for producing levelized O&M cost savings.

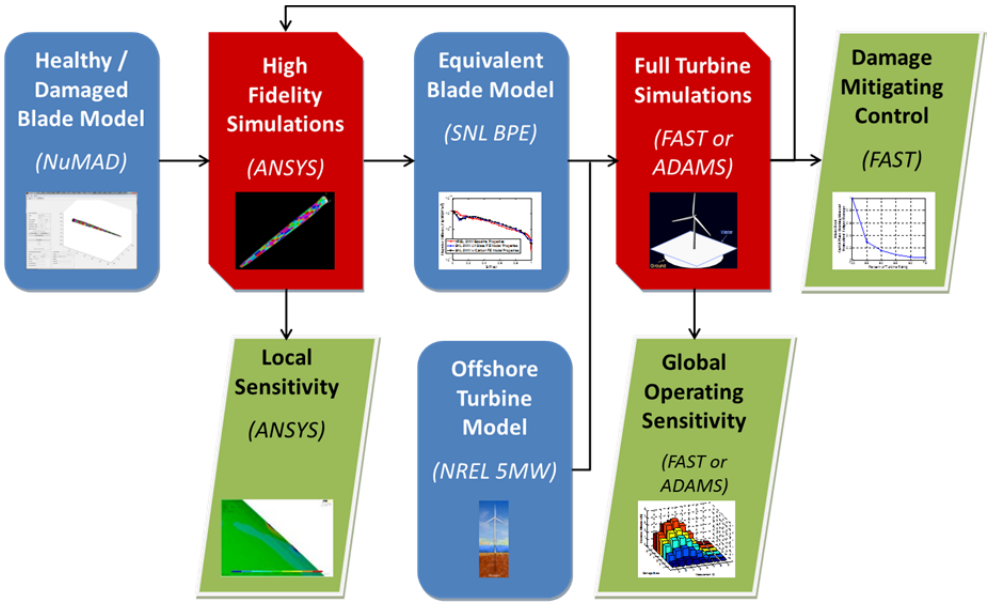

Figure 1. The multi-scale damage modeling and simulation methodology designed to aid in the development and optimization of health monitoring systems for wind turbine blades.

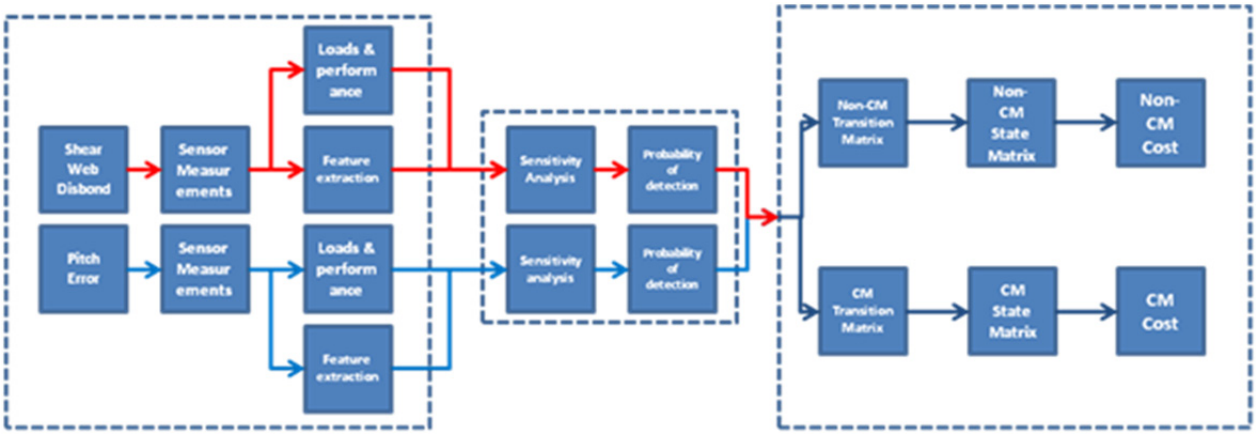

Figure 2. Overall approach for projecting COE benefits based on damage/fault detection strategies (Left Block: Operational Simulation of Damage (see Figure 1); Middle Block: Damage Sensitivity Analysis and Detection Evaluation; Right Block: Cost Analysis)

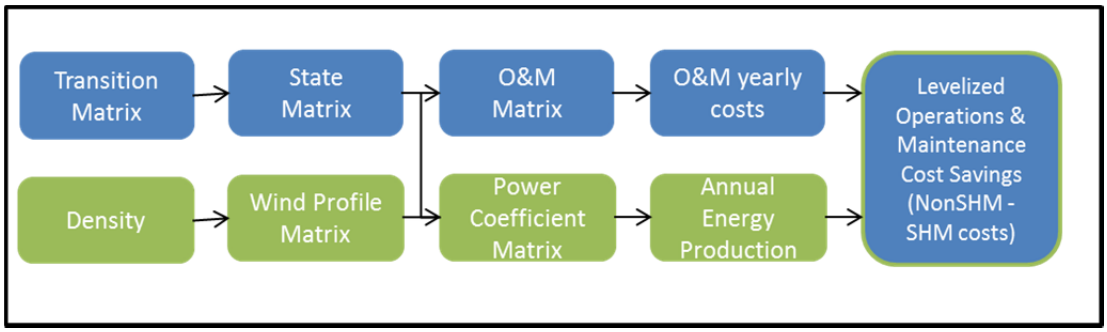

Figure 3. Cost Model Flowchart

To expand on work in FY11 where we implemented the multi-scale modeling and simulation methodology and exercised the process in analyzing the effects of a trailing edge (TE) disbond, the work in FY12 was focused on the effects of a shear web (SW) disbond as well as aerodynamic and mass imbalance on a 5-MW offshore wind turbine. Local analyses based on linear loads analysis of high-fidelity blade finite element models due to laminar aerodynamic loading indicated that the SW disbond resulted in; for example, small increases in blade tip deflection as shown in Figure 4. In global simulations of the full turbine aeroelastic model incorporating the simplified blade structural model, blade tip accelerations and root pitching moments proved to be good indicators of an imbalance and/or SW disbond (Figures 5, 6). Although tip deflection is not sensitive to the presence of a shear web disbond, this damage mechanism affects the operational response of the turbine significantly. **The simulations results illustrated the benefit of the multiscale modeling approach for detection of rotor imbalances and shear web disbonds and the usefulness of this multi-scale approach to resolve the effects of damage as they are manifested as localized damage in the blade structure and global signatures in the operational sensor measurements.**

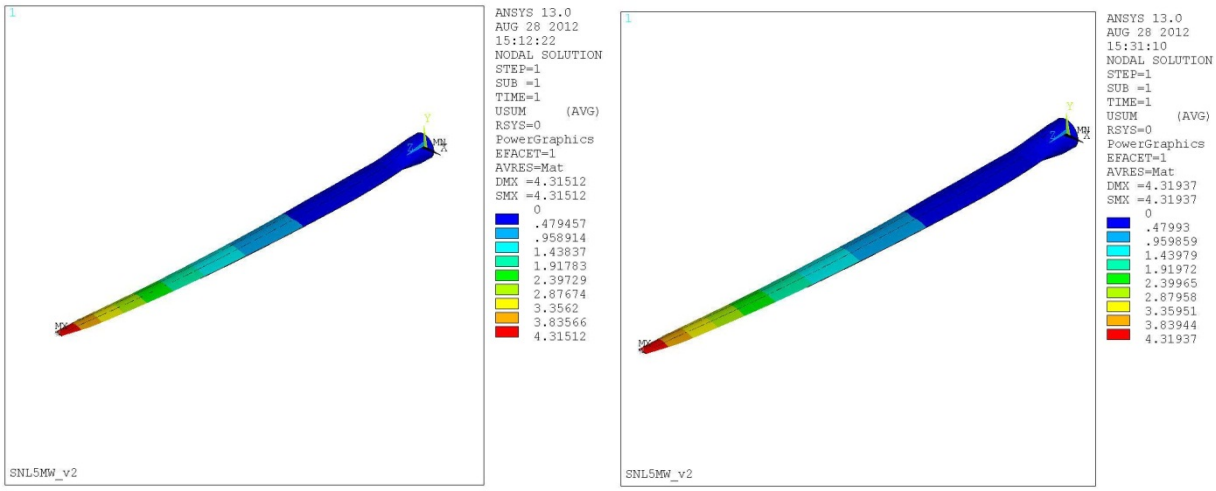

Figure 4. Blade deflection results for healthy blade (left) and blade with 5 meter shear web disbond originating at max chord (right)

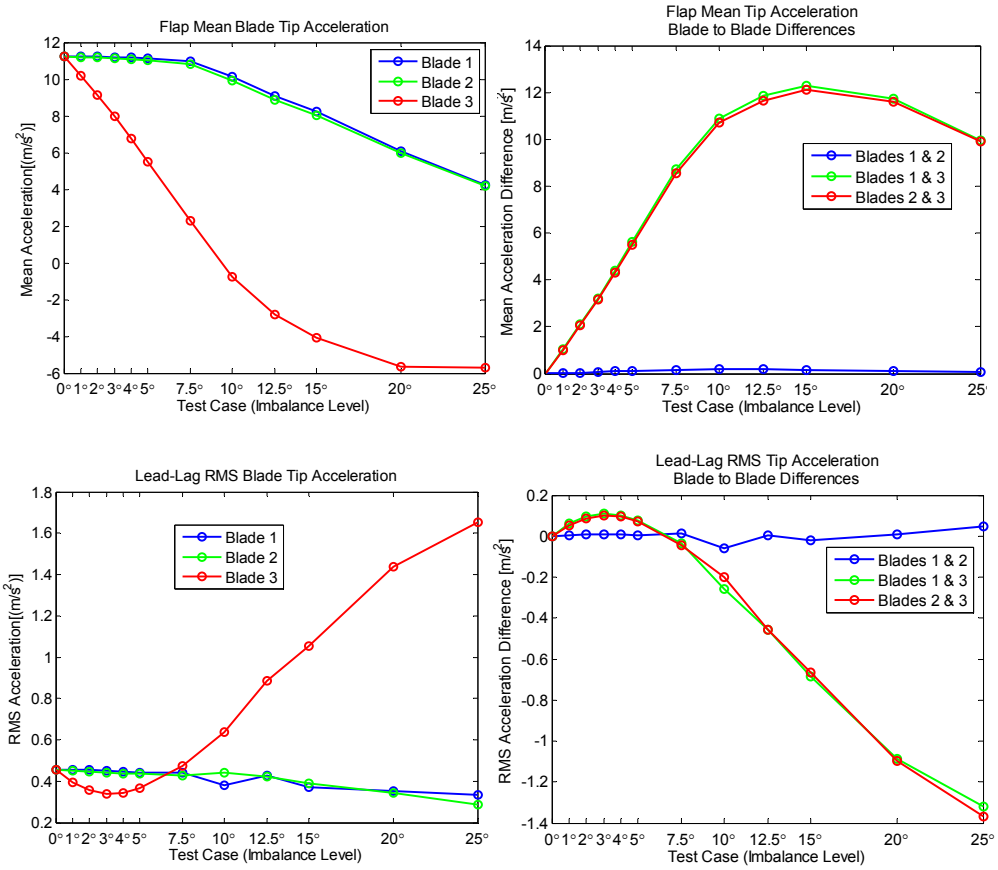

Figure 5. Flapwise and edgewise blade tip accelerations and blade-to-blade differences for pitch error.

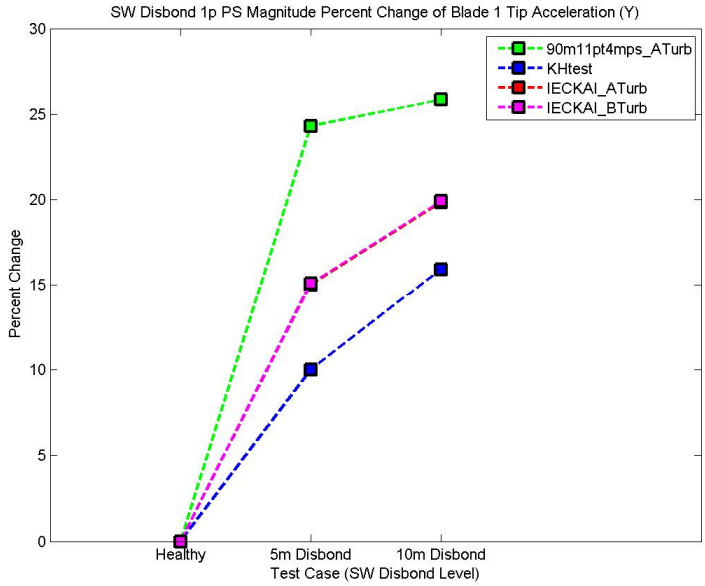

Figure 6. 1p magnitude percent change of edge-wise blade tip acceleration for shear web disbond for four different inflow conditions

A state-based cost model was developed to quantify the effect of a SHPM system on O&M costs. The cost sensitivity analysis shows that O&M COE is most sensitive to the O&M repair and replacement costs. The next most sensitive factor is the extent of damage (i.e. point at which the blade is repaired). Finally, of the factors evaluated in this initial cost sensitivity study, the O&M COE is the least sensitive to changes in the performance coefficient (rotor power coefficient). Figure 7 shows the base model of the cost savings as a result of implementing a SHPM system for the detection of a mass imbalance and/or shear web disbond.

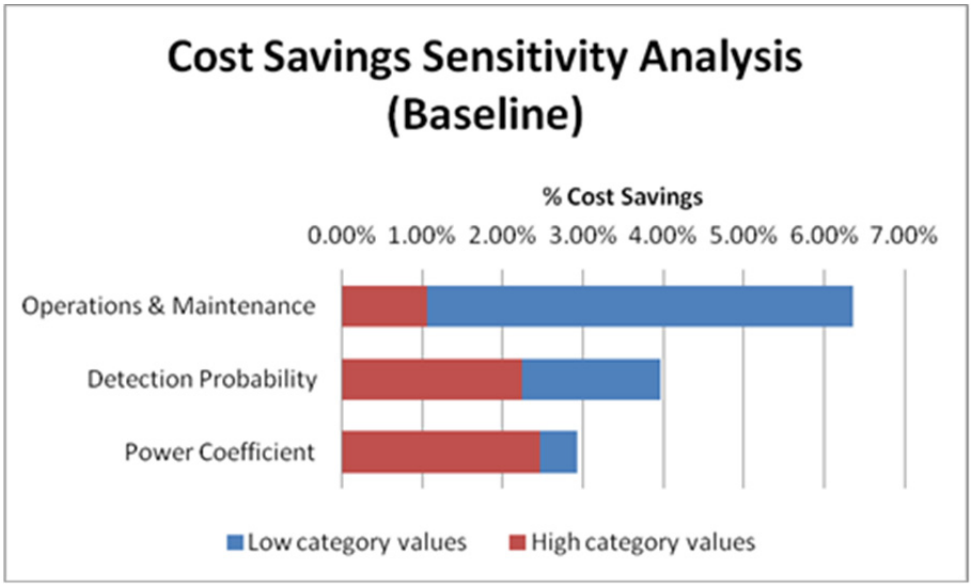

Figure 7. Cost savings sensitivity analysis for the proposed SHPM system.

1. INTRODUCTION

Offshore wind energy in the United States is an untapped energy resource that could play a pivotal role in helping the U.S. obtain an energy portfolio composed of clean, renewable and diversified resources. Some of the drivers for the utilization of offshore wind include the proximity of the offshore resources to population centers and the potential for higher capacity factors due to higher resource winds [1]. Because of these drivers and other potential benefits of offshore wind, the Offshore Wind Innovation and Demonstration initiative has developed an ambitious goal of deploying 10 GW of offshore capacity by 2020 at a cost of energy of only $0.10/kWh [2].

1.1. Drivers for Offshore SHPM

As of June 2011, while nine offshore projects totaling over 2 GW of capacity were in various stages of the permitting and development process, no offshore wind energy projects had been installed in the United States [4]. Part of the reason for this lack of development is that operations and maintenance (O&M) costs are expected to be significantly higher for offshore wind turbines than onshore wind turbines. Recent projections of O&M costs have ranged between $11 and $66 U.S. dollars per megawatt-hour with the majority of estimates being between 2 to 5 times the cost of land-based (onshore) O&M [1]. These higher O&M costs represent a larger overall proportion of the cost of energy than for onshore turbines even when the large initial investment required for the installation of offshore turbines is included [5]. One of the reasons that O&M costs are likely to be higher offshore is that the offshore environment will bring with it increased loading which is relatively uncharacterized due to the lack of existing offshore installations. Offshore turbines will also have to be built to withstand the environmental harshness of the offshore environment. Lastly, access to the turbines will be difficult, costly, and occasionally not possible due to high sea states [1,8].

1.2. SHPM Benefits

One potential way in which these O&M costs could be addressed is through the use of a structural health and prognostics management (SHPM) system as part of a condition based maintenance (CBM) paradigm [6-12]. By continuously monitoring the health, or condition, of structural components in each wind turbine, required maintenance actions can be scheduled ahead of time and performed when they are needed rather than on a preset schedule or only after failure has already occurred. The benefits of a CBM strategy are expected to include less regular maintenance, the avoidance or reduction of unscheduled maintenance and improved supply chain management [8-11].

Furthermore, because wind turbines are active systems, monitoring the health of wind turbine components will allow for smart turbine load management to optimize the profit of the entire wind plant. For example, if a turbine blade becomes damaged and that damage is detected at an early stage by the SHPM system, the turbine could be derated so that small less costly repairs could be performed on the turbine. While this action would reduce the amount of power generated by the turbine in the short-term, it may allow for less extensive maintenance actions to be performed, permit additional energy capture while maintenance is being planned, extend the

overall life of the turbine, and allow for multiple turbines to be serviced during the same visit to maximize the overall profit of the wind power plant.

1.3 Summary of Prior Work in Wind Turbine Rotor SHPM Development

Although the fields of structural health monitoring and prognostics management are fairly rich in general, research in application to wind turbine rotor blades in either field is somewhat limited. Integration of the two disciplines is even more limited. Sandia has had an active program for several years to investigate sensored blades with several blade-build and field testing demonstration projects. Blades for utility-scale wind turbines typically have no sensors in the blades, but if they do they have been limited to strain gauges in the blade root. The Sandia research involved embedding sensors along the entire blade span, which included acceleration, strain, and temperature sensors. The proposed applications for this "enhanced" blade sensing capability include structural health monitoring and active control of the rotor. These Sandia studies provided some important lessons learned regarding manufacturing of sensors into blades and selection of sensors.

In an effort to map out the SHPM problem and also provide an example case study, an initial roadmap was developed by Sandia National Laboratories for a combining structural health monitoring and prognostics assets into a SHPM system with application to wind turbine rotor blades as documented in Reference 16. The key element established in this initial roadmap, the so-called multi-scale damage modeling and simulation methodology, addresses both how damage is modeled at multiple resolutions of the model and also the resulting manifestation (or effects) of damage in both the global operating dynamic response and the localized effects related to remaining life (state of health). The intent of this approach is to combine structural health monitoring and prognostic management so as to bridge the gap between being able to detect and characterize the presence of damage and then being able to make revenue-optimizing operations and maintenance decisions.

This report provides the results for a few additional case studies. The aim of these studies is to provide some additional information to mature the SHPM technology development for wind turbine rotors. The key elements addressed in the report include an assessment of operating sensitivity of damage to additional damage/fault mechanisms and development/evaluation of an initial O&M cost model.

2. THE APPROACH: COMBINING SHM SYSTEM PERFORMANCE AND COST ANALYSES

To quantify the benefits of implementing an offshore structural health and prognostics management system, a multi-model methodology was developed that combines an evaluation of SHPM system performance with state-of-health based cost analysis. The approach permits an evaluation of O&M scenarios (O&M strategies) to identify; for example, turbine conditions strongly influenced by particular fault or damage mechanisms, detection strategies based on various measurement analysis approaches tailored for a wind turbine system, and project operations and maintenance costs with and without such a condition monitoring system. Figure 8 shows the overall approach.

The left-most block in Figure 8 describes modeling of the turbine and damage simulations. The middle block describes the sensitivity analysis performed on the operating response of the turbine including an assessment of sensors and their performance in detecting the modeled damage. The right-most block in Figure 8 describes the cost analysis for the SHPM system. The approach starts with simulations of turbines with damage then the operational response from these simulations is fed to the middle block were the data is analyzed via sensitivity of damage studies. This middle block addresses the performance of the SHPM system to identify which sensors are viable options to detect damage and also to quantify the ability to detect damage (i.e. probability of detection). State of health information and SHPM performance information is fed to the right-most block where SHPM economics is assessed. This concept should prove useful in assessing both performance and cost of SHPM system, and in the future it could prove useful in design of the SHPM system and in evaluation of SHPM return of investment. This approach could also be applied in real-time operation such that information from the right-most economics module could feedback to the turbine operator or turbine control system for decision making.

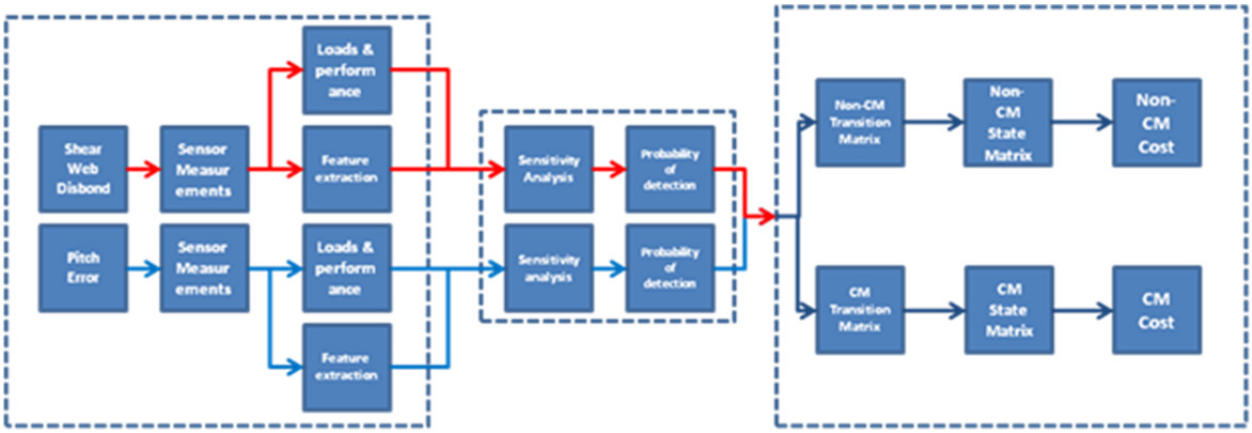

Figure 8. SHPM system feasibility quantification concept approach

Utilization of simulations is a cost-effective method to investigate the sensitivity of many different potential measurements and measurement locations while controlling/eliminating variability from sources other than the damage or fault that is being studied. The simulation approach of this work used high fidelity blade and damage models to represent the influence of damage. This model was then reduced to an equivalent blade model of sufficient resolution to

capture the influence of the damage while still being able to be integrated into simulations of a full offshore wind turbine operating under various inflow conditions. In addition to the analysis of the results from these full turbine simulations, the loads from these simulations can then be fed back into the high fidelity blade model so that localized damage sensitivity measures or effects can be obtained.

In order to perform the desired simulations, a variety of different software packages were integrated in order to obtain the results of interest. Sandia National Laboratories' (SNL's) NuMAD software was used to create a high fidelity blade model in the software package ANSYS. A shear web disbond was then created in the model and equivalent beam parameters were extracted which could be integrated with a turbine model for simulations of the damaged turbine in either FAST [13] or MSC.ADAMS [14]. Results from each stage of this modeling process were then used to assess the influence of the damage on the response of the blade and the turbine as a whole and to identify a subset of measurements that could prove beneficial for future SHPM investigations.

The cost model used for this study is a state-space Matlab model that calculates O&M costs ($/MWh) of a wind turbine for scenarios such as a turbine with and without an enhanced blade condition monitoring system. In the initial model, four states are defined in the cost model that correspond to different extents of damage and the associated different types of maintenance that would be required in each state; for example, state 1 is associated with a blade in a new or repaired condition and at the other extreme state 4 would be associated with a blade damaged to the point beyond which it can be repaired and must be replaced.

3. 5-MW OFFSHORE TURBINE MODEL

3.1. Turbine Model Description

As part of an ongoing structural health and prognostics management project for offshore wind turbines, the simulations in this report were performed using a representative utility-scale wind turbine model. The model, known as the NREL offshore 5-MW baseline wind turbine model, was developed by NREL to support studies aimed at assessing offshore wind technology [15]. It is a three-bladed, upwind, variable-speed, variable blade-pitch-to-feather-controlled turbine and was created using available design information from documents published by wind turbine manufacturers, with a focus on the REpower 5-MW turbine. Basic specifications of the model configuration are listed in Table 1.

Table 1. Gross Properties of the NREL 5-MW Baseline Wind Turbine [16].

Property	Value
Rating	5MW
Rotor Orientation, Configuration	Upwind, 3 blades
Control	Variable Speed, Collective Pitch
Drivetrain	High Speed, Multiple-Stage Gearbox
Rotor, Hub Diameter	126 m, 3 m
Hub Height	90 m
Cut-in, Rated, Cut-out Wind Speed	3 m/s, 11.4 m/s, 25 m/s
Cut-in, Rated Rotor Speed	6.9 rpm, 12.1 rpm
Rated Tip Speed	80 m/s
Overhang, Shaft Tilt, Precone	5m, 5°, 2.5°
Rotor Mass, Nacelle Mass, Tower Mass	110,000 kg; 240,000 kg; 347,460 kg
Water Depth	20 m
Wave Model	JONSWAP/Pierson-Moskowitz Spectrum
Significant Wave Height	6 m
Platform	Fixed-Bottom Monopile

A new blade model was developed to be used with the NREL 5-MW turbine model, which is the same model used in the initial studies (Ref). A detailed blade model did not exist and was needed so that damage could be introduced into the blade structure within the multi-scale modeling and simulation framework (as described above). The detailed blade model was developed by Sandia National Laboratories using blade geometry data from the Dutch Offshore Wind Energy Converter Project (DOWEC) and composite layup information from the European Union's UpWind program. The distribution of material layers along the blade span is illustrated in Figure 9.

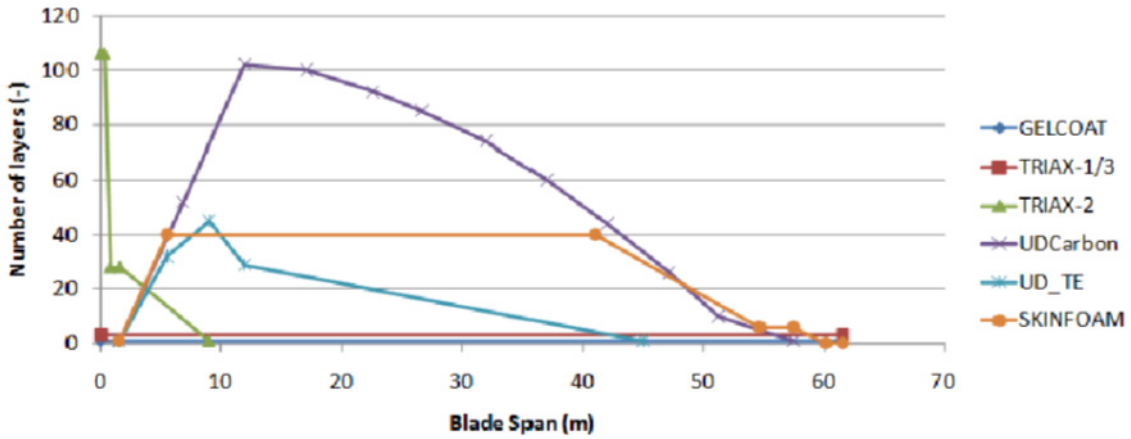

Figure 9. Model of the Distribution of Material Layers along the Span of the Blade, (Griffith, et al. 2011).

Two thirds of the blade span utilizes the TU-Delft family of airfoils, while the final one-third of the blade span utilizes the NACA 64-series airfoils. Intermediate airfoil shapes were developed that preserve the blending of camber lines as well as a smooth blade thickness profile. Figure 10 shows the finite element model of the blade in ANSYS with the colored sections representing different composite materials. This high degree-of-freedom model was translated into a model consisting of several beam elements using Sandia's Blade Property Extraction tool (BPE). BPE works by applying loads in each of the six degrees of freedom at the tip of the blade model in ANSYS, then processing the resulting displacements at selected nodes along the blade to generate the 6x6 Timoshenko stiffness matrices for the beam discretization. This reduced degree-of-freedom model is subsequently used to define the blade properties in FAST. For a more detailed description of BPE, see [16].

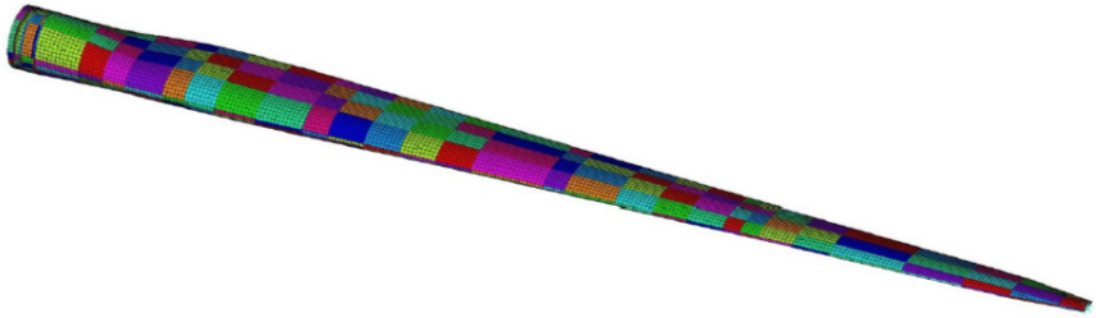

Figure 10. ANSYS finite element mesh for the 5-MW blade model.

3.1.1. *FAST Simulation Turbine Coordinate Systems*

FAST uses six coordinate systems for input and output parameters. Some of these coordinate systems will be referred to throughout this report, so they are reproduced here from the FAST User's Guide for convenience. Note that the FAST User's Guide coordinate system images use a downwind turbine configuration; however, the same coordinate systems apply in the case of the upwind turbine being referred to in this work, but the orientation of the x axis changes so that in either configuration it is pointing in the nominally downwind direction. The rotor shaft

coordinate system is shown in Figure 11. This coordinate system does not rotate with the rotor, but it translates and rotates with the tower and yaws with the nacelle. In addition to output variables related to the low speed shaft, the nacelle inertial measurements also use this coordinate system. Some shaft outputs, such as shear force in the low speed shaft, are measured in both a non-rotating coordinate system and a rotating coordinate system; these are differentiated by using an "s" or "a" subscript, respectively. The tower base coordinate system shown in Figure 12 is fixed in the support platform, thus rotating and translating with the platform. The tower-top/base-plate coordinate system shown in Figure 13 is fixed to the top of the tower. It translates and rotates with the motion of the platform and tower top, but it does not yaw with the nacelle.

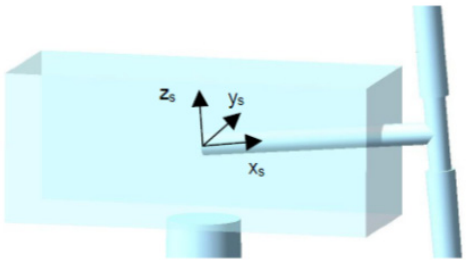

Figure 11. Shaft Coordinate System (Jonkman and Buhl 2005).

Figure 12. Tower Base Coordinate System (Jonkman and Buhl 2005).

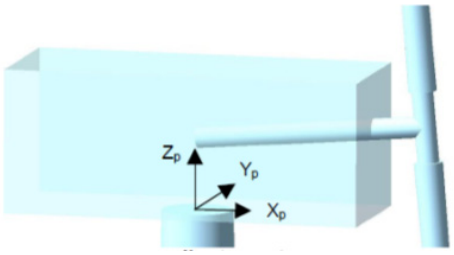

Figure 13. Tower-top/base-plate coordinate system (Jonkman and Buhl 2005).

4. ROTOR MASS/AERODYNAMIC IMBALANCE SENSITIVITY STUDY

4.1. Introduction

In order to evaluate the applicability of the pitch error detection method discussed in Section 4.7 on larger utility-scale wind turbines, computer simulations were carried out using the 5-MW turbine model described in Section 3.1. Modeling was performed using NREL's Fatigue, Aerodynamics, Structures and Turbulence (FAST) code, which is a comprehensive aeroelastic simulator for two and three-bladed horizontal axis wind turbines (HAWTs). The code provides the means to manipulate a variety of input parameters, including turbine control settings, environmental conditions, blade and tower models, drivetrain and generator parameters, and many others. There are also hundreds of possible outputs, including blade inertial measurements and generator power.

FAST uses AeroDyn to calculate the aerodynamics of HAWTs. AeroDyn is an aeroelastic simulation code which uses several subroutines for wind turbine applications, including the blade element momentum theory, the generalized dynamic-wake theory, the semi-empirical Beddoes-Leishman dynamic stall model, and a tower shadow model. The FAST model combines a modal and multibody dynamics formulation, and performs a time-marching analysis of the nonlinear equations of motion. For a more detailed description of the working principles of the code, see the FAST User's Guide [17].

Imbalance of the rotor can occur for a number of reasons, although the imbalance can generally be divided into two categories: mass imbalance or an aerodynamic imbalance. Pitch error is a common problem that fits into a more general class of turbine faults referred to as aerodynamic asymmetries. This means that the individual blades are not generating the same thrust and tangential forces when subjected to the same wind profile. Other reasons this can occur are blade profile differences as a result of manufacturing tolerances, blade surface roughness changes, and degradation or damage to a blade, such as tip delamination, erosion, or deformation of the structure. Since the effects of aerodynamic asymmetries are closely related to rotor mass imbalances and information to-date indicates that 20% of utility-scale wind turbines have a mass or aerodynamic imbalance [18], both types of imbalances were simulated in this work. Mass imbalances result from inhomogeneous mass distributions in the blades caused by manufacturing, water inclusions, icing, and loose material from manufacturing moving inside the blade towards the tip during rotation [19]. Existing or proposed imbalance detection methods in wind turbines use inertial measurements in the nacelle. However, there are difficulties using this method which are illustrated using a simplified rotor dynamics model in the next section. Therefore, several methods of detection were evaluated in order to compare the use of blade and non-blade measurements, and a detection algorithm was proposed and summarized in a flow chart in Section 4.7.

4.2. Simplified Rotor Dynamics Model

In order to demonstrate the dynamics effects at the nacelle, consider the simplified model formulated by [20]. To start, the mass imbalance of the rotor is modeled as a point mass *m* located in the rotor plane at a distance *r* from the center of rotation, O, and an angle ϕ_m from the zero mark of blade A, as shown in Figure 14. This is the typical setup for a static unbalance, which is defined as the eccentricity of the center of gravity of a rotor caused by a point mass located a specified radial distance from the center of rotation. Correcting a static unbalance requires placing a point mass of equal magnitude in the rotor plane, diametrically opposed to the unbalance mass. Dynamic imbalance on the other hand acts like an equivalent radial co-rotational moment fixed in the rotor [21]. Physically this means that the direction of the angular momentum vector is changing as the rotor rotates, and a rotor is dynamically balanced only if its angular velocity vector points along one of its principal axes of mass distribution [22, 23]. Correcting a dynamic imbalance requires balancing the rotor in two axial planes. A general rule of thumb; however, is that a rotor with bladed diameter that is more than 7 to 10 times its width is treated as a single-plane rotor [24]. This is certainly true for horizontal axis wind turbines, and therefore this work will only consider static mass imbalance. The blades in the simplified rotor dynamics model are separated by an angle φ and ϕ is the angle between blade A and the x axis. The rotor spins with angular velocity ω, therefore the point mass m generates a centrifugal force, F_c, with magnitude:

$$F_c = m\omega^2 r. \tag{1}$$

There will also be a gravitational load P due to the mass imbalance, but this load and its associated moments about the tower will be considered small relative to the centrifugal load and will be neglected. If a time variable, *t*, is introduced, then $\omega t = \phi$, and the projection of the centrifugal force onto the x and z axes are:

$$\begin{aligned} (F_c)_z &= F_c \sin(\omega t + \phi_m) \\ (F_c)_x &= F_c \cos(\omega t + \phi_m). \end{aligned} \tag{2}$$

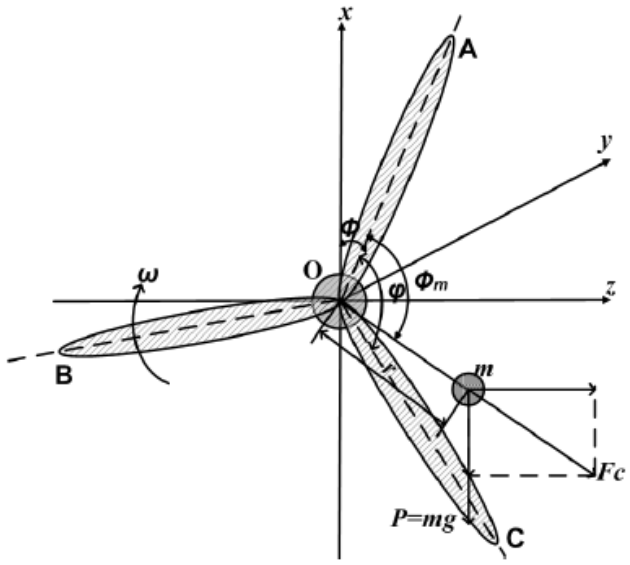

Figure 14. Mass imbalance model (Niebsch, Ramlau and Nguyen 2010).

The plane of rotation is located a distance L along the y-axis from the turbine's tower, therefore the forces $(F_c)_z$ and $(F_c)_x$ also create moments about the x and z axes centered on the tower, given by equation (3):

$$M_x^1 = (F_c)_z \cdot L$$
$$M_z^1 = (F_c)_x \cdot L. \tag{3}$$

The aerodynamic imbalance is modeled using an equivalent load formulated from the Blade Element Momentum (BEM) theory. BEM is a commonly used method for determining aerodynamic loads on a blade. The blade is divided into a finite number of elements in the radial direction, and the lift and drag forces are approximated at each radial position using the lift and drag coefficients of the two-dimensional airfoil profile. The local pitch angle, θ, for each element can be defined as the angle between the chord-line and the plane of rotation, as shown in Figure 15.

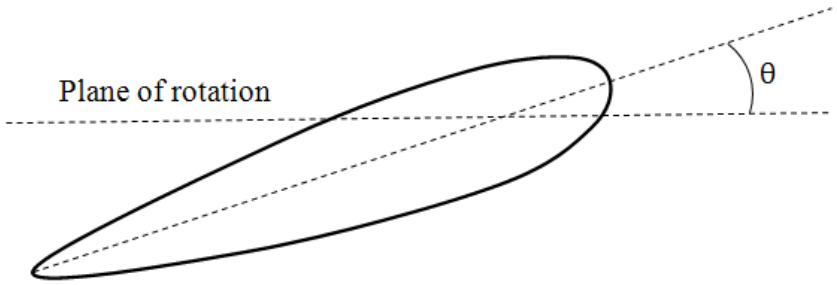

Figure 15. Local pitch angle.

The local pitch angle, θ, is a sum of the blade pitch angle at the root, θ_p, commanded by the turbine's control system, and the blade twist angle, β, at the blade element:

$$\theta = \theta_p + \beta. \tag{4}$$

Calculating the tangential and thrust (normal to the rotor plane) forces at each blade element results in force distributions along the blade. The distributed load can be rewritten as a single equivalent thrust force and single tangential force on each blade, as shown in the example of Figure 16. The distributed load is denoted by *f(x)*, and the blade elements are of width *dx*. Integrating the differential forces *df* along the length of the blade, *R*, results in the equivalent load, *F*:

$$F = \int_0^R df = \int_0^R f(x)dx. \tag{5}$$

The location *l*, where the equivalent load acts, is found using a moment balance: the total moment of all of the differential forces, *df*, about the root of the blade, $x = 0$, must equal the moment of *F* about the same point. Therefore, *l* is found with equation (6):

$$F \cdot l = \int_0^R xdf = \int_0^R xf(x)dx. \tag{6}$$

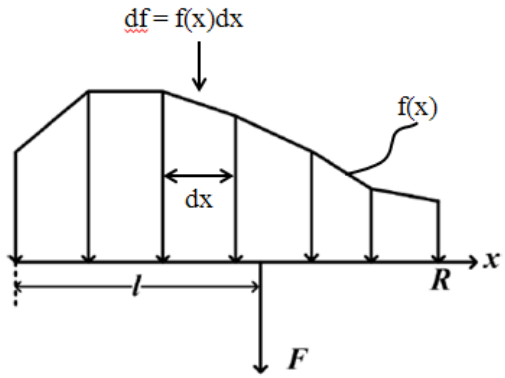

Figure 16. Equivalent Blade Point Loads (Niebsch, Ramlau and Nguyen 2010).

Thus, the aerodynamic forces can be modeled as three thrust forces and three tangential forces, one pair from each blade, as shown in Figure 17.

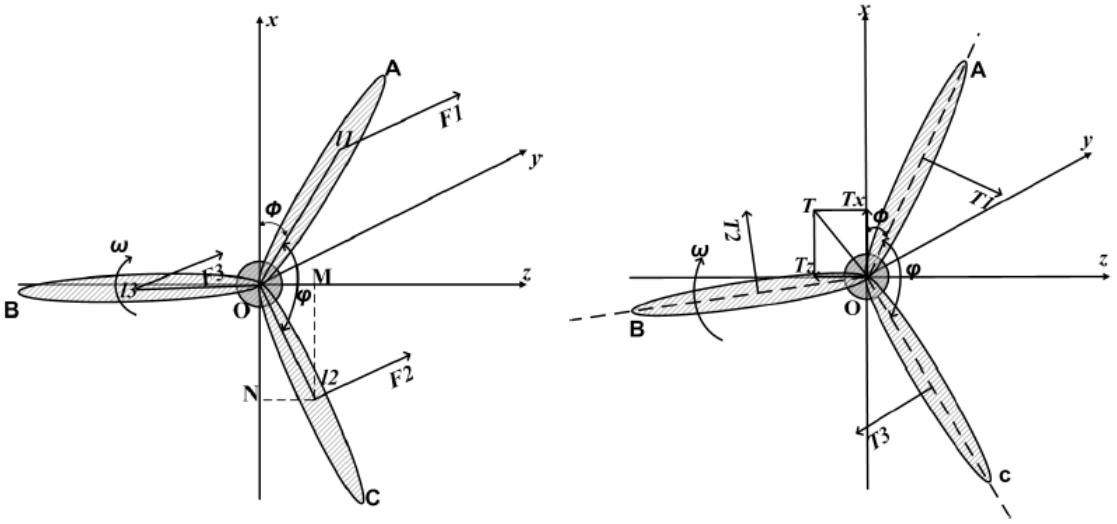

Figure 17. Equivalent blade thrust forces (Left); Equivalent blade tangential forces (Right) (Niebsch, Ramlau and Nguyen 2010).

The aerodynamic forces also generate moments about the x and z axes centered on the rotor, which are given by:

$$\begin{aligned} M_x{}^2 &= F_1 l_1 \sin(\omega t) + F_2 l_2 \sin(\omega t + \varphi) + F_3 l_3 \sin(\omega t + 2\varphi) \\ M_z{}^2 &= F_1 l_1 \cos(\omega t) + F_2 l_2 \cos(\omega t + \varphi) + F_3 l_3 \cos(\omega t + 2\varphi), \end{aligned} \tag{7}$$

where φ=120° for a three-bladed rotor. Furthermore, the tangential forces can be projected onto the x and z axes, yielding the following equations:

$$\begin{aligned} T_z &= T_1 \cos(\omega t) + T_2 \cos(\omega t + \varphi) + T_3 \cos(\omega t + 2\varphi) \\ T_x &= T_1 \sin(\omega t) + T_2 \sin(\omega t + \varphi) + T_3 \sin(\omega t + 2\varphi). \end{aligned} \tag{8}$$

These forces also produce moments about the x and z axes centered on the tower as a result of the distance L between the rotor plane and the tower center which are shown in the following equations:

$$\begin{aligned} M_x{}^3 &= T_z \cdot L \\ M_z{}^3 &= T_x \cdot L. \end{aligned} \tag{9}$$

Note that if all of the blades are identical (i.e. have the same airfoil profile), and have the same pitch angle, then $F_1 = F_2 = F_3$ and $l_1 = l_2 = l_3$, which means that the torques $M_x{}^2$ and $M_z{}^2$ are equal to zero. Finally, summing the forces and moments at the nacelle are shown in the following equations:

$$
\begin{aligned}
F_y &= F_1 + F_2 + F_3 \\
F_z &= T_z + (F_c)_z \\
M_x &= M_x{}^1 + M_x{}^2 + M_x{}^3 \\
M_z &= M_z{}^1 + M_z{}^2 + M_z{}^3.
\end{aligned}
\tag{10}
$$

It is evident from equations (7) through (10) that mass and aerodynamic imbalances contribute to the same moments and forces measured in the nacelle, and the fundamental frequency of that forcing function is ω, the rotational speed of the rotor, denoted 1p (once per revolution) in the order domain. Many of the recommended imbalance condition monitoring systems, which use accelerometers located in the nacelle to measure the transverse and axial (z- and y-directions in shown in Figure 11, respectively) accelerations, attribute 1p transverse responses to mass imbalance and the 1p axial and M_x responses to aerodynamic asymmetries [19, 25]. However, this analysis shows that those responses are coupled to both types of imbalances. Thus, in this work we also consider that blade response measurements also be used to detect and characterize imbalance. These methods are compared to the nacelle measurement based methods presented in the literature in sections 4.4 and 4.5.

4.3. Imbalance Simulation Methods

To eliminate possibilities of some confounding variables such as yaw error and to study the effects of aerodynamic asymmetries and mass imbalances alone, simulations were carried out in a unidirectional, constant-speed, vertically sheared wind environment, rather than using the random and turbulent wind input conditions that are also available as inputs in FAST. The wind direction was oriented at 0°, directly perpendicular to the rotor plane, and the yaw degree of freedom was turned off in the FAST input file. The wind speed was set to 11 m/s, with a 1/7 power law vertical shear profile. Setting the wind speed to just below the rated speed of 11.4 m/s ensured that in the case of pitch error of a single blade, the two actively-pitching blades would always pitch to zero degrees to maximize the power output of the turbine, thus keeping those variables constant. The sample time spacing was set to 0.01 seconds, corresponding to a sample rate of 100 Hz. Because the per-revolution harmonics were mainly of interest and the maximum rotor speed was 12.1 rpm, or 0.2 Hz, this sample rate was sufficient. Simulations were conducted in three phases: (1) aerodynamic asymmetries, (2) mass imbalances, and (3) simultaneous aerodynamic and mass imbalances. The simulation methods for each of the phases are detailed in sections 4.3.1 through 4.3.3. Two hundred output variables were recorded from the simulations, including generator power, low speed shaft torque, tri-axial blade accelerations along the span, nacelle accelerations, and many others for use in the sensitivity of damage/fault studies.

4.3.1. *Pitch Error Simulation Methods*

While aerodynamic asymmetries can also be caused by blade profile differences and damage, this work focused on the problem of pitch error in a single blade, as discussed in the previous chapter. Initial and final pitch positions for individual blades are user-defined input parameters in the FAST primary input file, as well as the simulation times at which the blades reach those

positions. It is possible to adjust these settings for a single blade while allowing the other two blades to actively pitch. To allow the rotor to reach its steady state operating speed within the first 30 seconds of simulation time, blade three, the blade with simulated pitch-error, was gradually adjusted from the start of the simulation to reach its final pitch error position after 15 seconds had elapsed. The first 30 seconds of simulations were discarded in analyzing the data to remove startup transients from the analysis – the FAST User's Guide recommends at least five seconds (Jonkman and Buhl 2005). The total simulation time for each test, eliminating the first 30 seconds, was ten minutes, allowing for averaging to take place. With all other variables remaining constant, tests were conducted with the pitch angle of blade three set to 0°, 1°, 2°, 3°, 4°, 5°, 7.5°, 10°, 12.5°, 15°, 20°, and 25°.

4.3.2. Rotor Mass Imbalance Simulation Methods

In this phase of simulation, a rotor mass imbalance was applied by increasing the mass density of blade three at a particular blade span-wise section in the FAST blade input file. The magnitudes of the mass imbalances chosen were based on two references. The first is the acceptable residual imbalance method employed by Pruftechnik Condition Monitoring GmbH, a German company which performs field-balancing of wind turbine rotors [18]. This company applies a fairly standard field balancing procedure: initial vibration measurements are taken from within the nacelle, a trial mass is added to the rotor and its effects are measured, and the balancing software then determines suggested balancing weights and locations. A detailed explanation of the general rotor balancing procedure and calculations can be found in Bruel & Kjaer's application notes [24]. Pruftechnik quantifies the permissible residual imbalance based on the standard DIN ISO1940-1: Mechanical Vibration – Balance Quality Requirements for Rotors in a Constant (Rigid) State – Part 1: Specification and Verification of Balance Tolerances. This standard provides permissible residual imbalance levels in the rotor, with different quality grades, G, depending on the application. The imbalance magnitude is found using the rotor's operational speed, rotor weight, and the balancing radius, which is the span location of the mass imbalance. Plots in the standard provide the permissible imbalance in gram-mm/kg which are based on the rotor speed and G grade. Alternatively, these curves can be written in the equation form [26]:

$$U_{per}(g-mm) = 9549 \cdot G \cdot \frac{W}{N}, \tag{11}$$

where U_{per} is the permissible residual imbalance in g-mm, G is the balance quality grade, N is the operating speed of the rotor in rpm, and W is the rotor weight in kg. Based on experience, Pruftechnik uses balancing grade G16. Sample calculations from their literature are shown in Figure 18 and equation (12).

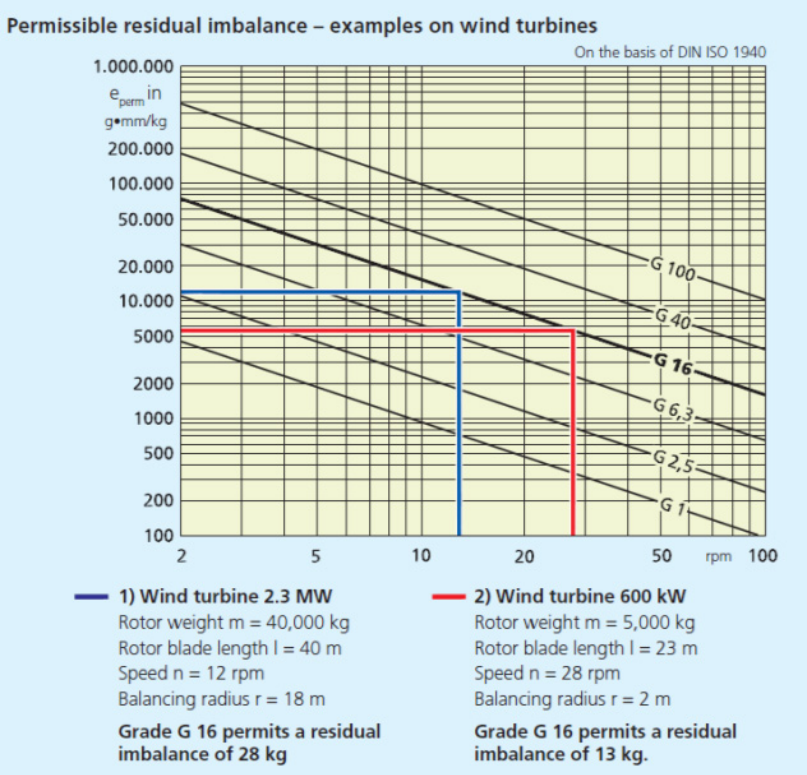

Figure 18. Permissible Residual Imbalance Examples (Losi and Becker 2009).

For the 2.3 MW turbine case, the permissible residual imbalance at 18 meters with quality grade 16 is calculated as follows:

$$U_{per} = 9549 \cdot 16 \cdot \frac{40,000kg}{12rpm} \cdot \frac{1kg \cdot m}{10^6 g \cdot mm} \cdot \frac{1}{18m} = 28kg. \qquad (12)$$

Note that a conversion factor of 10^{-6} was added to convert the result for U_{per} from g-mm to kg-m, and that result was further divided by the balancing radius of 18 meters so that the output would be a mass, rather than mass times distance. The 28 kg result represents the maximum additional mass that could be added to the rotor at a distance of 18 meters from its center without exceeding the G16 quality grade.

A second source for determining mass imbalance testing levels was Moog Incorporated's fiber-optic based rotor monitoring system, which claims imbalance detection down to 0.5% of the total blade mass of all three blades [27]. For consistency and ease of comparison, it will be assumed that this imbalance is acting at the mass center of a single blade, and it will be translated to an ISO1940-1 G quality grade.

The FAST blade input file for the Sandia National Laboratories' blade model contains 23 section locations for specifying section properties. However, for computational purposes, the 23 locations are interpolated down to 17 nodes as specified in the AeroDyn input file for application

of the aerodynamic forces in FAST. Therefore, the following procedure was followed to ensure that mass imbalance specified in the 23-section FAST blade input file would result in the intended G grade after interpolation:

1.) A MATLAB script was written to apply the same piecewise linear interpolation found in FAST's FORTRAN source code. The accuracy of the code was verified by adjusting the FAST input blade properties and comparing the output of the script to the interpolated blade properties that are output from FAST.

2.) The mass density of one or more of the 23 blade sections was altered and the interpolated blade section properties were then computed by the script.

3.) The script determined which interpolated blade sections incurred mass density changes compared to the interpolated properties of the unaltered blade.

4.) The effective span-wise location of the added mass was computed using a moment balance as follows in equation (13):

$$R_{eff} = \frac{\sum_{i=1}^{N} (dm)_i \cdot (dr)_i \cdot r_i}{\sum_{i=1}^{N} (dm)_i \cdot (dr)_i}, \tag{13}$$

where R_{eff} is the effective span-wise location of the added mass, N is the number of blade sections, $(dm)_i$ is the change in mass density of blade section *i* in kg/meter, $(dr)_i$ is the length of the i^{th} blade section in meters, and r_i is the radial location of the blade section in meters.

5.) Equation (11) was used to solve for the G grade. The rotor mass, W, was computed using the newly interpolated blade mass properties in addition to the hub mass. The rotational speed N was found by running the simulations, which was 11.8 rpm regardless of the mass imbalance applied in these tests. The imbalance being applied was equal to the calculated change in mass in step 4, which was input as U_{per}. Finally, the mass imbalance was applied at R_{eff}, and the equation was formulated as in equation (12) and solved for G:

$$G = \frac{U_{per} \cdot N}{9549 \cdot W} \cdot 10^6 R_{eff}. \tag{14}$$

To apply the 0.5% increase in blade mass (Moog), it was assumed that the added mass was distributed evenly along one blade and would therefore act at its center of mass. The center of mass of the unaltered blades was known to be 18.392 meters, and the total rotor mass was 105,773 kg, both indicated in the FAST *.fsm output file. The mass of each individual blade was 16331 kg, so 0.5% of the total blade mass was 245 kg. Therefore, applying equation (14), a mass of 245 kg acting at 18.392 meters corresponds to a G grade of approximately 53, which is quite a bit higher than the permissible level of 16 used in field balancing. These two imbalance levels provided reference points for simulations. Two additional imbalance grades were tested:

G6.3 and G40. As a reference, see Table 2 for groups of representative rigid rotors and their common balance quality grades. Note that a rigid rotor is defined as one whose operating speed is less than 50% of its first critical speed [24]. To verify this assumption, FAST was used as an ADAMS preprocessor to construct an ADAMS dataset of the complete aeroelastic properties of a wind turbine. ADAMS is a multibody dynamics simulation software package, and it was used to perform the linearization and eigenanalysis of the turbine model to obtain its modal frequencies and vectors. The first flexible rotor mode has a natural frequency of 0.65 Hz and the maximum rotor speed is 12.1 rpm, or 0.2 Hz, thus satisfying the rigid rotor assumption for the purposes of mass imbalance qualification.

Table 2. ISO 1940-1 Balance quality grades for groups of representative rigid rotors (IRD Balancing 2009).

Balance Quality Grade	Product of the Relationship ($e_{per} \times \omega$) [1] [2] mm/s	Rotor Types - General Examples
G 4 000	4 000	Crankshaft/drives[3] of rigidly mounted slow marine diesel engines with uneven number of cylinders[4]
G 1 600	1 600	Crankshaft/drives of rigidly mounted large two-cycle engines
G 630	630	Crankshaft/drives of rigidly mounted large four-cycle engines Crankshaft/drives of elastically mounted marine diesel engines
G 250	250	Crankshaft/drives of rigidly mounted fast four-cylinder diesel engines[4]
G 100	100	Crankshaft/drives of fast diesel engines with six or more cylinders[4] Complete engines (gasoline or diesel) for cars, trucks and locomotives[5]
G 40	40	Car wheels, wheel rims, wheel sets, drive shafts Crankshaft/drives of elastically mounted fast four-cycle engines with six or more cylinders[4] Crankshaft/drives of engines of cars, trucks and locomotives
G 16	16	Drive shafts (propeller shafts, cardan shafts) with special requirements Parts of crushing machines Parts of agricultural machinery Individual components of engines (gasoline or diesel) for cars, trucks and locomotives Crankshaft/drives of engines with six or more cylinders under special requirements
G 6.3	6.3	Parts of process plant machines Marine main turbine gears (merchant service) Centrifuge drums Paper machinery rolls; print rolls Fans Assembled aircraft gas turbine rotors Flywheels Pump impellers Machine-tool and general machinery parts Medium and large electric armatures (of electric motors having at least 80 mm shaft height) without special requirements Small electric armatures, often mass produced, in vibration insensitive applications and/or with vibration-isolating mountings Individual components of engines under special requirements
G 2.5	2.5	Gas and steam turbines, including marine main turbines (merchant service) Rigid turbo-generator rotors Computer memory drums and discs Turbo-compressors Machine-tool drives Medium and large electric armatures with special requirements Small electric armatures not qualifying for one or both of the conditions specified for small electric armatures of balance quality grade G 6.3 Turbine-driven pumps
G 1	1	Tape recorder and phonograph (gramophone) drives Grinding-machine drives Small electric armatures with special requirements
G 0.4	0.4	Spindles, discs and armatures of precision grinders Gyroscopes

4.3.3. *Simultaneous Pitch Error and Mass Imbalance Simulation Methods*

It is possible that aerodynamic asymmetry and mass imbalance are present simultaneously in a wind turbine rotor. This presents the greatest challenge for a rotor imbalance condition monitoring system, that is, distinguishing between mass and aerodynamic imbalance. Two basic cases are considered: (1) the mass imbalance was located on blade three, while the pitch error occurred for blade two, and (2) the mass imbalance and pitch error both occurred on blade three. Only a small number of test cases were run with the goal of determining which detection algorithms were successful at detecting the simultaneous imbalances, ignoring the sensitivity of the algorithms to simultaneous imbalances. The same mass imbalance grading system and pitch error methods described in the earlier sections were used for these tests.

4.4. Analysis of Imbalance without Blade Sensors

In order to compare the effectiveness of imbalance detection methods with and without blade sensors, algorithms were first generated for determining imbalance using only the outputs from FAST that would not require blade-mounted sensors. From the 200 variables which were generated at outputs from the FAST simulation, those which displayed a significant percentage change in their RMS value or frequency response magnitude at multiples of the operating speed for a given a mass imbalance or pitch error were identified as key measurement channels. As was shown in section 4.2, imbalance tends to excite the 1p frequency in the order domain. It has also been shown that the 2p and 3p harmonics can be influenced by aerodynamic imbalances, especially in the presence of wind shear [28], thus the 1p, 2p, and 3p frequencies were reviewed for changes in magnitude from the baseline tests.

The rotor azimuth position output from FAST was used as the reference signal for time synchronous averaging (TSA). To perform rotational resampling, the azimuth signal was converted to radians, was unwrapped and then the measurement signal was interpolated so that each revolution contained the same number of data samples with each sample corresponding to the same azimuth position of the rotor's rotation. Finally, blocks of three revolutions were averaged together; more than one revolution was used in the block size to increase the length of the block's time history, thereby increasing the frequency resolution of the DFT of the averaged signal. The imbalance detection algorithms for non-blade sensors all functioned similarly through the detection of changes from baseline measurements either in the RMS response or in the power spectral density magnitude at 1p, 2p, or 3p.

4.4.1. *Pitch Error Analysis Results*

The following sections summarize the trends in the results for pitch error aerodynamic imbalance, as measured in the generator power output, nacelle inertial sensors, and low speed shaft bending moments (a subset of non-blade virtual measurements with most significant sensitivity to imbalance).

4.4.1.1. Generator Power

The generator power output displayed unique and readily identifiable changes due to pitch error when the wind speed is below the rated speed for the turbine, as it was for these simulations.

Figure 19 shows the expected result that as the pitch error of blade three increases, the mean power output of the turbine decreases significantly due to the reduced aerodynamic efficiency of the incorrectly pitched blade. Moreover, the zoomed-in view of one revolution of the TSA power signal in Figure 20 shows that the power output shifts from having predominantly 3p oscillations for zero pitch error to a progressively larger 1p fluctuation with increasing pitch error. The magnitude of the 1p component most likely decreases as pitch error moves above 7.5° because the reduced rotor speed has consequently reduced the loading magnitude. The 3p oscillation for zero pitch error is a common occurrence due to the increased wind speeds caused by vertical wind shear and seen by the upright, 0° azimuth positioned blade. This occurs three times per revolution, once as each blade passes the 0° position, resulting in larger aerodynamic forces on that blade and thus a 3p oscillation in rotor torque. It should also be noted that the rotor torque signal displayed very similar characteristics to the generator power output. Because the generator power can be subject to electrical faults as well, analyzing rotor torque measured at the low speed shaft may be a better indicator of mechanical behavior in the field.

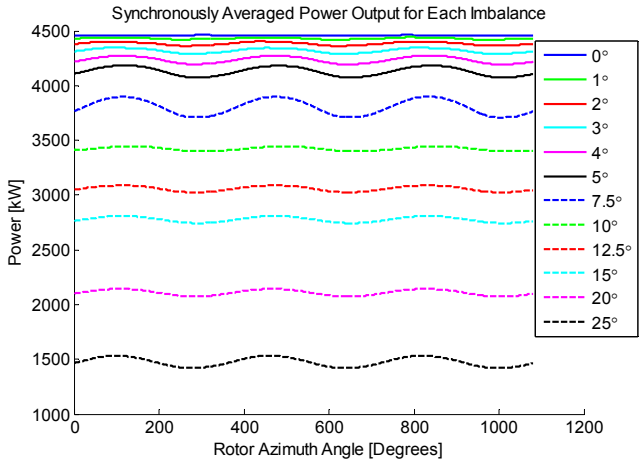

Figure 19. Three revolution time synchronously averaged power output for each pitch error test.

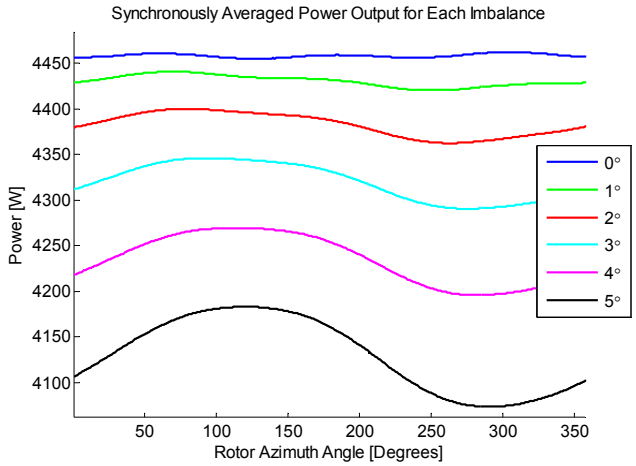

Figure 20. Single revolution zoomed-in single revolution TSA power output for pitch errors of 0° to 5°.

Figure 21 summarizes these findings by plotting the magnitude of the 1p component in the power spectrum (PS) of the generator power signal as well as the mean power. The 1p PS magnitude increases dramatically until a pitch error of 7.5°, after which the mean power is significantly reduced, and the 1p trend restarts at a lower initial level. Therefore, using the turbine's known power versus wind speed curve along with this data can help determine if a pitch error is present and could be used to estimate its level of severity. Significant deviations from the expected mean power output, given a particular wind speed, can indicate a possible pitch error. The magnitude of the 1p PS component, given the mean power, can help determine the severity of the pitch error.

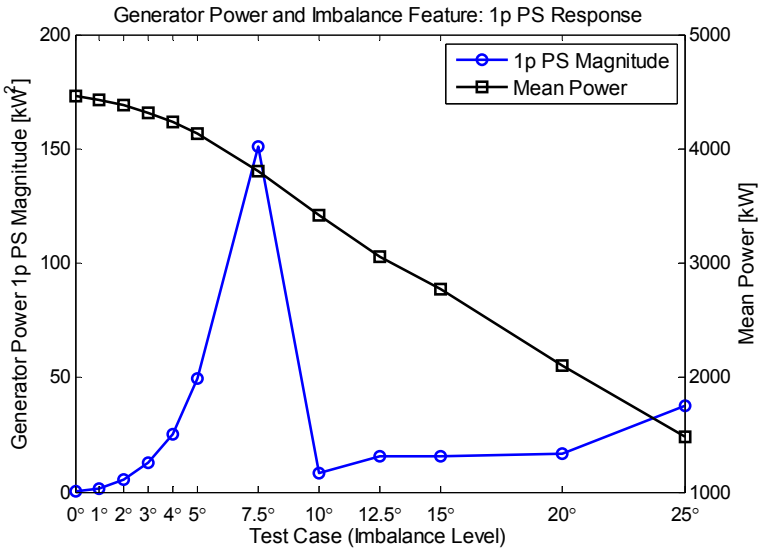

Figure 21. Mean generator power and 1p PS magnitude.

4.4.1.2. Nacelle Inertial Measurements

Nacelle inertial measurements are often recommended in wind turbine condition monitoring literature for detecting rotor imbalance. For all subsequent discussion, axial nacelle acceleration will refer to acceleration in the x_s direction in Figure 11, which is equivalent to the y direction in Figure 14. Transverse nacelle motion is in the side-to-side direction, which is the y_s axis in Figure 20 or the z axis in Figure 14. As was demonstrated in the dynamics model of section 4.2, the 1p component of the axial acceleration of the nacelle should be indicative of an aerodynamic imbalance. Similarly, the moments about the transverse and vertical axes, y_s and z_s shown in Figure 20, respectively, should also be affected in their 1p response by aerodynamic imbalance. However, instead of plotting the moment outputs from FAST, the nacelle angular acceleration outputs were used and the magnitude of the 1p PS of each of those measurements, as well as the nacelle axial and transverse accelerations, are shown in Figure 22.

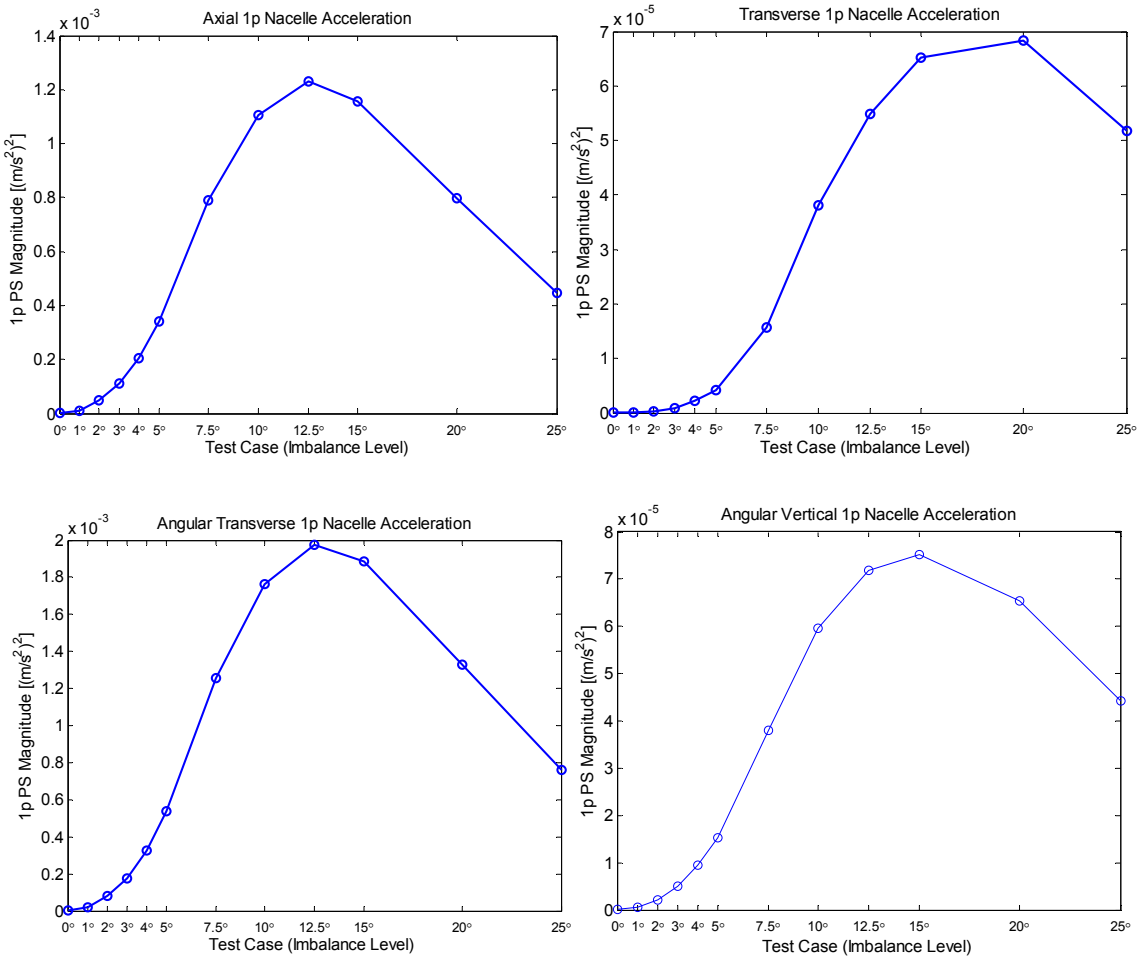

Figure 22. Nacelle axial and transverse accelerations and angular accelerations about the transverse and vertical axes vs. pitch error.

The 1p PS magnitude follows a similar trend in both the axial nacelle acceleration and the angular nacelle acceleration about the transverse axis. For 12.5° pitch error and greater, the 1p magnitude begins to fall, which is again likely due to decreased loading magnitude from the reduction in rotor speed. Interestingly, the transverse nacelle acceleration shows a similar trend and does not begin to fall off until 25° pitch error. However, these oscillations are two orders of magnitude lower than the axial acceleration, and the 1p magnitude changes less rapidly in the 0°-5° range, making this a less sensitive measurement channel for low pitch error. Finally, the angular acceleration about the vertical nacelle axis displays a similar trend to the transverse angular acceleration, but is two orders of magnitude lower.

4.4.1.3. Low Speed Shaft Bending Moments

The low speed shaft (LSS) bending moments also displayed significant changes due to pitch error. FAST outputs the bending moment in rotating and non-rotating frames, as well as shaft tip locations or strain gage locations. To coincide with measurements that would be taken on operating wind turbines in the field, the low speed shaft bending moment at the shaft's strain gage in the rotating frame of reference was used in this analysis. The rotating frame can be

referred to in the discussion in Section 3.0. Figure 23 shows a significant increase in the magnitude of the low speed shaft bending moment with increasing pitch error, and Figure 24 shows the increase in the magnitude of the low speed shaft bending moment in terms of the root mean square (RMS) value for each pitch error. Unlike the nacelle inertial measurements, the RMS LSS bending moment continues to increase up to 25° pitch error.

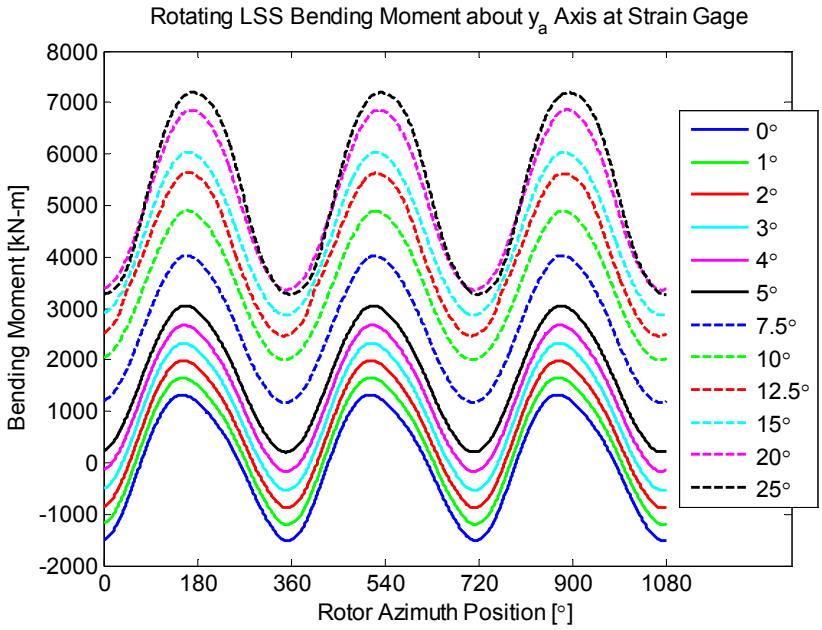

Figure 23. Three-revolution TSA rotating low speed shaft bending moment.

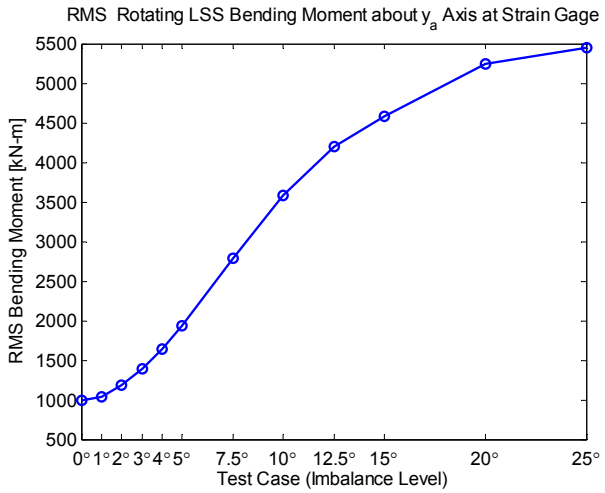

Figure 24. RMS rotating LSS bending moment vs. pitch error.

4.4.2. *Mass Imbalance Analysis Results*

The following sections summarize the trends in the results for mass imbalance, as measured in the same three non-blade measurements of generator power output, nacelle inertial sensors, and low speed shaft bending moments.

4.4.2.1. Generator Power

Figure 25 and Figure 26 indicate that the mean power remained unchanged with the five varying levels of rotor mass imbalance evaluated: G0 (baseline, no imbalance), G6.3, G16, G40, and G53 (representing the 0.5% total blade mass imbalance). However, the 1p PS magnitude of the generator power signal increased with increasing mass imbalance, and in the case of pitch error, the power oscillations shifted from a predominantly 3p frequency to 1p frequency when an imbalance was present. These results indicate that a decrease in mean power can be an indicator of aerodynamic imbalance, but an increase in the 1p PS magnitude of the generator power over the baseline test can be a result of either a mass or an aerodynamic imbalance. Therefore, further measurements are required to distinguish between the two.

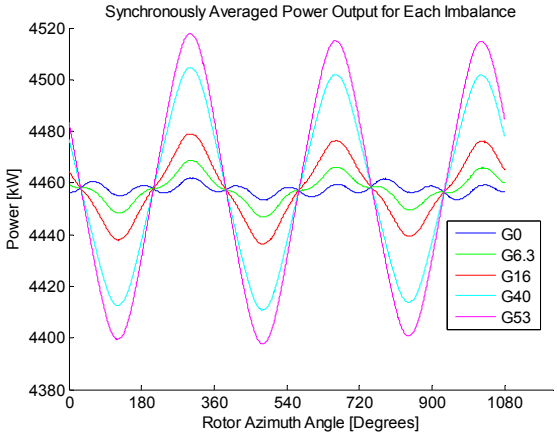

Figure 25. Three-revolution time synchronously averaged power output for each mass imbalance test.

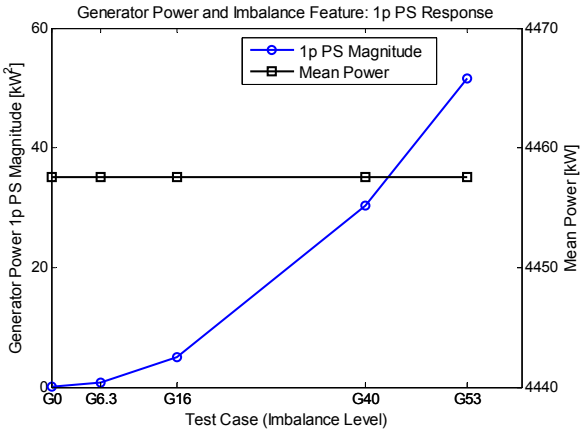

Figure 26. Mean generator power and 1p PS magnitude

4.4.2.2. Nacelle Inertial Measurements

In the case of mass imbalance, the magnitude of the 1p PS of the inertial measurements was three or more orders of magnitude lower than the acceleration generated by the pitch errors. The trend of increasing 1p PS is very similar in all four inertial measurements in Figure 27. The transverse nacelle acceleration is greater than the acceleration in the axial direction in agreement with the literature, but all four accelerations are so small that they would be very difficult to measure.

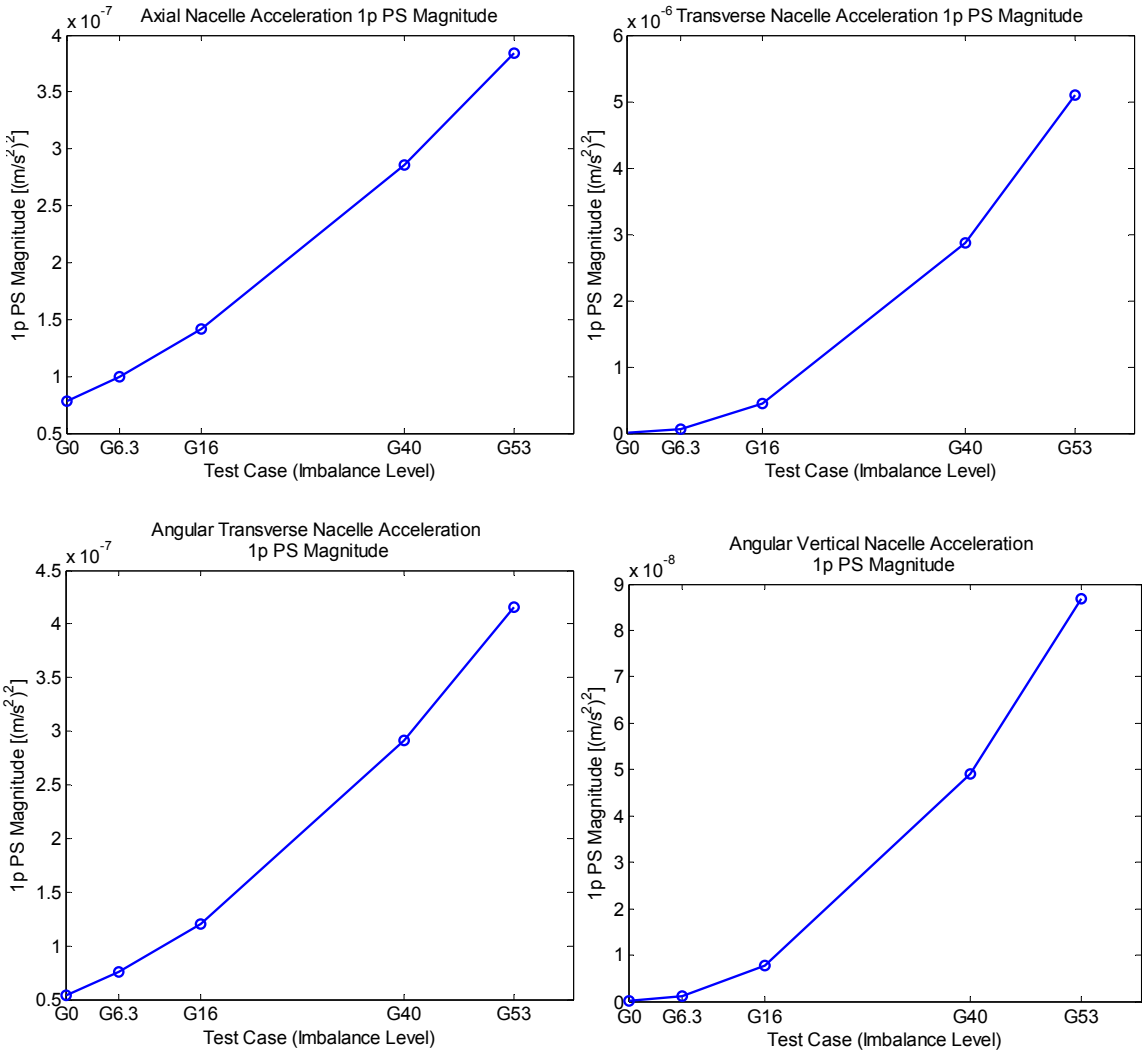

Figure 27. Nacelle axial and transverse accelerations and angular accelerations about the transverse and vertical axes for mass imbalance

4.4.2.3. Low Speed Shaft Bending Moments

The low speed shaft bending moment was virtually unaffected by mass imbalance, as demonstrated in the TSA signal in Figure 28. There was only a 0.46% increase in the shaft bending moment due to the largest mass imbalance simulated. Pitch error on the other hand caused a 5.5% increase in the RMS shaft bending moment for the smallest error of 1°. So, while

some measurements have been shown to be largely insensitive to mass imbalance and highly sensitive to aerodynamic imbalance, the converse situation has not presented itself in any of the non-blade outputs. Therefore, distinguishing between mass and aerodynamic imbalance using non-blade measurements is difficult, as will be expanded upon in the next section which considers simultaneous mass and aerodynamic imbalances.

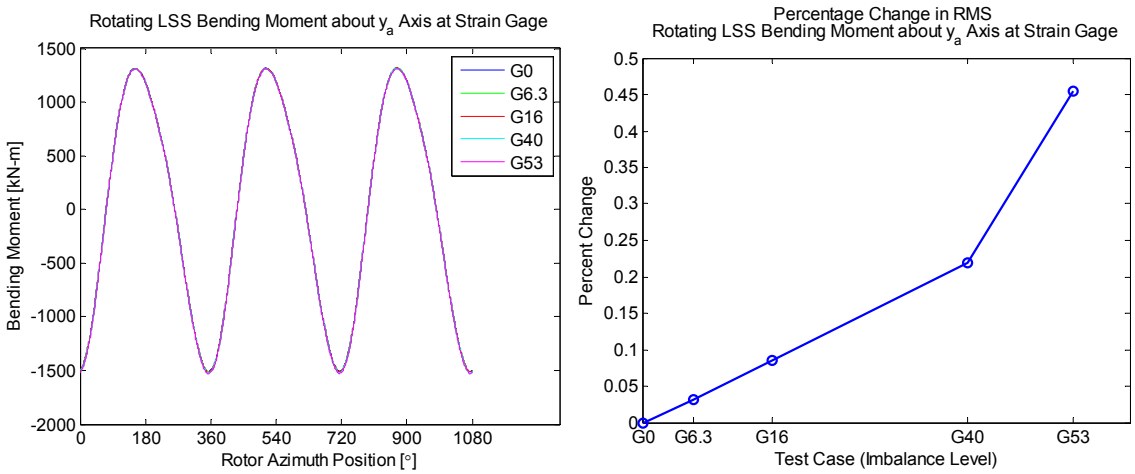

Figure 28. Three-revolution TSA rotating low speed shaft bending moment and percent change in RMS

4.4.3. *Simultaneous Mass Imbalance and Pitch Error Results*

The following sections will analyze the results of simulations performed with a simultaneous mass and aerodynamic imbalance applied to the rotor. Included are tests with mass and aerodynamic imbalances applied to the same blade, blade three, as well as tests in which blade three contained the increased mass and blade two exhibited pitch error. The syntax for the plot legends and axis labels referring to the different test cases is as shown in Figure 29. If no mass or aerodynamic imbalance was applied in the test, the "B" corresponding to that imbalance will be followed by a zero. Moderate mass and aerodynamic imbalance levels were chosen for these simulations: G16 and G40, and 3° and 5° pitch errors. To aid in quantifying the difference between the simultaneous imbalance cases, each mass imbalance was also applied with no simultaneous pitch error for comparison. The same three non-blade measurements, generator power output, nacelle inertial sensors, and low speed shaft bending moments are once again examined.

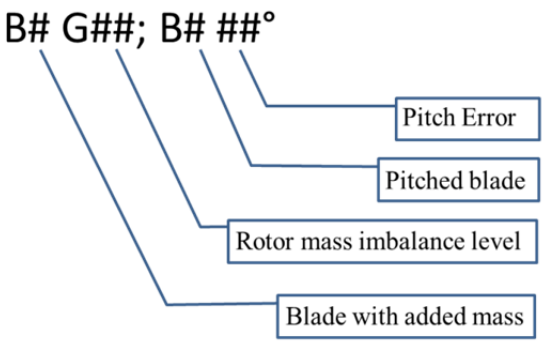

Figure 29. Simultaneous mass and aerodynamic imbalance test designation syntax

4.4.3.1. Generator Power

The generator power output for these tests coincides with what is expected from the results of individual mass and aerodynamic imbalance in the previous sections. Figure 30 and Figure 31 show that there are three distinct groups of test conditions with the same mean power output: those tests with the same pitch error, regardless of the mass imbalance or which blade was pitched, generate the same mean power. The mean power levels were 4458 kW, 4319 kW, and 4130 kW for pitch errors of 0°, 3°, and 5°, respectively.

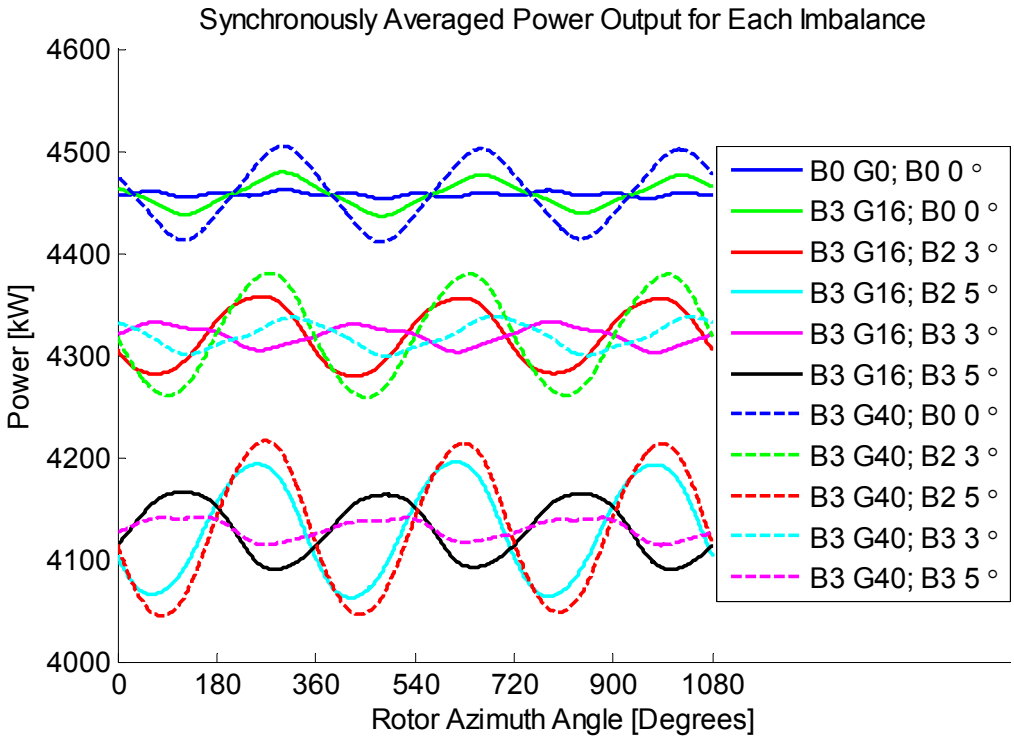

Figure 30. Three-revolution TSA power output for each simultaneous imbalance test

Figure 31 confirms that the 1p PS magnitude of the power signal is dependent on both the mass and aerodynamic imbalance, as was demonstrated in the previous sections. Interestingly, it also reveals that the 1p response is greater if the mass addition and aerodynamic imbalance are on different blades, as can be seen by comparing the B3G16, B2 3° case to the B3G16 B3 3° case, for instance. A more intuitive response is found when looking at the 2p frequency in the order domain, as shown in Figure 32. It shows that the 2p PS magnitude is largely dependent on the pitch error; however, when the added mass is on a different blade than the one undergoing pitch error, the 2p response is higher, again as in the B3G16, B2 3° and B3G16, B3 3° cases, where the magnitude changes by about 3.5%. This trend follows for the other three sets of imbalances as well (for example see cases B3G40, B2 5° and B3G40 B3 5°). Furthermore, the 2p response also increases for increasing mass imbalance. Although the changes look fairly small when compared to the changes brought about by pitch error, the response increases by about 3% from B3G16, B2 5° to B3G40 B2 5°, for example. So, it may be possible to determine if there are simultaneous mass and aerodynamic imbalances from the generator power. However, it would likely require a fairly accurate simulation model to determine the response PS thresholds and this method is still ineffective in determining which blades are responsible for the mass or aerodynamic imbalance.

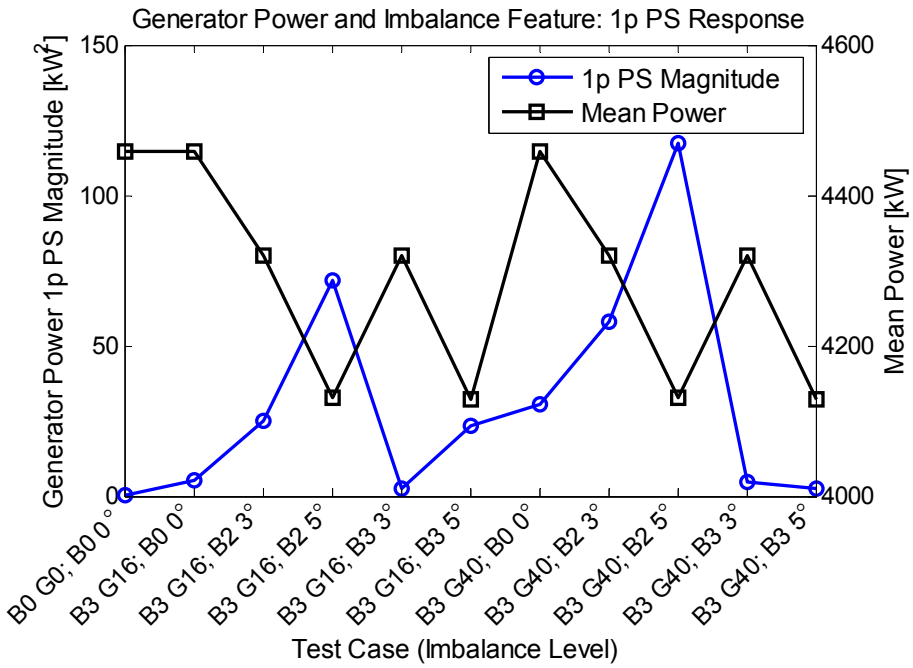

Figure 31. Mean generator power and 1p PS magnitude.

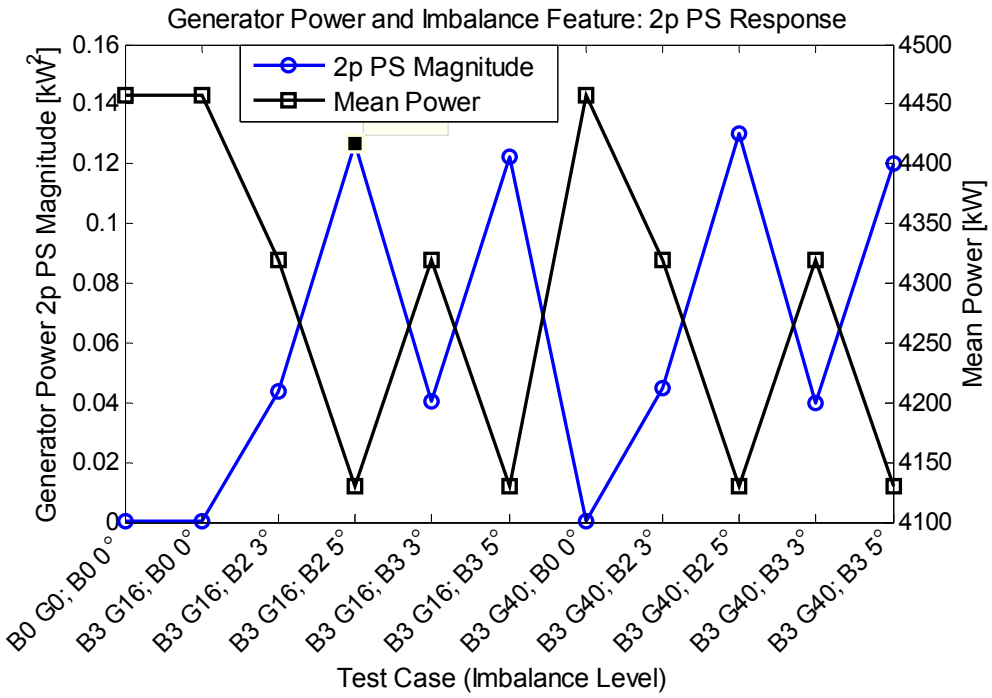

Figure 32. Mean generator power and 2p PS response.

4.4.3.2. Nacelle Inertial Measurements

To coincide with suggested methods from the literature, we again consider the 1p nacelle inertial responses. The axial nacelle acceleration and the two angular accelerations follow a very similar trend to the 2p generator power PS magnitude, as shown in Figure 33. The angular accelerations look nearly identical to the axial acceleration and have therefore been omitted. Pitch error accounted for the largest percentage differences in the response. When pitch and mass imbalances were applied to different blades, the response was higher than when the same imbalance levels were applied to the same blade. The transverse nacelle acceleration response is less clear. In theory, the transverse response should be more sensitive to mass imbalance than pitch error, but it is clearly affected largely by pitch error [41]. The response seems to follow an expected trend from the first test case up to B3 G16, B3 5°. After that point, it would seem that the trend should restart, but with a higher initial value due to the larger G40 mass imbalance. The B3 G40, B0 0° response is indeed higher than B3 G16, B0 0°, but the response takes an unexpected dip at B3 G40, B2 3° and 5°. The likely cause is that the B3G40 and B2 3° and 5° errors cause similar transverse nacelle accelerations, as indicated in Figure 22 and Figure 27, but these responses are out of phase when the imbalances are applied to different blades. Therefore, phase is another important consideration when examining non-blade measurements for simultaneous imbalances acting on different blades.

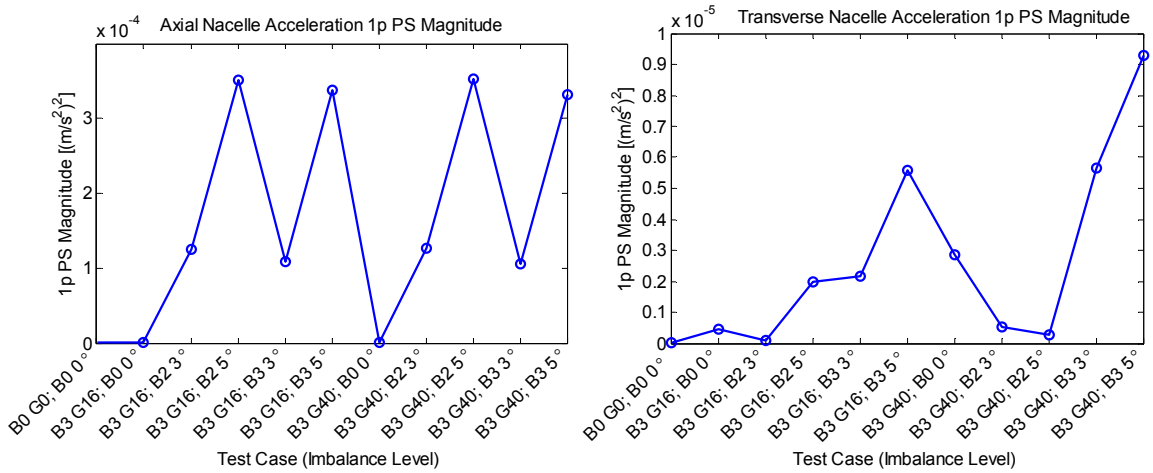

Figure 33. Nacelle axial and transverse accelerations for simultaneous imbalance

4.4.3.3. Low Speed Shaft Bending Moments

Similar to the other non-blade measurements considered thus far, the low speed shaft bending moment becomes less effective when trying to distinguish between mass imbalance and pitch error. Figure 34 demonstrates that different levels and locations of mass and aerodynamic imbalances produce very similar results. For instance, B3 G16, B3 5° has an RMS value nearly equal to that of the B3 G40, B2 5° imbalance.

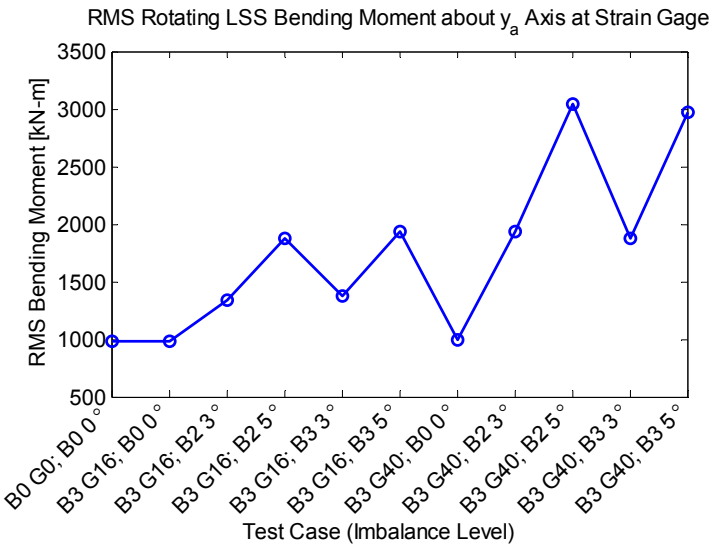

Figure 34. RMS rotating LSS bending moment vs. pitch error

4.5. Analysis of Imbalance with Blade Sensors

In Section 4.4, it was illustrated that some non-blade measurements provide good insight into detecting the presence of a mass or aerodynamic imbalance in the rotor and assessing its level of severity, but they lacked the ability to determine which blade(s) is the culprit (i.e location), and

in general provided confounding results when mass and aerodynamic asymmetries were simultaneously present. The next sections will examine outputs from the FAST simulations that would depend on blade-mounted sensors in an operating turbine.

4.5.1. *Pitch Error Analysis Results*

The following sections summarize the trends in the results for pitch error, as measured in blade tip acceleration responses and blade root bending moments.

4.5.1.1. Blade Tip Acceleration Response

The mean flap, RMS flap and edge degree-of-freedom blade accelerations are shown in the left two plots of Figure 35. The mean flap response of the pitched blade three decreases significantly with increasing pitch error. As with some of the non-blade responses, the other two blade flap responses also begin to decrease around 7.5° as a result of reduced forcing from the slowed rotor. For that reason, it is helpful to examine the blade-to-blade differences in the response, shown in the right two plots in Figure 35. The plot legend indicates which two blade responses have been subtracted from one another; the first blade listed has been subtracted from the second one. For instance, the blue line, Blades 1 & 2, shows the result of subtracting blade two's response from blade one's response. If the blade responses were all the same or very close, then no pitch error is present. When two blade-to-blade differences change, it can indicate the problematic blade. Figure 36 illustrates which blade may be problematic (the terminal point of the arrows) based on which pair of blade-to-blade differences is different than the third (the starting point of the arrows). This method is also beneficial because it can eliminate the need for baseline data, but thresholds would still need to be set to determine what level of response difference indicates an error. Note that in the blade-to-blade differences in Figure 35, blades 1 and 3 and blades 2 and 3 are grouped together, correctly indicating that blade 3 is the pitched blade. The absolute value of the difference was not plotted in Figure 35 because in some cases, the sign of the difference can be an indicator of the pitch error. For instance, the lead-lag RMS tip acceleration is lower for the pitched blade until 7.5° pitch error but at 7.5° and above the pitch error is higher. Therefore the sign of the difference helps distinguish between a 5° and 7.5° pitch error, which are close in magnitude but opposite in sign. Finally, the response of blade 1 and 2 is slightly different; this is thought to be caused by blade 2 passing through the wake of the incorrectly pitched blade 3 as it rotates.

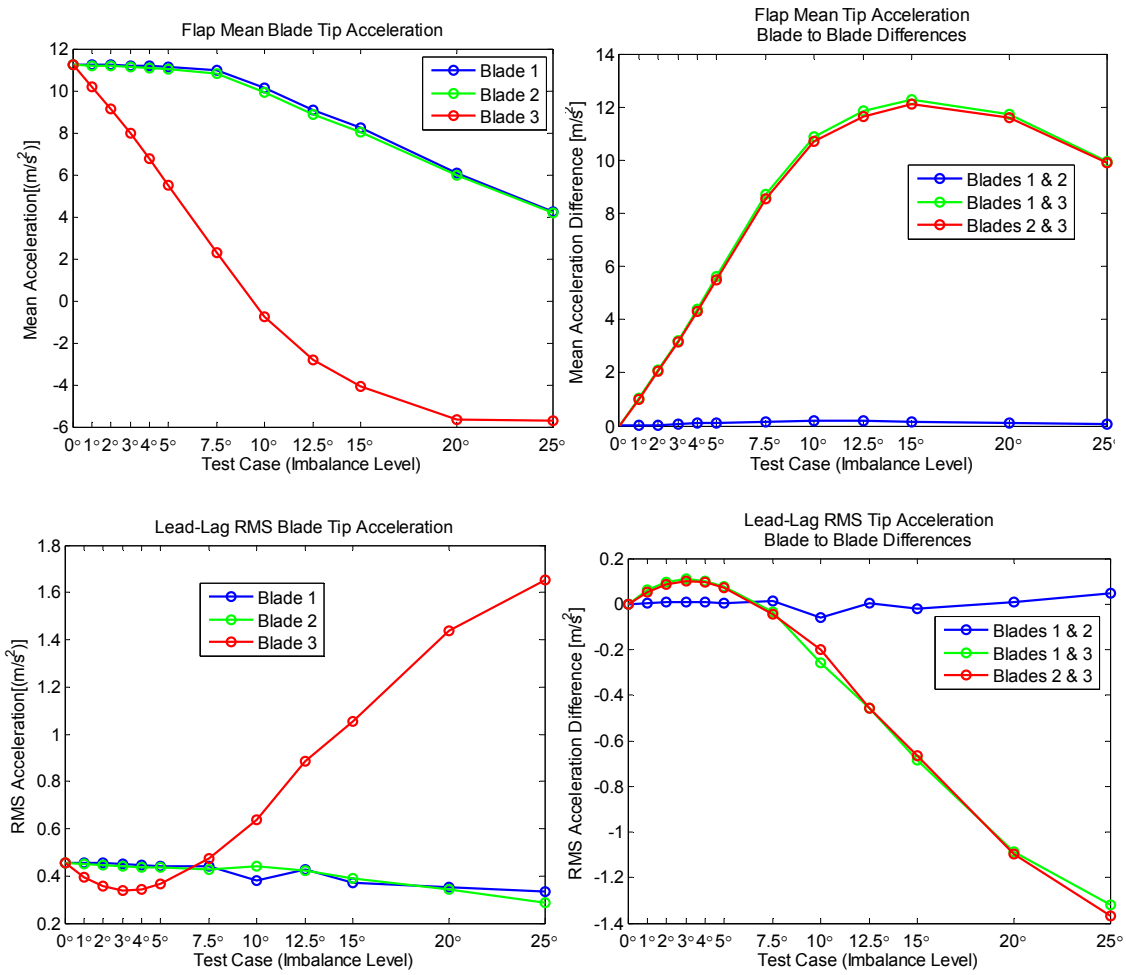

Figure 35. Span and edgewise blade tip accelerations and blade-to-blade differences for pitch error.

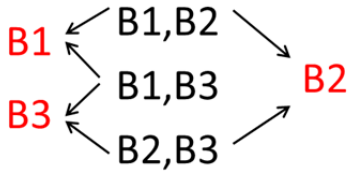

Figure 36 Diagram to determine faulty blade using blade-to-blade differences

Note that the flap response is much more sensitive to low pitch error, 5° or less, than the nacelle axial response shown previously in Figure 22. This makes the blade response a valuable tool in diagnosing aerodynamic imbalances. Lastly, Figure 37 demonstrates that the 1p PS magnitude of the edgewise blade tip acceleration is a fairly good indicator of pitch errors above about 3°. Again, the differences in the response magnitude of blade 1 and 2 are thought to be caused by blade 2 passing through the wake of the pitched blade 3 during rotation.

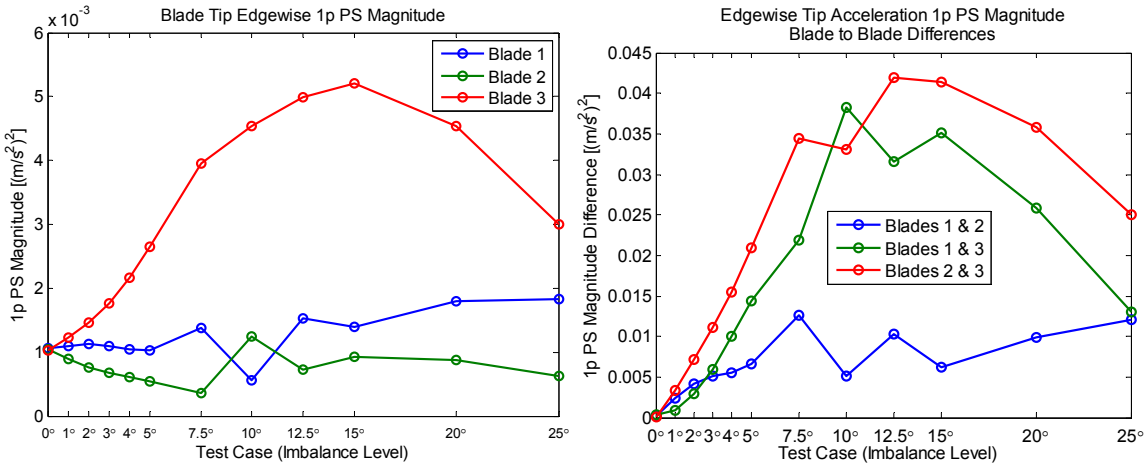

Figure 37. Blade tip edgewise 1p PS magnitude and blade to blade differences

4.5.1.2. Blade Root Pitching Moments

The moment of the blade about its pitch axis at the blade root is another good indicator of pitch error, as shown in Figure 38. It should be noted that the root pitching moment was also the most sensitive parameter to a trailing edge disbond, as shown in last year's work. This moment can be measured using strain gages located at the root of each blade. Again it is seen that the 1p PS magnitude tends to fall off due to reduced forcing from the slowed rotor for pitch errors greater than 10°, but the mean pitching moment of the pitched blade continues to decrease relative to the other two. Note that the plot in the lower right of Figure 38 displays the absolute value of the mean difference.

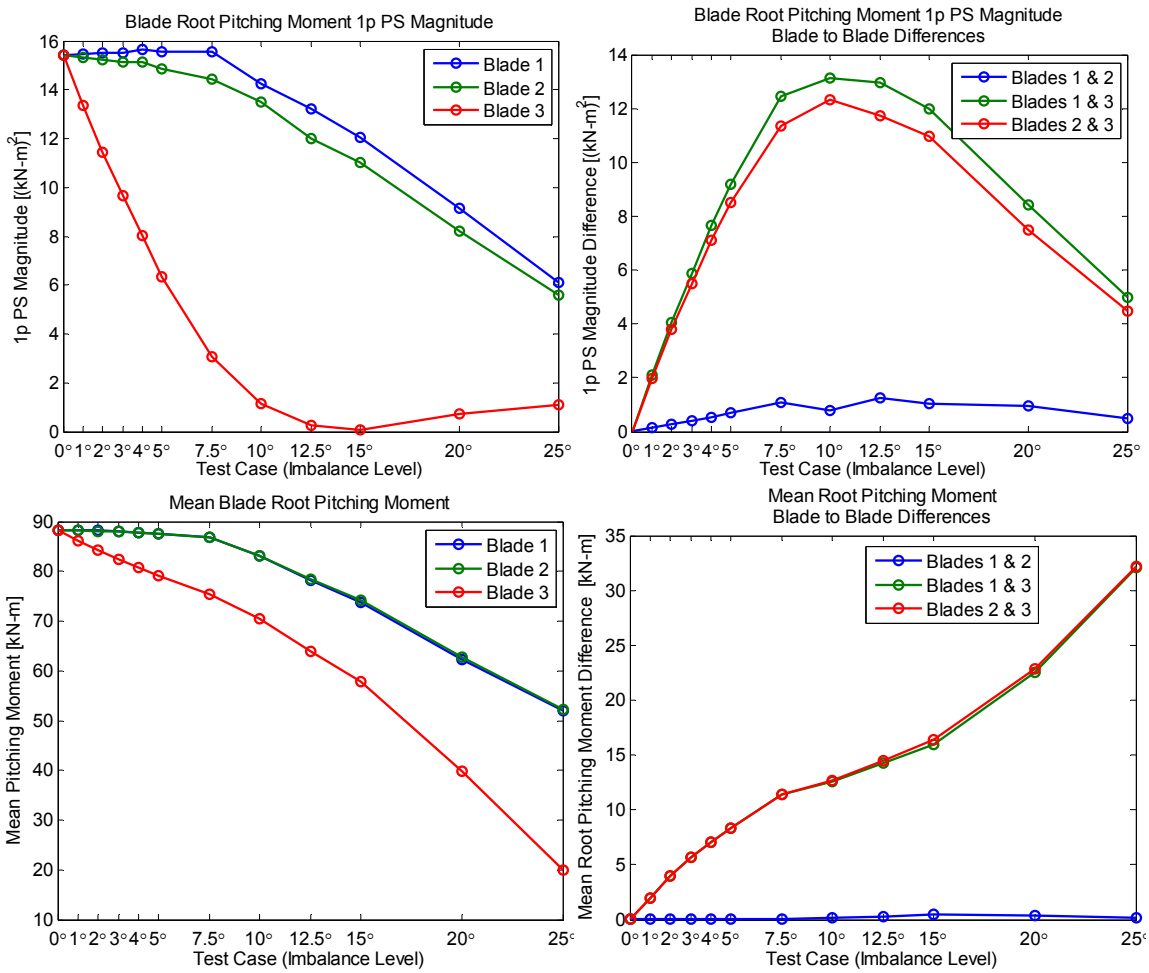

Figure 38. Blade root pitching moment 1p PS magnitude, RMS, and blade-to-blade differences

4.5.2. *Mass Imbalance Analysis Results*

4.5.2.1. Blade Root Axial Force

The mass imbalances produced essentially no differences in the blade tip accelerations or root bending moments. However, the axial (span-wise) force as measured in the blade root did increase for the blade containing increased mass, as shown in the RMS values and blade-to-blade differences in Figure 39. While axial force is the output variable from FAST, axial strain as measured by a strain gage or fiber optic sensor could provide the equivalent measurement on an operating turbine.

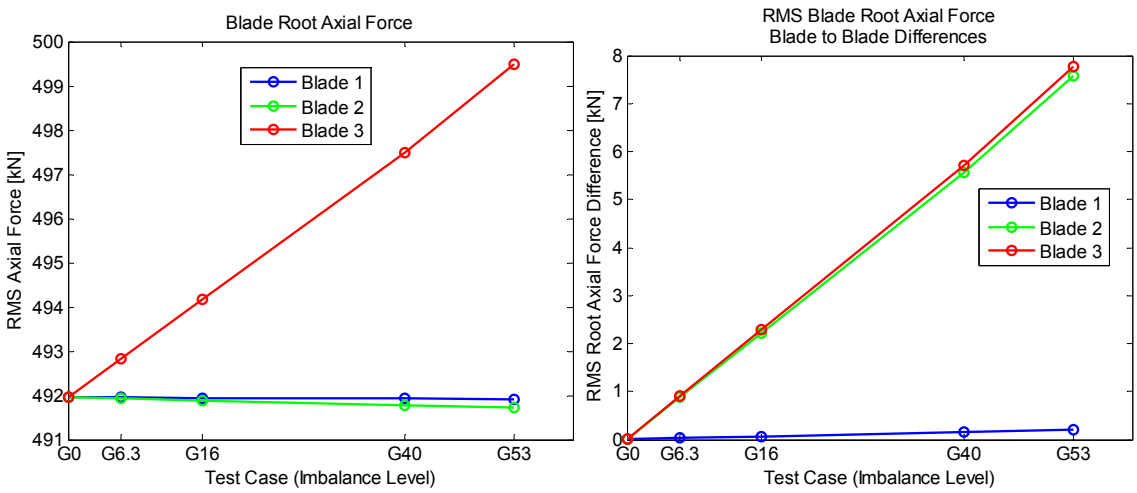

Figure 39. Blade root RMS axial force and blade-to-blade RMS differences

4.5.3. *Simultaneous Mass Imbalance and Pitch Error Results*

Section 4.4.3 demonstrated that it was difficult to distinguish simultaneous mass imbalance and pitch error using non-blade measurements. The following sections will demonstrate the advantages of blade measurements in detecting the presence of mass imbalance or pitch error, as well identifying which blade is responsible for each error.

4.5.3.1. Blade Tip Acceleration Response

As was indicated in section 4.5.1.1, the mean (or RMS) flap and edge blade tip acceleration responses were indicative of pitch error and could identify which blade was pitched incorrectly. This remained true even when mass imbalances were present, as shown in Figure 40. Note that the 1p lead-lag response was still a good indicator of pitch error, as was the span acceleration response, but both were left out for the sake of brevity. In experimental testing, the span and lead-lag degrees of freedom tend to exhibit less measurement noise and variance and therefore may be more beneficial than the flap degree of freedom measurement for use in statistics-based condition monitoring systems.

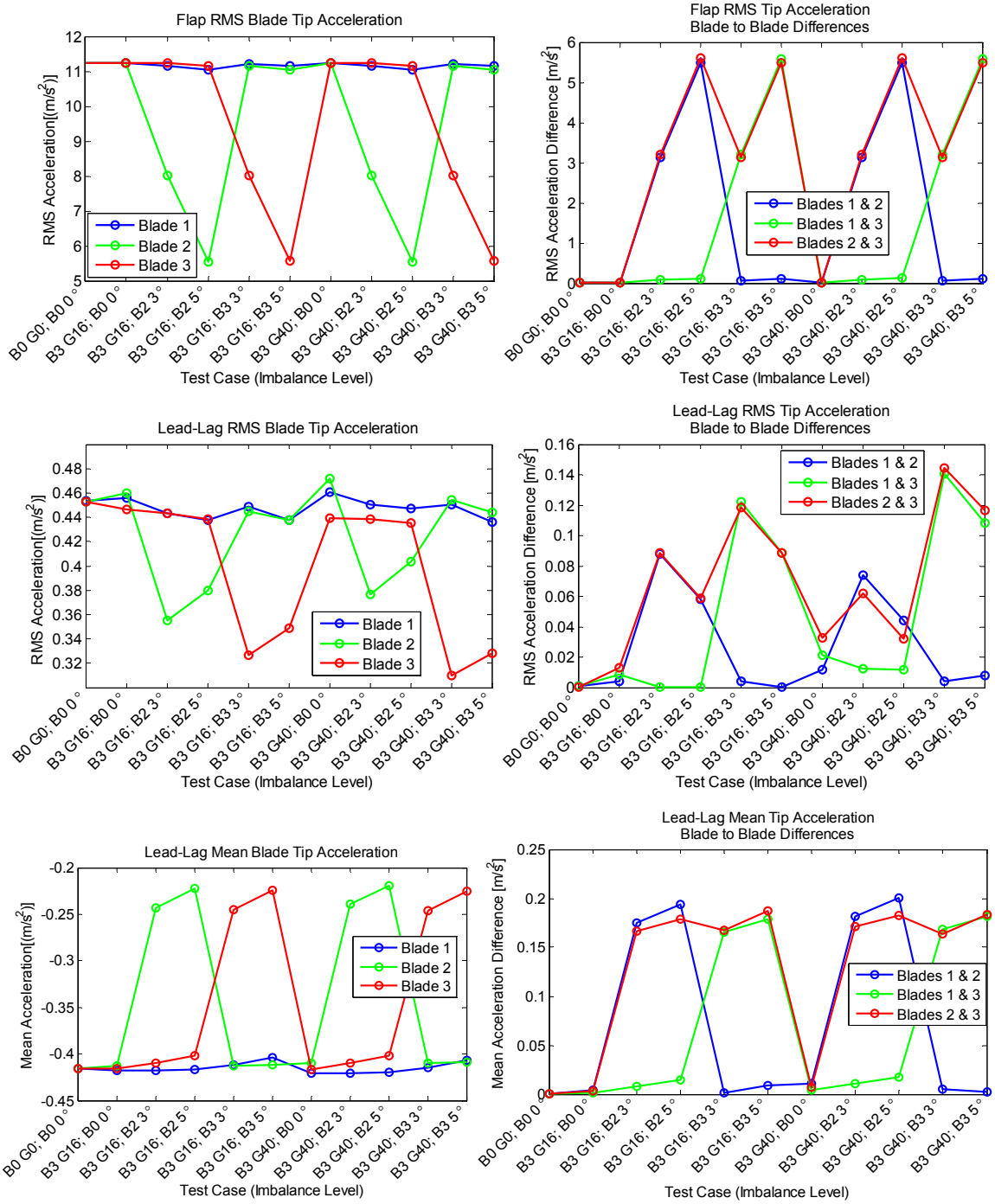

Figure 40. Span and edgewise blade tip accelerations and blade-to-blade differences for simultaneous mass imbalance and pitch error

4.5.3.2. Blade Root Pitching Moments

The RMS and 1p PS magnitude of the blade root pitching moments decreased very consistently for the pitched blade, as seen in Figure 41. For instance, the 1p PS magnitude of blade two's pitching moment when it had a pitch error of 3° is nearly the same as the pitching moment of

blade three when it had the same pitch error. Note that the mass imbalances were evenly distributed throughout the affected blade section(s). If the mass imbalance were concentrated on the leading or trailing edge of the blade, it is feasible that this too may increase the pitching moment of the blade.

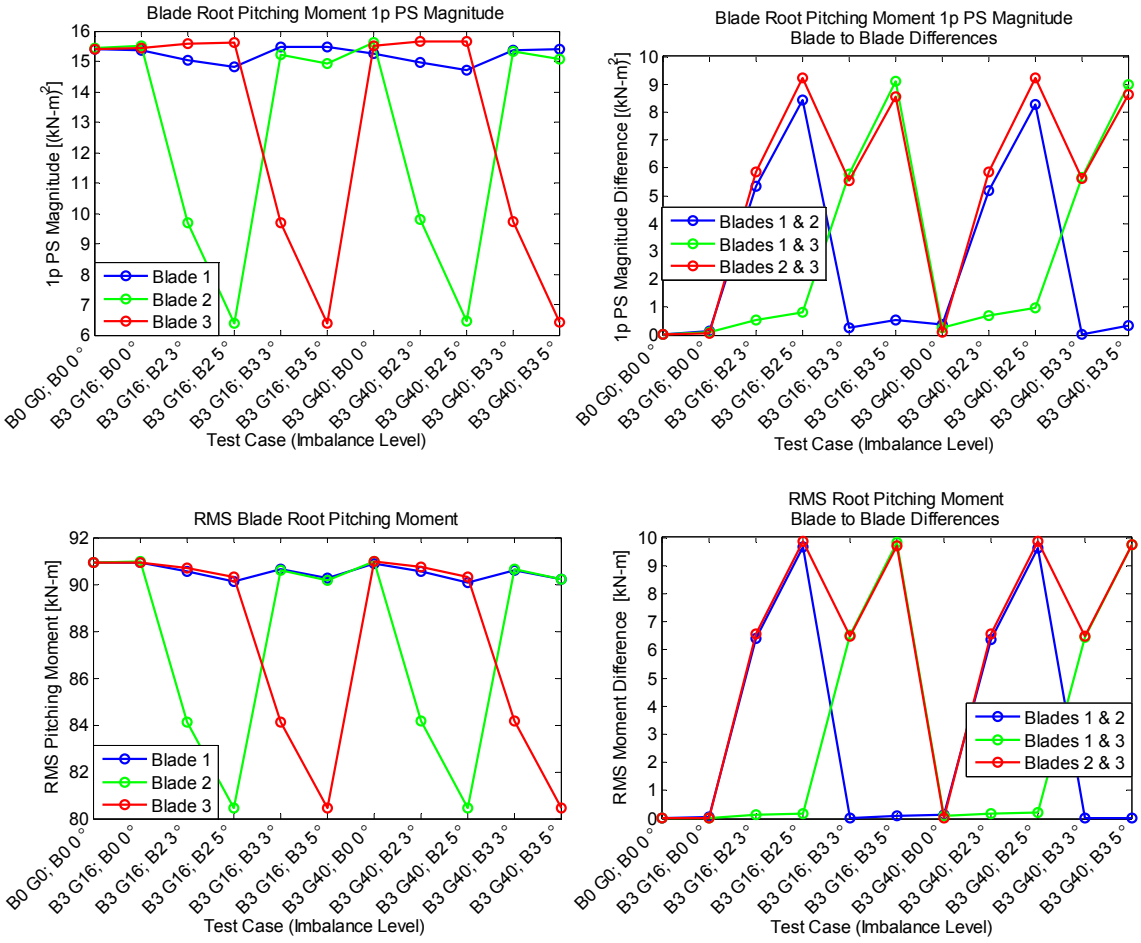

Figure 41. RMS, 1p PS, and blade-to-blade differences of blade root pitching moments for simultaneous mass imbalance and pitch error

4.5.3.3. Blade Root Axial Force

Figure 42 displays the blade root axial forces as well as the blade-to-blade differences in the measured forces. If the axial force was due entirely to centrifugal force, then the blade containing additional mass (blade 3) should always produce the largest axial force. However, this is not the case. When blade 2 is pitched, even for the larger G40 mass imbalance, the pitch error results in a larger axial force on the pitched blade than on the blade with increased mass. This effect results from the blade center of mass not being coincident with the pitch axis along which the axial force is being measured. As shown in Figure 43, the centrifugal force, F_c, is directed radially through the blade center of gravity. When the blade is pitched, θ_A, the angle from the hub to the pitch axis remains fixed, while θ_{CG}, the angle from the hub to the line of action through the center of gravity approaches θ_A. The axial force being measured is the projection of F_c onto the pitch axis, that is:

$$F_{Axial} = F_C \cos(\theta_A - \theta_{CG}). \quad (15)$$

Therefore, because the quantity (θ_A-θ_{CG}) decreases as a blade is pitched, the measured axial force increases. Consequently, blade root axial force is not effective in distinguishing between mass and aerodynamic imbalance, and unlike what the mass-imbalance-only results of section 4.5.2.1 may suggest, it would not be effective in locating which blade was producing a mass imbalance if there were also aerodynamic imbalances present.

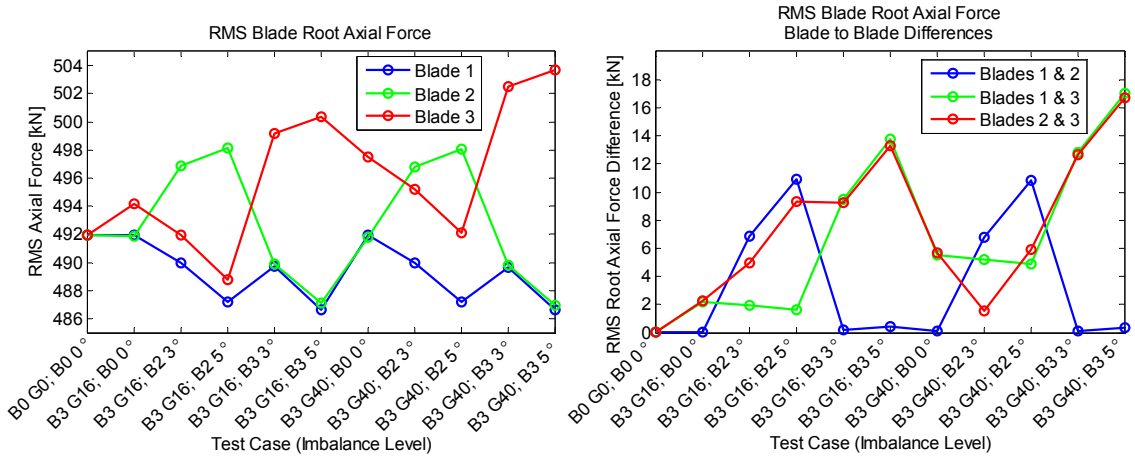

Figure 42. RMS blade root axial forces and blade-to-blade differences

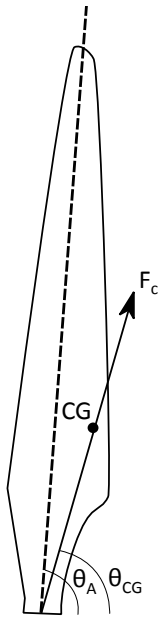

Figure 43. Blade center of gravity offset

4.6. Increased Loads due to Imbalances

An important result of rotor imbalances are the increased loads imparted to the turbine structure and drivetrain. The next three sections quantify load increases in the drivetrain, tower, and yaw joint as a result of pitch error, mass imbalance, and simultaneous pitch error and mass imbalance. The plots depict the percentage change in the forces and moments relative to the baseline simulation results.

4.6.1. *Pitch Error*

Pitch error resulted in significantly increased low speed shaft bending moments and shear forces. Figure 44 displays the low speed shaft bending moments at the shaft tip in the rotating reference frame about the y_a and z_a axes, LSSTipMya and LSSTipMza, respectively. It also shows the nonrotating low speed shaft shear force, LSShftFys, which is directed along the y_s axis and is constant along the shaft. All three forces and moments exhibited large increases due to pitch error, with percentage increases over 100% for as little as 2° error.

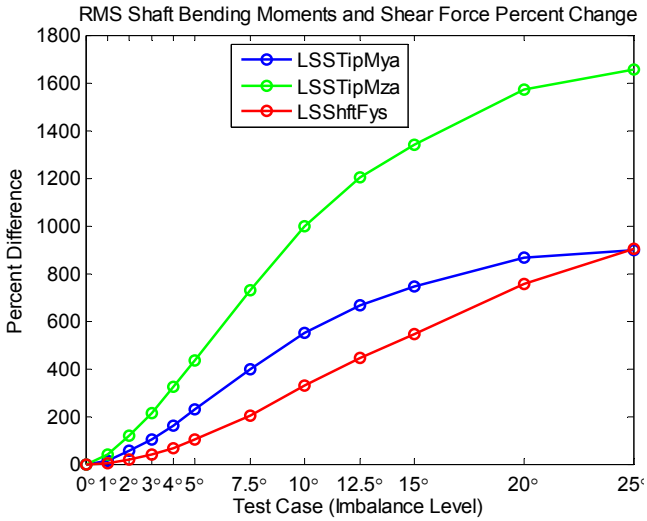

Figure 44. RMS Shaft bending moments and shear force percentage change due to pitch error

Several tower forces and moments also experience large increases, as indicated in Figure 45. The largest effect was on the tower yaw moment, labeled YawBrMzp in the figure. This moment increased from 124 kN-m to 434 kN-m for just a 1° pitch error, an increase of 250%, increasing by over 1700% for a pitch error of 5°. The plot on the right in Figure 45 adjusts the scale so the changes in the other forces are clearer. The tower-top/yaw bearing side-to-side shear force, YawBrFyp, as well as the moment about the y_p axis (see Figure 13 for coordinate system definitions), YawBrMyp, increase significantly as well. These forces and moments directly affect the yaw drive components in the turbine, which comprise a significant subsystem that experiences wear over a turbine's lifetime. The tower-top/yaw bearing roll moment (about the x_p) axis, YawBrMxp and the shear force at the tower top directed along the x_p axis decrease with

pitch error, which may be expected due to decreased thrust from the pitched blade, as well as the slowed rotor for large pitch errors. These reductions, however, are much smaller than the increases in the other moments and forces.

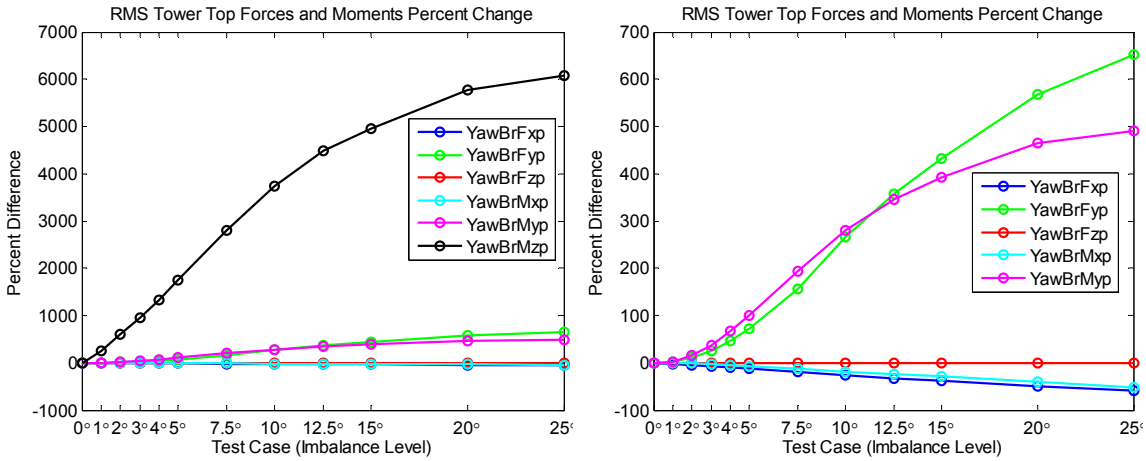

Figure 45. RMS tower top force and moment percent changes due to pitch error

The yaw (torsional) moment about the vertical tower axis at its base, TwrBsMzt, as well as the side-to-side shear force at the tower base, TwrBsFyt, also increase significantly due to pitch error as shown in Figure 46.

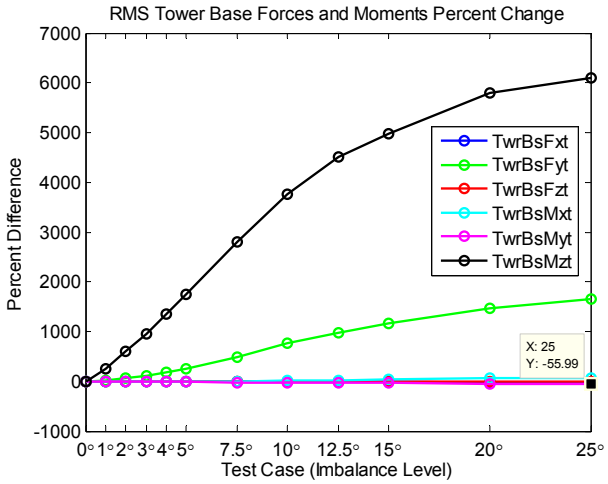

Figure 46. RMS tower base force and moment percent changes due to pitch error.

4.6.2. *Mass Imbalance*

As was shown previously, mass imbalances do not greatly affect the low speed shaft tip bending moments, but Figure 47 shows increases in the shear force. Even the permissible G16 imbalance grade produces an 8% increase, while the 0.5% blade mass imbalance, G53, results in a 60%

shear force increase. Moreover, Figure 48 indicates that the tower side-to-side shear force and yaw moment, YawBrFyp and YawBrMzp, respectively, increase due to mass imbalance.

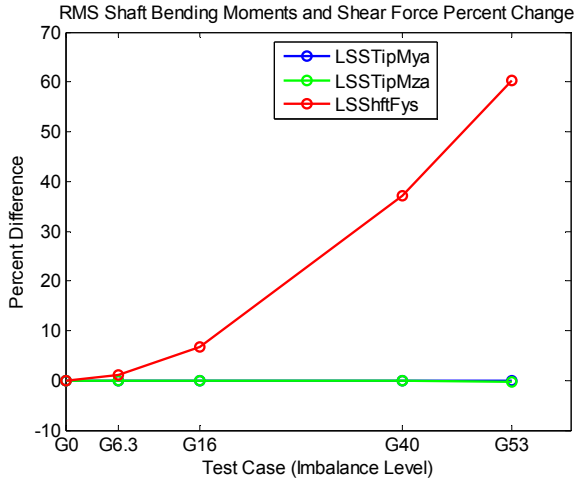

Figure 47. RMS Shaft bending moments and shear force percentage change due to mass imbalance

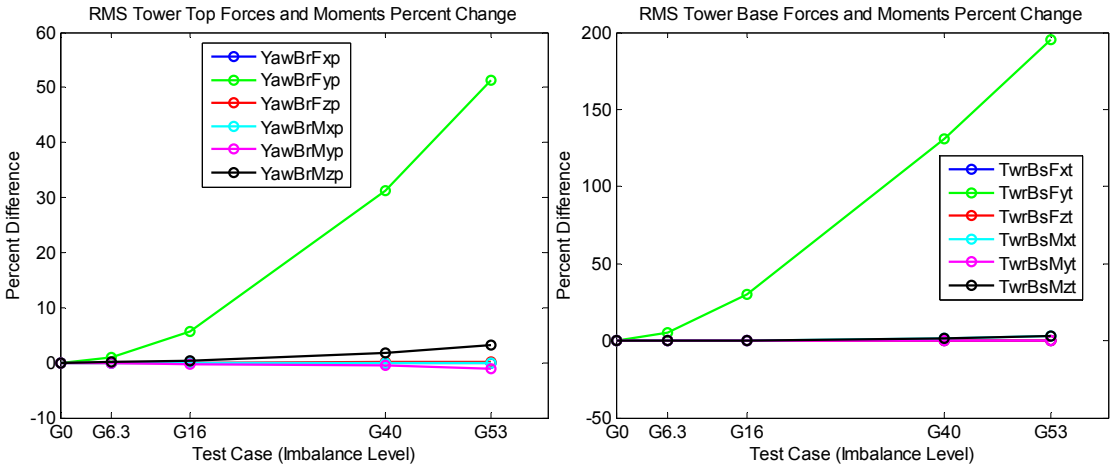

Figure 48. RMS tower force and moment percent changes due to mass imbalance

4.6.3. *Simultaneous Pitch Error and Mass Imbalance*

As would be expected, having both pitch errors and mass imbalances result in increased tower and drivetrain loads, as indicated in Figure 49, Figure 50, and Figure 51. These asymmetric loads propagate from the blades through the low speed shaft to the gearbox, tower, and other drivetrain components.

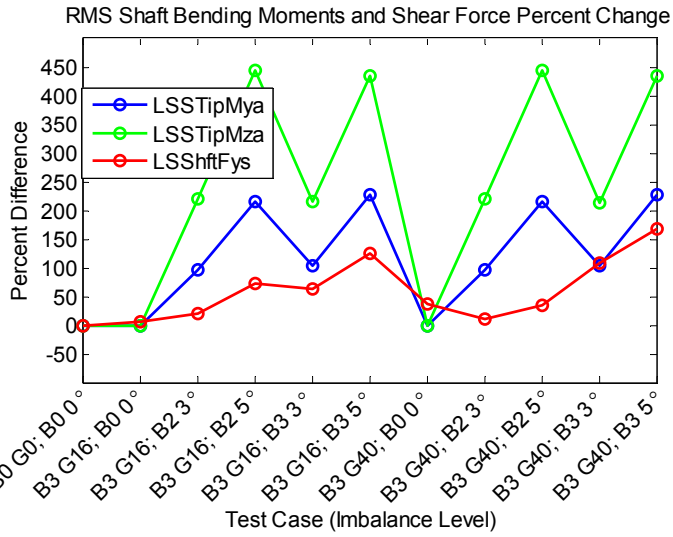

Figure 49. RMS shaft bending moments and shear force percentage change due to simultaneous pitch error and mass imbalance

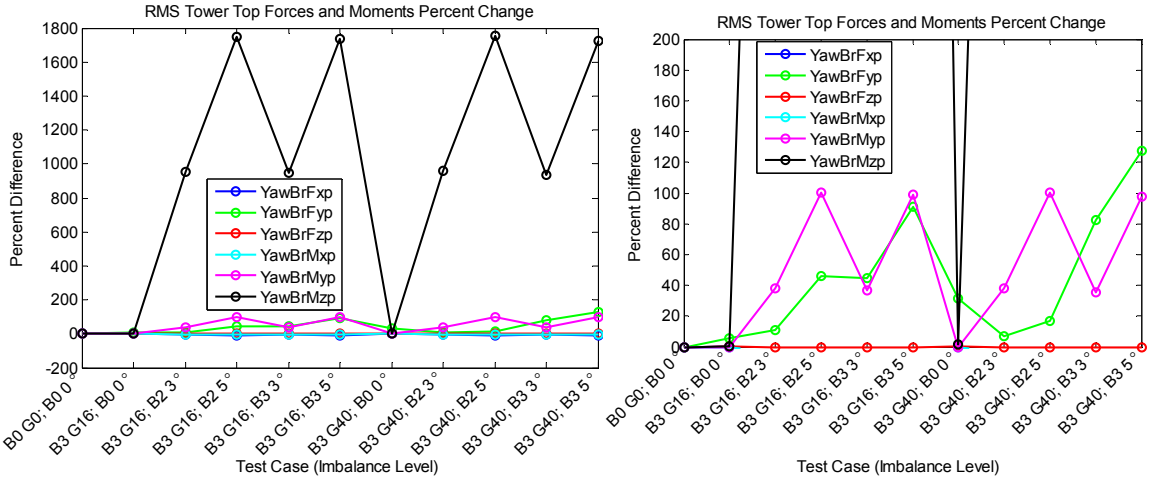

Figure 50. RMS tower top force and moment percent changes due to simultaneous pitch error and mass imbalance

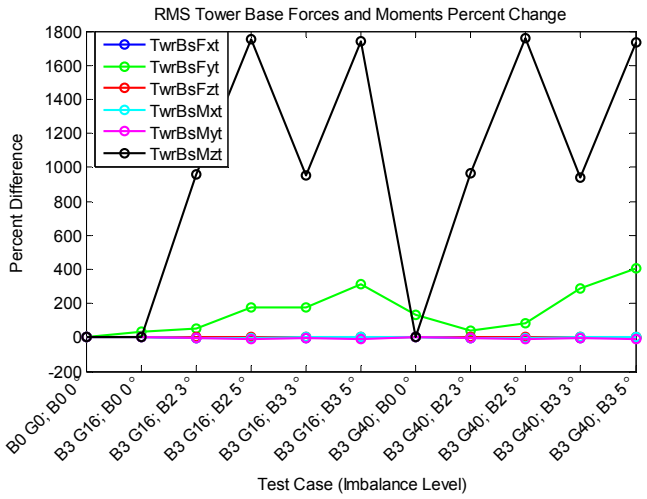

Figure 51. RMS tower base force and moment percent changes due to simultaneous pitch error and mass imbalance

4.7 Summary of Imbalance Detection Strategy

The results of these analyses of the operational response of a wind turbine rotor to various types and levels of rotor imbalance can be synthesized into a flow chart, as shown in Figure 52, for detection of rotor imbalances using a combination of sensors and analysis methods. This strategy utilizes both blade and non-blade sensor measurements. None of the methods evaluated thus far were successfully able to identify the blade having a mass imbalance; however, based on the above sensitivity studies of various imbalance conditions several methods have been developed to detect the presence of pitch error, its severity, as well as to identify which blade the pitch error is present. Therefore, and in summary, the strategy is as follows:

(1) Detect if an imbalance exists in the rotor

(2) Determine if the imbalance is strictly a mass imbalance, or whether it is a pitch or pitch and mass combination (it cannot yet be distinguished if there is just a pitch error or a simultaneous pitch error and mass imbalance at this stage)

(3) If the error is due to pitch or pitch and mass, determine which blade is pitched incorrectly and by how much. Correct this blade pitch through the blade control algorithm.

(4) Iterate until pitch error has been eliminated. If a mass imbalance is still present, it will then be identified, including which blade is the source of the imbalance.

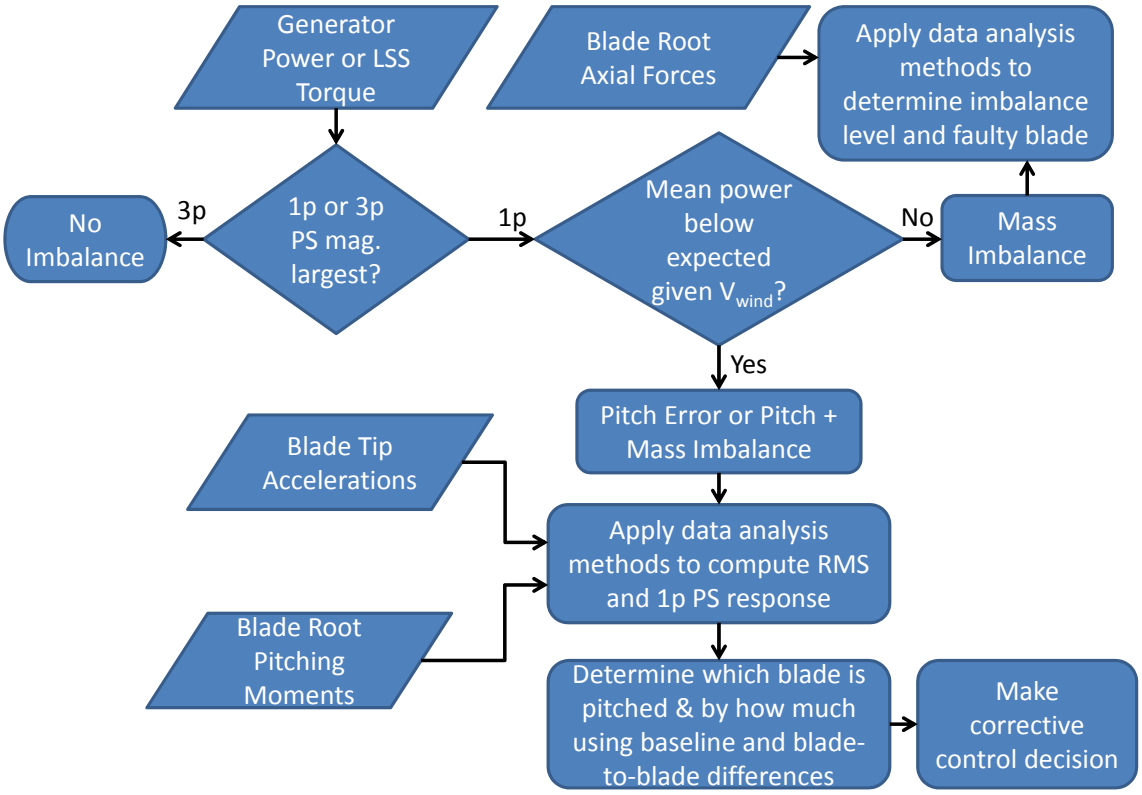

Figure 52. Pitch error and mass imbalance detection flow chart

5. SHEAR WEB DISBOND SENSITIVITY STUDY

5.1. Introduction

The developed multi-scale modeling methodology was utilized to investigate the sensitivity of a wide range of potential operational measurements to the presence of a shear web (SW) disbond. This representative form of damage was chosen because it is a damage mechanism that is routinely seen in the field. For this initial investigation all of the disbonds were assumed to have initiated at max chord of the blade (at the 14.35 meter span location) and propagated outwards toward the tip of the blade. This section includes a variety of different sensitivity analyses that were conducted at various stages throughout the modeling and simulation processes.

5.2. Shear Web Disbond Damage Modeling Methodology and Simulation Methods

To model the presence of a shear web disbond on a wind turbine blade, the NuMAD blade model was modified so that shear web nodes were split into two different nodes. This effectively split the blade model at the shear web in a similar way to how the blade is physically constructed through bonding the high pressure clam shell to the shear webs. To simulate a healthy bond across the blade, the top and bottom shear web nodes were connected using constraint equations in all six degrees of freedom. In the area of the blade in which the shear web disbond existed, the constraints were removed so that there was no connection between the top of the blade and the shear web. A similar approach was done by Griffith, et al. (2011, Reference 1) to simulate a trailing edge disbond on the same blade model. While this modeling disbond methodology is effective in modeling a disbond in which the blade and shear web do not come into contact, it fails to take into account the possible interaction of the top and bottom surfaces of the disbond. For large cracks in which interaction between the top of the blade and the shear web may have a significant influence, the relative decrease in stiffness due to the disbond is likely over-estimated because the added stiffness due to the disbond face interaction was not taken into account. Modeling the interaction between the two surfaces could be achieved using nonlinear surface contact constraints between the top of the blade and the shear web but this was not accomplished during this initial investigation and remains as future work.

FAST simulations were performed for several wind profiles and turbine blade conditions. Among the wind profiles used were constant wind speed and direction, IEC Kaimal Model with A turbulence, IEC Kaimal Model with B turbulence, and the NREL NWTC wind model with a KHTEST intense disturbance. For the constant wind profile, the wind speed was set to 11.4 m/s, with a 1/7 power law vertical shear profile. The IEC Kaimal model is defined in IEC 61400-1 2nd ed. [29] and assumes neutral atmospheric stability. A mean wind speed of 13 m/s was used. The spectra for the three wind components, K = u, v, w, are given by

$$S_K(f) = \frac{4\sigma_K^2 L_K / \bar{u}_{hub}}{(1 + 6fL_K / \bar{u}_{hub})^{5/3}} \tag{16}$$

where f is the cyclic frequency and L_k is an integral scale parameter. More information can be found in IEC 61400-1 [29] or the *TurbSim User's Guide* [30].

The NREL NWTCUP model represents turbulent inflow characteristics at the NWTC, downwind of a major mountain range. A mean wind speed of 13 m/s was used. For neutral and stable flows, the NWTCUP spectra are defined by adding scaled versions of the SMOOTH-model spectra:

$$S_K(f) = \sum_{i=1}^{NumPeaks_K} p_{i,K} S_{K,SMOOTH}(F_{i,K} f) \tag{17}$$

where $NumPeaks_K = 2$ for all wind components $K = u, v, w$ and the function $S_{K,SMOOTH}$ is defined within the SMOOTH model. More information can be found in the *TurbSim User's Guide* [30].

The sample time spacing was 0.01 seconds, corresponding to a sample rate of 100 Hz. Since the per-revolution harmonics were mainly of interest and the maximum rotor speed was 12.1 rpm, or 0.2 Hz, this sample rate was sufficient. Simulations were conducted under three conditions: (1) all three blades are healthy, (2) one of the three blades having a 5-meter shear web disbond, (3) one of the three blades having a 10-meter shear web disbond. Two hundred output variables were recorded from the simulations, including generator power, blade root moments, tri-axial blade accelerations along the span, nacelle accelerations, and many others. The first 30 seconds of simulations were discarded in analyzing the data to allow any startup transients to damp out, which was also performed for the imbalance simulations. The total simulation time for each test, eliminating the first 30 seconds, was one hour, allowing for averaging to take place.

5.3. ANSYS Strain Field Results and Shear Web Disbond Sensitivity

As was done in FY11 (Reference 1), aerodynamic loads from the full system aeroelastic simulation can be translated to a set of equivalent forces for application to finite element nodes in the blade model. This corresponds to the "Local Sensitivity" step in the multi-scale simulation methodology. Figure 53 shows the 5-MW blade model with force vectors representing the steady aerodynamic load for normal operation at 11.4 m/s wind speed.

Figure 53. Force vectors representing aerodynamic load applied to the 5-MW blade finite element model

A 5 meter long shear web disbond, representing 8.13% of blade span, has been modeled in the detailed blade model. The response of the blade structure to the applied aerodynamic forces was computed for both healthy blade and damaged blade and localized displacements were determined in each element for both scenarios. The displacements for healthy and unhealthy blade are shown in Figure 54. As a result, the displacements increased across the blade for the damaged blade model and the tip deflection increased from 4.31512 meters to 4.31937 meters (or 0.0985% increase). The span-wise strain field is shown in Figure 55 for the blade with the 5 meter shear web disbond. Near the disbond on the shear web there was a clear redistribution of strains (50-160 micro-strain).

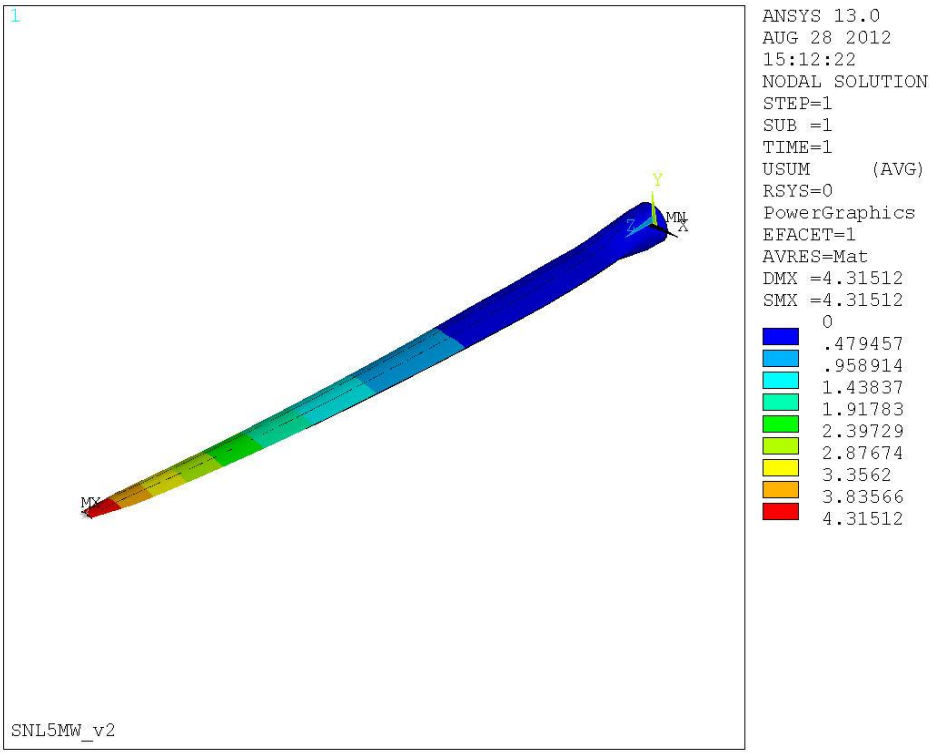

(a)

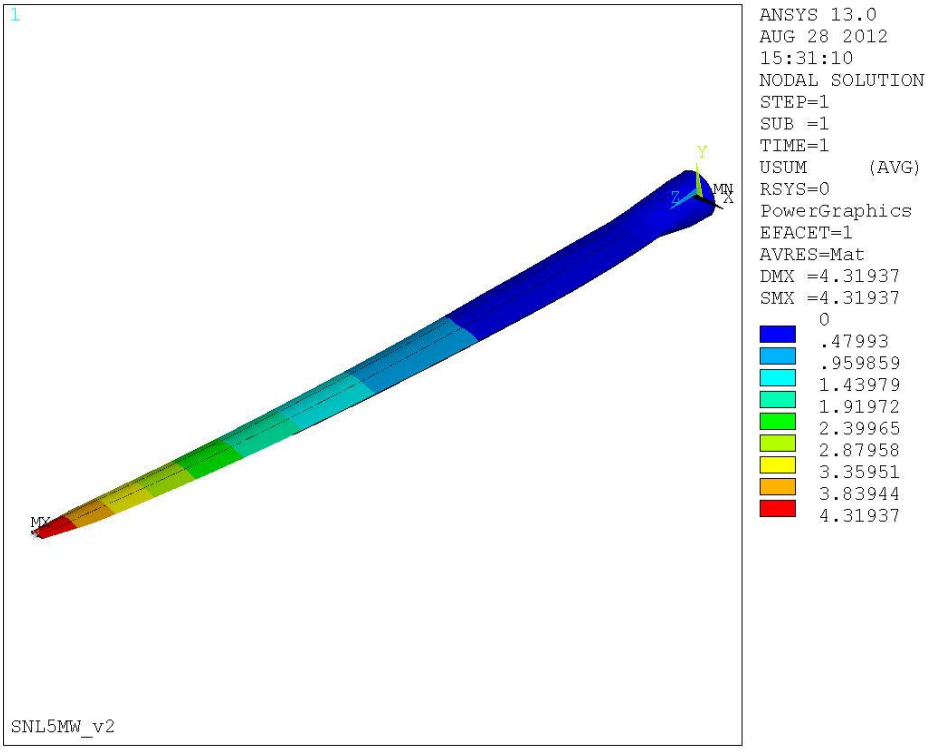

(b)

Figure 54. Blade deflections for (a) healthy blade and (b) blade with 5 meter SW disbond

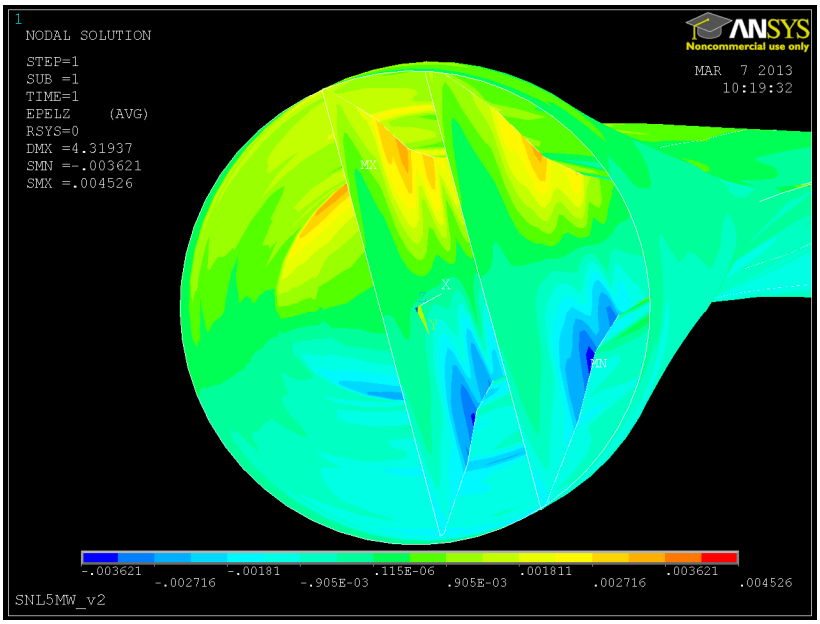

Figure 55. Span-wise strain field for blade with 5 meter SW disbond

The sensitivity of the extracted stiffness values to the shear web disbond was determined by calculating the percent decrease in each of the stiffness values for all of the sections in the reduced order model. Figures 56-59 show the percent decrease in flap-wise, edge-wise, torsional, and axial stiffness, respectively. The effect of the disbond is shown for the health (blue), 5 meter disbond (green) and 10 meter disbond cases (red). Clearly the effect of the disbond is localized at the location of the disbond and correlated in magnitude with the extent of the disbond. The blade with a 10 meter shear web disbond clearly showed an increase in percent decrease in all of the evaluated stiffness values for blade stations 10 and 11. The disbond had the largest effect on torsional stiffness in those blade sections, although the effect on flap-wise stiffness was nearly as large. The reduction in torsional stiffness in the model suggests that the torsional operational responses may be the best indicator in the case of SW disbond.

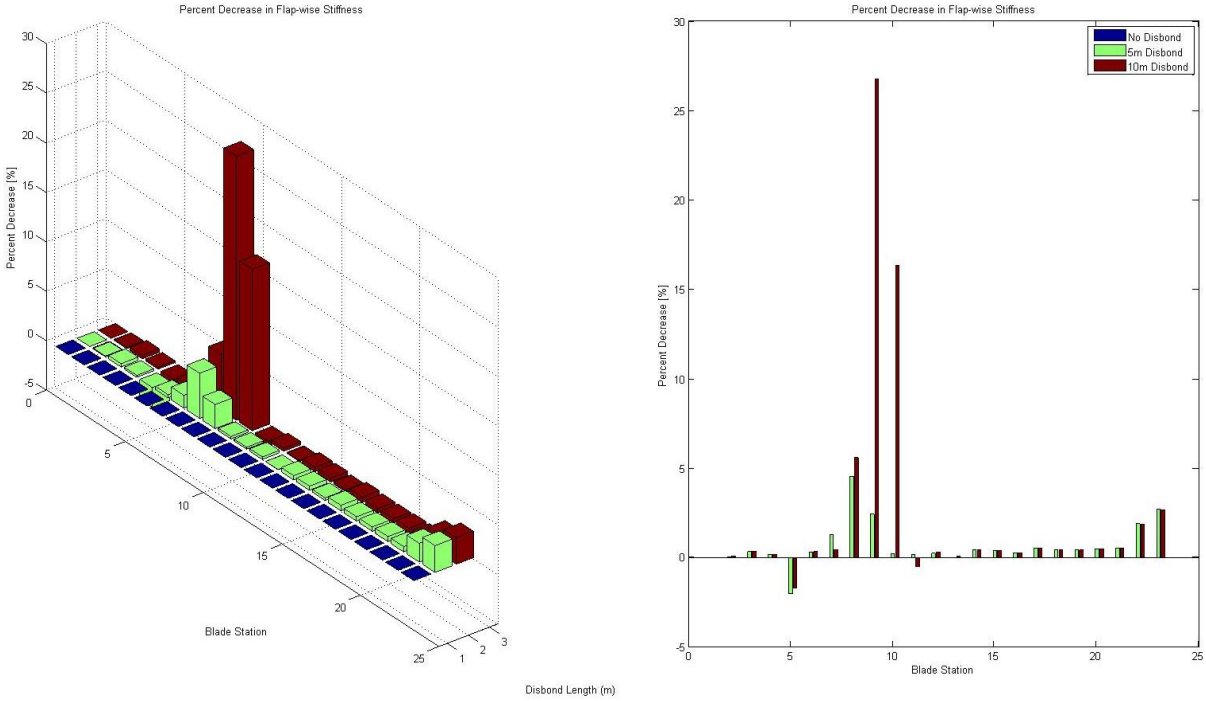

Figure 56. The percent decreases of the flap-wise stiffness value for varying length disbonds for segments spaced along the length of the blade.

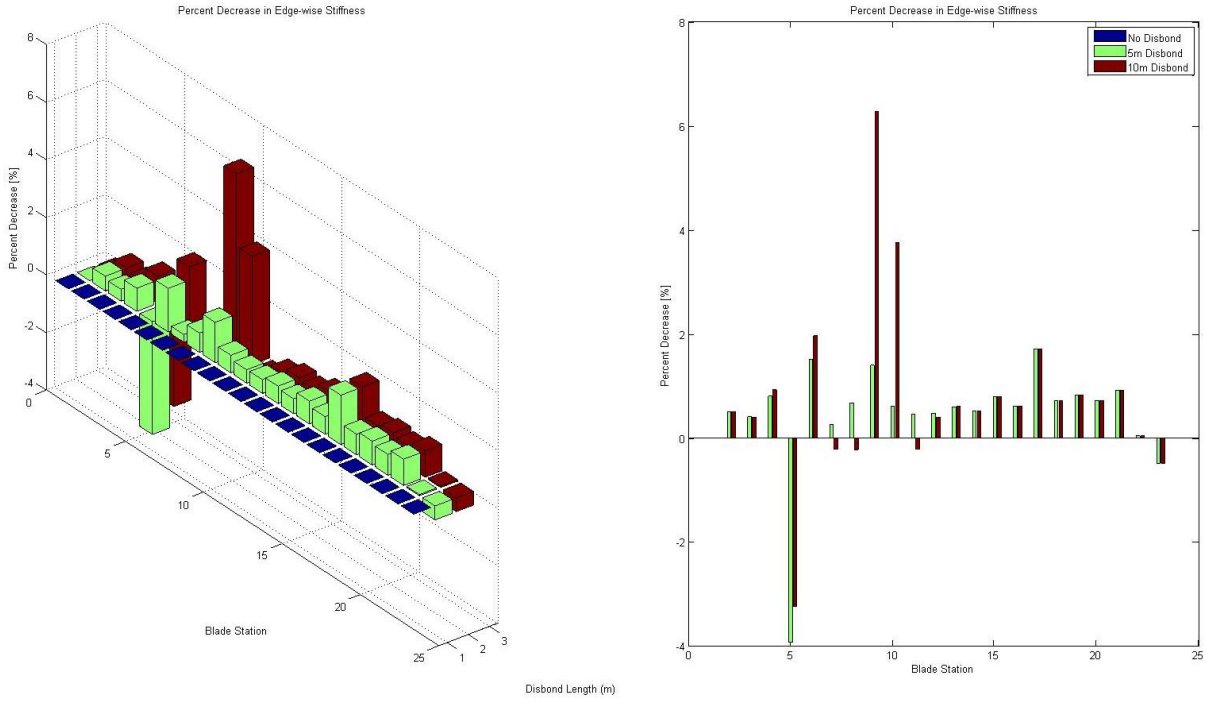

Figure 57. The percent decreases of the edge-wise stiffness value for varying length disbonds for segments spaced along the length of the blade.

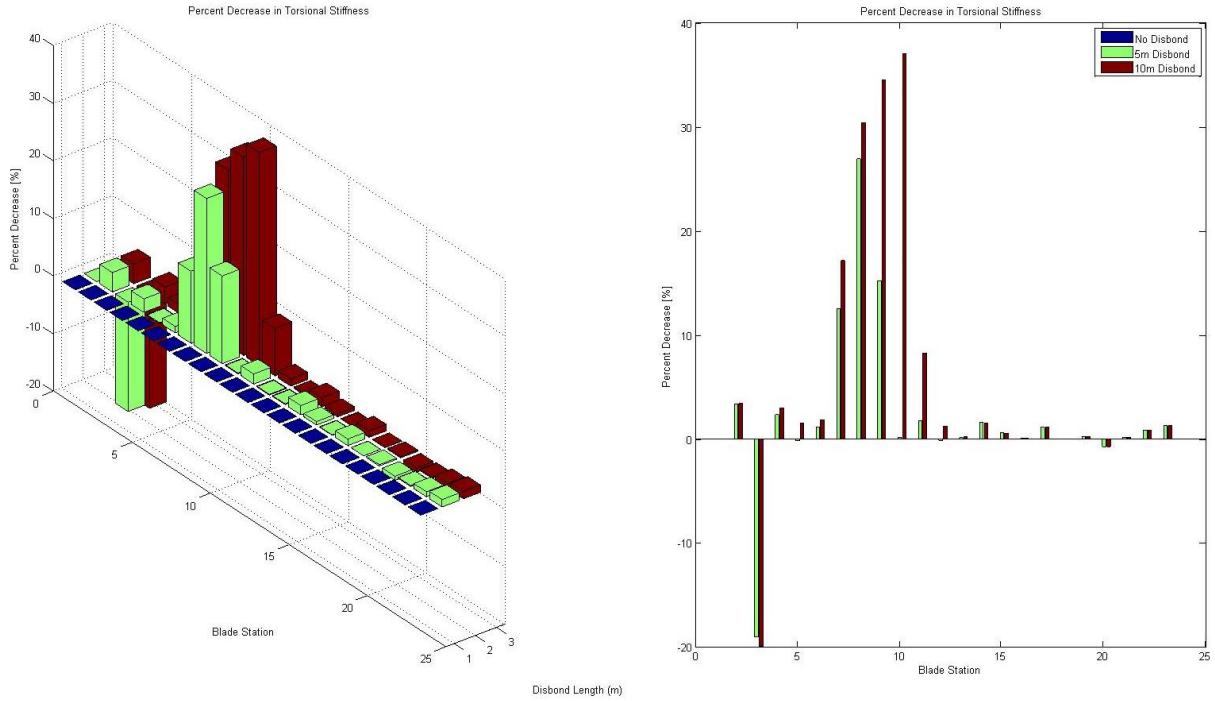

Figure 58. The percent decreases of the torsional stiffness value for varying length disbonds for segments spaced along the length of the blade.

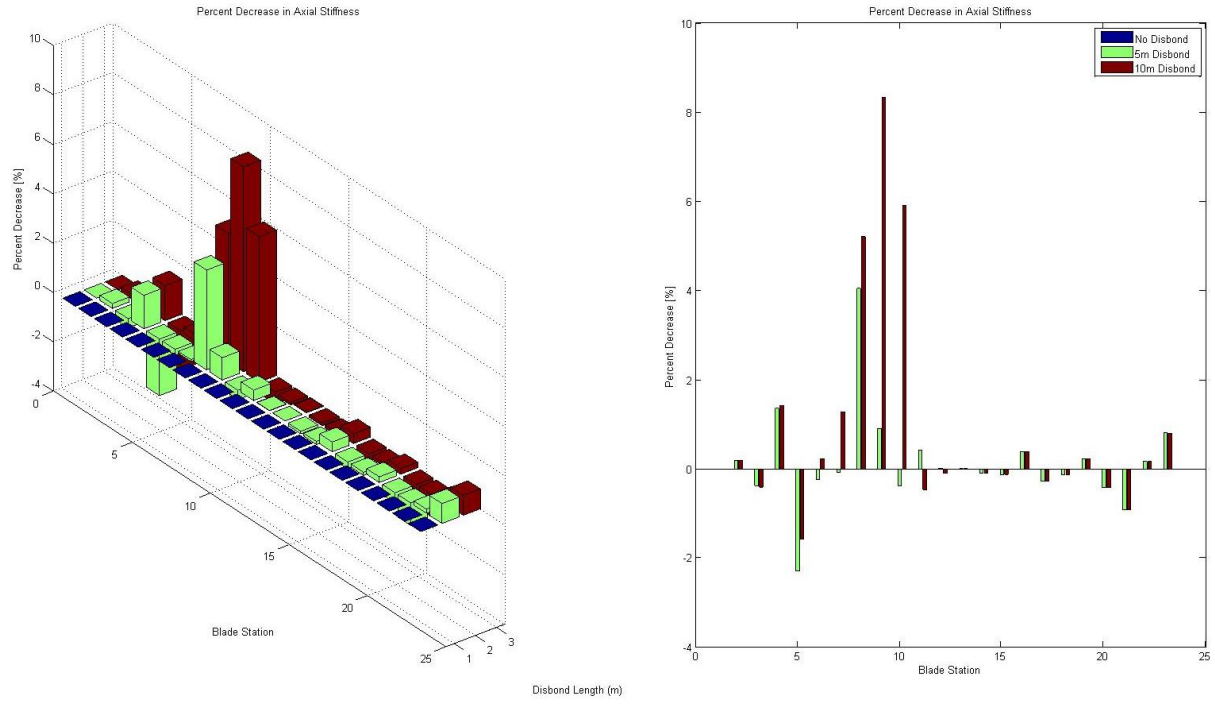

Figure 59. The percent decreases of the axial stiffness value for varying length disbonds for segments spaced along the length of the blade.

5.5. Analysis of Shear Web Disbond without Blade Sensors

In order to compare the effectiveness of shear web disbond detection methods with and without blade sensors, algorithms were first generated for determining the disbond using only the outputs from FAST that would not require blade-mounted sensors. From the 200 variables that are provided as output from the FAST simulation, those which displayed significant percentage changes in their RMS value or frequency response magnitude at the operating speed given a shear web disbond were identified as key measurement channels. The rotor azimuth position output from FAST was used as the reference signal for time synchronous averaging. The rotational resampling was performed in the same way as described above in the rotor imbalance studies. The azimuth signal was converted to radians, unwrapped and then the measurement signal was interpolated so that each revolution contained the same number of data samples with each sample corresponding to the same azimuth position of the rotor's rotation. Finally, blocks of three revolutions of data were averaged together. More than one revolution was used in the block size to increase the length of the block's time history, thereby increasing the frequency resolution of the DFT of the averaged signal. The shear web disbond detection algorithms for non-blade sensors all functioned in a similar way: detecting changes from baseline measurements either in the RMS response or 1p power spectral density magnitude.

5.5.1. *Shear Web Disbond Analysis Results*

The following sections summarize the trends in the results for shear web disbond, as measured in the generator power output and nacelle inertial sensors.

5.5.1.1. Generator Power

Overall, the generator power output did not change significantly between the healthy model and those models with a shear web disbond. Interestingly, a phase shift occurred in the synchronously averaged power output under the presence of a SW disbond. However, the RMS power output did not change more than ~0.035% when the three turbine models were examined under the four different wind profiles.

5.5.1.2. Nacelle Inertial Measurements

For all of the following discussion, axial nacelle acceleration will refer to acceleration in the x_s direction, vertical nacelle acceleration (or tower axis) will refer to acceleration in the y_s direction, and transverse (or side-to-side) nacelle acceleration will refer to acceleration in the z_s direction (all directions as defined in Figure 11). For all wind cases, nacelle accelerations increased in all three directions with the presence of the shear web disbond. In addition, the percent changes were correlated with the extent of damage (i.e. length of the disbond). In addition, the x_s and y_s 1p response differences as well as the RMS differences in the z_s direction indicated the presence and severity of disbond. However, no feature could be extracted to indicate which blade contained the damage. Figure 60 shows the 1p PS magnitude percent change of nacelle acceleration in the z_s direction and Figure 61 shows the RMS percent change of nacelle acceleration in the y_s direction.

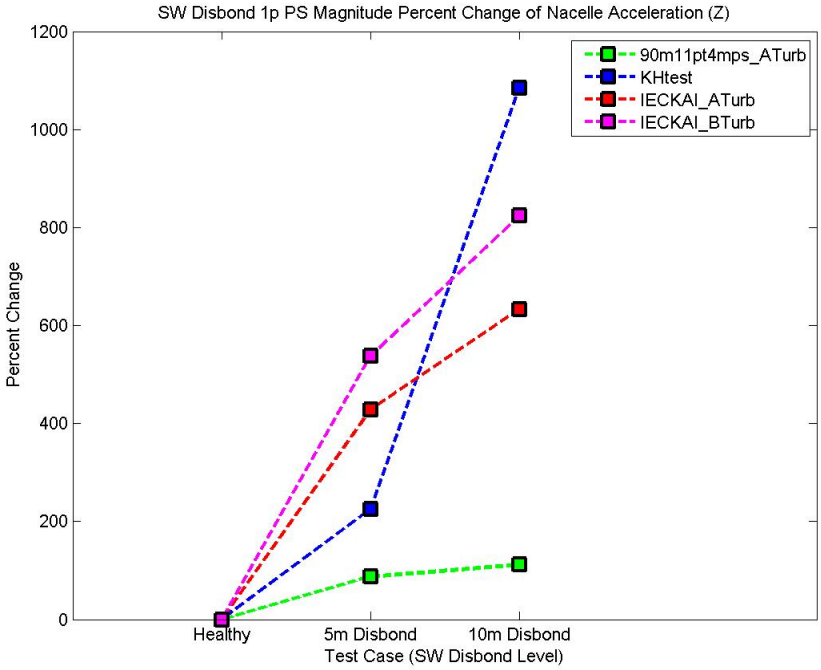

Figure 60. 1p magnitude percent change of nacelle acceleration in the z_s direction for shear web disbond

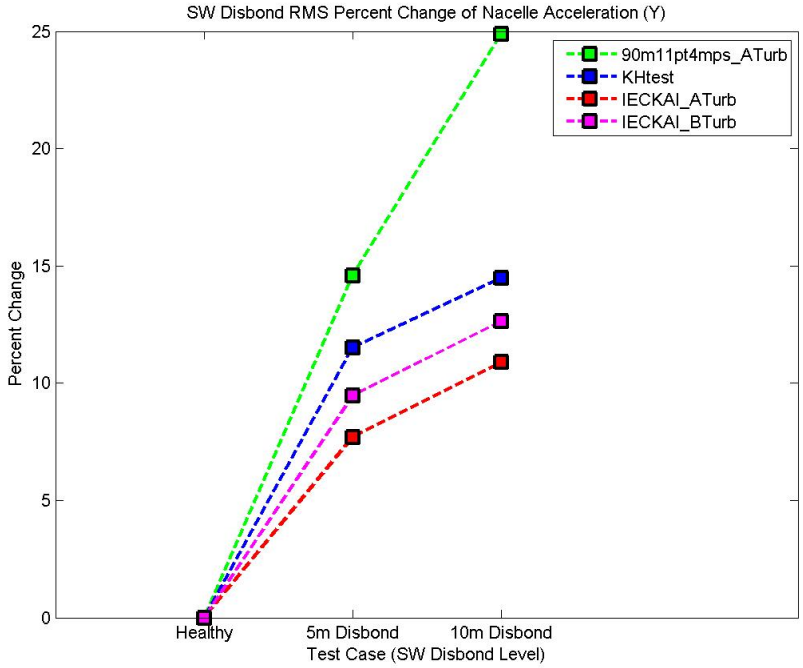

Figure 61. RMS percent change of nacelle acceleration in the y_s direction for shear web disbond

5.6. Analysis of Shear Web Disbond with Blade Sensors

Section 5.5 illustrated that some non-blade measurements are sensitive to the presence of a shear web disbond in one of the three blades, but they lacked the ability to determine which blade(s) contains the disbond. The next sections will investigate outputs from the FAST simulations that would depend on blade-mounted sensors in an operating turbine.

5.6.1. *Shear Web Disbond Analysis Results*

The following sections summarize the trends in the results for shear web disbond, as measured in blade tip acceleration responses, blade root bending moments and flap-wise acceleration response.

5.6.1.1. Blade Tip Acceleration Response

The blade tip acceleration response in all three directions showed positive trends as the shear web disbond was introduced and increased in length. The 1p edge-wise blade acceleration response differences are shown in Figure 62. These 1p response differences increased significantly with increasing shear web disbond (as much as a 25% increase for a 10 meter SW disbond). The blade tip span-wise acceleration 1p response differences (shown in Figure 63) and flap-wise acceleration RMS response differences (shown in Figure 64) also increase in the presence and increase of a shear web disbond. Note that the 1p magnitude percent change in the side-to-side nacelle acceleration was the most sensitive parameter to a shear web disbond, but the trend lines vary for the different wind profiles. On the other hand, the blade tip acceleration responses follow very similar trends for all four wind profiles.

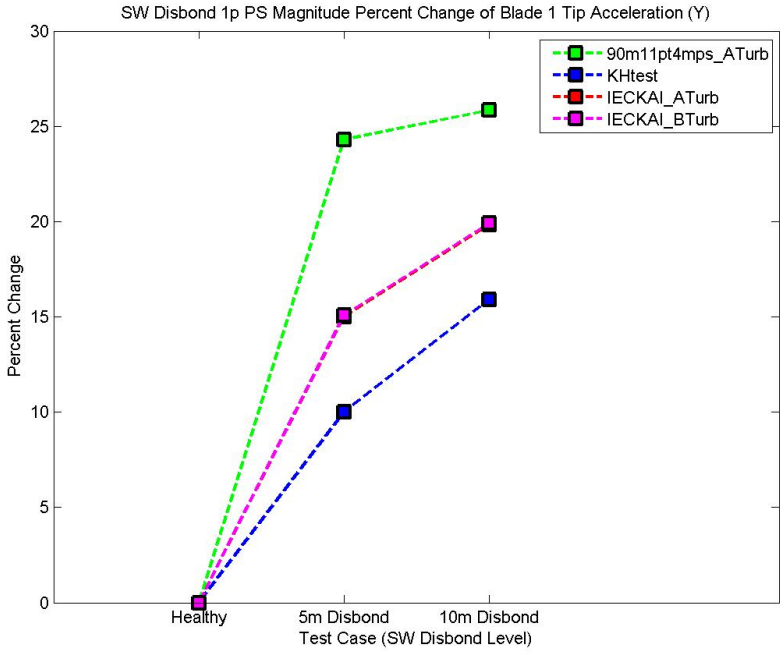

Figure 62. 1p magnitude percent change of edge-wise blade tip acceleration for shear web disbond

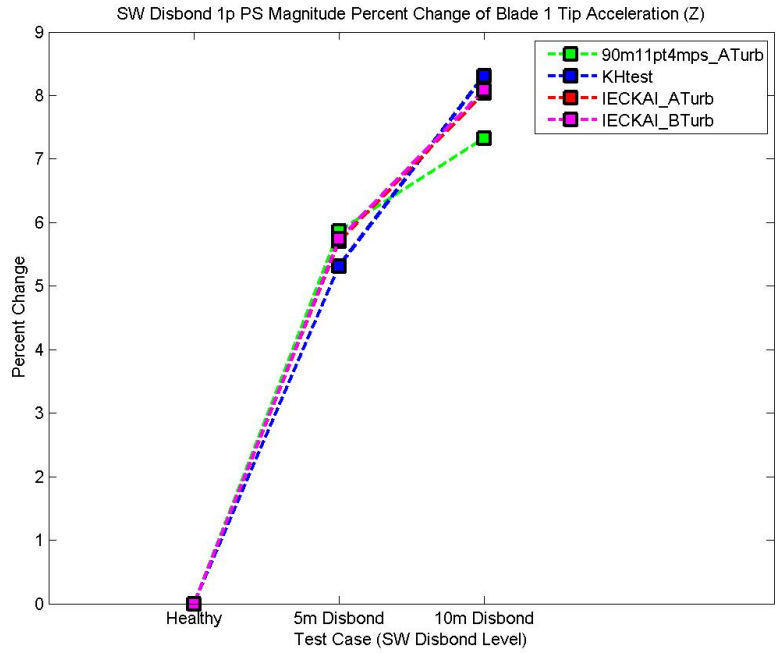

Figure 63. 1p magnitude percent change of span-wise blade tip acceleration for shear web disbond

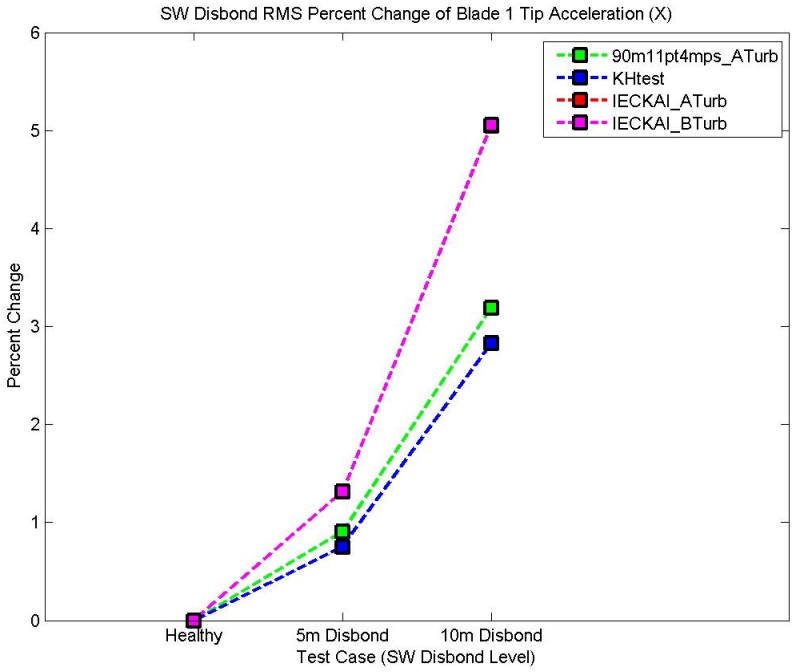

Figure 64. RMS response percent change of flap-wise blade tip acceleration for shear web disbond

5.6.1.2. Blade Root Pitching Moments

The moment of the blade about its pitch axis at the blade root is another good indicator of a shear web disbond, as shown here. This moment can be measured using strain gages located at the root of each blade and this parameter was also shown to be a good indicator of pitch error, as shown in Section 4.5.1.2. In addition, the FY11 report 1 detailed how the blade root pitching moment is also a good indicator of the presence of a trailing edge disbond. The blade root pitching moment 1p response differences (shown in Figure 65) increase while the RMS response differences (shown in Figure 66) are small and decrease with increased disbond length. The RMS response difference is very small, however the increase in the root pitching moment 1p response is expected since a shear web disbond would cause a reduction in torsional stiffness and the disbond originates at max chord, relatively close to the root of the blade. Both measurement sets also follow very similar trends for all four wind profiles as the shear web disbond is increased.

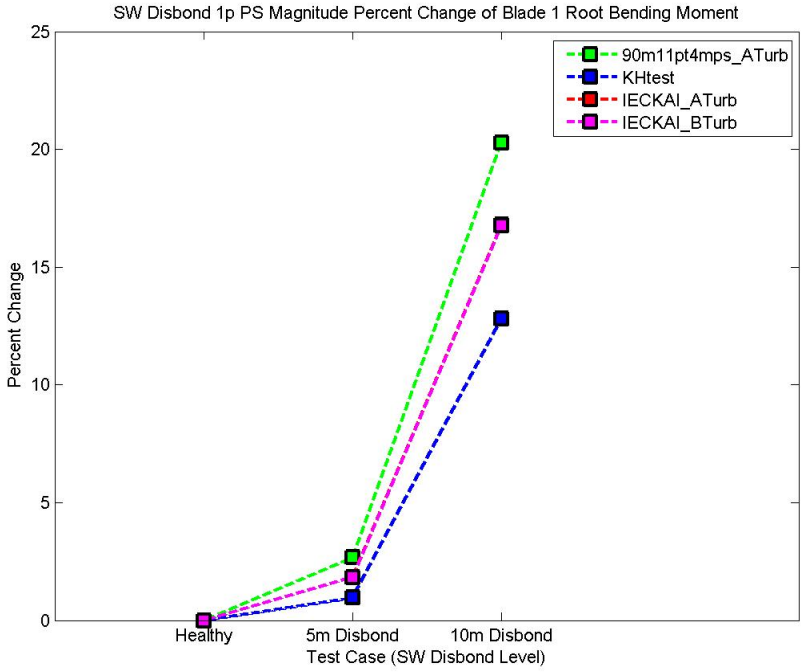

Figure 65 1p magnitude percent change of blade root pitching moment for shear web disbond

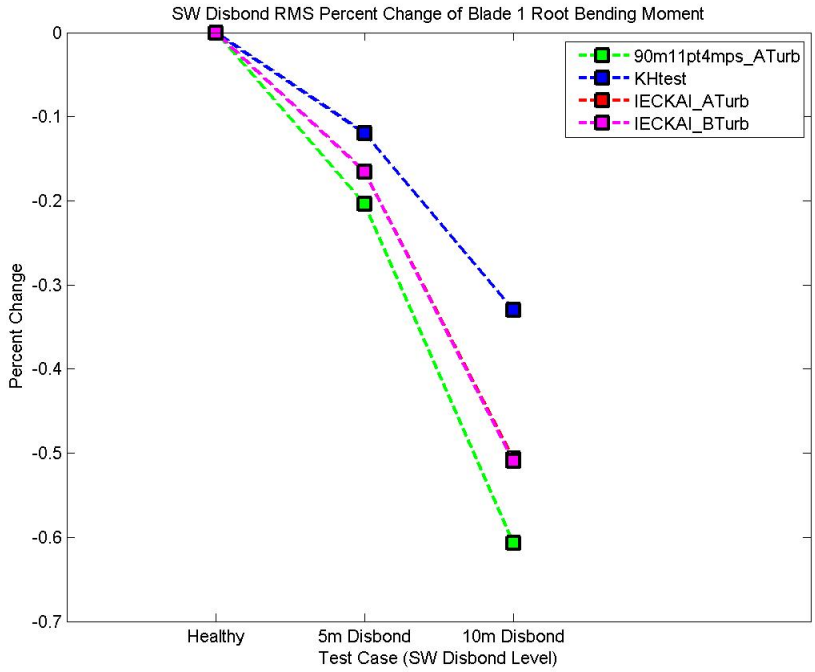

Figure 66. RMS response percent change of root blade pitching moment for shear web disbond

5.6.1.4. Blade Root Acceleration Response

The shear web disbonds produced notable differences in the blade root acceleration response in the flap-wise direction (see Figure 67). However, it is not yet clear how sensitive this parameter would be to a disbond located further down the span of the blade. Future work involving the analysis of shear web disbonds at different locations along the blade would provide better insight.

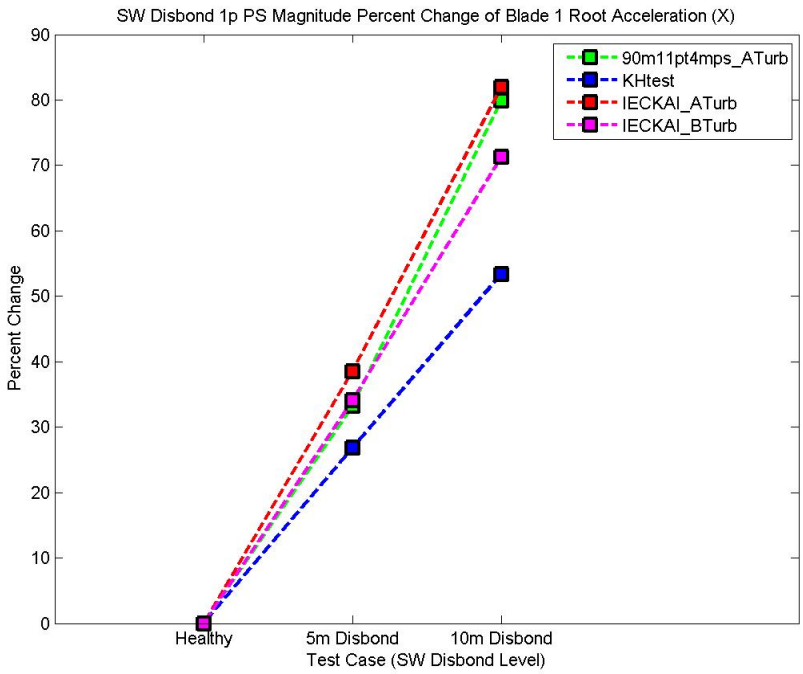

Figure 67. Blade root 1p flap-wise acceleration response differences for shear web disbond

5.7 Summary of Shear Web Disbond Detection Strategy

The results of these analyses can be synthesized into a flow chart, as shown in Figure 68, for detection of shear web disbonds using a combination of sensors and analysis methods. The proposed strategy is to:

(1) Detect if a shear web disbond exists in one of the blades

(2) Determine the severity of the shear web disbond

(3) Notify turbine operator of the disbond and severity so that a repair can be scheduled or coordinated with other maintenance

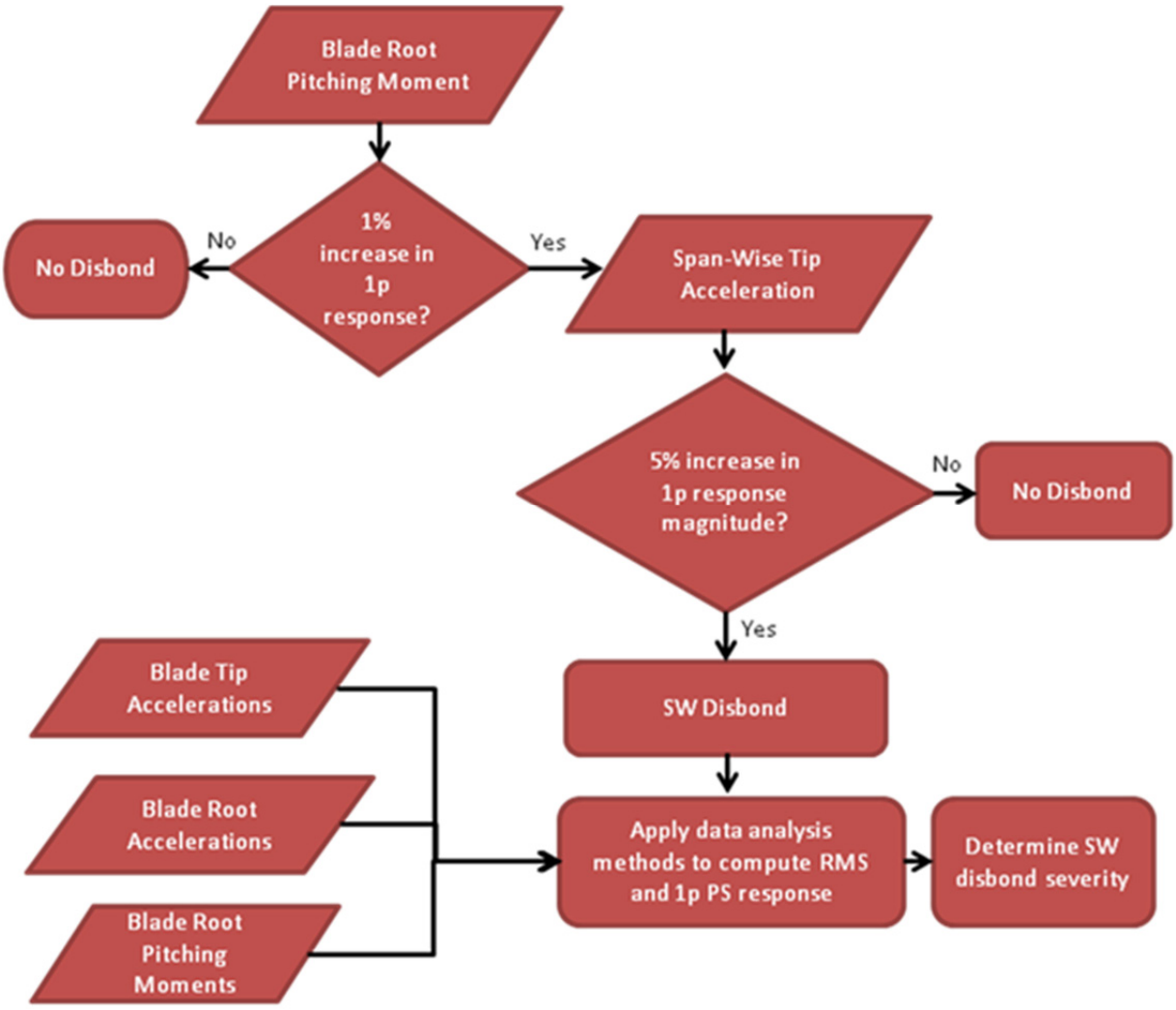

Figure 68. Shear web disbond detection flow chart

6. OPERATIONS AND MAINTENANCE COST MODEL DEVELOPMENT

This section covers the initial development of a cost model to determine the cost-benefit of the proposed blade SHPM system. Shear web disbond and mass imbalance were the defect mechanisms used to exercise the preliminary case studies for this cost model.

6.1 Literature Review

6.1.1 Wind Turbine Blade Cost Drivers

As noted earlier, determining the cost-benefit of the proposed SHM system is one of the key elements of this research. To better understand wind turbine SHPM costs, there needs to be an understanding of how the costs related to blade damage are calculated. Wind turbine researchers use the equation shown in Figure 69 to calculate the cost of energy [31].

$$COE = \frac{ICC*FCR + LRC}{AEP_{net}} + O\&M$$

COE- Cost of Energy ($/kWh)
ICC- Initial Capital Cost ($)
FCR- Fixed Charge Rate (%/yr)
LRC- Levelized Replacement Cost ($/year)
O&M- Operations and Maintenance Costs($/kWh)
AEP- Annual Energy Production (kWh/yr)

Figure 69. Cost of Energy Equation

Blade failures impact three categories of this equation: Levelized Replacement Cost (LRC), Operations and Maintenance Cost (O&M), and Annual Energy Production (AEP). Levelized replacement costs are impacted because total blade failures require a blade replacement. Operations & maintenance costs rise if blade repairs are unscheduled and require special equipment such as a crane. These costs also rise if there are more blade repairs than initially estimated. Annual energy production is decreased if the turbine is not operating due to damage in a blade or if there is a condition such as a pitch error that causes sub-optimal energy capture.

6.1.1.1 Levelized Replacement Cost

Wind turbine blades account for roughly 22% of the cost for a 5MW wind turbine [32], so the corresponding levelized replacement costs can increase significantly as blade replacements increase. The main driver of LRC is component life estimates [31]. If these estimates are lower than what is experienced in the field, then the LRC will be higher than expected.

6.1.1.2 Operations and Maintenance Cost

Operations and Maintenance costs account for 10 – 20% of the total COE for an onshore wind project; however, there is significant uncertainty in O&M Cost [31]. In fact, the difference

between low and high estimates regarding impact on COE is approximately 10%. These uncertainties are cause by factors such as:

- Lack of data relating to component reliability since manufacturers maintain records of warranty claims
- Limited information on the root cause of failure
- Difficulty obtaining useful component failure
- Many variations on the basic horizontal-axis configuration

These factors are also present in offshore operations and maintenance where O&M can constitute as much as 30% of overall project costs [32].

6.1.1.3 Annual Energy Production

When the wind turbine is being repaired (or has failed) the AEP is lowered -- unless the wind is below the cut-in speed. Increased amounts of wind turbine repairs can cause a reduction of energy production during downtime which will increase the COE.

6.1.2 Cost Models

There are a number of cost models that have been created to try to quantify and understand the cost associated with wind turbines. For ease of review, these cost models have been assigned to three categories: general, component reliability, and decision models. The general cost models evaluate costs by generalizing costs such as maintenance costs across the wind turbine/farm and do not incorporate multiple decisions. The component reliability models evaluate cost through the use of component failure rates and component repair costs. Finally, the decision models evaluate cost by incorporating the decisions to be made into the model.

6.1.2.1 General Models

One of the general cost models uses average 5 year maintenance costs to determine the cost of energy over a 20 year period [33]. The model calculates the costs of maintaining the wind farm with a repair or replace strategy that performs maximum maintenance (returns the turbines to like new condition) and/or minimal maintenance (may only replace some parts). This model was the basis of the cost model for this study. Other models emphasized varying costs by geographic region or state (i.e. Wyoming) [34], wind farm layout or by the size of wind turbines used. The Monte Carlo Markov Chain was also used in studies. This process leverages state space analysis to determine turbine states (i.e. new, deteriorated, and failed), wind speeds, and other stochastic features.

6.1.2.2 Component Reliability Models

The studies that used component reliability either used values from reviewing field experiences or from industry contacts [35]. This highlights the fact that it is difficult to obtain reliability data without information from industry. The Weibull distribution was used in one of the studies to model turbine reliability and other studies used the exponential distribution. There were more

general reliability models found than component reliability models and many of the component reliability models dealt with the gearbox.

6.1.2.3 Decision Models

The studies that employed decision-making models incorporated the possible decisions that could be made. For instance, one of the studies incorporated the weather conditions in the model to determine the feasibility of maintenance as part of the decision [36]. A few of the studies incorporated the Partially Observed Markov Decision Process (POMDP). This process can accommodate decisions where the outcome is partly probabilistic (i.e. weather conditions and turbine state) and partly deterministic (i.e. decision on whether to perform maintenance).

6.1.3 Wind Turbine Blade Reliability

Reliability is "the probability that an item will perform a required function without failure under the stated conditions for the stated period of time [37]." The mathematical definition of reliability can be found in Equation 18 where f(t) is the failure probability density function.

$$R(t) = 1 - F(t) = 1 - \int_0^t f(t)dt \tag{18}$$

Figure 70 shows a hypothetical bathtub curve. In reliability, the bathtub curve depicts the life of an average part. The beginning infant mortality failures are usually caused by manufacturing defects and many are caught in house by quality control methods. This first portion usually has a decreasing failure rate as manufacturers resolve the quality or material issues. The second portion is called the normal or useful life. This is the longest portion of a product's life and it has a constant failure rate. The end of life wear rate is an increasing rate and occurs when a product is at the end of its useful life. The Weibull distribution can characterize all three portions of the bathtub curve.

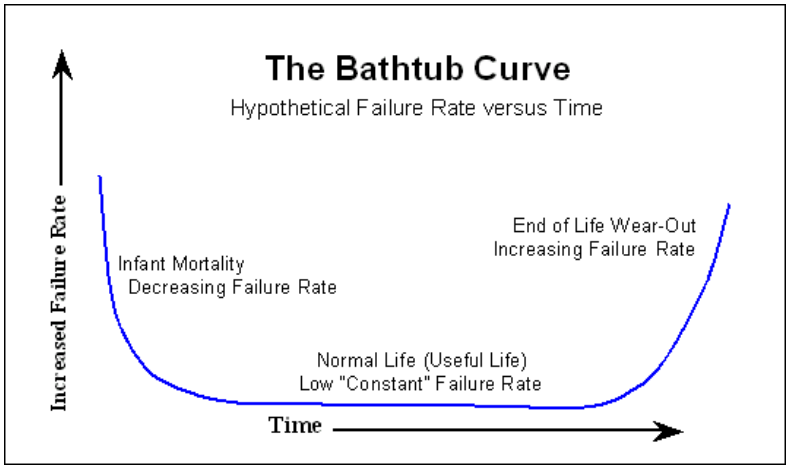

Figure 70. Bathtub Curve

The Weibull distribution is shown in Equation 19. A special case of the Weibull distribution where β equals 1, the exponential distribution, can characterize the useful life. The exponential distribution is shown in Equation 20.

$$f(t) = \lambda^{\beta}\beta t^{\beta-1}e^{-(\lambda t)^{\beta}} \quad (19)$$

$$f(t) = \lambda e^{-\lambda t} \quad (20)$$

For wind turbines, European studies indicate that electrical systems, blades/pitch, control system, hydraulics, and have the most number of failures [38]. In the United States, the top failures are reported as rotor/blades, electric generator, controls, yaw, and gearbox [39]. Blade failures are a concern since they are expensive and more time consuming than some other component repairs. The percentage of blade failures varies by manufacturer and location; however, blade failures are notable and shear web disbond and mass imbalance are two causes of blade failure.

6.2 SHPM Cost Model Description and Assumptions

The cost model used for this study is a state-space Matlab model that calculates O&M costs ($/MWh) of a wind turbine with and without a blade condition monitoring system for a period of 20 years. This preliminary cost model was developed to determine when and under what conditions a particular structural health monitoring system option will be economically viable. Figure 71 below shows the cost model flow chart and the following sections describe the inputs and outputs of each major portion of the cost model.

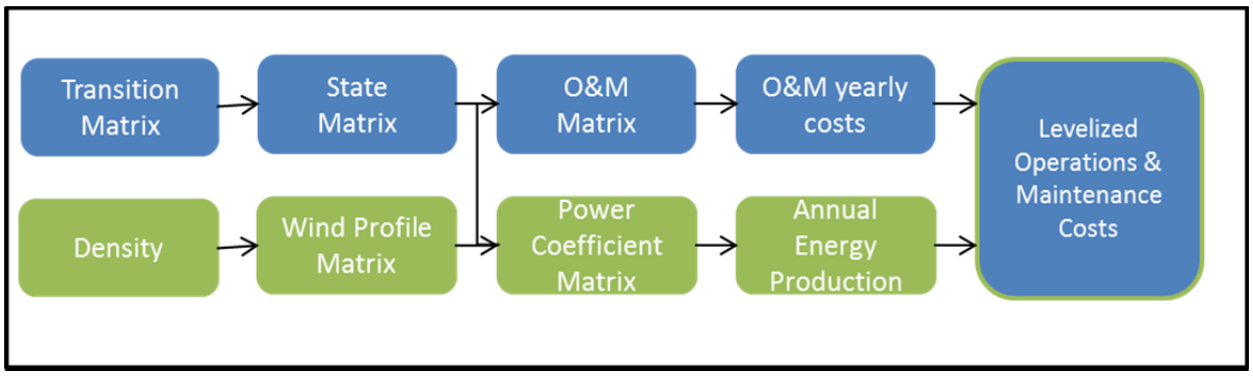

Figure 71. Cost Model Flowchart

6.2.1 Transition Matrix

The transition matrix is comprised of the probabilities (a_{ij}) shown in Figure 72 that dictate the probability of going from state i to state j, where state in this case refers to a state of health. A conceptual representation of the defect size versus the cost of repair for each of the four states of health used in this model is shown in Figure 73. State 1 is defined as small defects that do not need to be repaired, state 2 are moderate defects which can be repaired up-tower, state 3 are large defects which require blade removal, and state 4 are very large defects that require blade removal

and replacement. The model moves from state to state based upon a random number (from 0 to 1) and the resulting states are for each step of one hour.

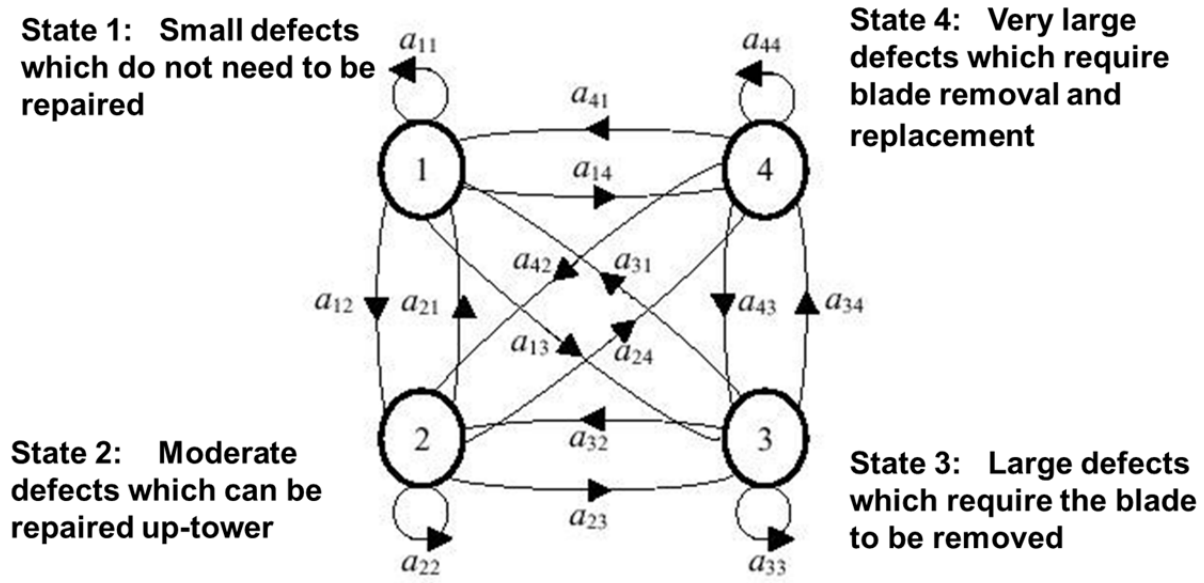

Figure 72. Markov Chain with Transition Matrix elements

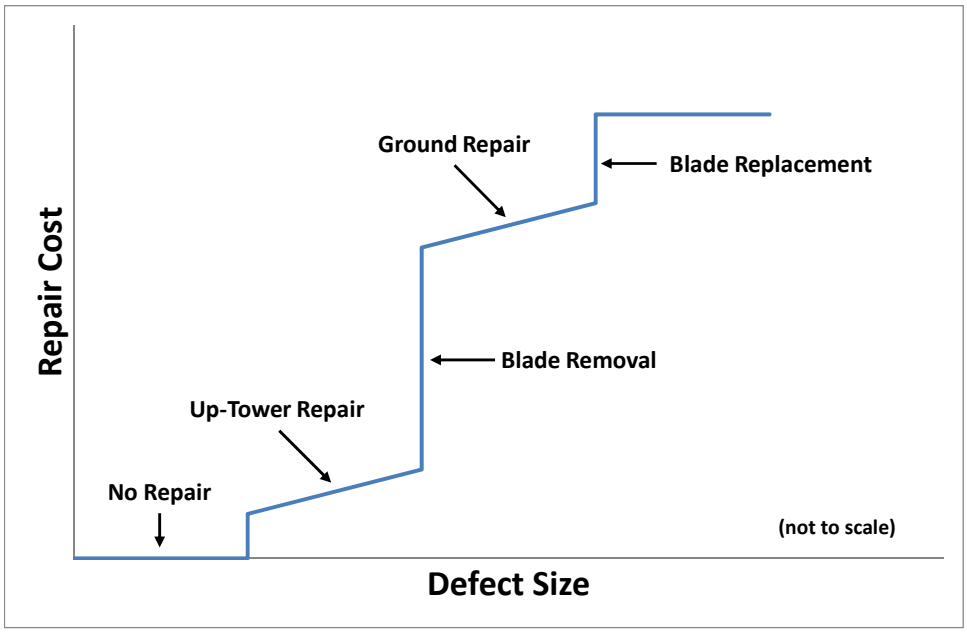

Figure 73. Example defect-cost model demonstrating the piecewise nature of defect size versus repair cost.

Figure 74 shows the transition matrix for the baseline SHM case. As seen below, there is a 0.88 probability that a blade at state 1 will remain in state 1 (a_{11}). There is a 0.175 probability that a blade at state 2 will remain in state 2 (a_{22}). A zero probability is inputted to prevent the blade from returning to a lower state without being repaired as seen by a_{32}. If a blade is currently at

state 3, there is a 0.135 probability of it remaining in state 3, a 0.015 probability of it degrading further to state 4, and a 0.85 probability that it will be detected and fixed (returning it to state 1). The zero does not allow the turbine to spontaneously fix itself by going back to state 2 since one of the model assumptions is the turbine will be repaired once detected. Therefore, column 1 contains all of the probabilities of detection (a_{11}-State 1, a_{21}- State 2, a_{31}- State 3, a_{41}- State 4)

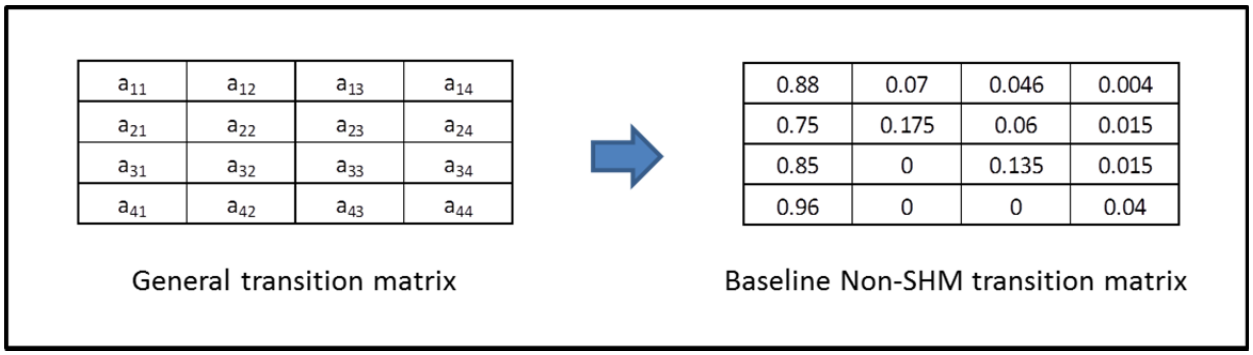

Figure 74. Baseline SHM transition matrix

6.2.2 State Matrix

The inputs for the state matrix are the random number for that time interval and the transition matrix. The output is a matrix that shows the state of the turbine for each hour during a twenty year period. This matrix consisting of the previously described four states is used later to generate both the O&M and power coefficient matrices.

6.2.3 Operations & Maintenance Matrix

The inputs for the O&M matrix are the state matrix and a matrix that indicates the cost to return the blade from state 2 and higher to state 1. At state 1 the matrix has a value of 0 since no repairs are done at state 1. Table 3 shows the O&M matrix values that were used for the baseline case (both SHM and Non-SHM).

Table 3. O&M values for Baseline case

State	O&M
1	0
2	30
3	72.5
4	100

6.2.4 Wind Profile Matrix

The wind profile matrix was created with a random Weibull distribution with k=2 and c=11.4. The graph in Figure 75 shows the probability distribution function using the parameters from this study (average wind speed of 11.4 m/s). The values of the wind profile matrix are altered for the wind turbine used in this study. The wind speed is changed to zero for values below the cut-in

speed and above the cut-out speed. Also, the speed is changed to the rated speed for all values between the rated speed and the cut-out speed.

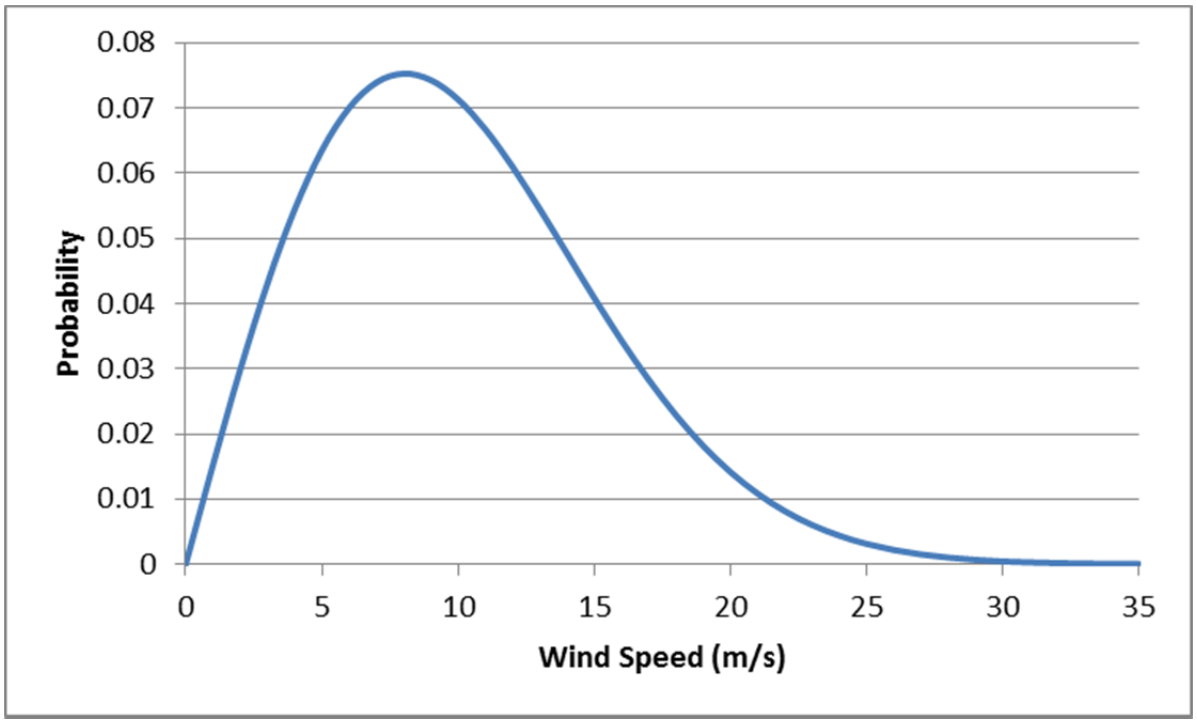

Figure 75. Wind speed versus Probability

6.2.5 Power Coefficient Matrix

Similar to the O&M matrix, the power coefficient matrix inputs the state matrix and a matrix that indicates the power coefficients at each state. The output is a power coefficient matrix. Table 4 shows the power coefficient matrix values for the baseline case.

Table 4. Power coefficient matrix for baseline case

State	Power Coefficient
1	0.45
2	0.4
3	0.36
4	0

6.2.6 AEP – Annual Energy Production

The inputs for the annual energy production are the power coefficient matrix and the air density calculated using equation 21 where p is the pressure at the hub height, M is the molar mass of dry air, R is the ideal gas constant, and T is temperature at the hub height. Equation 22 shows the calculation for the hourly energy production. As seen in equation 22, the power is calculated using the density (ρ), wind speed (V), and power coefficient (C_p) for each hour.

$$\rho = \frac{pM}{RT} \tag{21}$$

$$P_T = \frac{1}{2}\rho A V^3 C_p \tag{22}$$

6.2.7 Levelized Operations & Maintenance Cost

Both the O&M matrix and the Power Coefficient matrix are summed to obtain the yearly O&M costs and annual energy production. The O&M yearly costs are divided by the AEP to obtain the O&M Costs in $/MWh/yr. These values are calculated for the blades with and without the structural health monitoring (SHM). The resulting cost savings comes from subtracting the SHM costs from the Non-SHM costs to determine the savings of having the system.

6.2.8 Cost Model Assumptions

There were several assumptions for this model which are listed below. First, the blade is repaired when the defect is detected which means that the probability of detection is also the repair rate. For simplicity, pitch error and shear web disbond are considered equally likely in these initial calculations to exercise the model. As stated earlier, the wind was modeled as a Weibull distribution since it has been accepted as a good wind profile in the literature. Although a state space system is used, each increment is assumed to be one hour. In addition, the probabilities (rate of degradation) remains constant throughout the simulation since a transition matrix is used. This assumption is reasonable since many products have a constant useful life as seen in Figure 65. The average time for a repair is assumed to be one hour which corresponds well to Sandia's CREW estimate of one hour and fifteen minutes [39]. There are four states assumed as described in section 6.2.1.

6.3 Cost Model Simulation Methods

6.3.1 Cost Model Input Values

A summary table of the cost model input values is shown below in Table 5. The first category is noted as reliability and it is the probability that a turbine currently in state 1 will remain in state 1. A more reliable wind turbine will have a higher state 1 probability, while a less reliable wind turbine will have a lower state 1 probability. The O&M costs have been scaled with a total failure (State 4) noted at a value of 100 (100%) and can be refined later using actual costs. The power coefficient values are the power coefficient responding with each state. The power coefficient is at its maximum for state 1 and 0 for state 4 since no power will be generated if the rotor must be parked due to a failure. The probability of detection is also the repair rate since one of the assumptions is to repair the blade when the defect is found. This means that a higher probability of detection (repair rate) may have more repairs. All of these assumptions will be revisited as the model is matured and also due to changing conditions for different site location characteristics, different turbine characteristics, and variation in maintenance strategies.

Table 5. Cost Model Input Values Table

	State 1	State 2	State 3	State 4
Reliability	.75-L, .88-B, .9-H	NA	NA	NA
Operations & Maintenance Costs	0	10-L, 30-B, 50-H	50-L, 72.5-B, 95-H	100
Power Coefficient	0.45	.35-L, .4-B, .44-H	.29-L, .36-B, .43-H	0
Probability of Detection (Non CM)	NA	0.75	0.85	0.95
Probability of Detection (CM)	NA	.8-L, .95-B, .98-H	.88-L, .98-B, .99-H	.9-L, .99-B, 1-H

L="Low", B="Baseline", H="High"

6.3.1 Cost Model Sample

In this section, a sample set of conditions is used to demonstrate how the model calculates the yearly levelized O&M costs for the baseline case. Table 6 shows a sample set of random numbers generated for the first five hours of a year. The first hour of each year defaults to state 1; therefore, a random number is not needed for the first hour.

Table 6. Random numbers for sample set

Hour	Random Number
1	NA
2	0.913
3	0.885
4	0.617
5	0.980

Both the Non-SHM and SHM cumulative assumed transition matrices are shown below in Table 7.

Table 7. Cumulative Transition Matrices

Non-SHM Cumulative Matrix

0.88	0.95	0.996	1
0.75	0.925	0.985	1
0.85	0.85	0.985	1
0.96	0.96	0.96	1

SHM Cumulative Matrix

0.88	0.95	0.996	1
0.95	0.985	0.997	1
0.98	0.98	0.998	1
0.99	0.99	0.99	1

Table 8 shows the resulting states for the first 5 hours of the sample case. Note that the SHM system detects the defect during hour 2.

Table 8. State matrices for sample set

Hour	Non-SHM State	SHM State
1	1	1
2	2	2
3	2	1
4	1	1
5	3	3

The state matrix is used to create a power coefficient matrix. As seen in Table 9 below, all of the state 1 values are changed to .45, all of the state 2 values are changed to .4 and all of the state 3 values are changed to .36.

Table 9. Power Coefficient matrices for sample set

Hour	Non-SHM State	Non-SHM Power Coeff
1	1	0.45
2	2	0.4
3	2	0.4
4	1	0.45
5	3	0.36

Hour	SHM State	SHM Power Coeff
1	1	0.45
2	2	0.4
3	1	0.45
4	1	0.45
5	3	0.36

This power coefficient matrix is combined with the random Weibull wind profile to determine the hourly energy production for each hour of the year. As noted earlier in section 6.2.3, the state matrix is also used to create an O&M cost matrix that is dependent upon the level or repair. In the sample set, there was one repair from state 2 to state 1. This corresponds to a value of 30 in the O&M costs matrix. The other values are 0 since there is no cost incurred unless there is a repair. The yearly O&M costs are then divided by the AEP to obtain the LRC.

6.4 Cost Model Simulation Results

6.4.1 Results as percent cost savings

As seen in Table 3, the input parameters such as O&M costs and performance coefficients were varied between baseline, low, and high values. The results from this cost sensitivity analysis can be seen in Figures 76-78 for the baseline, low, and high reliability cases. The results have been changed to percent change to facilitate comparison. The percent savings is calculated by subtracting the ratio of the SHM output divided by the Non-SHM output from 1. Figure 76 is the cost savings analysis for the baseline reliability case and the baseline percent savings is 2.68% per year for each turbine. Section 6.4.2 shows how this percentage can be used to obtain an

annual cost savings estimate for each turbine using cost averages published by the National Renewable Energy Laboratory (NREL).

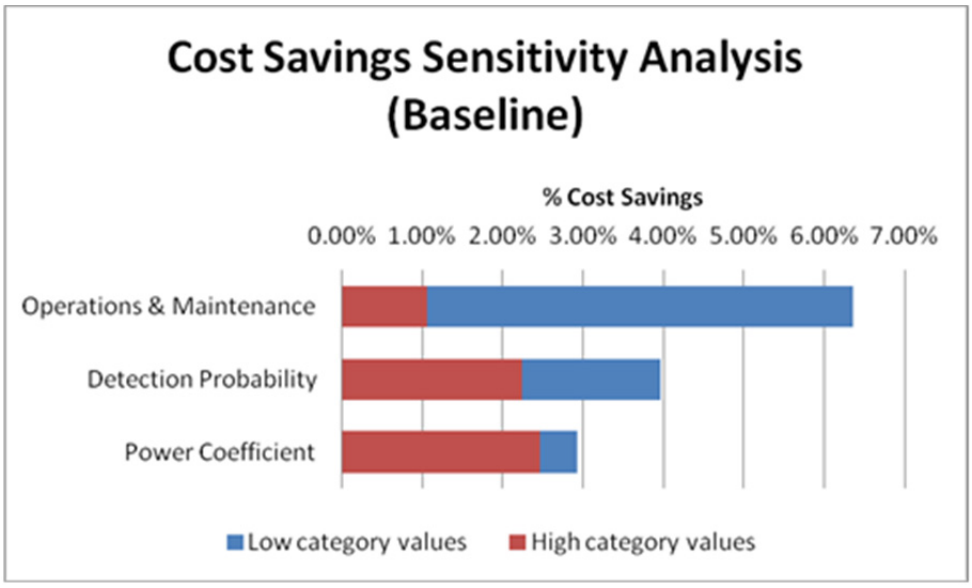

Figure 76 Cost Savings Sensitivity Analysis Results- Baseline Case

Figure 77 is the cost savings analysis for the baseline reliability case and the baseline percent savings is 3.42% per year for each turbine.

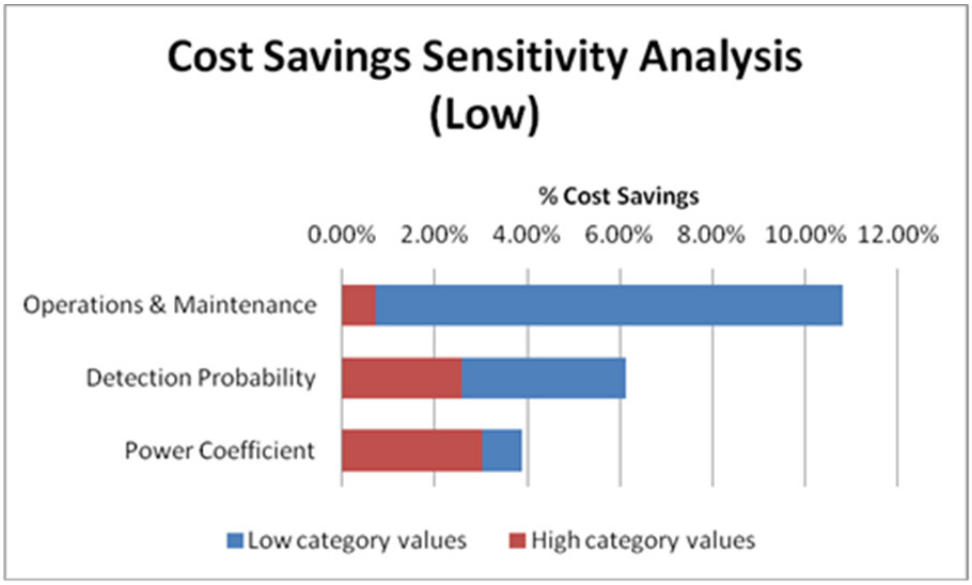

Figure 77. Cost Savings Sensitivity Analysis Results- Low Reliability Case

Figure 78 is the cost savings analysis for the baseline reliability case and the baseline percent savings is 4.19% per year for each turbine.

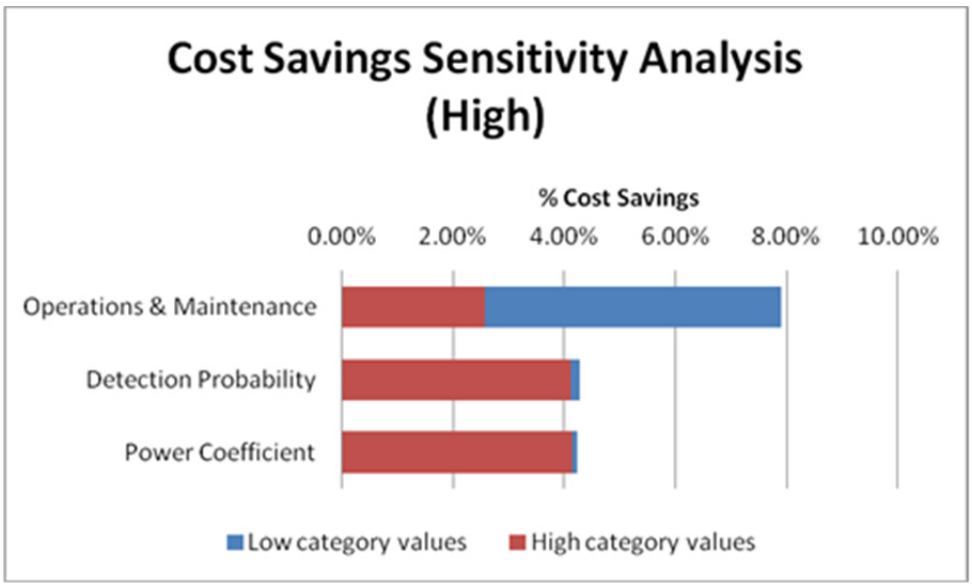

Figure 78. Cost Savings Sensitivity Analysis Results- High Reliability Case

All of the cost savings sensitivity analyses had the same trend of increasing cost savings for lower O&M costs, lower detection probabilities (repair rates), and lower power coefficient values.

6.4.2 Results using NREL values

The 2010 Cost of Wind Energy Review was used to determine estimates of cost savings for the baseline reliability case [40]. Only the LRC and O&M costs are considered for the model since they are the only parameters in the cost of energy equation that are affected by the SHM system. Table 10 shows all of the values used to determine the yearly LRC and O&M costs for the blades of a 5MW offshore wind turbine. The LRC & O&M costs for the blades was determined to be 7% of the total from the 2011 Sandia CREW benchmark results showing 7% unavailability due to blade failures [38].

Table 10. NREL values for estimate

NREL 2010 Cost of Wind Energy	Values
Offshore Levelized replacement cost	$40/kW/yr
Offshore Labor, equipment, facilities (O&M)	$46/kW/yr
Yearly LRC & O&M for 5 MW	$ 430,000
7% of Yearly LRC & O&M for 5 MW	$ 30,100

The yearly cost of $30,100 is then taken to be the cost for the Non-SHM system. With a percent savings of 2.68%, the SHM system will yield an $807/yr per turbine cost benefit over the Non-SHM system.

6.5 Summary of CM System Cost Benefit

This section contains the preliminary analysis summary using the cost benefit model. The current model produced a good initial analysis of the cost benefits for the SHPM system, showed cost trends, and highlighted parameters that should be further investigated. All of the cases used in this study resulted in a cost savings with the SHPM system. With more accurate operations and maintenance costs from the field, the model can be refined to yield better cost savings estimates. The trends that were observed with the sensitivity analysis were O&M COE was most sensitive to the O&M repair and replacement costs followed by the level of detection (point at which the blade is repaired). The O&M COE was the least sensitive to changes in the performance coefficient. All of these results show a greater cost savings at the lower values of these parameters. These sensitivity analysis results show that obtaining field data is very important since the initial results show a strong sensitivity of the resulting cost savings to the repair costs. Including the actual time to repair can further refine the cost model since averages have been used. Further development of the cost model can be accomplished by incorporating factors such as seasonal affects and multiple decisions. Seasonality can affect the cost savings since offshore wind farms have periods when performing maintenance can be difficult or impossible. Decisions such as derating the turbine can extend the life of the blade and reduce the occurrence of unscheduled maintenance. In addition, deciding to wait to perform maintenance can also produce an additional cost savings. This initial cost model has provided insight about the potential cost savings of the proposed SHM system and further work will be done to improve the model.

7. CONCLUSIONS

A multi-scale simulation of damage methodology has been expanded for the investigation and development of SHPM methods for offshore wind turbine blades. Two cases studies were performed to further demonstrate the methodology in analyzing the sensitivity of blade damage in the operating response of the rotor. The method utilizes the propagation of damage from a high fidelity component level model up to a reduced order model of a full turbine so that the changes in the turbine's operational responses due to the damage can be examined. Furthermore, these full turbine simulations can be used to replicate fault mechanisms such as pitch error and estimate the loads on the turbine blades which can then be propagated back to the high fidelity model to allow for further local analyses to be conducted. By investigating the effects of damage on multiple scales, the developed methodology takes advantage of available software to investigate the underlying physical consequences of damage/faults on both a local and global level which leads to the identification of operational responses that are most sensitive to these physical changes.

This document has described the application of the developed methodology to investigate the effects of rotor imbalance and a shear web disbond on an offshore 5-MW wind turbine. The 61.5 meter blade model was developed in SNL's NuMAD software and exported to ANSYS where the shear web disbond was simulated by separating the nodes of the shear web from the blade at the location of the disbond. The reduced order blade models with varying levels of damage were included into a model of an offshore turbine on a fixed monopole in 20 meters of water. The response of these offshore turbine models with varying levels of damage/imbalance was then simulated in FAST. From these simulations it was apparent that the measurements which were the most sensitive to the present and extent of the shear web disbond or pitch error were the blade tip accelerations and the root pitching moments. The aerodynamic loads from the FAST simulations were calculated and applied to the high fidelity ANSYS model which also demonstrated an increased blade tip deflection and increased localized strains due to the presence of a shear web disbond.

To examine how the structural health of each turbine could be used to optimize the operation and maintenance practices of an offshore wind plant, an initial cost model was developed and used to investigate the operations and maintenance costs due to the fault/damage. The combination of the repair cost information and the structural health of each turbine could be utilized in the optimization of damage mitigating control strategies and maintenance schedule to reduce the operations and maintenance costs associated with running an offshore wind energy plant.

8. FUTURE WORK

In FY13, the presently reported work of FY12 documented in this report will be expanded including further integration of the sensitivity of damage study with the cost analysis. A cost benefit analysis of SHPM systems including an assessment of uncertainty of the SHPM system to important sources of variability (including inflow and sensor options). The expanded cost model will use a larger set of representative parameters so that the SHPM cost benefit figures are more realistic. Laboratory experiments to validate the detection strategies outlined in the report will be pursued.

9. REFERENCES

[1] A.C. Levitt, W. Kempton, A.P. Smith, W. Musial and J. Firestone, "Pricing offshore wind power." *Energy Policy* (In Press) 2011.

[2] W. Musial and B. Ram, *Large-Scale Offshore Wind Energy for the United State: Assessment of Opportunities and Barriers*, NREL Report No. TP-500-49229, Golden, CO, September 2010.

[3] U.S. Department of Energy, *A National Offshore Wind Strategy: Creating an Offshore Wind Energy Industry in the United States,* Washington: Wind & Hydropower Technologies Program Report No. 5040, February 2011.

[4] R. Wiser and M. Bolinger, *2010 Wind Technologies Market Report*, Lawrence Berkeley National Laboratory: Lawrence Berkeley National Laboratory. LBNL Paper LBNL 4820E, June 2011.

[5] B. Snyder and M.J. Kaiser, "Ecological and economic cost-benefit analysis of offshore wind energy." *Renewable Energy* 34(6), pp. 1567-1578, 2009.

[6] G. van Bussel, A.R. Henderson, C.A. Morgan, B. Smith, R. Barthelmie, K. Argyriadis, A. Arena, G. Niklasson, and E. Peltola, "State of the Art and Technology Trends for Offshore Wind Energy: Operation and Maintenance Issues," *Offshore Wind Energy EWEA Special Topic Conference*, Brussels, Belgium, December 2001.

[7] L.W.M.M. Rademakers, H. Braam, M.B. Zaaiger, and G.J.W. van Bussel, "Assessment and optimisation of operation and maintenance of offshore wind turbines," in *Proceedings of the European Wind Energy Conference*, Madrid, Span, June 2003.

[8] Y. Amirat, M.E.H Benbouzid, B. Bensaker, and R. Wamkeue, "Condition monitoring and fault diagnosis in wind energy conversion systems: a review." In *Proceedings 2007 IEEE International Electric Machines and Drives Conference*, Vol 2., pp. 1434-1439, 2007.

[9] J. Nilsson and L. Bertling, "Maintenance management of wind power systems using condition monitoring systems – Life cycle cost analaysis for two case studies," *IEEE Transactions on Energy Conversion* 22(1), pp. 223-229, 2007.

[10] C.C. Ciang, J.R. Lee, and H.J. Bang, "Structural health monitoring for a wind turbine system: a review of damage detection methods." *Measurement Science and Technology* 19(12), pp. 1-20, 2008.

[11] F. Besnard, K. Fischer, and L. Bertling, "Reliability-centred asset maintenance – A step towards enhanced reliability availability and profitability of wind power plants" in *2010 IEEE PES Innovative Smart Grid Technologies Conference Europe (ISGT Europe)*, 2010.

[12] Z. Hameed, S.H. Ahn, and Y.M. Cho, "Practical aspects of a condition monitoring system for a wind turbine with emphasis on its design, system architecture, testing and installation," *Renewable Energy*, 35(5), pp. 879-894, May 2010.

[13] NWTC Design Codes (FAST by Jason Jonkman, Ph.D.). http://wind.nrel.gov/designcodes/simulators/fast/. Last modified 05-November-2010; accessed 05-November-2010.

[14] R.R. Ryan, ADAMS – Multibody System Analysis Software, Multibody Systems Handbook. Berlin: Springer-Verlag, 1990.

[15] J. Jonkman, S. Butterfield, W. Musial, and G. Scott, "Definition of a 5-MW Reference Wind Turbine for Offshore System Development," NREL/TP-500-38060, Golden, CO: National Renewable Energy Laboratory, February 2009.
[16] D.T. Griffith, N. Yoder, B. Resor, J. White, and J. Paquette, "Structural Health and Prognostics Management for Offshore Wind Turbines: An Initial Roadmap," Sandia National Laboratories Technical Report, SAND2012-10109, Sandia National Laboratories; Albuquerque, NM, Printed December 2012.
[17] J. Jonkman and L. Buhl, "FAST User's Guide," NREL/EL-500-38230, Golden, CO: National Renewable Energy Laboratory, August 2005.
[18] J. Losi, and E. Becker, "Imbalance: A danger to components," Erneuerbare Energien, August 2009.
[19] J. Giebhardt and WP7 Partners, "Condition Monitoring for Wind Turbines 'State of the Art' Report," Kassel, Germany: European Commission, 2007.
[20] J. Niebsch, R. Ramlau, and T. Nguyen, "Mass and Aerodynamic Imbalance Estimates of Wind Turbines," Energies, 2010: 696-710.
[21] M. Adams, Jr., Rotating Machinery Vibration. New York, NY: Marcel Dekker, 2001.
[22] J.P. Borg R.H. Kirchoff, "The Effects of Static and Dynamic Imbalance on a Horizontal Axis Wind Turbine," Journal of Solar Energy Engineering (ASME) 119 (1997): 261-262.
[23] B. Petersen, et al., "Evaluate the Effect of Turbine Period of Vibration Requirements on Structural Design Parameters: Technical Report of Findings," Technical Report, Groton, CT: Applied Physical Sciences, 2010.
[24] M. MaCamhaoil, "Bruel & Kjaer Application Notes: Static and Dynamic Balancing of Rigid Rotors," n.d. http://www.bksv.com/doc/bo0276.pdf (accessed March 2012).
[25] P. Caselitz and J. Giebhardt, "Rotor Condition Monitoring for Improved Operational Safety of Offshore Wind Energy Converters," ASME Journal of Solar Energy Engineering (ASME Journal of Solar Energy Engineering), 2005: Vol. 127 (261).
[26] IRD Balancing, Balance Quality Requirements of Rigid Rotors - The Practical Application of ISO 1940/1, Louisville, KY: IRD Balancing, 2009.
[27] Moog Incorporated, Rotor Monitoring Systems, June 2011. http://www.moog.com/literature/ICD/Moog-Wind-Rotor-Monitoring-System-Overview-en.pdf (accessed March 13, 2012).
[28] J.P. Borg and R.H. Kirchoff, "Mass and Aerodynamic Imbalance of a Horizontal Axis Wind Turbine," Journal of Solar Energy Engineering 120 (Feburary 1998): 66-74.
[29] IEC 61400-1, "Wind turbine generator systems-Part 1: Safety requirements," 2nd edition, Geneva, Switzerland: International Electrotechnical Commission, 1999.
[30] B.J. Jonkman and L. Kilcher, "TurbSim User's Guide: Version 1.06.00," NREL/TP-xxx-xxxx (Draft Version), Golden, CO: National Renewable Energy Laboratory, September 2012.
[31] C. A. Walford, Wind turbine reliability: understanding and minimizing wind turbine operation and maintenance costs: United States. Department of Energy, 2006.
[32] M. I. Blanco, "The economics of wind energy," Renewable and Sustainable Energy Reviews, vol. 13, pp. 1372-1382, 2009.
[33] K. Fernandes and K. Marais, "Value of Energy Model," ed, 2012.

[34] A. Olson, M. Chait, and A. Pacheco, "Wind Costing Model," State of Wyoming Revenue Committee of the State Legislature, http://legisweb.state.wy.us/2010/WyomingWindModel_7_01_2010.pdf2010.
[35] Vachon, W. (2002). “Long-Term O&M Costs of Wind Turbines Based on Failure Rates and Repair Costs.” Presented at Windpower 2002, American Wind Energy Association, Annual Conference, June 2-5.
[36] E. Byon and Y. Ding, "Season-dependent condition-based maintenance for a wind turbine using a partially observed Markov decision process," Power Systems, IEEE Transactions on, vol. 25, pp. 1823-1834, 2010.
[37] P. O'Connor and A. Kleyner, Practical reliability engineering: Wiley, 2011.
[38] J. Ribrant, "Reliability performance and maintenance, a survey of failures in wind power systems," Unpublished doctoral dissertation, XR-EE-EEK, 2006.
[39] V. Peters, B. McKenney, A. Ogilvie, and C. Bond, "Continuous Reliability Enhancement for Wind (CREW) Database," Sandia National Laboratories, 2011.
[40] S. Tegen, M. Hand, B. Maples, E. Lantz, P. Schwabe, and A. Smith, "2010 Cost of Wind Energy Review," National Renewable Energy Laboratory2012.
[41] Y. Nam, T. Yoon, K. Kim, and H. Cuong, 41. “Estimation of a Nacelle Dynamic Motion of a Wind Turbine,” *Control, Automation, Robotics and Vision, 2008, ICARCV 2008. 10th International Conference on* , pp. 1017-1020, 2008.

CHAPTER 5. ANALYSIS OF LOCAL DAMAGE EFFECTS AND IMPROVEMENT IN DAMAGE MODELING – FY13

In the earlier chapters, the simulation work focused on damage detection, which within the multi-scale simulation of damage framework is referred to as "global sensitivity" of damage. In this chapter, another element of the multi-scale modeling of damage method (local sensitivity of damage) is considered. Here, the impacts of damage on state of health are addressed. This analysis provides important information for decision making including to ensure operation in a safe manner or to better operate a damaged machine to maximize revenue generation. See Chapter 7 for a discussion of progressive damage analysis and illustration of operations decisions for local damage effects mitigation.

The highlights of this chapter[3] include:

- Improvement in blade damage modeling for disbonds using contact elements
- Improvement in blade damage modeling and analysis by progressing from linear to nonlinear analysis methods
- Buckling analysis of blades with trailing edge and shear web disbonds to demonstrate local sensitivity of damage effects and to quantify remaining life by determining critical values for disbond length
- A new approach to extracting beam properties for damaged blade models by applying nonlinear methods within the SNL/BPE (Beam Property Extraction) software.

[3] Excerpts from Contractor Report: "Integration of Nonlinear Finite Element Analysis of Disbonds of Wind Turbine Blades Into the NUMAD Analysis System," Prepared for Sandia National Laboratories (Technical Monitor, D. T. Griffith) by ATA Engineering, Inc. (Rory R. Davis, Project Manager and Senior Technical Advisor)

Integration of Nonlinear Finite Element Analysis of Disbonds of Wind Turbine Blades into the Sandia/NuMAD Blade Modeling and Analysis System

ABSTRACT

This chapter documents analysis work of

(1) adding automated nonlinear disbond finite element analysis capability to Sandia's NUMAD wind turbine blade analysis system,
(2) comparing linear vs. nonlinear analysis results for loaded blades with and without disbonds, and
(3) investigating the sensitivity of disbond location and size on analysis results with disbonds.

Analysis results of interest included predicted blade buckling load capacity, shapes, and tip deflections; equivalent blade beam section properties as would be used in whole machine simulations; blade natural frequencies; and local blade stresses and strains. The analysis was done with one sample blade NUMAD model provided by Sandia representing the turbine blade of a 5 MW HAWT machine, 61.5 m long with maximum chord of 4.6 m. Automated capability was developed and exercised for both trailing-edge blade skin disbonds and spar web to blade skin disbonds (i.e shear web disbonds).

LIST OF ABBREVIATIONS
ANSYS – Finite element code, used as solver with NUMAD
APDL – ANSYS Parametric Design Language (scripting code)
ATA – ATA Engineering, Inc.
BMODES – Single-blade modal calculation code from Sandia, run by NUMAD
BPE – Equivalent blade properties calculation code from Sandia, run by NUMAD
FEA – Finite element analysis
FEM – Finite element model
HAWT – Horizontal Axis Wind Turbine
NUMAD – Blade modeling/analysis code written in MATLAB code, from Sandia

1. INTRODUCTION AND EXECUTIVE SUMMARY

This report documents analysis work of (1) adding automated nonlinear disbond finite element analysis capability to Sandia's NUMAD wind turbine blade analysis system, (2) comparing linear vs. nonlinear analysis results for loaded blades with and without disbonds, and (3) investigating the sensitivity of disbond location and size on analysis results with disbonds. Analysis results of interest included predicted blade buckling load capacity, shapes, and tip deflections; equivalent blade beam section properties as would be used in whole machine simulations; blade natural frequencies; and local blade stresses and strains. The analysis was done with one sample blade NUMAD model (see Figure 1-1) provided by Sandia representing a 5 MW HAWT turbine blade, 61.5 m long with maximum chord of 4.6 m (Sandia NUMAD file SNL5MW_v2.nmd). Automated capability was developed and exercised for both trailing-edge blade skin disbonds and spar web to blade skin disbonds (i.e. shear web disbonds).

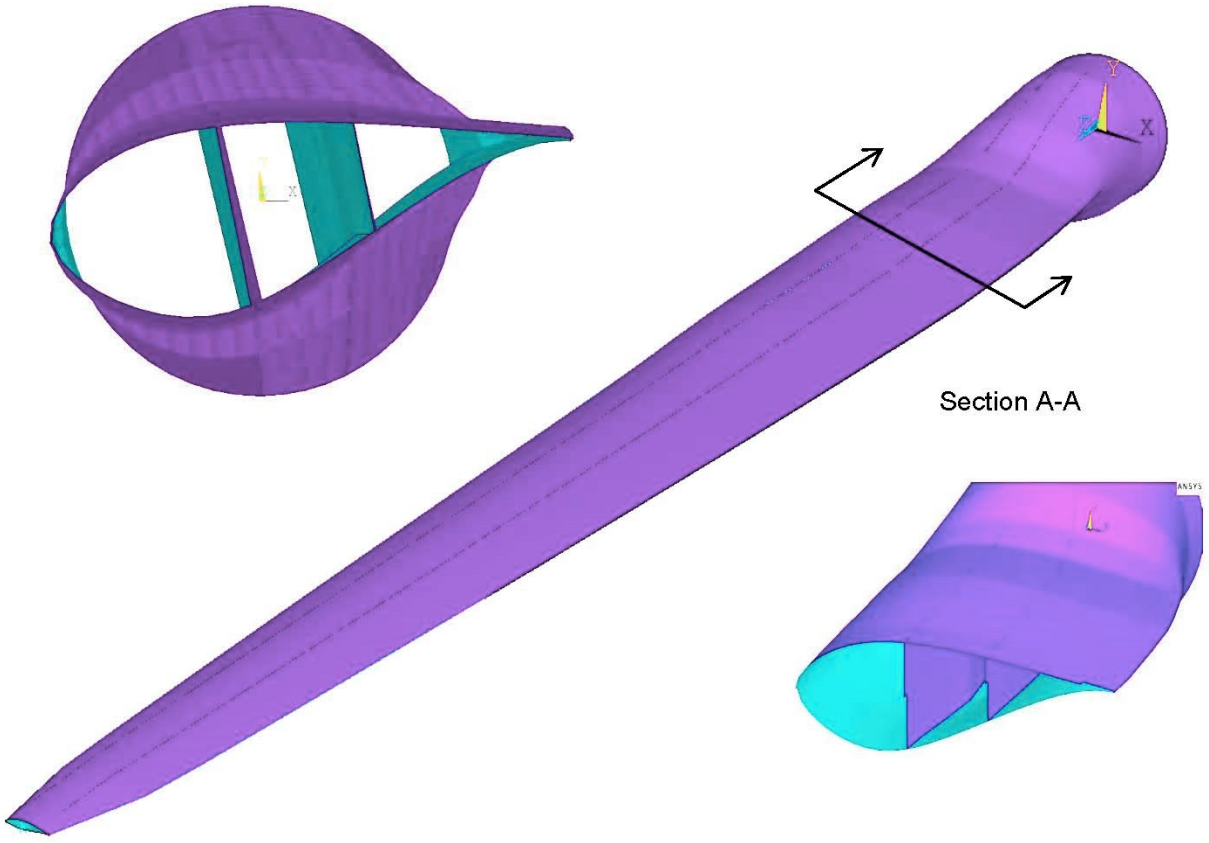

Figure 1-1. Finite element model of sample wind turbine blade.

Several major findings for the work are apparent:

- First, nonlinear analysis is much more accurate for the effects of disbonds and blade buckling response and is recommended over linear analysis. Aside from disbond-specific response, more accurate nonlinear analysis may also illuminate buckling limit

issues of a blade geometric and material configuration that are not detected by linear analysis.

- Second, the lowest buckling limit load for a blade may not be influenced by disbonds until the disbonds reach a certain substantial size (see Figure 1-2). Critical buckling may rather be nominally governed by non-disbond influenced geometry such as skin free span size or relatively abrupt surface geometry that acts as a "crease" where buckling can initiate (see Figure 1-3).
- Third, buckling deformation with nonlinear disbond modeling may not be abrupt or involve bifurcation (as assumed by linear buckling analysis) but rather may exhibit a relatively gradual and smooth response.

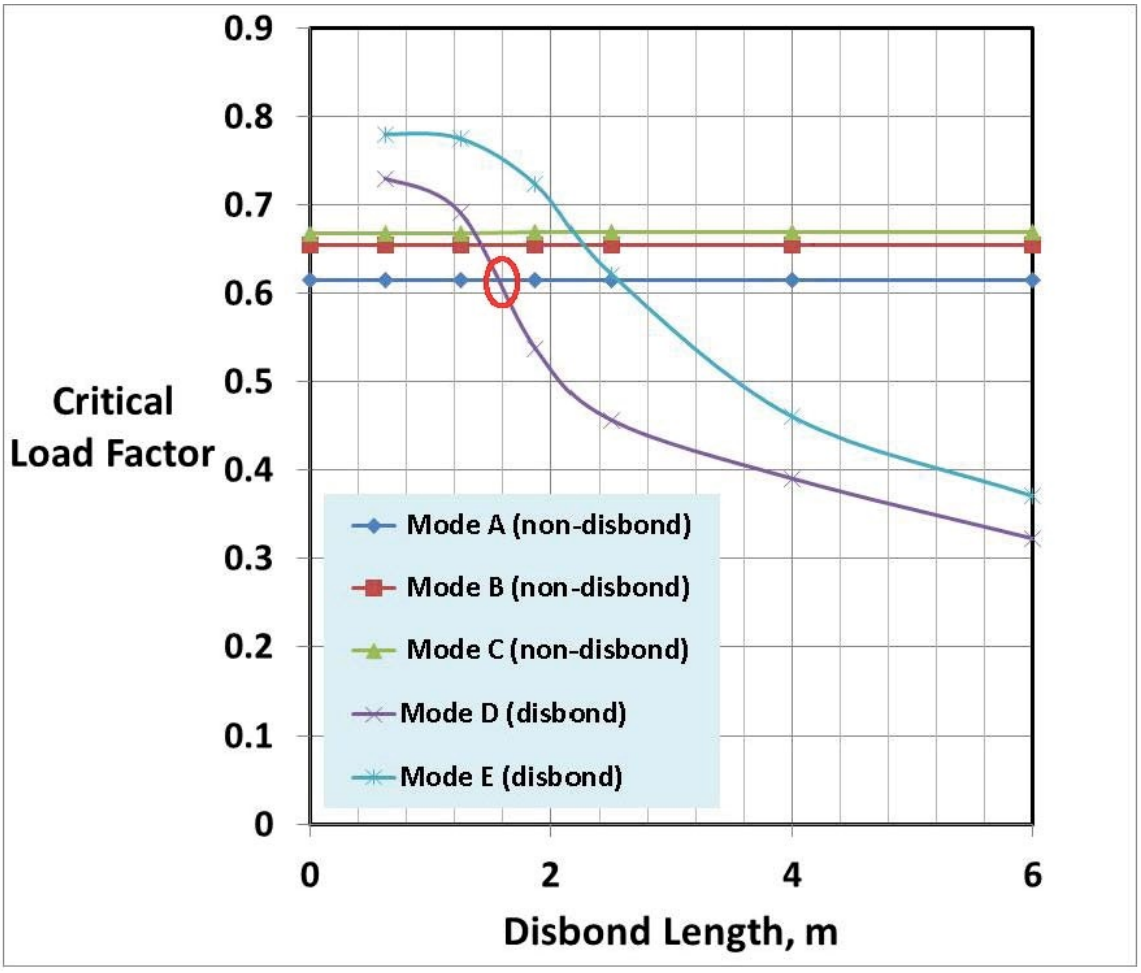

Figure 1-2. Exemplar buckling mode evolution with disbond size. Disbond governs lowest buckling capacity only above 1.6 m disbond length (crossing marked where disbond-related buckling deformation becomes critical).

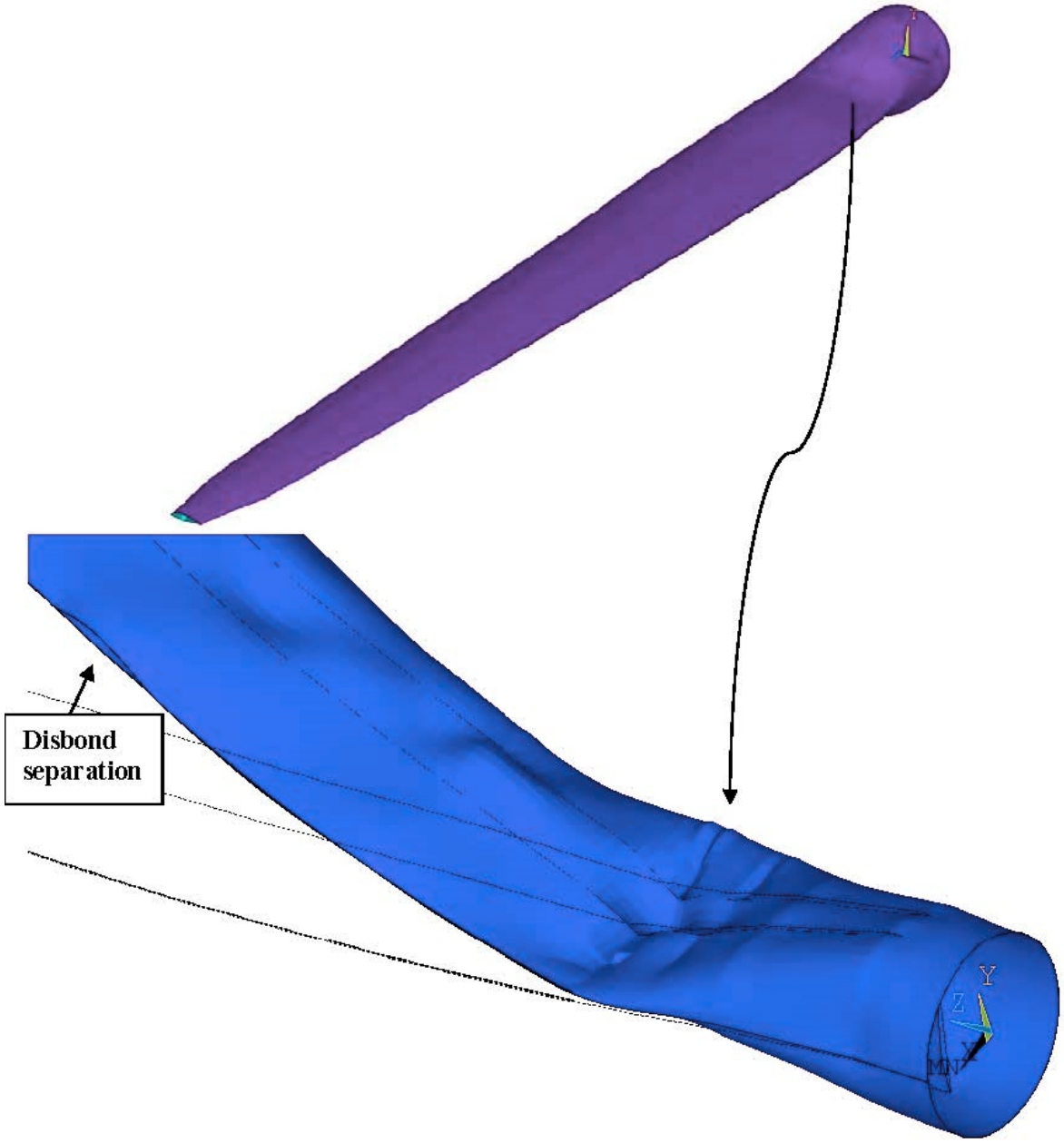

Figure 1-3. Exemplar buckling tendency at relatively sharp geometric change in blade surface (exaggerated deformation shown for clarity). Disbond occurs but is not critical for buckling.

The recommendation for future work is primarily checking downstream analysis tools for tolerance of disbonded blade equivalent beam properties. Equivalent beam properties predicted by the BPE code for large disbonds have been problematic in the BMODES code, preventing modal solutions due to matrix ill-conditioning. This is likely due to unrealism of linear equivalent blade properties when the disbonds are very large. On the other hand, as large disbonds are easily observed visually and would not be tolerable in an operating machine, analyzing for them with BMODES and beyond in the FAST whole-machine simulations may not be a priority.

Another recommendation is to consider how the blade load level changes equivalent beam properties and how this effect may be efficiently included in a whole machine model. A certain level of load is needed to induce disbond separation and local skin bowing deformation, at which point the equivalent beam rigidities also change in accordance with the deformed geometry, causing "softening" of the cross section. Conceptually, accounting for this effect simply involves using more than one set of beam properties as a function of the current loads on a simulated machine blade, but implementation is code-specific and not trivial.

2. NEW DISBOND MODELING DESCRIPTION

The Sandia NUMAD code operates within MATLAB in conjunction with ANSYS as the finite element analysis (FEA) solver, using ANSYS Parametric Design Language (APDL macro language) to great advantage for automation. ANSYS is also a good solver for nonlinear behavior, including contact modeling, large deflections and rotations, and elasto-plastic material response. ATA work began with NUMAD already capable of building reasonably accurate blade models within ANSYS and optionally running them via linear solutions for follow-on tasks.

NUMAD provides for interactive generation of wind turbine blade shell models (including aerodynamic cross-section shapes and composite laminate definitions of skin and web materials), and that capability was augmented by ATA to modify the blade model, post-creation, to include disbonded regions at the trailing edge or spar web to skins. This was done by adding APDL code at the bottom of the ANSYS command routines to effect the disbond modification. MATLAB routines write the necessary ANSYS commands into the ANSYS command files, with MATLAB handling the bookkeeping of node and element information related to the disbond regions. It was generally possible to add the necessary modification code into MATLAB by utilizing much of the existing code structure and variables.

The general approach for ANSYS model modification is as follows:

- -At a longitudinal span line of a possible disbond, "separate" the finite elements by generating coincident nodes instead of single nodes used by adjacent shell elements, and adjust element nodal connectivity accordingly.
- -Insert contact elements between the coincident nodes created.
- -Couple back again any remaining coincident nodes wherever disbond is not specified for the particular case currently requested.

All the ANSYS model modification code is generated in an automated manner within MATLAB as part of the NUMAD "Generate ANSYS" function. The desired disbond spanwise starting location(s) and length(s) are entered via interactive prompting during the ANSYS file-creation phase in MATLAB. The ANSYS model can then be run via the NUMAD procedure to feed BPE (equivalent blade properties) and BMODES (modal extraction for clamped root blade) analysis, and the solution steps have been modified to use nonlinear analyses equivalent to the previous linear solves. Alternatively, any ANSYS solves or further modification can be done offline with the ANSYS command file generated by NUMAD usable to build the FE model, including disbonds. This option can be used, for example, to solve blade-buckling problems with desired blade loading.

2.1. Blade Trailing-Edge Disbond

Typical trailing-edge disbonds, which we intend to simulate, are shown in Figure 2-1. ANSYS provides for a wide range of contact modeling options, including friction or not, adjustable contact stiffness, and other details. Different approaches were implemented by ATA, but the final configuration chosen (see Table 2-1) provides the most reliable and reasonably adjustable contact modeling given the NUMAD-generated shell model topology as it stands at this time.

Table 2-1. ANSYS contact-element configuration.

ANSYS ELEMENT	FUNCTION AT DISBOND NODE PAIR	OPTIONS
COMBIN39 (Nonlinear Spring)	Normal contact via general nonlinear load deflection	Nonlinear force-deflection definition
COMBIN37 - Rotational (Control Element)	Rotational restraint only when in contact	Rotational stiffness level, friction limit moment

It should be noted that the contact approach chosen is not the most commonly used in ANSYS. The more common approach is surface-to-surface contact via CONTAC170 contact and TARGET174 target elements, where these elements are "skinned" over 3-D surfaces that come into contact—on one side the 170s and on the other the 174s. The topology of the NUMAD-generated blade model includes shells joining at an edge at the potential disbond locations, which is natural for shell modeling but not highly representative for the real situation of finite-width contact as seen in Figure 2-1, which would require 3-D solids modeling. The mating shells are not always overlapping and near-parallel, either (see Figure 2-3), but rather in some cases they are perpendicular or on edge to each other (see Figure 2-2), resulting in essentially edge-to-edge contact between the elements once they are separated by coincident nodes. In such a case, the common method's CONTAC/TARGET pair may still simulate contact given the proper element settings, but the rotational coupling that would take place during contact is not included due to there being only line contact. Similarly, other ANSYS contact elements intended for line contact also do not include the rotational restraint during contact that we need here with the use of shells. Thus, the less-common COMBIN39/COMBIN37 element approach for contact was applied, primarily to more properly simulate surface rotational restraint during contact. The COMBIN39 element provides for a general nonlinear load/deflection curve contact definition, which can easily be adjusted to simulate contact with adjustable high interference stiffness, near-zero separation stiffness, and contact/separation transition as desired. The element acts in a single selectable nodal DOF direction when the defining nodes are coincident. The nodal direction of interest may be either a global axis direction (default) or may be defined by specific nodal rotations applied to the defining nodes. In our case, the global Y direction (see Figure 1-3) is always used, though this could be easily changed.

Then, COMBIN37, a control element, allows the application of a stiffness in another direction across the same node pair of the COMBIN39, but only conditionally upon the closure of the contact gap defined by the COMBIN39. A rotational COMBIN37 is applied in each of two lateral planes (Y-X and Y-Z global) with a linear rotational stiffness that is adjustable (but nominally very stiff), using the COMBIN39 node pair displacement difference as a control variable to turn the stiffness on or off. If ever desired (though this is not currently implemented), the COMBIN37 definitions also can include a finite friction limiting moment in line with the spring stiffness to simulate sliding.

Currently, the disbond node pairs are not coupled in any way perpendicular to the contact, simulating frictionless sliding when the gap is closed. This is the simplest modeling approach in the absence of information about the contact characteristics, and it allows the most freedom of

motion when the gap is closed. It would not be difficult to add translational stiffness and friction perpendicular to the contact if this is thought more accurate for a particular case. This would most easily be implemented by copying the existing rotational COMBIN37s and changing the TYPE and REAL settings to represent translation with appropriate properties. This could be done with a small additional APDL routine.

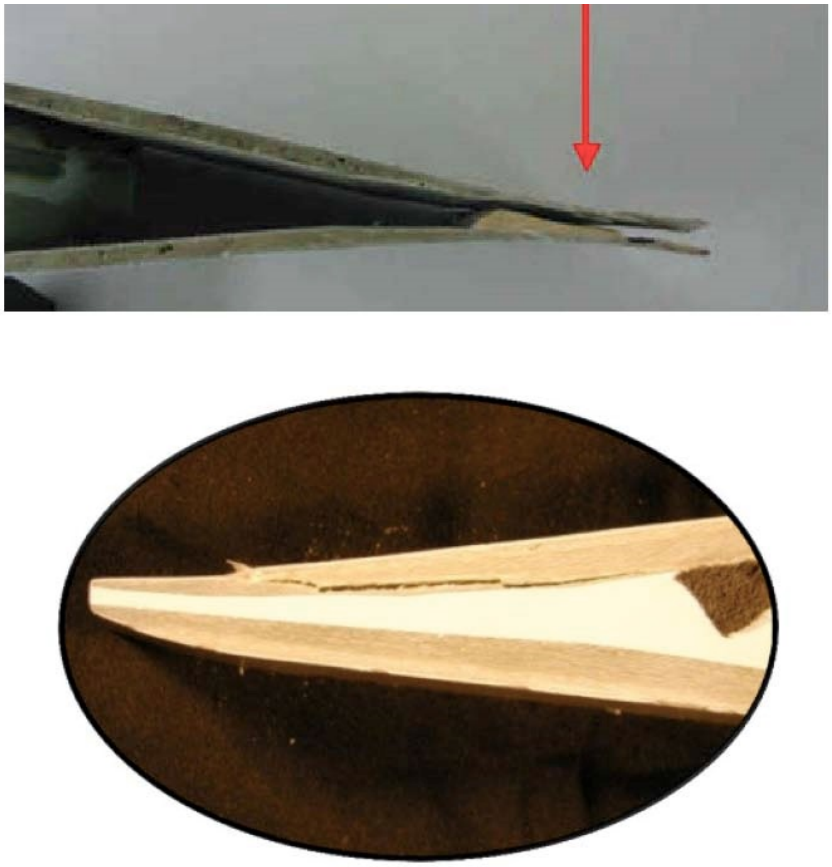

Figure 2-1. Typical turbine blade trailing edge disbonds, viewed in blade cross sections.

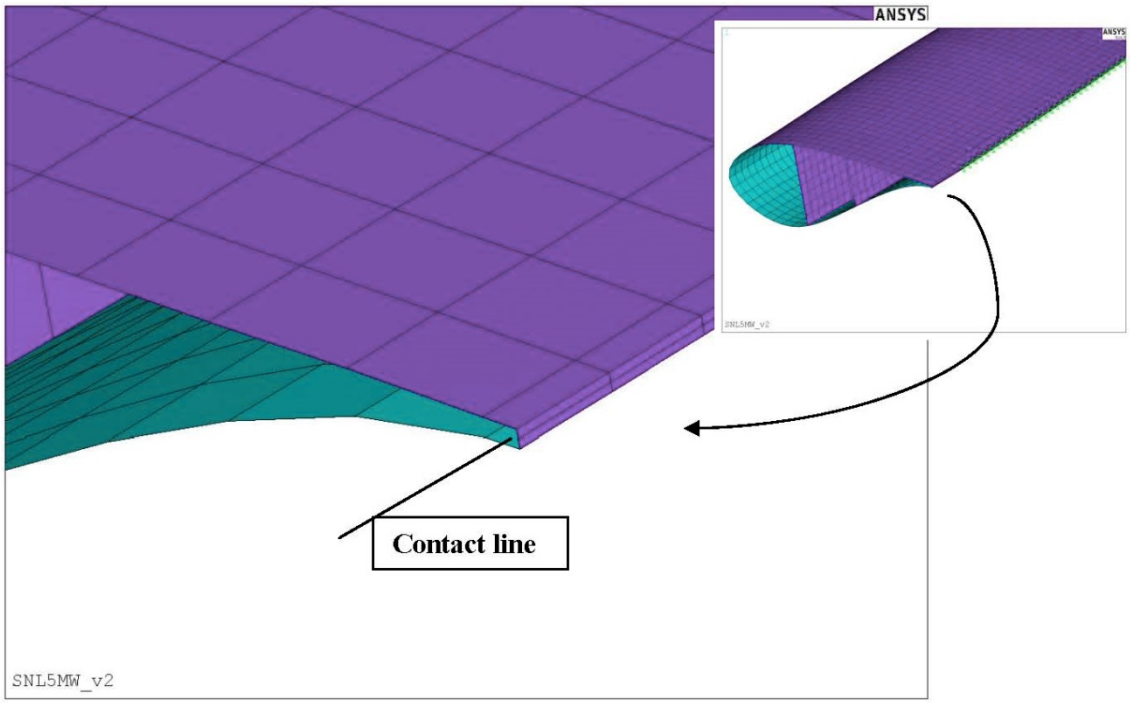

Figure 2-2. Inboard trailing edge in sample turbine blade model. Trailing edge is defined by shells on edge.

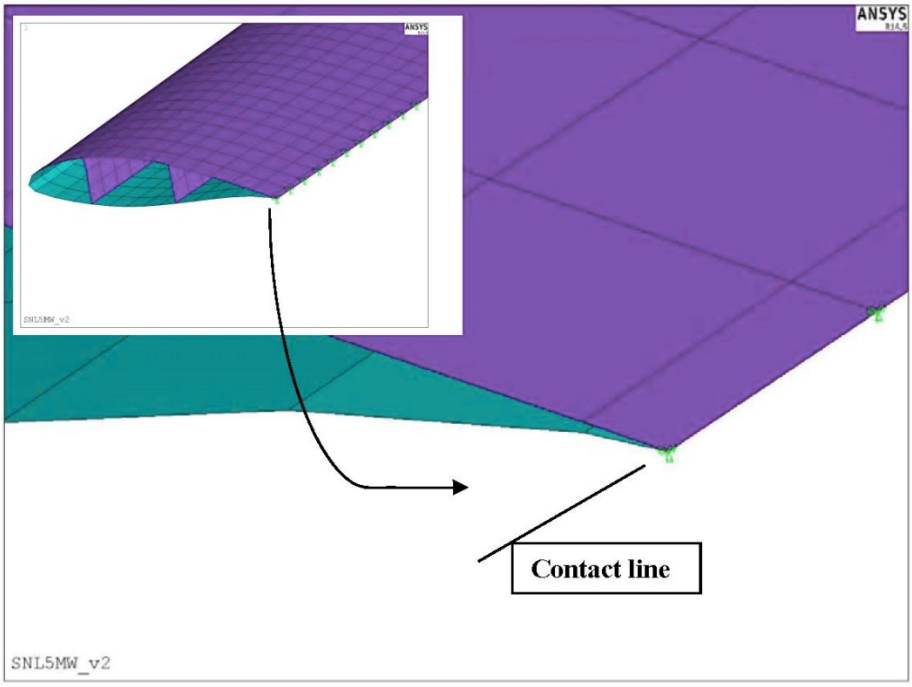

Figure 2-3. Outboard trailing edge in sample turbine blade model. Elements come together near parallel.

Given the prompted starting location and length of a disbond from the user, the new MATLAB code inserts the COMBIN39 and COMBIN37 described at the line segment of nodes desired. Then, outside that region, the coincident nodes are simply fully coupled in all six degrees of freedom, which gives the same effect as if the nodes were simply merged. We thus arrive at a blade model with an embedded trailing-edge disbond (see Figure 2-4), ready for any ANSYS solution of interest.

It is notable that the recoupling of coincident nodes is done with coupling equations, simply setting a nodal displacement equal to another; when the use of nonlinear large deflection analysis is anticipated later, this is the best method to use.
Constraint equations that implement rigid body rotations of any kind are not applicable in large deflection analysis, as the equations do not account for large rotations, only infinitesimal ones.

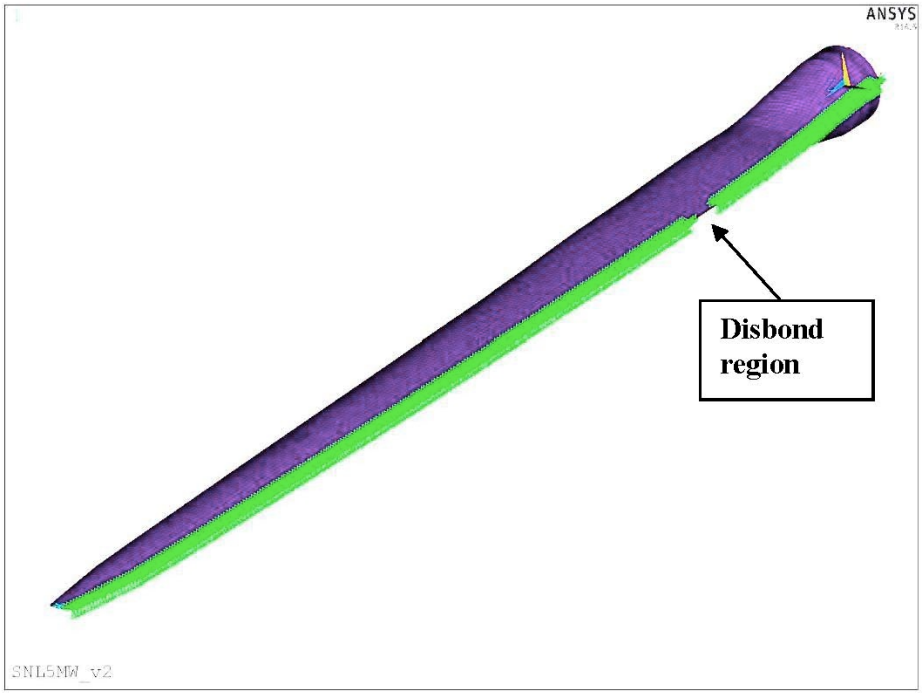

Figure 2-4. Blade model with trailing edge disbond. Non-disbond coupling is denoted by green symbols.

The use of constraint equations is thus to be avoided in such problems. If a rigid region or body is needed in such an analysis, very stiff elements should be used instead, where the elements are properly formulated for nonlinear large rotations (BEAM188, for example). In this work, application of tip loading does require such a rigid load transfer at the blade tip from load point to the blade skin. Figure 2-5 shows the implementation of a rigid region with stiff beams as an alternative to constraint equations. This was used in the nonlinear buckling analyses described later to avoid any constraint-equation-induced errors, though it was observed that the errors using constraint equations were not significant in this particular case.

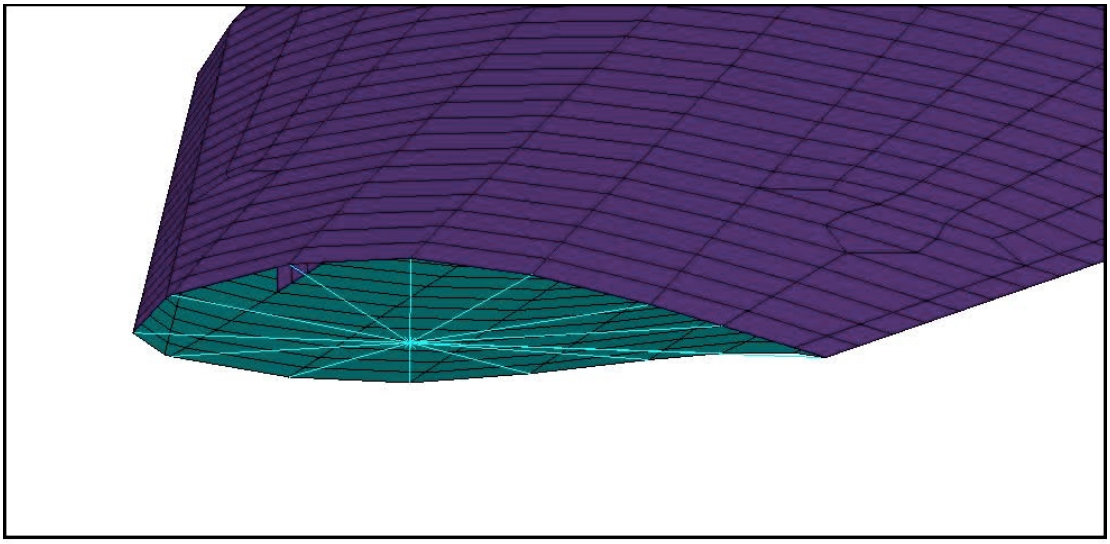

Figure 2-5. Stiff beam "spider" used for blade-tip load transfer in nonlinear analysis.

2.2. Spar-Web Disbond (i.e. Shear Web Disbond)

Spar-web disbond modeling is done with exactly the same COMBIN39/37 elements as for the trailing edge, but in this case the shells come together at a slight skew angle near perpendicular due to the skin airfoil contour. Again, the contact approach provides rotational restraint when the gap is closed.

There are two spar webs inside this blade, and disbonds can be specified at either the leading web or trailing web or both, prompted and entered by the user for start location and length.

Figure 2-6 shows an example spar-web disbond with surrounding coupled nodes along the spar-web edge.

Figure 2-6. Typical spar-web disbond definition. Green symbols indicate coupling.

The MATLAB code for spar-web disbonds currently has the capability for disbonds at the upper blade skin with matching disbond positions for leading and trailing webs. Changing the leading vs. trailing web disbond positions is relatively easy by manual modification of the ANSYS model, if desired for a particular application. Simulation of disbonds at the lower blade skin would require some change to the current MATLAB code. In addition, the MATLAB codes for trailing-edge and spar-web disbonds are separate and have not been used in combination as yet.

The non-perpendicular contact between spar web and blade skin can have some influence on disbond response when in contact. Using a line contact is a substantial simplification here, where there might in actuality be a composite angle clip joining the pieces, with one leg of the clip along a substantial width of contact on the skin. If contact forces are substantial from the skin flex, one may expect the spar web to be pushed laterally in response, and—depending on the coordinate direction of the contact modeling—this response could be affected by the direction assumption. Currently, we are using global Y direction for contact, which is close to the spar-web direction, so the spar web should be mostly, but not perfectly, loaded in plane by contact. If the contact nodal coordinates were rotated to be perpendicular to the skin, the potential for lateral bending of the shear web would be increased. Unfortunately, with only edge contact, there is no perfect choice for the contact angle: one part will always be off the contact angle, so the choice of global Y is as good as any. As such, it will be difficult to improve on this aspect without 3D solids modeling with finite contact width.

3. LINEAR BUCKLING ANALYSIS RESULTS

A Sandia-supplied 5 MW HAWT turbine blade, 61.5 m long with a maximum chord of 4.6 m was used for the following studies. For buckling analysis, both a blade-tip load of 10 kN and a distributed aero force load case were used. Figure 3-1 shows the nodal load vector on the ANSYS blade model, indicating a distribution that is relatively uniform over the entire blade skin. Both the tip load and distributed load cause the blade to bend primarily in the +Y direction, which compresses the top skin, so that is where buckling would be expected to appear at some multiplier of the load. If there are disbonds, however, one might expect the disbonded skin to locally buckle sooner by bowing out of plane.

In the case of linear analysis, the eigenvalue method of buckling is generally applied, in which instability is determined based on when effectively negative stress stiffening or differential stiffness effects overcome or cancel the nominal structural stiffness, most likely in a local region. It is well known that this linear solution representing abrupt bifurcation buckling can be unconservative, in that real structures may begin to buckle sooner and not as abruptly, with the load carried only asymptotically approaching the eigenvalue prediction level.

Given the disbond model, linear analysis requires the assumption of no contact whatsoever at disbonds, so the separated parts may "move through" each other during buckling (we simply remove the COMBIN39/37 elements at the disbond for linear analysis). This is not realistic, but it allows for the simplification of the simulation to a linear solution. Also note that there are a number of buckling modes and associated eigenvalues representing load levels initiating instability, and usually only the lowest one is of interest, as it governs the safe load-carrying capacity.

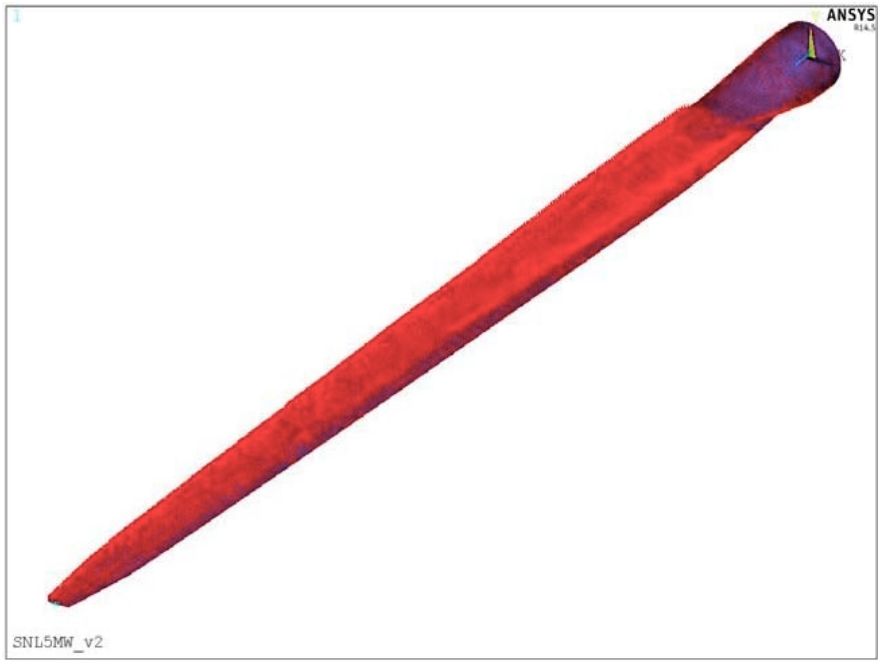

Figure 3-1. Load vector display for Sandia-supplied distributed aero load.

3.1. Trailing-Edge Disbond

Linear buckling critical load factors for the distributed load case are given in Table 3-1 below. The buckling mode shapes were reviewed and an attempt was made to follow the modes as disbond size changed, and the most critical data is provided in Figure 3-2 as a graph for the 14.36 m disbond start location only.

Table 3-1. Critical load factors for linear buckling, distributed wind load, with disbonds.

		Run Number Designation								
		0	5	10	15	20	28	36	40	50
		Disbond Start Distance Along +z (m)								
		14.36	14.36	14.36	14.36	14.36	14.36	14.36	19.0	24.0
		Disbond Length (m)								
		0	0.625	1.25	1.875	2.5	4.0	6.0	2.0	2.0
Mode Number	1	0.614	0.614	0.614	0.537	0.456	0.390	0.322	0.565	0.614
	2	0.654	0.654	0.654	0.614	0.614	0.460	0.370	0.614	0.654
	3	0.668	0.668	0.668	0.654	0.621	0.615	0.507	0.654	0.668
	4	0.675	0.675	0.675	0.669	0.654	0.654	0.573	0.668	0.675
	5	0.721	0.721	0.691	0.675	0.669	0.669	0.615	0.675	0.721
	6	0.723	0.723	0.721	0.721	0.675	0.670	0.654	0.721	0.723
	7	0.723	0.723	0.723	0.722	0.721	0.675	0.669	0.723	0.723
	8	0.728	0.728	0.727	0.723	0.723	0.721	0.675	0.723	0.728
	9	0.732	0.732	0.728	0.728	0.726	0.723	0.722	0.728	0.732
	10	0.733	0.733	0.733	0.733	0.728	0.725	0.723	0.732	0.733
	11	0.748	0.748	0.736	0.735	0.733	0.729	0.724	0.733	0.748
	12	0.754	0.754	0.749	0.748	0.736	0.733	0.729	0.747	0.753
	13	0.754	0.754	0.754	0.754	0.748	0.737	0.732	0.754	0.754
	14	0.757	0.757	0.754	0.754	0.754	0.748	0.733	0.754	0.757
	15	0.764	0.764	0.757	0.757	0.754	0.754	0.746	0.757	0.764
	16	0.780	0.780	0.764	0.764	0.757	0.754	0.748	0.764	0.780
	17	0.787	0.787	0.780	0.770	0.764	0.757	0.754	0.778	0.787
	18	0.789	0.787	0.787	0.784	0.783	0.764	0.755	0.787	0.789
	19	0.793	0.793	0.793	0.787	0.787	0.782	0.757	0.789	0.793
	20	0.801	0.801	0.793	0.793	0.793	0.787	0.764	0.793	0.800

Clearly, there are some buckling modes that are not influenced whatsoever by the disbond and others that are strongly influenced by disbond length. In this particular case, a buckling mode not involving disbond is the most critical if disbond length is less than about 1.6 m, shown in Figure 3-3. This mode appears to be governed by free span size near the blade root leading edge and has a very complex shape. When the disbond length exceeds about 1.6 m, as in Run 15 (1.875 m), we have a critical mode as shown in Figure 3-4, involving only the disbonded blade skin, and a relatively simple shape. These results show that disbonds must reach a certain (here substantial) size to be a critical buckling driver relative to other blade skin characteristics such as free span size. The disbond mode load factor decreases with disbond length.

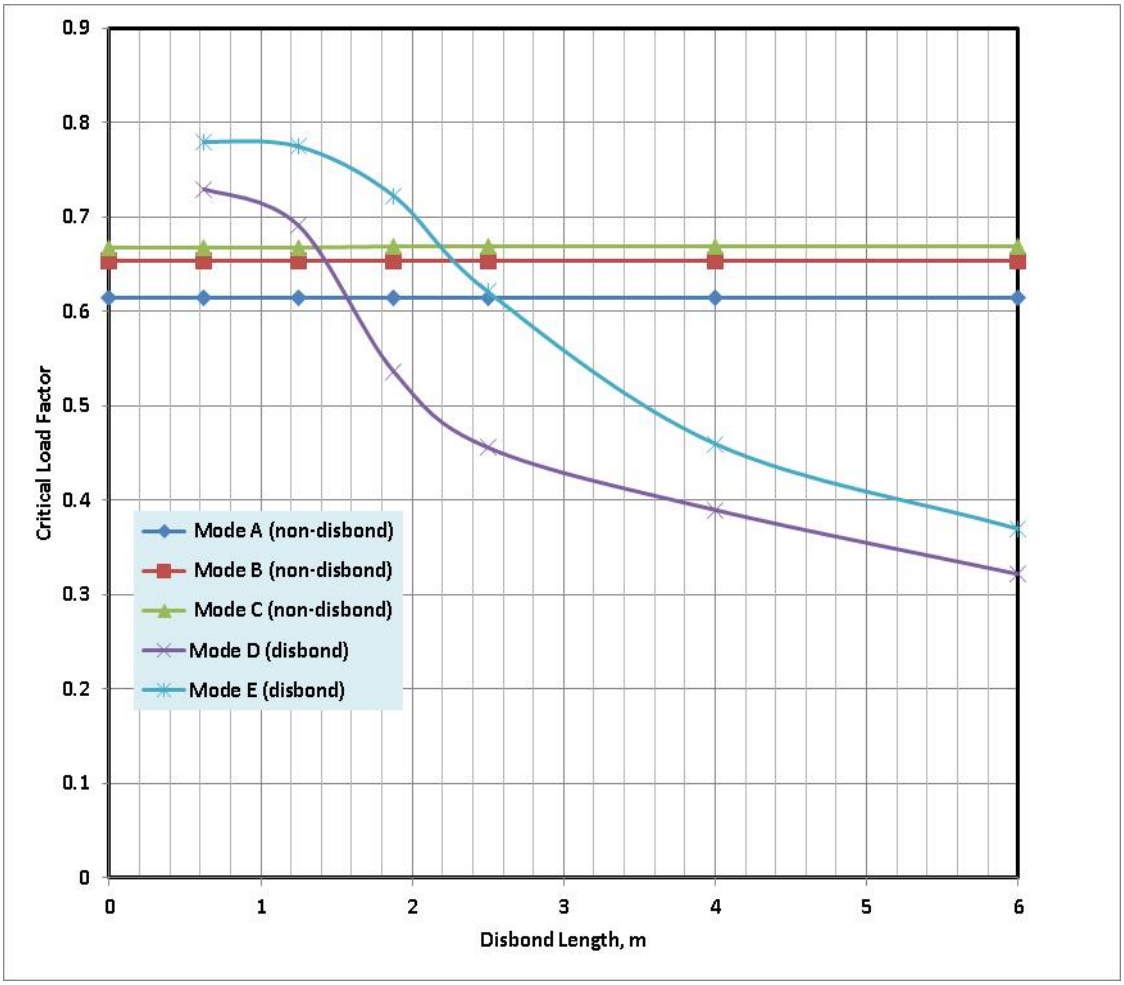

Figure 3-2. Critical buckling load factor as a function of disbond size for 14.36 m disbond start location.

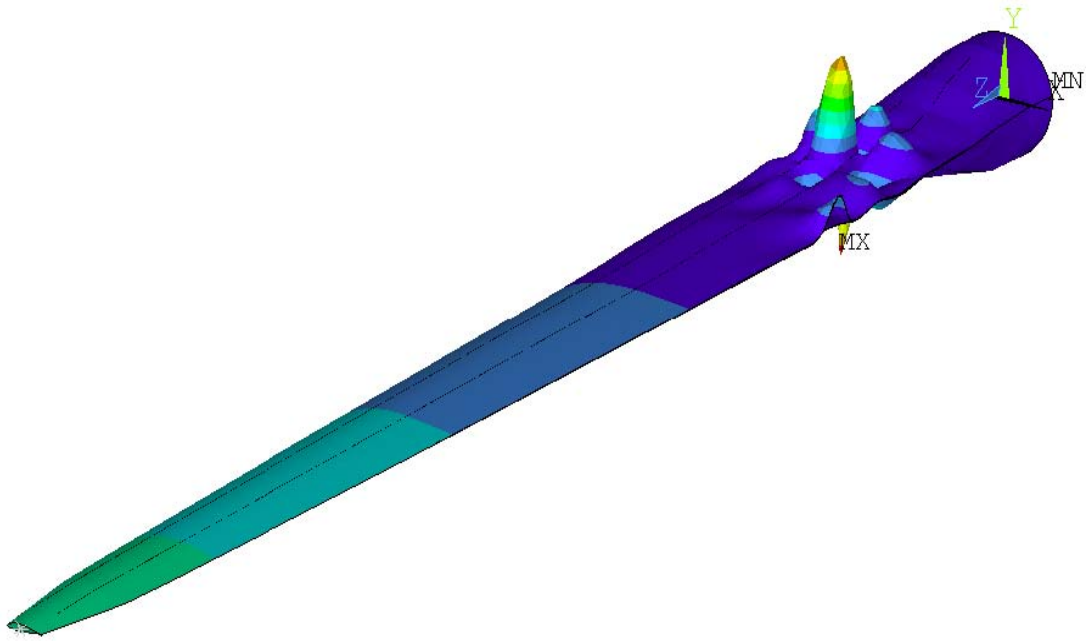

Figure 3-3. Mode A, non-disbond buckling mode with load factor 0.614 (Run 15).

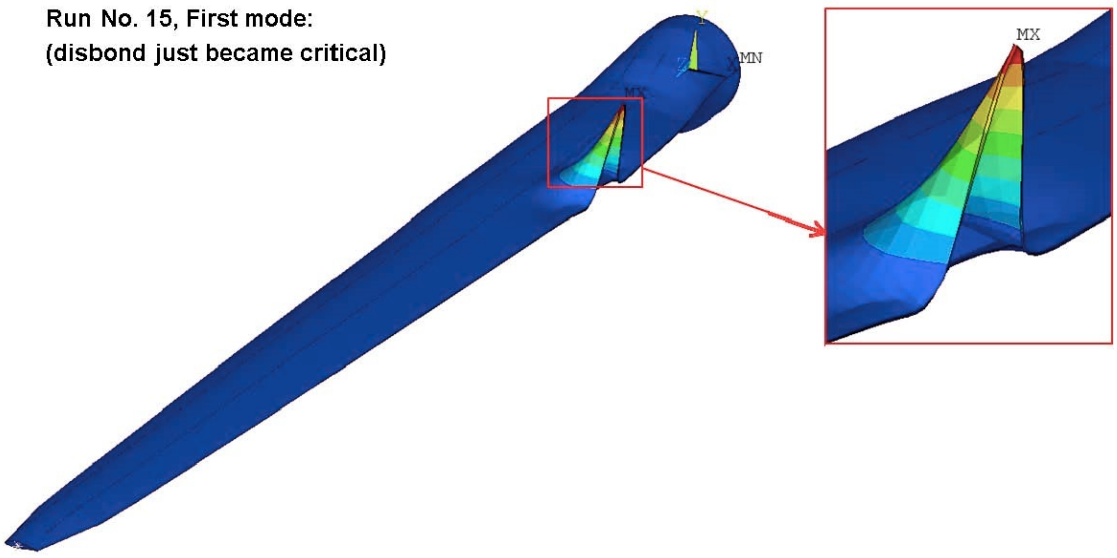

Figure 3-4. Mode D, disbond-dominated buckling mode with load factor 0.537 (Run 15).

It is also observed in the data that disbond-influenced buckling load factors generally increase with greater start location radius (see Runs 15 vs. 40 and 50), which is consistent with lower skin compression further from the blade root, as a result of bending, as well as smaller chordwise skin free span. Also, buckling mode density is relatively high (with most modes not influenced by disbond), which is not surprising with the tapered nature of the skin free spans and similarly varying compression loading.

3.2. Spar-Web Disbond (i.e. Shear Web Disbond)

Similar linear buckling analyses were done for spar-web disbonds, all starting at 14.36 m radius, summarized in Table 3-2 and depicted in Figure 3-5. Critical results are displayed graphically as in Figure 3-6 and Figure 3-7.

Table 3-2. Spar-web disbond linear buckling load factors, distributed aero load case.

		Spar Disbond Location										
Run No.	Disbond Length (m)	Trailing Edge Web	Leading Edge Web	Buckling Load Factor								
0b	none	-	-	0.622	0.662	0.685	0.687	0.729	0.733	0.734	0.735	0.737	0.738
41	1.875	x		0.541	0.622	0.662	0.685	0.687	0.698	0.730	0.733	0.735	0.737
42			x	0.520	0.622	0.660	0.678	0.679	0.685	0.734	0.735	0.737	0.737
43		x	x	0.436	0.617	0.634	0.667	0.685	0.687	0.733	0.734	0.736	0.737
44	4	x		0.342	0.439	0.623	0.649	0.671	0.684	0.687	0.731	0.732	0.735
45			x	0.443	0.459	0.622	0.627	0.666	0.679	0.685	0.734	0.734	0.735
46		x	x	0.253	0.356	0.552	0.624	0.647	0.664	0.672	0.684	0.687	0.710
47	6	x		0.326	0.351	0.466	0.558	0.624	0.663	0.684	0.686	0.699	0.731
48			x	0.437	0.444	0.552	0.591	0.623	0.661	0.679	0.685	0.692	0.734
49		x	x	0.222	0.267	0.371	0.470	0.556	0.580	0.617	0.624	0.665	0.684
471	10	x		0.288	0.293	0.340	0.388	0.478	0.510	0.610	0.624	0.648	0.668
472			x	0.429	0.432	0.455	0.479	0.556	0.564	0.622	0.645	0.665	0.679
473		x	x	0.199	0.225	0.243	0.277	0.347	0.410	0.492	0.509	0.532	0.567

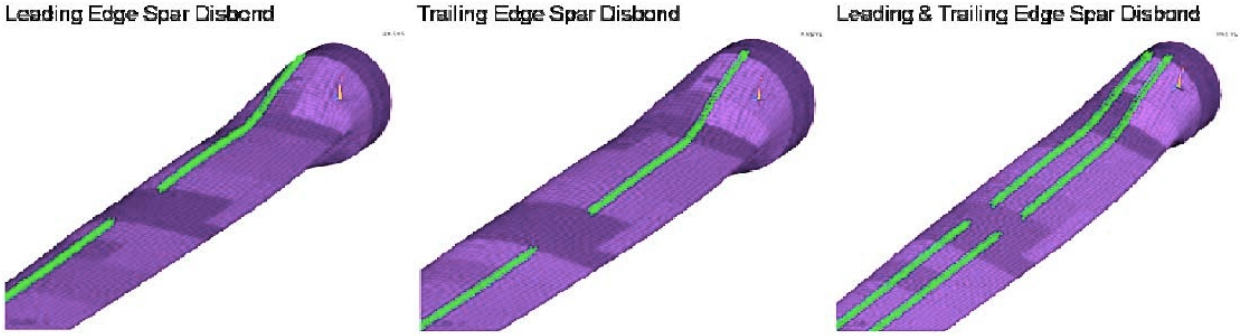

Figure 3-5. Typical spar-web disbonds simulated (green symbols indicate coupling outside the disbond)

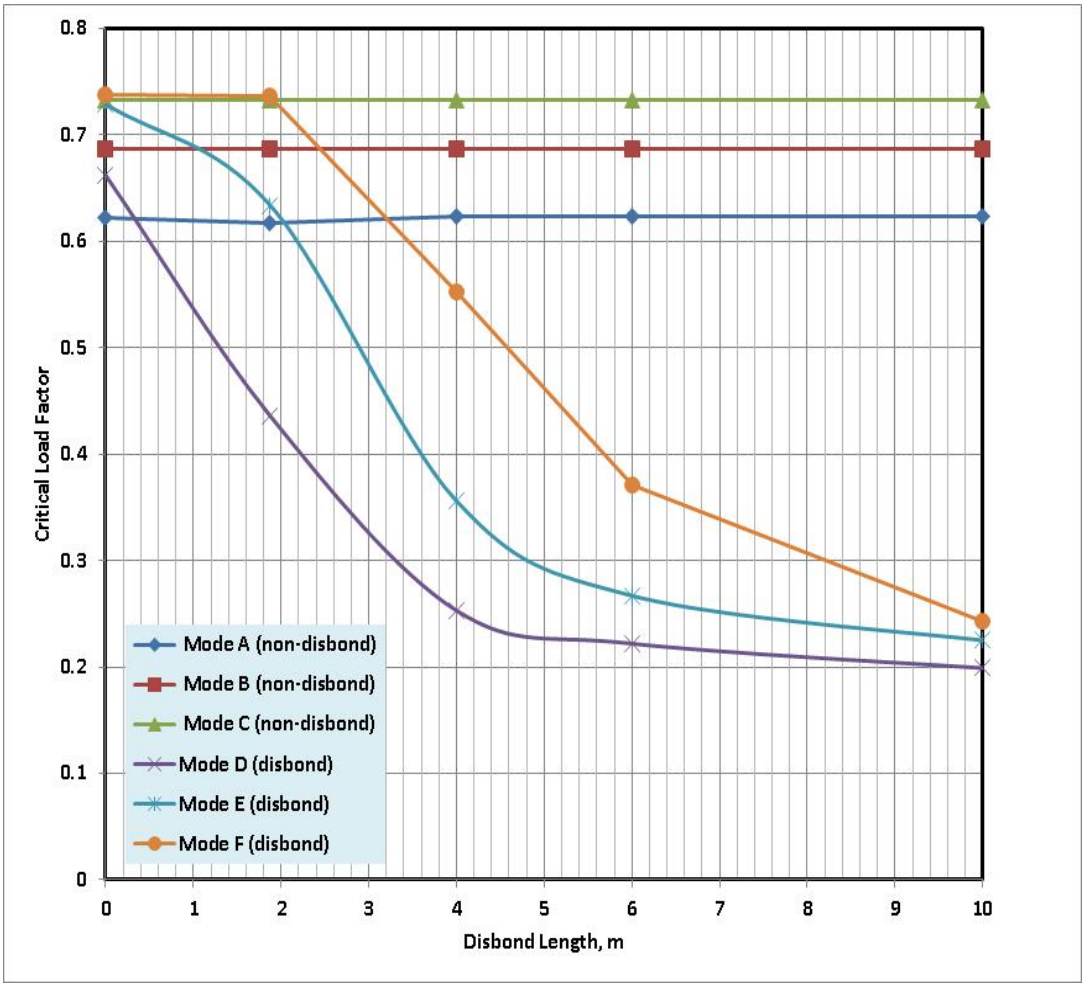

Figure 3-6. Critical buckling load factors for both spar webs disbonded, 14.36 m start location.

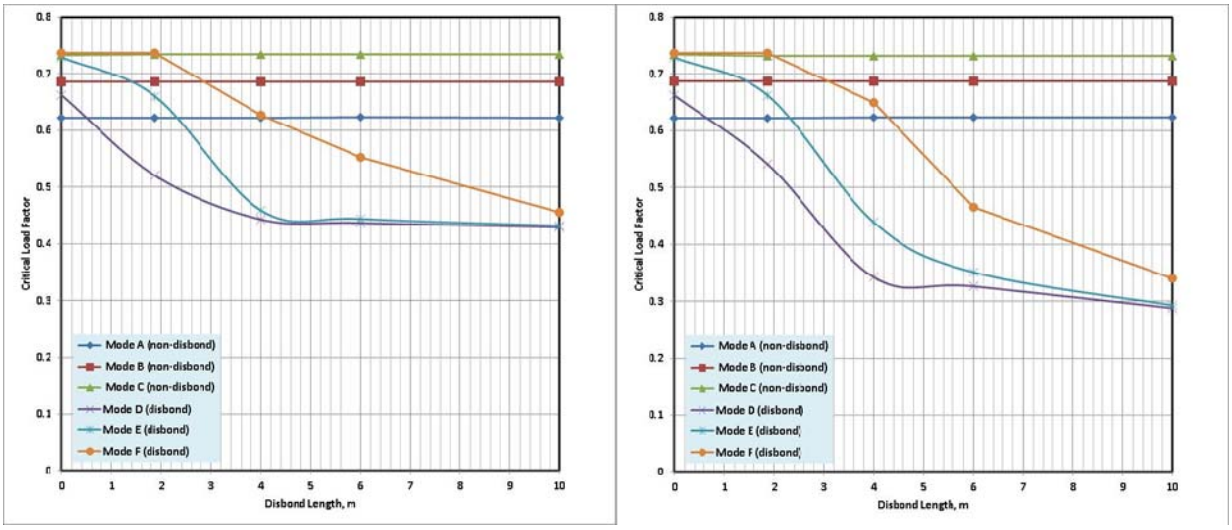

(a) Leading-edge disbond only (b) Trailing-edge disbond only

Figure 3-7. Critical buckling load factors for individual spar webs disbonded, 14.36 m start location.

These results are conceptually similar to those for trailing-edge disbond, though disbond-related buckling becomes critical at much lower disbond lengths for spar-web disbond compared to trailing-edge disbond. For example, with both webs disbonded, only a 0.3 m long disbond becomes critical, while criticality is at about 0.50 m for leading-web only and 0.65 m for trailing-web only. This is primarily due to the disbonds being in the region of highest skin compression under blade bending, and disbonds greatly increase local skin free span. As expected, the scenario leading to the most skin free span—both webs disbonded—leads to the lowest buckling factors. Figure 3-8 shows the critical buckling mode shape, which again shows disbond-influenced shape to be relatively simple and non-influenced to be complex.

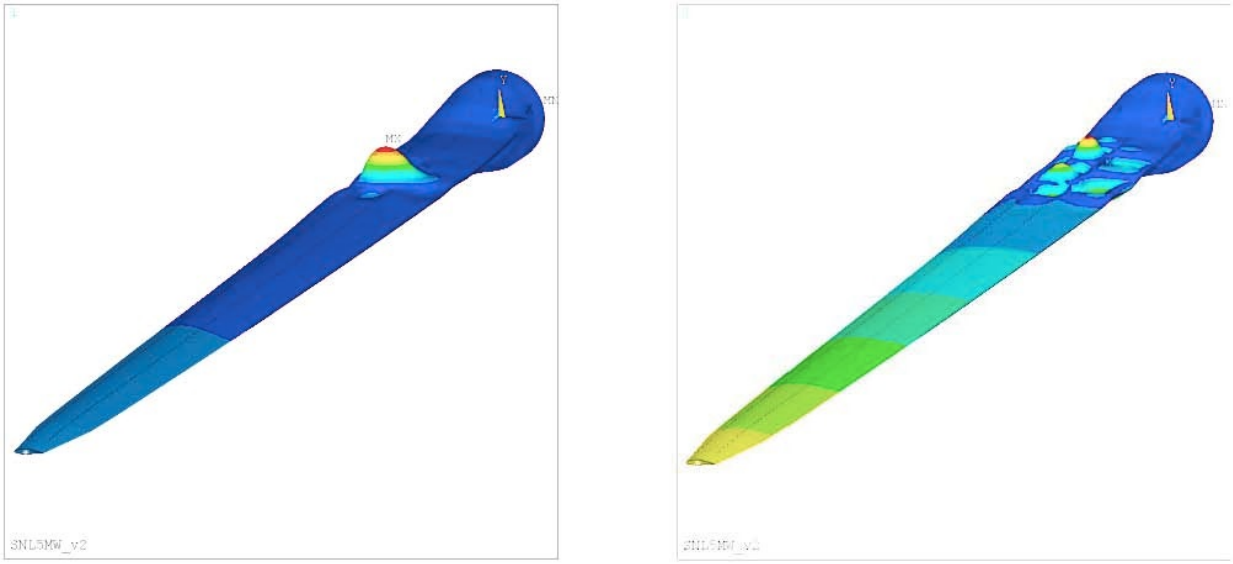

(a) Mode D, disbond influenced (0.54 factor)

(b) Mode A, non-disbond influenced (0.62 factor)

Figure 3-8. Both spar webs disbanded 1.875 m long, Run 41, lowest buckling mode shapes.

To summarize, the linear buckling analysis can be boiled down to understandable disbond-dependent and non-dependent buckling modes, where a disbond-dependent mode becomes critical at some disbond size. The complex nature of the non-dependent mode shapes is discomforting in a sense, as one may expect that these complex shapes cannot be readily initiated in the appropriate relative phasing, and one may then further reasonably expect that they will not be observed in practice, as opposed to the simpler disbond-influenced modes.

4. NONLINEAR BUCKLING ANALYSIS RESULTS

We now repeat the buckling analysis with nonlinear large deflection methods with the same distributed aero load case and compare to linear results. For use in later interpretation, some of the effects that nonlinear analysis considers (that linear analysis does not consider) are enumerated below:

1) Nonlinear analysis accounts for complete 3-D deformation of a skin panel, particularly out-of plane "diaphragmming" under a given normal pressure load. Thus, the direction of skin normal deflection is initiated and biased in a certain direction by pressure, which is likely to preclude the linear buckling mode complex differential deflections.
2) Nonlinear analysis accounts for progressive eccentric load effects; that is, as out-of-plane deflection takes place, in-plane loads generate additional bending response (some call this the "Pdelta effect" or "eccentricity effect," and it is analogous to compression of a bent vs. flat beam or plate).
3) Nonlinear analysis accounts for local membrane in-plane stress due to local pressure diaphragmming, whereas in linear analysis, in-plane stress only comes from macroscopic deformation (total blade bending). As in-plane stresses drive buckling, the results of the two approaches can be substantially different for this reason.
4) Nonlinear analysis involves gradually increasing the load on the structure until a critical instability prevents further loading (manifested as solution numerical instability with default solvers). As such, only the most critical buckling mode with the lowest buckling factor is obtained (though post-buckling solutions are possible, they are more difficult and not generally attempted). In contrast, linear analysis includes numerous buckling modes.
5) Nonlinear analysis accounts for contact forces during disbond gap closure; linear assumes none.
6) Nonlinear analysis accounts for changes in geometry as a function of load level. The most important example is disbonded skin that may bow out of plane above certain load levels.

4.1. Trailing-Edge Disbond

For the cases previously run linearly (shown in Table 3-1), nonlinear solutions all arrived at the same result, a load factor of 0.649, and a shape as shown in Figure 4-1. It is apparent that the near-root area, with some abrupt angle changes in the top skin, exhibits the "P-delta" nonlinear effect fairly strongly, resulting in a "crease" gradually developing into buckling as the load is incremented. At the same time, the disbonded trailing edge does bow out but does not govern stability of the solution, i.e., does not lead to global instability before the crease buckling does.
The crease effect seen here may not be entirely real but rather an artifact of the four-node shells used for modeling, which must be near flat to avoid warping; this causes a faceting effect in the model that does not really exist. This issue only shows itself in nonlinear analysis. One way to avoid it would be to use eight-node quadratic shells to simulate curvature. However, the nonlinear result does point to a potential buckling problem, indicating that abrupt geometry in the highly loaded near-root blade skin should be avoided.

It is notable that the nonlinear 0.649 factor is greater than the linear critical factors, disbond-influenced or not. The bowing of the disbonded skin is not globally unstable and so does not

define the nonlinear critical factor, though one could look at intermediate steps in the nonlinear solution and see the disbonded skin start to buckle/bow at a certain finite load factor lower than 0.649. On the other hand, we do not see the linearly predicted non-disbond-influenced mode at 0.61 factor because of the greater dominance of the creasing nonlinear effect in the near-boss area, which causes deflections to depart from those necessary for the linearly predicted complex mode shape to develop.

The creasing effect seen in Figure 4-1 also by necessity involves substantial lateral deformation of the spar webs, though this is not visible in this view.

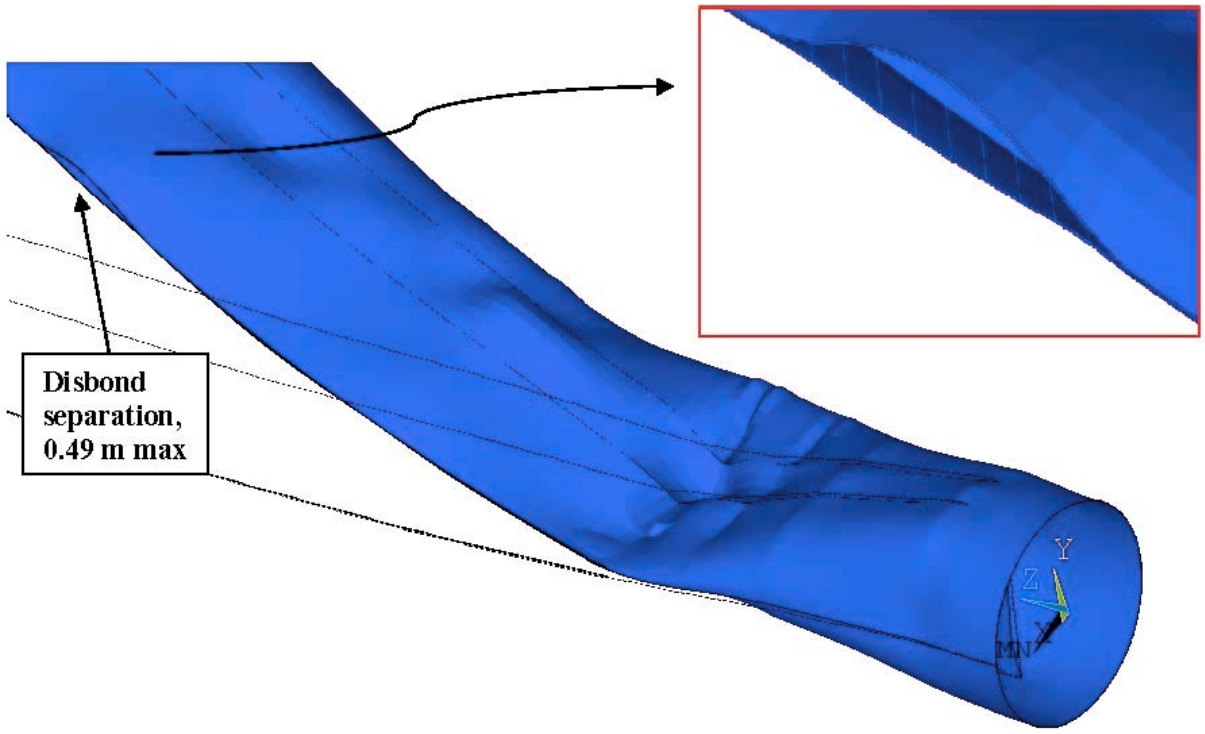

Figure 4-1. Nonlinear buckled shape with trailing edge disbond, distributed aero load (0.649 factor for any disbond length, exaggerated deflection scale of 10x), Run 15 nonlinear.

In summary, this is a case where the nonlinear analysis shows an entirely different effect than linear analysis, pointing to a real design issue if the modeled geometry is accurate. It also shows how local disbonded skin buckling is not necessarily a global blade stability issue.

4.2. Spar-Web Disbond (i.e. Shear Web Disbond)

In the case of spar-web disbond, nonlinear analysis showed more "interesting" results as a function of disbond size. Table 4-1 summarizes the nonlinear cases directly corresponding to the previous linear cases of Table 3-2. Comparing the two tables, the nonlinear critical buckling factor is found to be consistently higher than the lowest factor from the linear solution. Looking

at the nonlinear deformed shapes, especially for single web disbonds, the creasing effect is seen to occur again as it did for trailing-edge disbonds (see Figure 4-2).

Table 4-1. Nonlinear buckling results for distributed aero load, spar-web disbonds (all 14.36 m start location).

		Spar Disbond Location		
Run No.	Disbond Length (m)	Trailing Edge Web	Leading Edge Web	Buckling Load Factor
0c	none	-	-	0.659
51	1.875	x		0.662
52			x	0.661
53		x	x	0.461
54	4	x		0.657
55			x	0.637
56		x	x	0.301
57	6	x		0.664
58			x	0.630
59		x	x	0.326
571	10	x		0.663
572			x	0.655
573		x	x	0.310

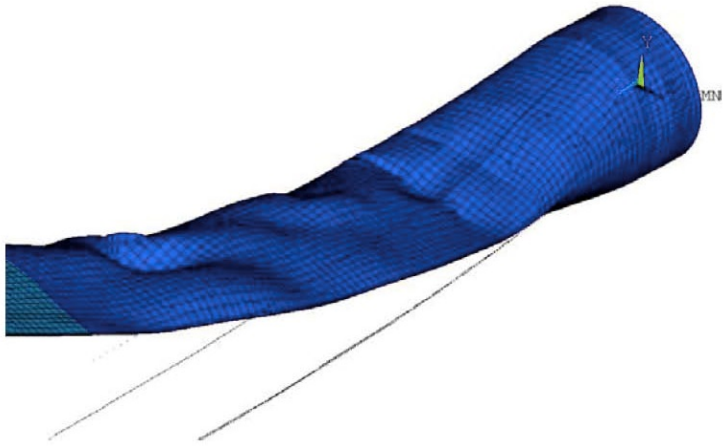

Figure 4-2. Nonlinear buckled shape for Run 51; creasing effect is observed (5x actual deformation).

During the nonlinear analysis, it was necessary to experiment with the COMBIN39 contact stiffness to minimize deflection at the spar-web contacts. Increasing the stiffness reduced the contact deflection but also increased the lateral movement of the spar web relative to the skin and slightly increased the critical load factor. To keep parts from passing through each other, relatively high contact stiffness is necessary— but then spar-web lateral movement may be higher than actual. There is no easy solution to this dichotomy without modeling the blade structure in greater detail in which the contact region is finite width.

5. EQUIVALENT BEAM PROPERTIES FOR LINEAR AND NONLINEAR DAMAGE MODELS

Equivalent beam properties can be extracted by the BPE code in both the linear and nonlinear cases, but in the nonlinear case it is possible to put a preload on the blade first. Then unit tip load perturbations are applied to the blade in a series of ANSYS solves (linear or nonlinear), and the deflection results are input to BPE for the beam properties calculation.

Although specific preload on the blade is a complicating factor, the fact is that a certain level of preload will cause disbonded skins to bow/buckle out of plane without a loss of global stability. The equivalent blade beam properties can be substantially different before and after this occurrence, especially in flatwise bending, as the bowed skin is much softer in compression or tension than when flat. The difference in stiffness will also manifest itself in natural frequency differences.

Trailing-edge disbonds especially, but also spar-web disbonds, are also expected to substantially change torsional characteristics, as the disbond breaks the torsional shear flow path in the cross section.

Table 5-1 shows the cases investigated for beam properties variation, concentrating on spar-web disbonds first, with both webs disbonded. In all cases, the disbond start point was 14.36 m radius. In the nonlinear cases, a preload of 25% of the distributed aero load previously used was applied, and case 620 alone used a reversed direction of preload to see what the opposite-sense load would do.

Table 5-1. Beam properties cases for investigation.

LINEAR RUNS

Run No.	Disbond Length (m)
500	0
503	**1.875**
506	**4.0**
509	**6.0**
512	**10.0**
515	**15.0**

NONLINEAR RUNS

Run No.	Disbond Length (m)
600	0
606	**4.0**
612	**10.0**
620*	**10.0**

***applied preload in opposite sense (i.e. using scale factor SF = -0.25)**

In executing solutions for the beam properties, it was necessary to experiment in the nonlinear cases to find a level of preload that would adequately "upset" the geometry in the disbond areas without getting too close to the limit of global stability, so that the perturbation cases superimposed on the preload could be solved stably and easily. In general, this kind of analysis may require some knowledgeable user intervention, adjusting solution load scales and solver settings before arriving at a complete set of data.

The key point is that for linear, the results show some flatwise bending and torsional variation

from the non-disbonded case. Nonlinear preloaded cases show substantially more deviation from nominal for shorter disbonds mainly in the local area of the disbond, but for very large disbonds there is more general variation. This behavior can be aptly attributed to the local buckling of skins and resulting stiffness loss in the nonlinear cases only. We also observe that for the reversed preload direction, when bowing of the blade skin should not occur, the beam properties do not change as greatly, as expected.

We also see some large, more general shifts in properties in the nonlinear case. In particular, axial rigidity is changed substantially for any disbond length relative to linear solutions. This is a result of the multi-axis coupling of bending and axial motion that only exists in nonlinear analysis. However, as most important blade dynamics is flatwise and edgewise, this is not likely a very substantive effect in machine simulations. Also note that this analysis did not include centrifugal preload.

6. STRESS/STRAIN AND DEFLECTION RESULTS

Load cases for buckling were processed for load-deflection curves for some dual spar-web disbond cases. Figure 6-1 shows the typical load-deflection comparisons (deflection is tip Y deflection), indicating that overall linearity is held relatively well until loss of global stability, and blade stiffness is near nominal. Trailing-edge disbonds show less load-deflection nonlinearity (not shown), which is consistent with the lesser change of beam-bending properties with disbond length.

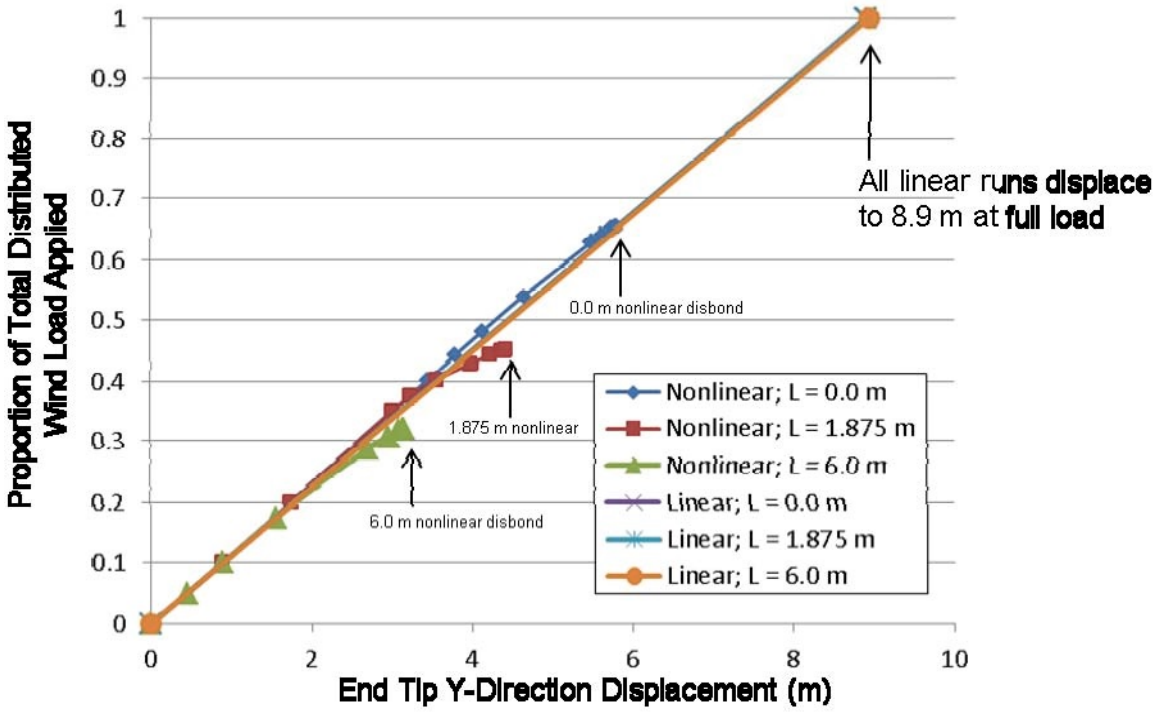

Figure 6-1. Load-deflection curves for both spar webs disbonded, distributed aero load.

Stress results can only be reasonably reviewed from nonlinear analysis where the skins bow out of plane and bending stresses and strains are generated. Figure 6-2 shows the spanwise outer-surface strain response at 0.65 distributed load factor for trailing-edge disbond of several sizes, where the limit of blue/red color is −1%/+0.15% strain and the deflection is exaggerated to 10x. The creasing near the blade root drives the high responses, and peaks and valleys of skin wave shapes also show higher stress due to bending curvature. It is additionally observed that the disbonded skin stress is not very high relative to nominal for large disbond of 6.0 m; the 1.875 m disbond length actually shows higher stress at the disbond, though very localized, because the curvature is greater at the shorter disbond "peak" of the bowed skin. So, generally, the stresses in buckling are concentrated at high curvature locations of the deformed shape due to bending, and the disbond location may not be the critical one for maximum stress. It is to be expected that there are also substantial transverse tensile stresses at the ends of the disbond when the skin bows, and the disbond is likely to propagate, but such analysis is beyond the current analysis scope.

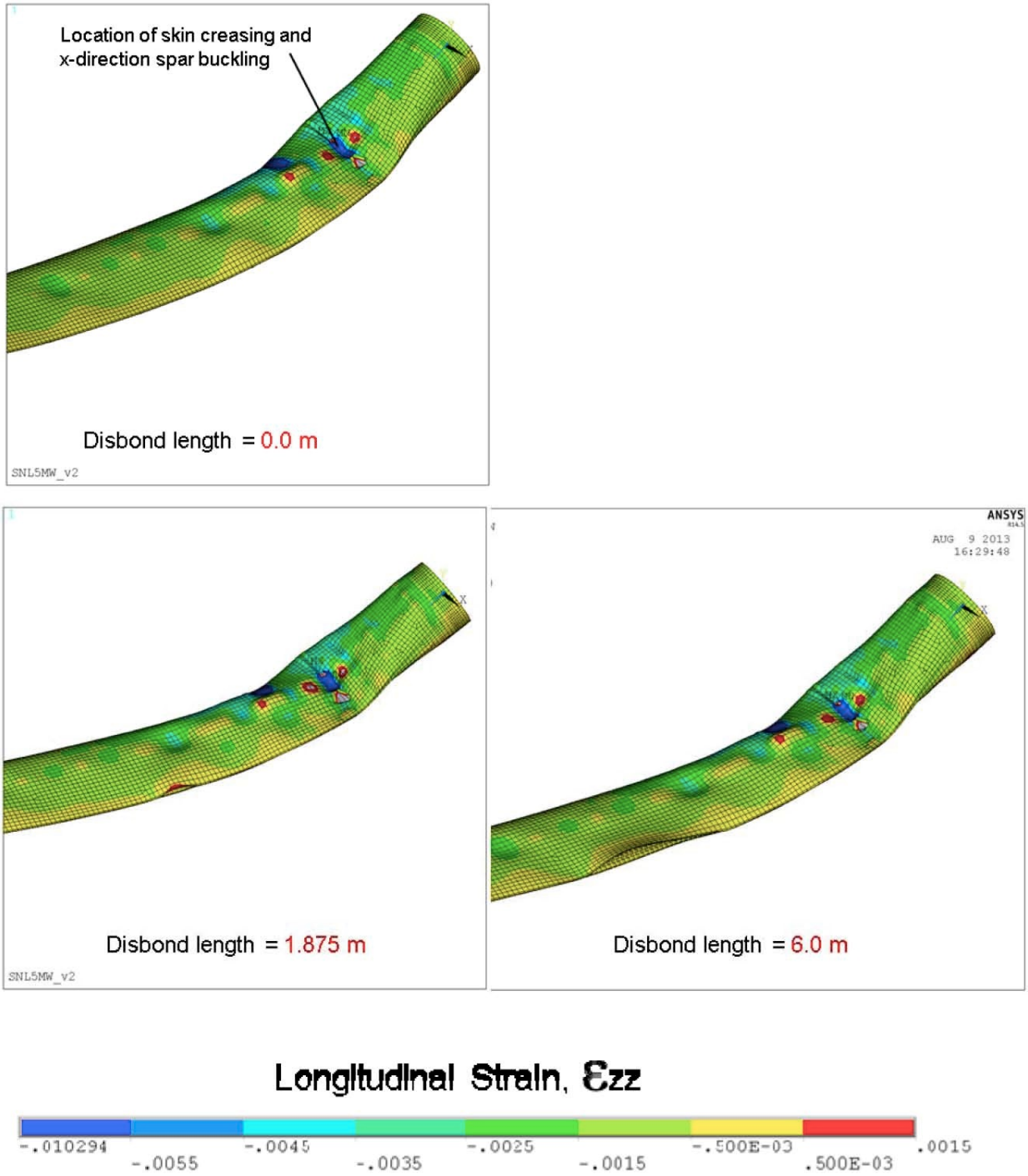

Figure 6-2. Longitudinal strains for trailing edge disbonds at 0.65x distributed load factor.

A similar result is seen in Figure 6-3 for spar-web disbonds, for example (with same strain color scale as the trailing-edge case, for comparison). Note that the scale of deformations is exaggerated, making it look like the shear webs are penetrating the skin substantially, which is not the case. Spar-web disbonds are more severe as far as critical load, and for substantial disbond length, the near-boss area is not a driver because the critical load level is lower and the crease has not yet developed. So, we see that for the disbond cases, strains are highest in the disbond area. Again, the shorter 1.875 m disbond actually results in higher stresses due to high skin curvature, and it appears that in that particular case, the wave number of the bowed skin is higher (greater than just a half wavelength), and the wave peak is inward rather than outward. This results in higher strains at the ends of the disbond than would otherwise be seen, but the midspan is still the worst for bending strain—here about 1% compression on the outer surface. In comparison, the longitudinal strains for the 6.0 m disbond are relatively benign.

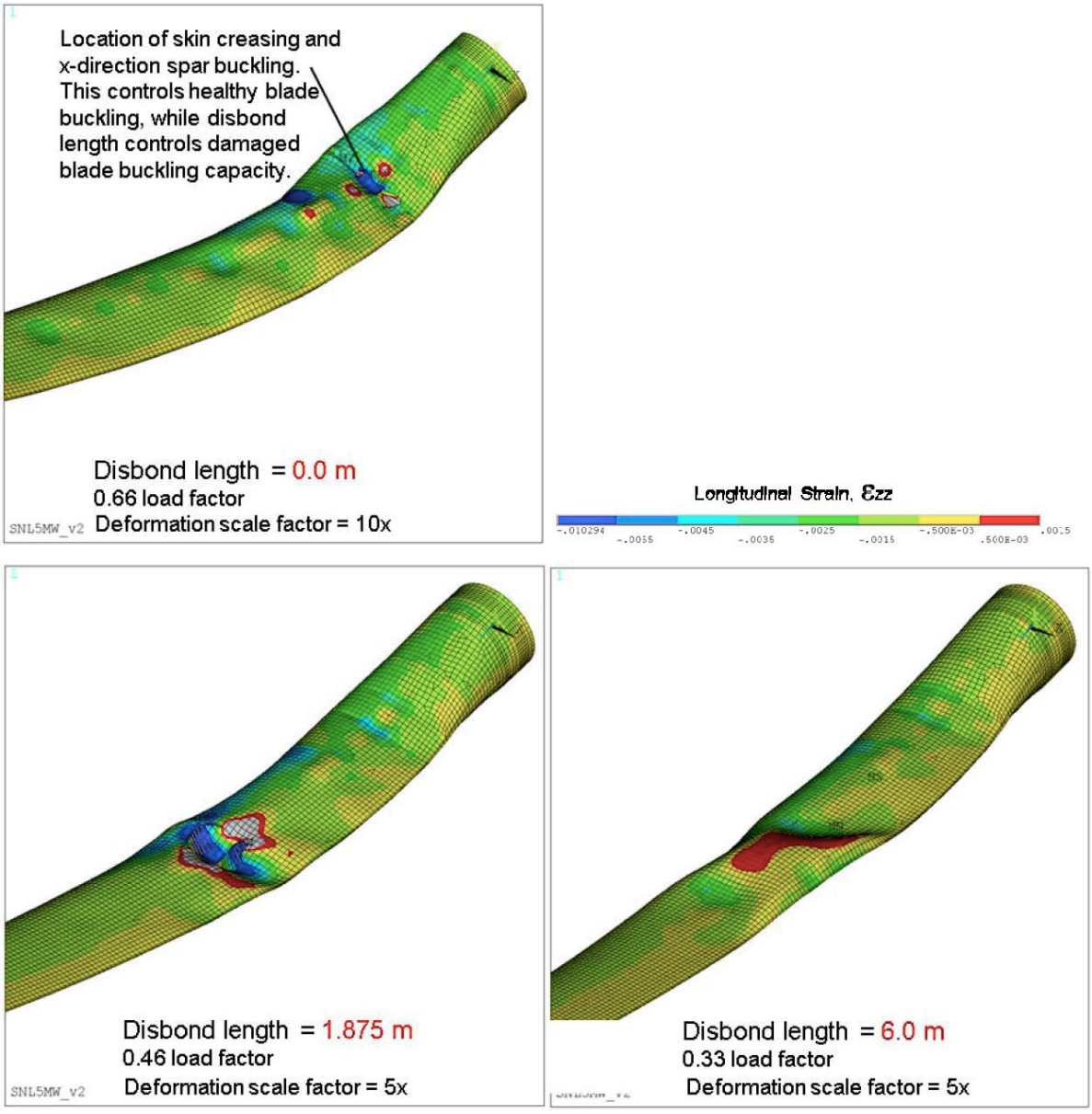

Figure 6-3. Longitudinal strains for spar-web disbonds for distributed load.

7. CONCLUSIONS

Automated disbond modeling was implemented into the NUMAD system and demonstrated its usage with some sample analyses. Results were reviewed and some general conclusions were arrived at, including the following:

1) Nonlinear analysis is more suitable for buckling analysis than linear analysis for damaged blade models (here, disbonding type damage). As one example, a blade with disbonds preloaded to a level that bows the disbonded skin will exhibit significant drops in some natural frequencies that linear analysis does not predict. The preloading effects are readily solved with conventional nonlinear methods including contact elements, with results feeding to existing analysis tools.
2) Disbonded skin bowing does not necessarily drive overall blade stability and may be stable and gradual to high deflection values.
3) Blade preloading has a substantial effect on equivalent beam properties, not only due to the loss of disbonded skin connection and relative slippage, but also because disbonded skins bow out of plane and change cross-section stiffness. The effect can only be predicted using preloaded nonlinear analysis (in this instance, feeding the BPE code without difficulty). Analysis simulating slippage but not bowing will not be very accurate for blade beam properties.
4) Disbonds in some cases (in particular, trailing-edge disbonds for our sample subject) will not become critical for buckling until they reach a certain substantial size. Below this disbond size, non-disbond-influenced buckling will drive critical load capacity, either driven by skin free span size or abruptly changing skin geometry.
5) Abruptly changing skin geometry can be a major driver for real buckling of blades, and one should take care in accurate modeling at large cross-section changes in the blade. The faceting effect of four-node shells can be a potential accuracy-reducing factor; if they are used, mesh density should be relatively high. Also consider using eight-node shells as a way to eliminate faceting error.

(this page intentionally left blank)

CHAPTER 6. ROBUSTNESS OF OPERATIONAL DAMAGE DETECTION STRATEGIES UNDER VARIABLE INFLOW CONDITIONS – FY13/FY14

In this chapter, a damage detection sensitivity analysis is presented in which the inflow conditions are varied[4]. Damage detection strategies developed in prior studies (see Chapter 4) are tested for realistic and variable inflow conditions. The highlights of this chapter include:

- Aeroelastic simulations of damaged wind turbines are performed with varied inflow conditions (varied wind speed from cut-in to cut-out, varied turbulence intensity, and varied shear profiles). In addition to the varied inflow conditions, these simulations were performed for multiple damage types and for a wide range of extents or size of damage to more comprehensively test the damage detection strategies.
- Based on this database of aeroelastic simulations, a probability of detection (POD) analysis was performed providing a statistical characterization of the performance of the damage detection strategies to identify a damaged condition using onboard sensors under the above varied inflow conditions and varied extents of damage (again, this analysis was performed for multiple damage types).
- Optimized wind speed ranges, in which probability of detecting damage is improved, were identified.
- Improved confidence was gained in the damage detection strategies (presented in Chapter 4 and refined in Chapter 6) as the detection strategies performed well in simulation testing for realistic and variable inflow conditions.

[4] Sandia Technical Report: SAND2014-15588.

SAND2014-15588
Unlimited Release
Printed July 2014

Structural Health and Prognostics Management for Offshore Wind Turbines: Sensitivity Analysis of Rotor Fault and Blade Damage with O&M Cost Modeling

Noah J. Myrent, Natalie C. Barrett, and Douglas E. Adams,
Vanderbilt Laboratory for Systems Integrity & Reliability
566 Mainstream Dr.
Nashville, TN 37228

D. Todd Griffith
Wind Energy Technology Department
Sandia National Laboratories
P.O. Box 5800
Albuquerque, New Mexico 87185-MS1124

Abstract

Operations and maintenance costs for offshore wind plants are significantly higher than the current costs for land-based (onshore) wind plants. One way to reduce these costs would be to implement a structural health and prognostic management (SHPM) system as part of a condition based maintenance paradigm with smart load management and utilize a state-based cost model to assess the economics associated with use of the SHPM system. To facilitate the development of such a system a multi-scale modeling and simulation approach developed in prior work is used to identify how the underlying physics of the system are affected by the presence of damage and faults, and how these changes manifest themselves in the operational response of a full turbine. This methodology was used to investigate two case studies: (1) the effects of rotor imbalance due to pitch error (aerodynamic imbalance) and mass imbalance and (2) disbond of the shear web; both on a 5-MW offshore wind turbine in the present report. Sensitivity analyses were carried out for the detection strategies of rotor imbalance and shear web disbond developed in prior work by evaluating the robustness of key measurement parameters in the presence of varying wind speeds, horizontal shear, and turbulence. Detection strategies were refined for these fault mechanisms and probabilities of detection were calculated. For all three fault mechanisms, the probability of detection was 96% or higher for the optimized wind speed ranges of the laminar, 30% horizontal shear, and 60% horizontal shear wind profiles. The revised cost model provided insight into the estimated savings in operations and maintenance costs as they relate to the characteristics of the SHPM system. The integration of the health monitoring information and O&M cost versus damage/fault severity information provides the initial steps to identify processes to reduce operations and maintenance costs for an offshore wind farm while increasing turbine availability, revenue, and overall profit.

CONTENTS

FIGURES

TABLES

NOMENCLATURE

AEP	annual energy production
BEM	Blade Element Momentum
BPE	Beam Property Extraction
CBM	condition based maintenance
COE	cost of energy
dB	decibel
DOE	Department of Energy
DOWEC	Dutch Offshore Wind Energy Converter Project
FAST	Fatigue, Aerodynamics, Structures, and Turbulence
FCR	fixed charge rate
FEA	Finite Element Analysis
HAWT	horizontal axis wind turbine
ICC	initial capital cost
LRC	levelized replacement cost
LSS	low speed shaft
NREL	National Renewable Energy Laboratory
NuMAD	Numerical Manufacturing and Design Tool
NWTC	National Wind Technology Center
O&M	operations and maintenance
POD	probability of detection
POMDP	Partially Observed Markov Decision Process
PS	power spectrum
RMS	root mean square
SHPM	structural health prognostics management
SNL	Sandia National Laboratories
SW	shear web
TE	trailing edge
TSA	time synchronous average

EXECUTIVE SUMMARY

Offshore wind energy could potentially play a significant role in helping the U.S. obtain an energy portfolio composed of clean, renewable and diversified resources. One current obstacle to the utilization of offshore wind energy is that most projections put the operations and maintenance (O&M) costs of offshore wind farms between 2 to 5 times the current average O&M costs for onshore wind farms [1]. One way in which those costs may be reduced is through the use of a simple yet effective structural health monitoring system as part of an overall condition based maintenance paradigm. A successful health monitoring system would be able to prevent catastrophic failures, reduce or eliminate unplanned or unnecessary maintenance, and as well reduce logistic lead times and optimize supply chain management through the use of prognostics. In addition to the use of prognostics management for maintenance process improvement, potential exists to also use prognostics to increase energy capture through smart loads management; for example, by derating the turbine so that damage growth is mitigated while revenue production continues until maintenance can be performed.

A methodology has been created to aid in the development, evaluation, and optimization of a structural health and prognostics management (SHPM) system for wind turbines using physics-based simulations and state-space cost modeling. The developed scheme is a multi-scale modeling and simulation approach [16] that propagates the effects of damage from high fidelity local simulations to full turbine simulations using reduced order models as illustrated in Figure 1. Fault and damage detection algorithms have been developed which provide information that feeds into a cost model to compare the cost of energy (COE) between a wind farm that would use a SHPM system to optimize the maintenance schedule and a wind farm which would not use such a system. Figure 2 shows the overall approach to utilizing SHM for optimizing O&M costs.

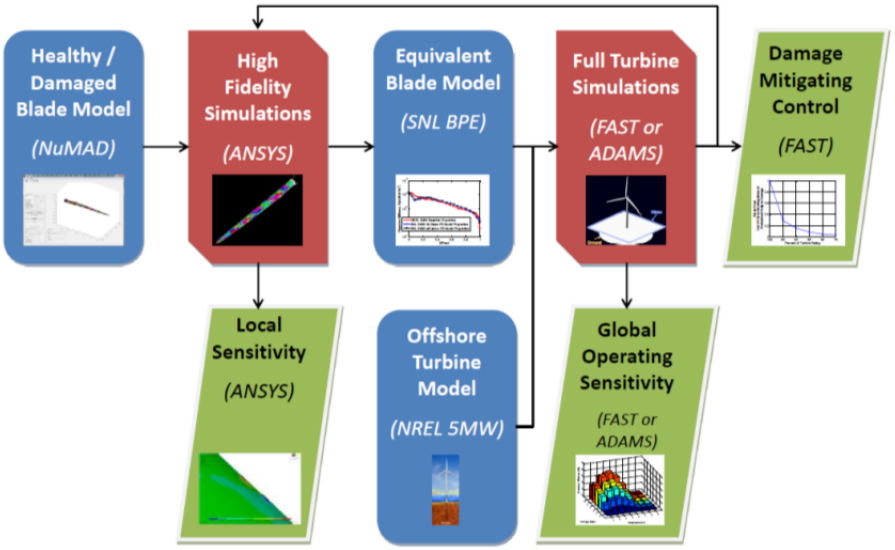

Figure 1. The multi-scale damage modeling and simulation methodology designed to aid in the development and optimization of health monitoring systems for wind turbine blades.

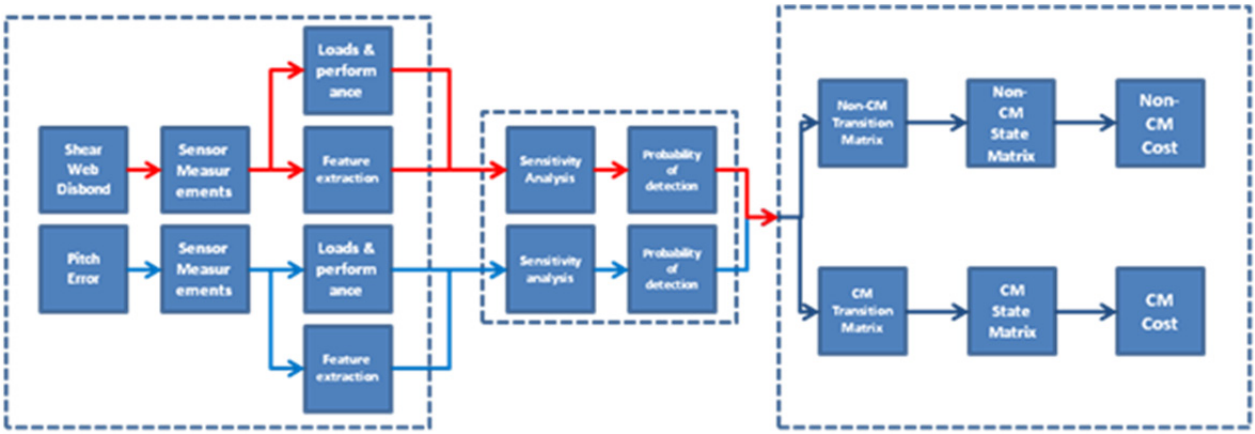

Figure 2. Overall approach for projecting COE benefits based on damage/fault detection strategies (Left Block: Operational Simulation of Damage (see Figure 1); Middle Block: Damage Sensitivity Analysis and Detection Evaluation; Right Block: Cost Analysis)

To expand on work in FY12 [16] where the multi-scale modeling and simulation methodology was implemented and the process in analyzing the effects of a rotor imbalance and shear web disbond was excercised, the work in FY13 was focused on the detection strategies developed for those faults and their sensitivity to several different inflow conditions. Stiffness analysis of the reduced degree-of-freedom beam model of the blade indicated that the SW disbond resulted in; for example, decreases in the blade's flap-wise and torsional stiffness as shown in Figure 3 (the blade root is at blade station 0 in the plots). In sensitivity analyses of the full turbine aeroelastic model incorporating the simplified blade structural model and a wide range of aerodynamic input parameters, the root mean square (RMS) power signal was a good indicator of a pitch error and the blade axial force differences proved to be a good indicator of a mass imbalance (as shown in Figures 4, 5). In addition, a combination of the RMS transverse nacelle acceleration and synchronously averaged 1p blade root pitching moment measurements were able to identify the presence and severity of a shear web disbond. Because the blade's flap-wise and torsional stiffness have a large decrease in the presence of a shear web disbond, this damage mechanism significantly affects the flap-wise and torsional operational response of the turbine. **The simulations results illustrated the benefit of the multiscale modeling approach for detection of rotor imbalances and shear web disbonds and the usefulness of this multi-scale approach to resolve the effects of damage as they are manifested as localized damage in the blade structure and global signatures in the operational sensor measurements.**

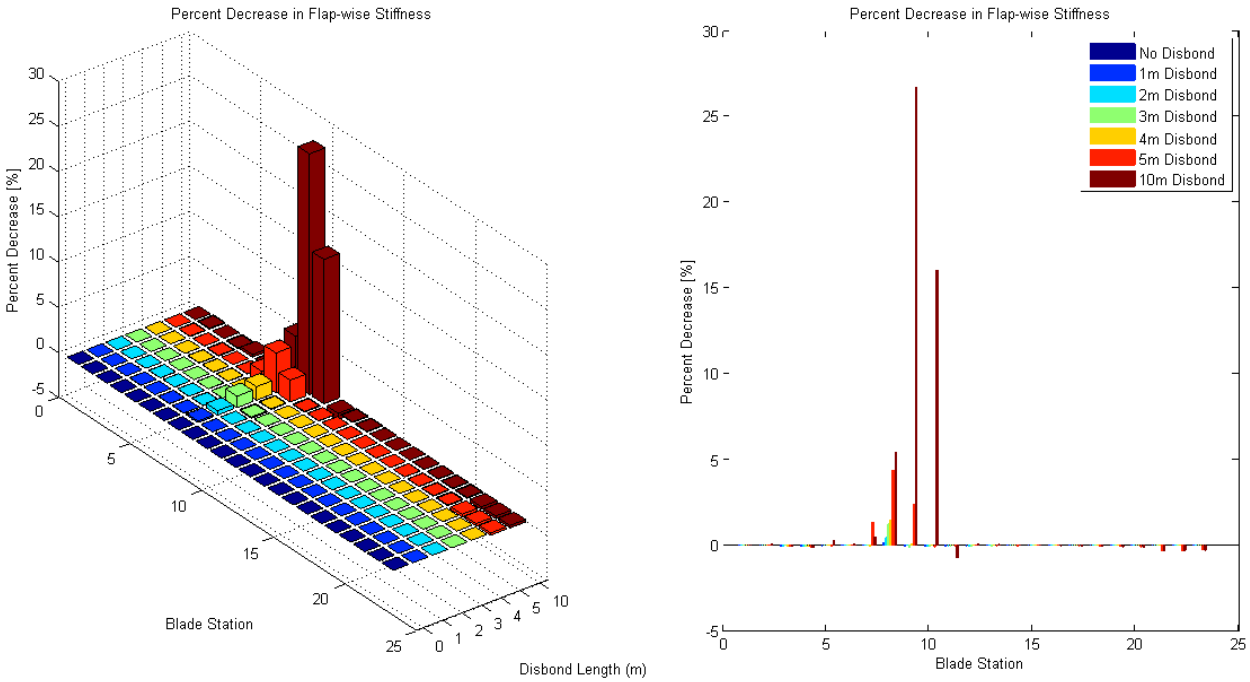

(a)

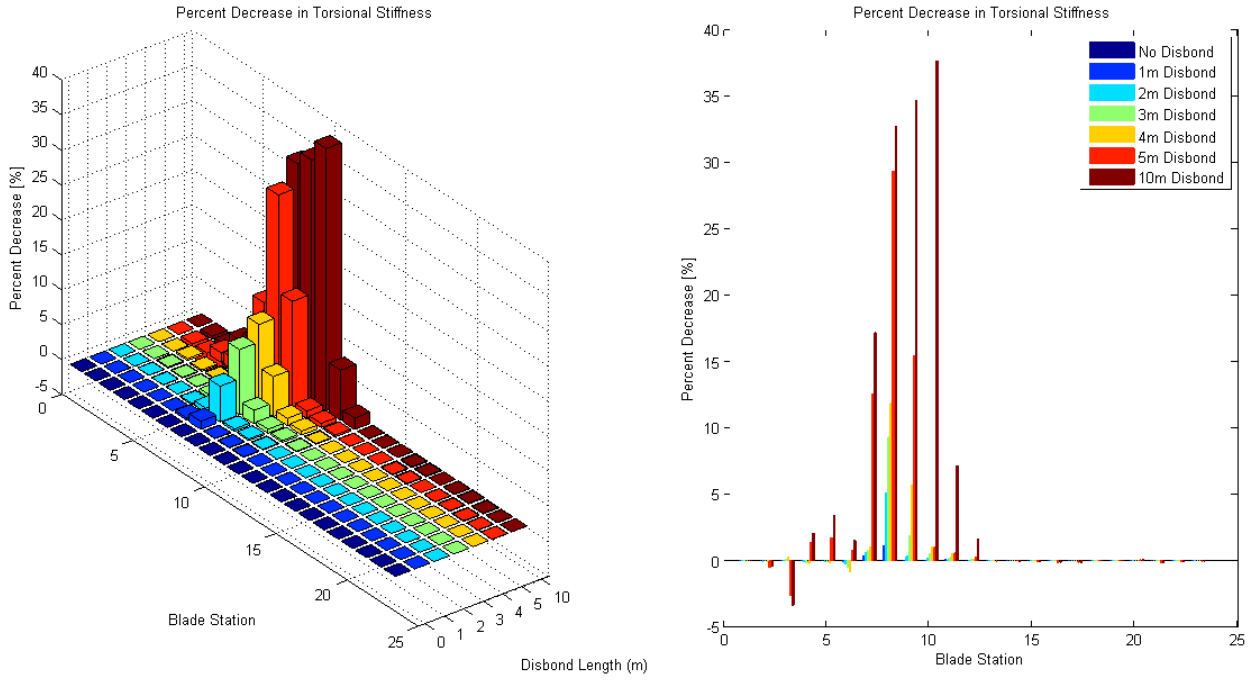

(b)

Figure 3. The percent decreases of the (a) flap-wise stiffness and (b) torsional stiffness values for varying length shear web disbonds along the span of the blade

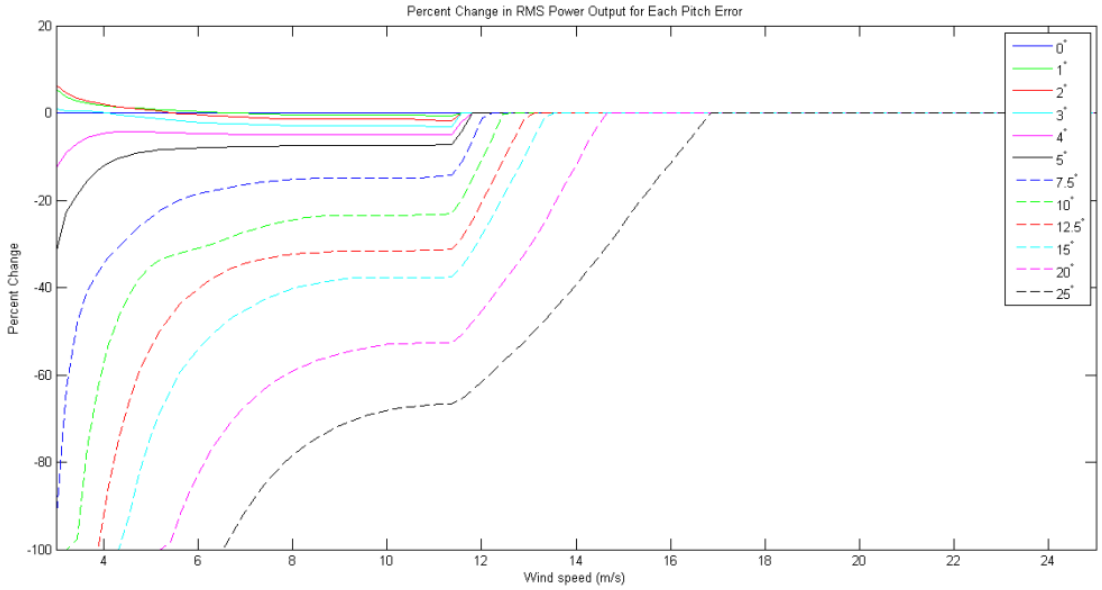

Figure 4. RMS percent change of power output for each pitch error case in varying wind speeds.

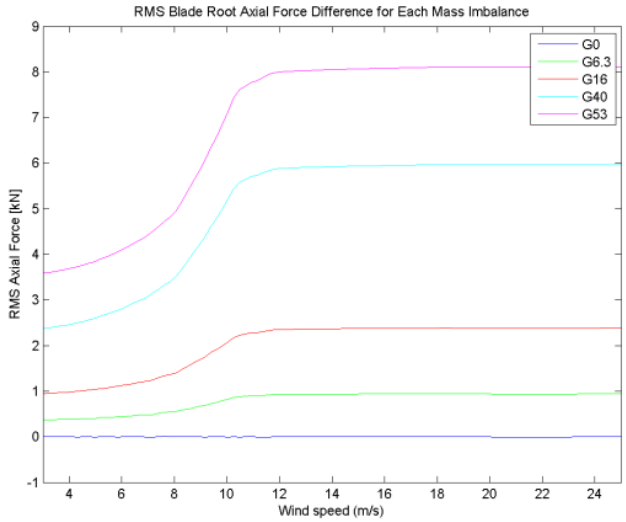

Figure 5. 1p magnitude percent change of edge-wise blade tip acceleration for shear web disbond for four different inflow conditions

A state-based cost model was developed to quantify the effect of a SHPM system on O&M costs. The cost sensitivity analysis shows that the probability of detection of rotor imbalance and shear web disbond increases with the implementation of a SHPM system. In addition, the annual energy production (AEP) increases with the use of a SHPM system. Table 1 shows the POD values of rotor imbalance and shear web disbond, collectively, for SHPM and non-SHPM systems. Figure 6 shows the AEP for SHPM and non-SHPM systems.

Table 1. Weighted Probabilities of detection for SHPM and non-SHPM systems.

Wind Speed	With SHPM	Without SHPM		
	All states	State 2	State 3	State 4
3	21%	5%	10%	16%
6.74	83%	21%	41%	62%
10.48	89%	22%	44%	67%
14.22	92%	23%	46%	69%
17.96	66%	17%	33%	50%
21.7	67%	17%	34%	50%

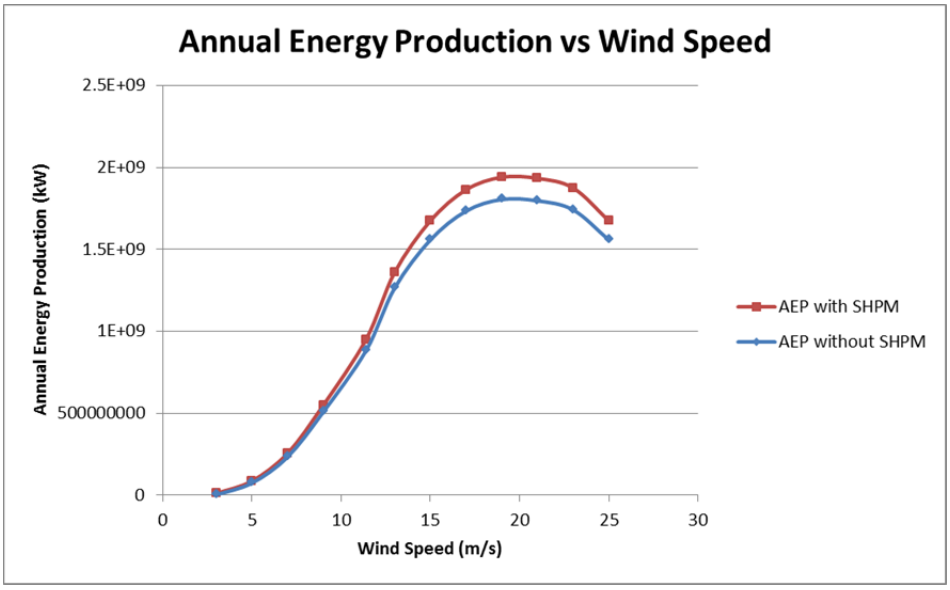

Figure 6. Annual Energy Production versus Wind Speed.

1. INTRODUCTION

Offshore wind energy in the United States is an untapped energy resource that could play a pivotal role in helping the U.S. obtain an energy portfolio composed of clean, renewable and diversified resources. Some of the drivers for the utilization of offshore wind include the proximity of the offshore resources to population centers and the potential for higher capacity factors due to higher resource winds [1]. Because of these drivers and other potential benefits of offshore wind, the Offshore Wind Innovation and Demonstration initiative has developed an ambitious goal of deploying 10 GW of offshore capacity by 2020 at a cost of energy of only $0.10/kWh [2,3].

1.1. Drivers for Offshore SHPM

As of June 2011, while nine offshore projects totaling over 2 GW of capacity were in various stages of the permitting and development process, no offshore wind energy projects had been installed in the United States [4]. Part of the reason for this lack of development is that operations and maintenance (O&M) costs are expected to be significantly higher for offshore wind turbines than onshore wind turbines. Recent projections of O&M costs have ranged between $11 and $66 U.S. dollars per megawatt-hour with the majority of estimates being between 2 to 5 times the cost of land-based (onshore) O&M [1]. These higher O&M costs represent a larger overall proportion of the cost of energy than for onshore turbines even when the large initial investment required for the installation of offshore turbines is included [5]. One of the reasons that O&M costs are likely to be higher offshore is that the offshore environment will bring with it increased loading which is relatively uncharacterized due to the lack of existing offshore installations. Offshore turbines will also have to be built to withstand the environmental harshness of the offshore environment. Lastly, access to the turbines will be difficult, costly, and occasionally not possible due to high sea states [1,8].

1.2. SHPM Benefits

One potential way in which these O&M costs could be addressed is through the use of a structural health and prognostics management (SHPM) system as part of a condition based maintenance (CBM) paradigm [6-12]. By continuously monitoring the health, or condition, of structural components in each wind turbine, required maintenance actions can be scheduled ahead of time and performed when they are needed rather than on a preset schedule or only after failure has already occurred. The benefits of a CBM strategy are expected to include less regular maintenance, the avoidance or reduction of unscheduled maintenance and improved supply chain management [8-11].

Furthermore, because wind turbines are active systems, monitoring the health of wind turbine components will allow for smart turbine load management to optimize the profit of the entire wind plant. For example, if a turbine blade becomes damaged and that damage is detected at an early stage by the SHPM system, the turbine could be derated so that small less costly repairs could be performed on the turbine. While this action would reduce the amount of power generated by the turbine in the short-term, it may allow for less extensive maintenance actions to be performed, permit additional energy capture while maintenance is being planned, extend the

overall life of the turbine, and allow for multiple turbines to be serviced during the same visit to maximize the overall profit of the wind power plant.

1.3 Summary of Prior Work in Wind Turbine Rotor SHPM Development

Although the fields of structural health monitoring and prognostics management are fairly rich in general, research in application to wind turbine rotor blades in either field is somewhat limited. Integration of the two disciplines is even more limited. Sandia has had an active program for several years to investigate sensored blades with several blade-build and field testing demonstration projects. Blades for utility-scale wind turbines typically have no sensors in the blades and blades with sensors have been limited to strain gauges in the blade root. The Sandia research involved embedding sensors along the entire blade span, which included acceleration, strain, and temperature sensors. The proposed applications for this "enhanced" blade sensing capability include structural health monitoring and active control of the rotor. These Sandia studies provided some important lessons learned regarding manufacturing of sensors into blades and selection of sensors.

In an effort to map out the SHPM problem and also provide an example case study, an initial roadmap was developed by Sandia National Laboratories for combining structural health monitoring and prognostics assets into a SHPM system with application to wind turbine rotor blades as documented in Reference 16. The key element established in this initial roadmap, the so-called multi-scale damage modeling and simulation methodology, addresses both how damage is modeled at multiple resolutions of the model and also the resulting manifestation (or effects) of damage in both the global operating dynamic response and the localized effects related to remaining life (state of health). The intent of this approach is to combine structural health monitoring and prognostic management so as to bridge the gap between being able to detect and characterize the presence of damage and then being able to make revenue-optimizing operations and maintenance decisions.

Reference 17 documents the work performed the following year in which a pilot study consisting of a simulation methodology was carried out to determine the parameters which affect the turbine's operational response in the presence of rotor imbalance and shear web disbond. Preliminary detection strategies were developed for these fault mechanisms and this report provides the results of the sensitivity analyses performed in order to ensure robustness of the detection strategies. The aim of these studies is to provide some additional information to mature the SHPM technology development for wind turbine rotors. The key elements addressed in the report include an assessment of operating sensitivity of damage to damage/fault mechanisms and development/evaluation of an updated O&M cost model.

2. THE APPROACH

In FY12, a multi-model methodology was developed that combines an evaluation of SHPM system performance with state-of-health based cost analysis. The approach permits an evaluation of O&M scenarios (O&M strategies) to identify; for example, turbine conditions strongly influenced by particular fault or damage mechanisms, detection strategies based on various measurement analysis approaches tailored for a wind turbine system, and project operations and maintenance costs with and without such a condition monitoring system. Figure 7 shows the overall approach.

The left-most block in Figure 7 describes modeling of the turbine and damage simulations. The middle block describes the sensitivity analysis performed on the operating response of the turbine including an assessment of sensors and their performance in detecting the modeled damage. The right-most block in Figure 7 describes the cost analysis for the SHPM system. The approach starts with simulations of turbines with damage then the operational response from these simulations is fed to the middle block were the data is analyzed via sensitivity of damage studies. This middle block addresses the performance of the SHPM system to identify which sensors are viable options to detect damage and also to quantify the ability to detect damage (i.e. probability of detection). State of health information and SHPM performance information is fed to the right-most block where SHPM system economics is assessed. This concept should prove useful in assessing both performance and cost of the SHPM system, and in the future it could prove useful in design of the SHPM system and in the evaluation of the return on investment of the SHPM system. This approach could also be applied in real-time operation such that information from the right-most economics module could feedback to the turbine operator or turbine control system for decision making.

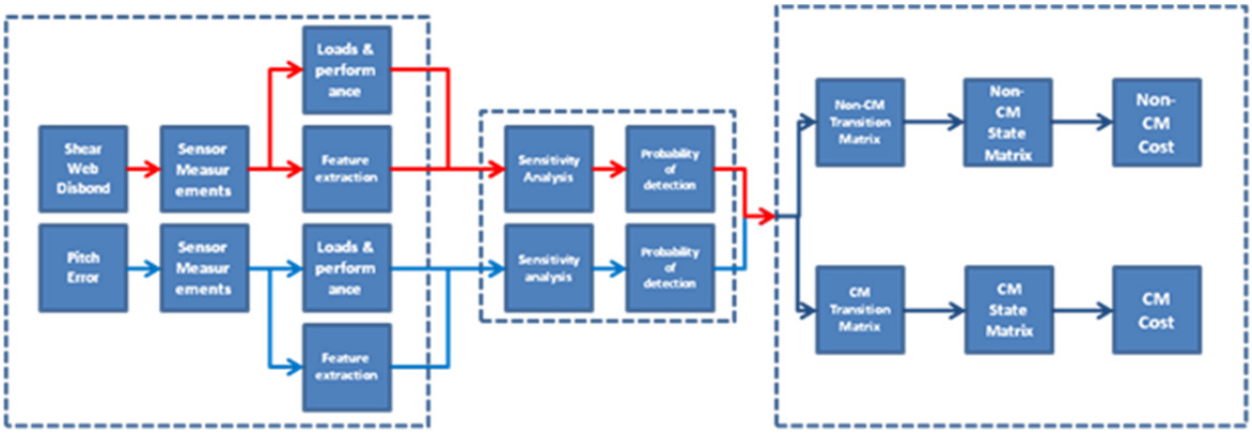

Figure 7. SHPM system feasibility quantification concept approach

The FY13 effort focused on the middle and right blocks. A sensitivity analysis was performed on the rotor imbalance and shear web disbond detection strategies in order to derive probability of detection (POD) values based on the variation of aerodynamic parameters and the extent of damage. In addition, the cost model was revised so that POD values could be used as an input to compare the cost of a wind turbine with and without a SHPM system.

In order to perform the desired simulations, a variety of different software packages were integrated in order to obtain the results of interest. Sandia National Laboratories' (SNL's) NuMAD software was used to create a high fidelity blade model in the software package ANSYS. A shear web disbond was then created in the model and equivalent beam parameters were extracted which could be integrated with a turbine model for simulations of the damaged turbine in either FAST [13] or MSC.ADAMS [14]. Results from each stage of this modeling process were then used to assess the influence of the damage on the response of the blade and the turbine as a whole and to identify a subset of measurements that could prove beneficial for future SHPM investigations.

The cost model used for this study is a state based Excel model that calculates O&M costs of a wind turbine for scenarios such as a turbine with and without an enhanced blade condition monitoring system. Four states are defined in the cost model that correspond to different extents of damage and the associated different types of maintenance that would be required in each state; for example, state 1 is associated with a blade in a new or repaired condition and at the other extreme state 4 would be associated with a blade damaged to the point beyond which it can be repaired and must be replaced.

3. 5-MW OFFSHORE TURBINE MODEL

3.1. Turbine Model Description

As part of an ongoing structural health and prognostics management project for offshore wind turbines, the simulations in this report were performed using a representative utility-scale wind turbine model. The model, known as the NREL offshore 5-MW baseline wind turbine model, was developed by NREL to support studies aimed at assessing offshore wind technology [15]. It is a three-bladed, upwind, variable-speed, variable blade-pitch-to-feather-controlled turbine and was created using available design information from documents published by wind turbine manufacturers, with a focus on the REpower 5-MW turbine. Basic specifications of the model configuration are listed in Table 2.

Table 2. Gross Properties of the NREL 5-MW Baseline Wind Turbine [16].

Property	Value
Rating	5MW
Rotor Orientation, Configuration	Upwind, 3 blades
Control	Variable Speed, Collective Pitch
Drivetrain	High Speed, Multiple-Stage Gearbox
Rotor, Hub Diameter	126 m, 3 m
Hub Height	90 m
Cut-in, Rated, Cut-out Wind Speed	3 m/s, 11.4 m/s, 25 m/s
Cut-in, Rated Rotor Speed	6.9 rpm, 12.1 rpm
Rated Tip Speed	80 m/s
Overhang, Shaft Tilt, Precone	5m, 5°, 2.5°
Rotor Mass, Nacelle Mass, Tower Mass	110,000 kg; 240,000 kg; 347,460 kg
Water Depth	20 m
Wave Model	JONSWAP/Pierson-Moskowitz Spectrum
Significant Wave Height	6 m
Platform	Fixed-Bottom Monopile

A new blade model was developed to be used with the NREL 5-MW turbine model, which is the same model used in the initial studies (Ref). A detailed blade model did not exist and was needed so that damage could be introduced into the blade structure within the multi-scale modeling and simulation framework (as described above). The detailed blade model was developed by Sandia National Laboratories using blade geometry data from the Dutch Offshore Wind Energy Converter Project (DOWEC) and composite layup information from the European Union's UpWind program. The distribution of material layers along the blade span is illustrated in Figure 8.

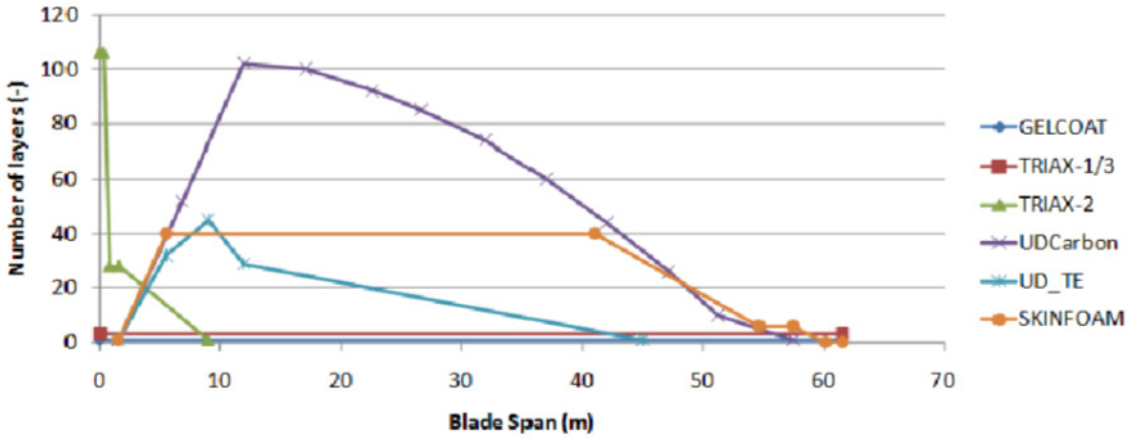

Figure 8. Model of the Distribution of Material Layers along the Span of the Blade, (Griffith, et al. 2011).

Two thirds of the blade span utilizes the TU-Delft family of airfoils, while the final one-third of the blade span utilizes the NACA 64-series airfoils. Intermediate airfoil shapes were developed that preserve the blending of camber lines as well as a smooth blade thickness profile. Figure 9 shows the finite element model of the blade in ANSYS with the colored sections representing different composite materials. This high degree-of-freedom model was translated into a model consisting of several beam elements using Sandia's Blade Property Extraction tool (BPE). BPE works by applying loads in each of the six degrees of freedom at the tip of the blade model in ANSYS, then processing the resulting displacements at selected nodes along the blade to generate the 6x6 Timoshenko stiffness matrices for the beam discretization. This reduced degree-of-freedom model is subsequently used to define the blade properties in FAST. For a more detailed description of BPE, see [16].

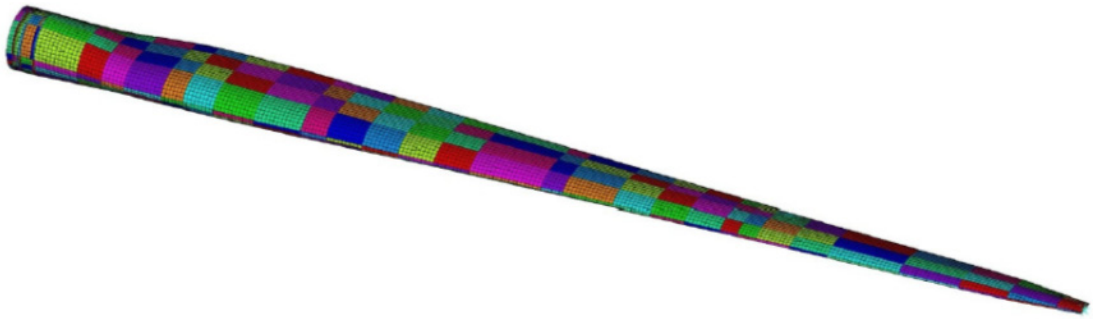

Figure 9. ANSYS finite element mesh for the 5-MW blade model.

3.1.1. *FAST Simulation Turbine Coordinate Systems*

FAST uses six coordinate systems for input and output parameters. Some of these coordinate systems will be referred to throughout this report, so they are reproduced here from the FAST User's Guide for convenience. Note that the FAST User's Guide coordinate system images use a downwind turbine configuration; however, the same coordinate systems apply in the case of the upwind turbine being referred to in this work, but the orientation of the x axis changes so that in either configuration it is pointing in the nominally downwind direction. The rotor shaft

coordinate system is shown in Figure 10. This coordinate system does not rotate with the rotor, but it translates and rotates with the tower and yaws with the nacelle. In addition to output variables related to the low speed shaft, the nacelle inertial measurements also use this coordinate system. Some shaft outputs, such as shear force in the low speed shaft, are measured in both a non-rotating coordinate system and a rotating coordinate system; these are differentiated by using an "s" or "a" subscript, respectively. The tower base coordinate system shown in Figure 11 is fixed in the support platform, thus rotating and translating with the platform. The tower-top/base-plate coordinate system shown in Figure 12 is fixed to the top of the tower. It translates and rotates with the motion of the platform and tower top, but it does not yaw with the nacelle.

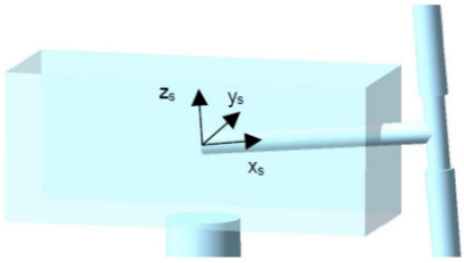

Figure 10. Shaft Coordinate System (Jonkman and Buhl 2005).

Figure 11. Tower Base Coordinate System (Jonkman and Buhl 2005).

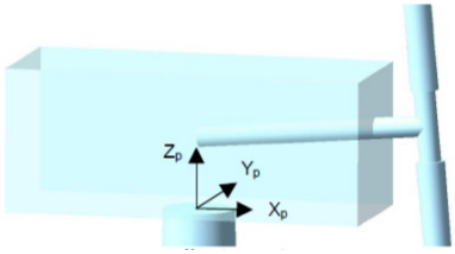

Figure 12. Tower-top/base-plate coordinate system (Jonkman and Buhl 2005).

4. ROTOR MASS/AERODYNAMIC IMBALANCE SENSITIVITY STUDY

4.1. Introduction

A comprehensive aerodynamic uncertainty analysis was conducted to evaluate the detection strategies developed using operational measurements as features to assert the presence and severity of a pitch error or a mass imbalance. Although simultaneous pitch error and mass imbalance was investigated in the pilot study, this sensitivity analysis focuses on solely detecting either a pitch error or mass imbalance. 11,312 FAST simulations were performed to evaluate the robustness of the pitch error and mass imbalance detection strategies and examine their sensitivity to varying parameters including wind speed, horizontal shear, turbulence, and imbalance severity. All of the damage cases for both types of imbalance were applied the same way as in the pilot study. This section includes a variety of different sensitivity analyses that were conducted at various stages throughout the modeling and simulation processes.

4.2. Sensitivity Analysis Methods and Parameters

For this sensitivity analysis, the parameters which were varied include the extent of damage and inflow conditions for the turbine. The NREL offshore 5-MW baseline wind turbine model and FAST were used to simulate the varying parameters. Table 3 shows the matrix of FAST simulations performed for the sensitivity analysis. Operational measurements were analyzed for a healthy turbine in addition to turbines with one of the three blades having a certain level of pitch error or mass imbalance. Mean wind speed, horizontal shear, and turbulence were among the aerodynamic parameters used in this study. For all of the wind profiles, a 1/7 power law vertical shear profile was applied. For all wind profiles, the wind speed was varied from 3 m/s to 25 m/s in 0.22 m/s increments (totaling 101 simulations per turbine damage type). Horizontal shear parameters of 0.3, 0.6, and 0.9 (or 30%, 60%, and 90% horizontal shear) were used (totaling 303 simulations per turbine damage type). The horizontal wind shear parameter is expressed as a linear spectrum of wind speed across the rotor disc. The horizontal wind shear parameter is ranged between -1 and 1, and it represents the wind speed at the blade tip on one side of the rotor minus the wind speed at the blade tip on the opposite side of the rotor, divided by the hub-height wind speed. The horizontal shear is measured in the direction perpendicular to the normally prevailing wind vector. The turbulence models used include the IEC Kaimal Model with A turbulence, the IEC Kaimal Model with B turbulence, and the NREL NWTC wind model with a KHTEST intense disturbance (totaling 303 simulations per turbine damage type).

Table 3. Number of FAST simulations run for each blade imbalance type.

	Pitch Error (0^o, 1^o, 2^o, 3^o, 4^o, 5^o, 7.5^o, 10^o, 15^o, 20^o, 25^o)	**Mass Imbalance (G00, G06, G16, G40, G53)**
Wind Speed (3 – 25 m/s)	**1111**	**505**
Horizontal Shear (30%, 60%, 90%)	**3333**	**1515**
Turbulence (A, B, KHTEST)	**3333**	**1515**

4.3. Analysis of Measurements Used for Detection Strategy

4.3.1. *Pitch Error Analysis Results*

The following sections summarize the trends in the results for pitch error aerodynamic imbalance in the aerodynamic sensitivity study, as measured in the generator power output, nacelle inertial sensors, and low speed shaft bending moments.

4.3.1.1. Generator Power

Since the generator power was used to determine a blade pitch error in the pilot study, this parameter was once again analyzed in order to determine if it can be used for the refined rotor imbalance detection strategy. The rotor azimuth position output from FAST was used as the reference signal for time synchronous averaging. The rotational resampling was performed in the same way as described in the pilot study. The azimuth signal was converted to radians, unwrapped and then the measurement signal was interpolated so that each revolution contained the same number of data samples with each sample corresponding to the same azimuth position of the rotor's rotation. Three revolutions of data blocks were averaged together. By using more than one revolution in the block size, the length of the block's time history could be increased which in turn increases the frequency resolution of the DFT of the time-averaged signal.

As expected, the generator power decreased in the presence of increasing pitch errors when varying the wind speed, horizontal shear, and turbulence wind profiles. As the wind speed increases beyond the turbine's rated speed of 11.4 m/s, the generator power for the damage cases converge with the healthy case. In addition, the wind speed at which the generator power for damage and healthy cases converge increases as the amount of pitch error is also increased. These results reinforce the importance of detecting an aerodynamic imbalance before it becomes severe. Figures 13 and 14 show the RMS power and percent change in power output for the laminar wind profile in the presence of a pitch error.

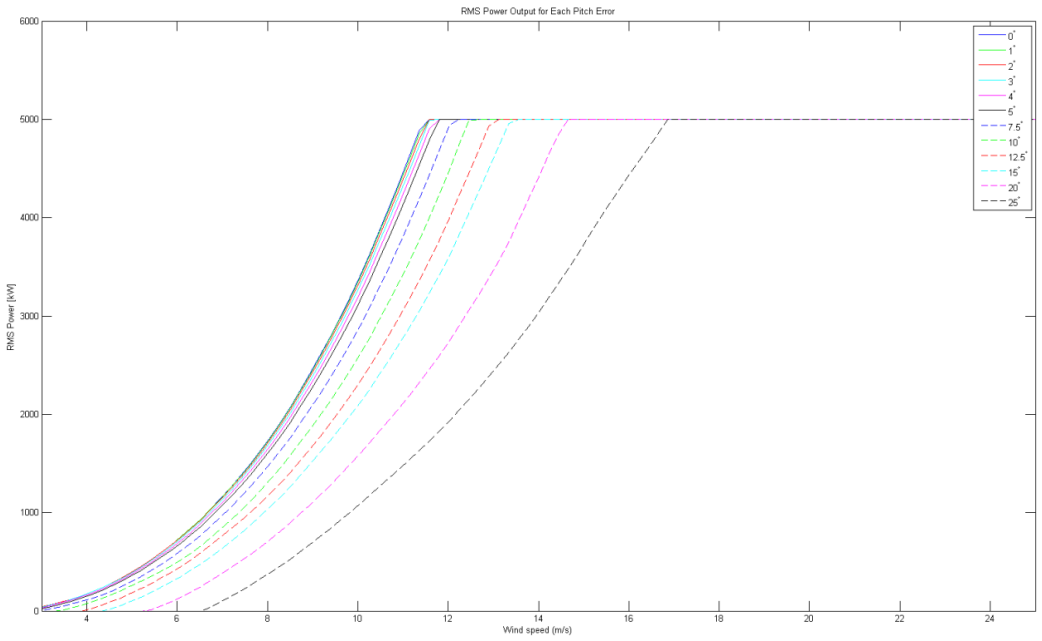

Figure 13. RMS power output for each pitch error case in varying wind speeds.

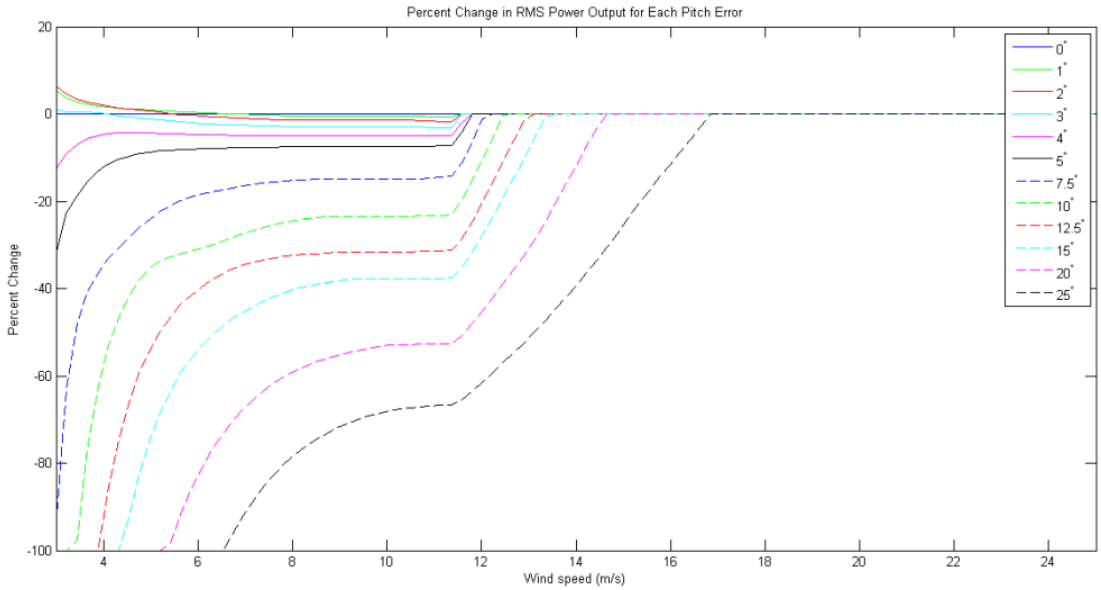

Figure 14. RMS percent change of power output for each pitch error case in varying wind speeds.

4.3.1.2. Low Speed Shaft Bending Moment

The low speed shaft (LSS) bending moment also displayed significant changes due to pitch error. Figure 15 shows the RMS rotating LSS bending moment for each pitch error case. As was seen in the RMS power output, the RMS LSS bending moment decreased as the pitch error increased for wind speeds up to 16.86 m/s. Since the generator power can be subject to electrical faults, measurements of the LSS torque may be a better feature choice, especially since it shares the same trends as the RMS power output.

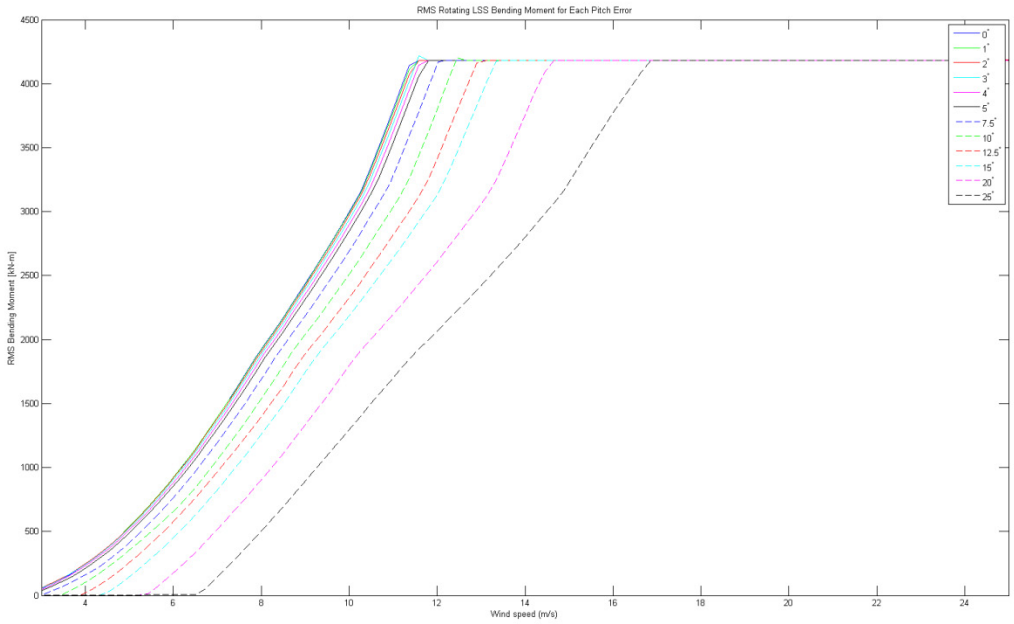

Figure 15. RMS low speed shaft bending moment for each pitch error case in varying wind speeds.

4.3.2. *Mass Imbalance Analysis Results*

The following sections summarize the trends in the results for mass imbalance in the aerodynamic sensitivity study, as measured in the same non-blade measurements of generator power output and low speed shaft bending moment.

4.3.2.1. Generator Power

Figure 16 shows the percent change in RMS power output under several mass imbalance cases. The figure indicates that the RMS power output remained unchanged in the presence of five different levels of mass imbalance: G0 (baseline, no imbalance), G6.3, G16, G40, and G53 (representing the 0.5% total blade mass imbalance). Since only pitch error affects the RMS power output, this would serve as a good indicator of an aerodynamic imbalance.

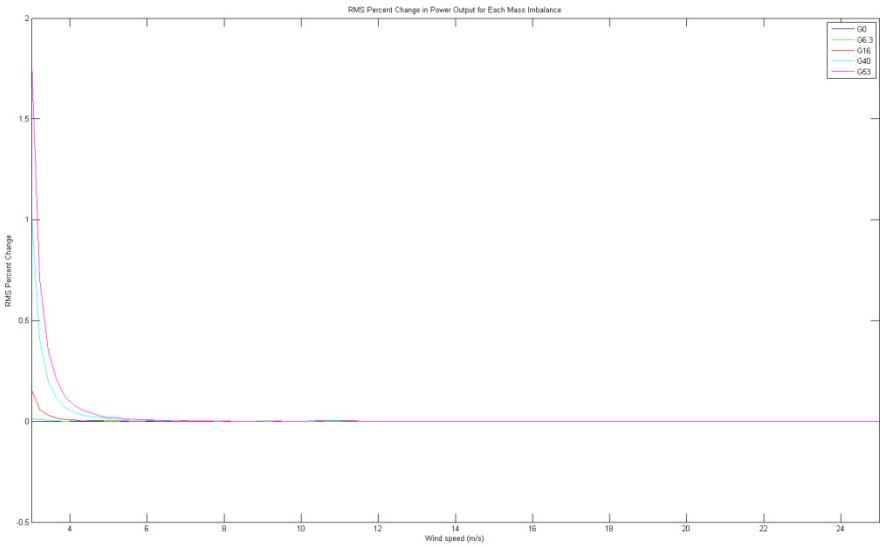

Figure 16. Percent change in RMS power output for each mass imbalance case in varying wind speeds.

4.3.2.2. Blade Root Axial Force

The blade root axial force was used to determine a blade mass imbalance in the pilot study, so this parameter was again analyzed in order to determine if it can be used for the refined rotor imbalance detection strategy. The time synchronous averaging and rotational resampling were performed the same way as described in Section 4.3.1.1.

The blade root axial force again increased in the presence of increasing mass imbalances for all wind profiles. Up to the rated speed of the turbine, the RMS axial force diverged with wind speed as the mass imbalance increased. After the turbine reaches its rated speed, the blade root axial force differences remain constant. Figures 17 and 18 show the RMS blade root axial force differences for the laminar and A turbulence wind profiles in the presence of a mass imbalance.

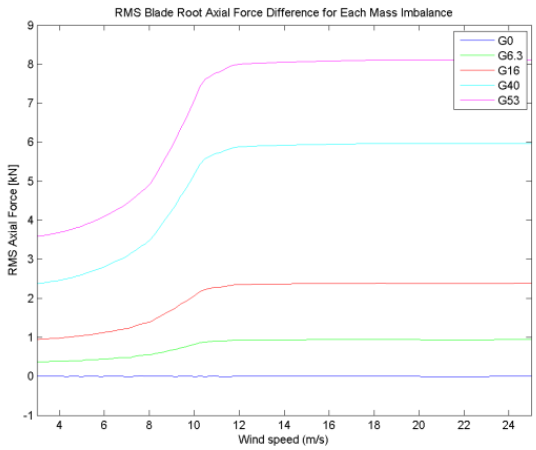

Figure 17. RMS blade root axial force for mass imbalance in varying wind speeds.

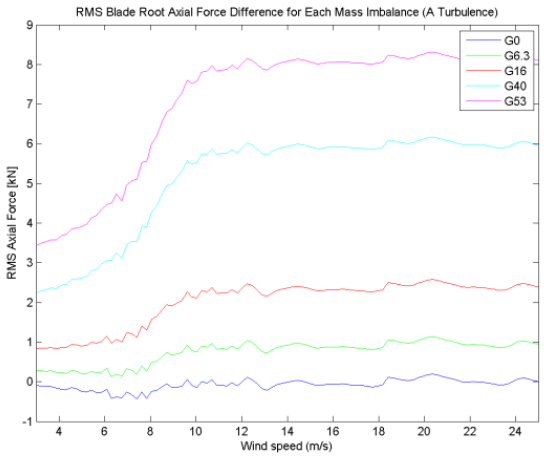

Figure 18. RMS blade root axial force for mass imbalance in A turbulence.

4.4. Summary of Imbalance Detection Strategy Refinements

The results of the sensitivity analysis and key measurements have been used to refine a rotor imbalance detection strategy. This strategy employs both blade and non-blade sensor measurements. Specifically, non-blade sensor measurements are used as the indicator for a pitch error and the blade sensors (strain gages at the blade root to measure the axial force) are used to detect a mass imbalance and its level of severity. The action strategy and flow chart have not changed; however, each rotor imbalance has been assigned thresholds corresponding to the severity of the imbalance, as shown below in Tables 4 and 5 for pitch error and mass imbalance, respectively.

Table 4. Pitch error damage state and corresponding feature used for classification

State 1 (Healthy, 0^o pitch error)	Measured RMS power >= expected healthy RMS power
State 2 (2^o, 3^o, 4^o, 5^o pitch errors)	Greater than zero and less than 10% decrease in measured RMS power
State 3 (7.5^o, 10^o, 12.5^o, 15^o pitch errors)	Greater than 10% and less than 51% decrease in measured RMS power
State 4 (20^o, 25^o, and higher pitch errors)	Greater than 51% decrease in measured RMS power

Table 5. Mass imbalance damage state and corresponding feature used for classification

State 1 (Healthy, no mass imbalance)	Measured blade axial force difference >= 300 N increase in expected healthy blade axial force difference
State 2 (G6.3 mass imbalance)	Greater than or equal to 300 N and less than 950 N increase in measured blade axial force difference
State 3 (G16 mass imbalance)	Greater than 950 N and less than 2300 N increase in measured blade axial force difference
State 4 (G40, G53, and higher mass imbalances)	Greater than 2300 N increase in measured blade axial force difference

Probability of detection values were calculated for detecting the presence of a pitch error or mass imbalance in addition to detecting three different damage states which vary by severity. See

Tables 4 and 5 for the damage state classifications of pitch error and mass imbalance, respectively. These damage state classifications were used for each FAST simulation and inflow condition. **If the measurement at a given wind speed, profile, and damage state met the criteria described in the tables above, then it was deemed a success. Otherwise, it was deemed a failure.** For example, the blade root axial force is extracted from the simulation for the 3.88 m/s laminar wind profile and for a turbine with a blade which has a G16 mass imbalance. If the blade root axial force difference is greater than 950 N and less than 2300 N, then the detection is a success and given a "1" value at that data point. If it does not meet the criteria, it is given a "0" value. The number of successes is then added up for each POD category and that total is divided by the total number of simulations in that category (101 simulations for the full wind speed range of 3–25 m/s). The resultant percentage is the probability of detection for that damage state and wind profile. For state 2 through 4, the POD is calculated for the probability that the presence of damage is detected in addition to the classification for that damage class, respectively. Tables 6 and 7 show the POD values for detecting the presence of a pitch error or mass imbalance and then categorizing the damage into each damage case, respectively.

The PODs were calculated over the entire wind speed range in addition to an enhanced wind speed range which optimizes the resulting POD value for accurate damage detection for all wind loading cases. In other words, the measurements, algorithms, and probability of detection calculations are only done within the wind speed range defined in the tables below. The optimized wind speed range and corresponding POD values are highlighted in green in the table. In addition, each POD value was weighted by the Weibull distribution to incorporate the frequency of each wind speed used within the analyzed range. The weighted pitch error POD results show that the developed algorithms are at least 96.28% successful for all of the FAST simulations except the turbulence cases for damage states 3 and 4. Since the weighted success rate of detecting the presence of a pitch error is 96.28% or higher, those pitch errors which fail to be classified in states 3 and 4 in turbulent conditions will still be detected as being in a damaged state. If the algorithm is unable to classify the pitch error severity, then another measurement will be made as soon as the inflow is no longer turbulent. Inflow characteristics can be defined with an ultrasonic anemometer in order to determine the wind profile. As for mass imbalance, its PODs were 100% successful in the optimized wind speed range for all wind profiles.

Table 6. Probabilities of detection for pitch error

		PRESENCE OF DAMAGE		STATE 2 (2, 3, 4, 5 deg error)		STATE 3 (7.5, 10, 12.5, 15 deg error)		STATE 4 (20, >= 25 deg error)	
		3 - 25 m/s	6 - 11.4 m/s	3 - 25 m/s	6 - 11.4 m/s	3 - 25 m/s	6 - 11.4 m/s	3 - 25 m/s	6 - 11.4 m/s
LAMINAR	Raw	36.63%	100.00%	34.09%	100.00%	9.07%	96.00%	14.15%	100.00%
	Weibull Weighted	59.12%	100.00%	54.16%	100.00%	25.13%	96.10%	36.52%	100.00%
30% SHEAR	Raw	41.58%	100.00%	38.70%	100.00%	10.29%	96.00%	16.06%	100.00%
	Weibull Weighted	64.99%	100.00%	59.54%	100.00%	27.62%	96.10%	40.14%	100.00%
60% SHEAR	Raw	39.60%	100.00%	36.86%	100.00%	9.41%	96.00%	15.29%	100.00%
	Weibull Weighted	63.36%	100.00%	58.05%	100.00%	25.98%	96.10%	39.13%	100.00%
90% SHEAR	Raw	36.63%	50.00%	33.73%	96.00%	9.07%	96.00%	14.15%	96.00%
	Weibull Weighted	60.05%	96.41%	54.17%	96.41%	25.62%	96.41%	37.09%	96.41%
A TURBULENCE	Raw	92.08%	96.00%	87.52%	96.00%	17.32%	61.44%	22.79%	42.24%
	Weibull Weighted	89.97%	96.28%	84.84%	96.28%	29.50%	63.11%	34.44%	43.28%
B TURBULENCE	Raw	94.06%	100.00%	89.40%	100.00%	18.63%	64.00%	23.28%	44.00%
	Weibull Weighted	93.30%	100.00%	87.97%	100.00%	32.02%	65.55%	35.71%	44.95%
KHTEST TURBULENCE	Raw	36.63%	100.00%	34.82%	100.00%	6.17%	52.00%	8.71%	40.00%
	Weibull Weighted	60.48%	100.00%	57.03%	100.00%	17.59%	53.26%	22.07%	40.78%

Table 7. Probabilities of detection for mass imbalance

		PRESENCE OF DAMAGE		STATE 2 (G6.3 IMBALANCE)		STATE 3 (G16 IMBALANCE)		STATE 4 (G40, >= G53 IMBALANCE)	
		3 - 25 m/s	11.4 - 25 m/s	3 - 25 m/s	11.4 - 25 m/s	3 - 25 m/s	11.4 - 25 m/s	3 - 25 m/s	11.4 - 25 m/s
LAMINAR	Raw	100.00%	100.00%	99.01%	100.00%	99.01%	100.00%	100.00%	100.00%
	Weibull Weighted	100.00%	100.00%	98.98%	100.00%	98.98%	100.00%	100.00%	100.00%
30% SHEAR	Raw	100.00%	100.00%	99.01%	100.00%	99.01%	100.00%	100.00%	100.00%
	Weibull Weighted	100.00%	100.00%	98.98%	100.00%	98.98%	100.00%	100.00%	100.00%
60% SHEAR	Raw	100.00%	100.00%	100.00%	100.00%	100.00%	100.00%	100.00%	100.00%
	Weibull Weighted	100.00%	100.00%	100.00%	100.00%	100.00%	100.00%	100.00%	100.00%
90% SHEAR	Raw	100.00%	100.00%	100.00%	100.00%	100.00%	100.00%	100.00%	100.00%
	Weibull Weighted	100.00%	100.00%	100.00%	100.00%	100.00%	100.00%	100.00%	100.00%
A TURBULENCE	Raw	80.20%	100.00%	71.46%	100.00%	71.46%	100.00%	78.61%	100.00%
	Weibull Weighted	70.46%	100.00%	60.40%	100.00%	60.40%	100.00%	68.98%	100.00%
B TURBULENCE	Raw	80.20%	100.00%	71.46%	100.00%	71.46%	100.00%	79.40%	100.00%
	Weibull Weighted	70.52%	100.00%	60.40%	100.00%	60.40%	100.00%	69.80%	100.00%
KHTEST TURBULENCE	Raw	85.15%	100.00%	79.25%	100.00%	79.25%	100.00%	84.31%	100.00%
	Weibull Weighted	78.83%	100.00%	72.19%	100.00%	72.19%	100.00%	78.03%	100.00%

5. SHEAR WEB DISBOND SENSITIVITY STUDY

5.1. Introduction

A comprehensive aerodynamic uncertainty analysis was also conducted to evaluate the detection strategy developed using operational measurements as features to assert the presence and severity of a shear web disbond (as described in the FY12 report). 4,949 FAST simulations were performed to evaluate the robustness of the shear web disbond detection strategy and examine its sensitivity to varying parameters including wind speed, horizontal shear, turbulence, and disbond length. All of the disbonds were assumed to have initiated at max chord of the blade (at the 14.35 meter span location) and propagated outwards toward the tip of the blade. This section includes a variety of different sensitivity analyses that were conducted at various stages throughout the modeling and simulation processes.

5.2. Sensitivity Analysis Methods and Parameters

For this sensitivity analysis, the parameters which were varied include the extent of damage and inflow conditions for the turbine. The NREL offshore 5-MW baseline wind turbine model and FAST were used to simulate the varying parameters. Table 8 shows the matrix of FAST simulations performed for the sensitivity analysis. Operational measurements were analyzed for a healthy turbine in addition to turbines with one of the three blades containing a shear web disbond of 1, 2, 3, 4, 5, or 10 meters in length. Mean wind speed, horizontal shear, and turbulence were among the aerodynamic parameters used in this study. The wind profiles were defined as described for the rotor imbalance sensitivity analysis in Section 4.

Table 8. Number of FAST simulations performed for each blade damage type.

	Healthy	1m Disbond	2m Disbond	3m Disbond	4m Disbond	5m Disbond	10m Disbond
Wind Speed (3 – 25 m/s)	101	101	101	101	101	101	101
Horizontal Shear (30%, 60%, 90%)	303	303	303	303	303	303	303
Turbulence (A, B, KHTEST)	303	303	303	303	303	303	303

5.3. Shear Web Disbond Sensitivity and Structural Effects

The shear web disbond damage cases were expanded to include disbond lengths of 1, 2, 3, 4, 5, and 10 meters. The stiffness values of each blade damage case were extracted from each section of their reduced order models. Figures 19-22 show the percent decreases in edge-wise, flap-wise, torsional, and axial stiffness, respectively. As expected, all four stiffness parameters decreased at the damage location as the disbond length was increased. The shear web disbond also greatly affected the blade's torsional stiffness, reiterating that measurements which are sensitive to the blade's torsional response will be good indicators that a shear web disbond is present.

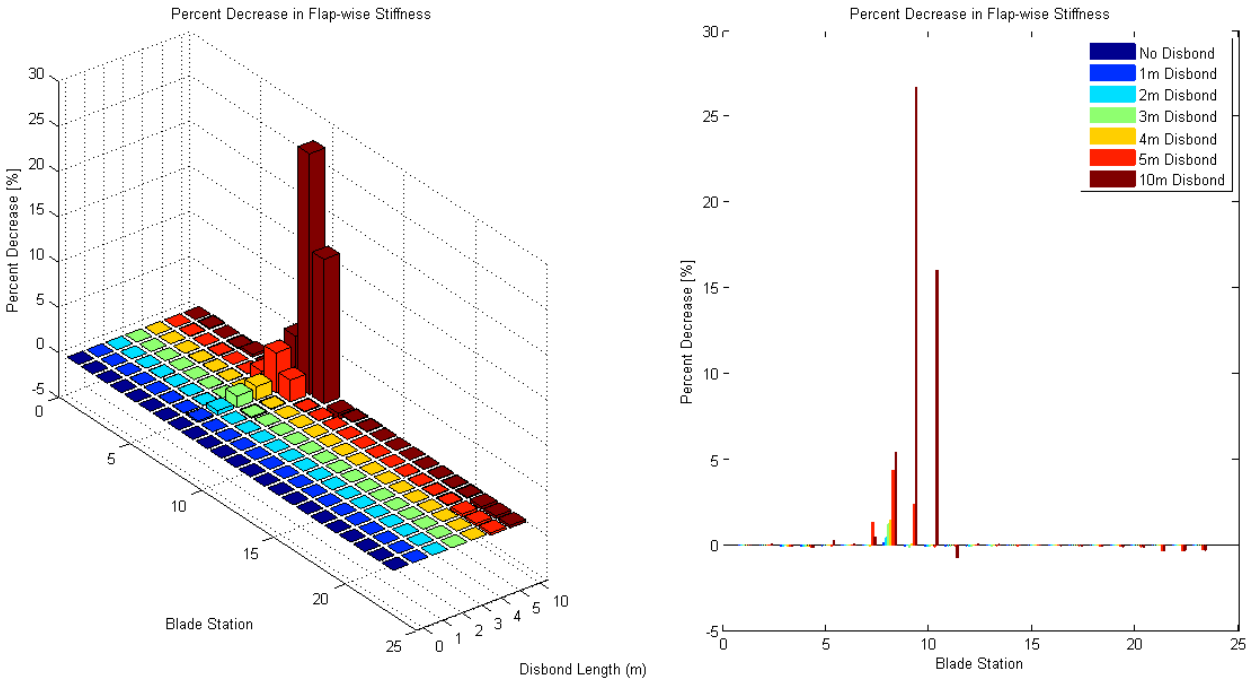

Figure 19. The percent decreases of the flap-wise stiffness value for varying length disbonds for segments spaced along the length of the blade

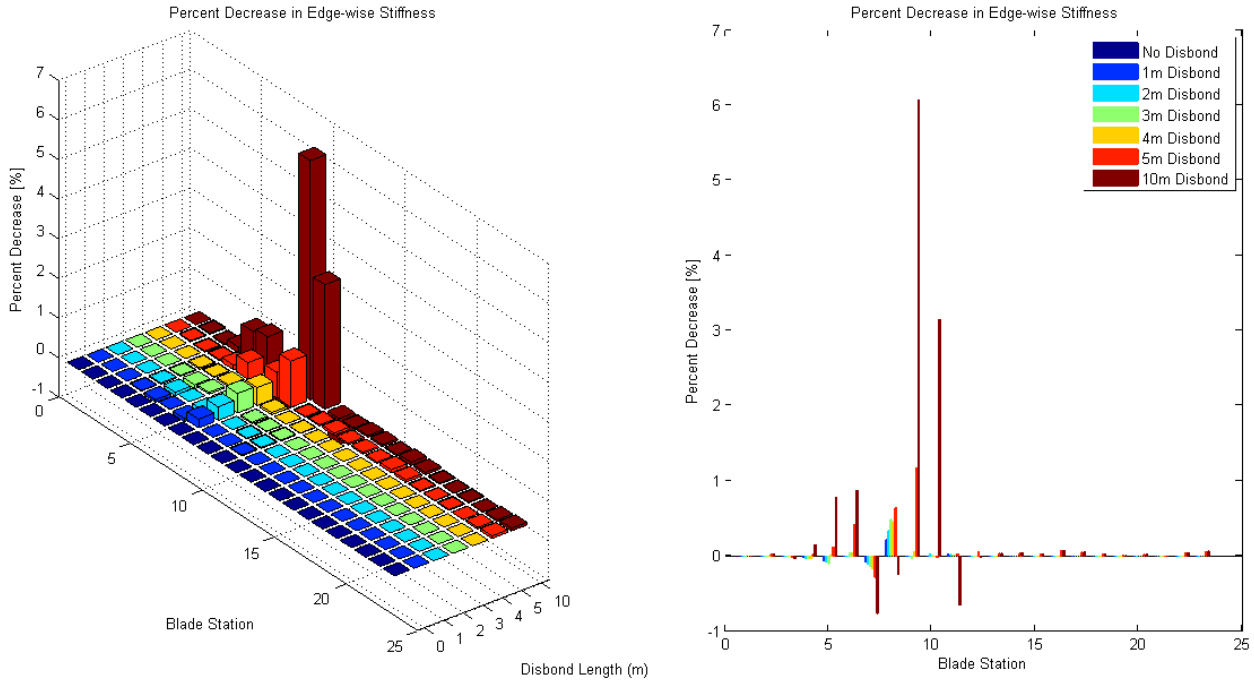

Figure 20. The percent decreases of the edge-wise stiffness value for varying length disbonds for segments spaced along the length of the blade

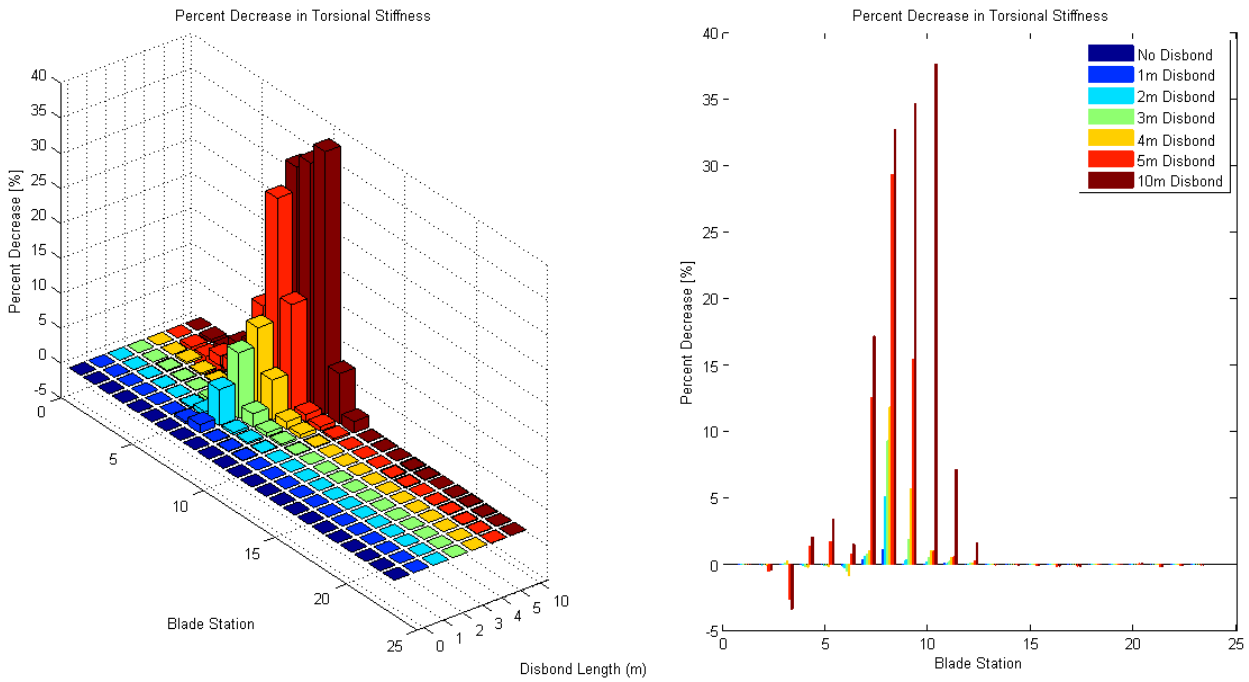

Figure 21. The percent decreases of the torsional stiffness value for varying length disbonds for segments spaced along the length of the blade

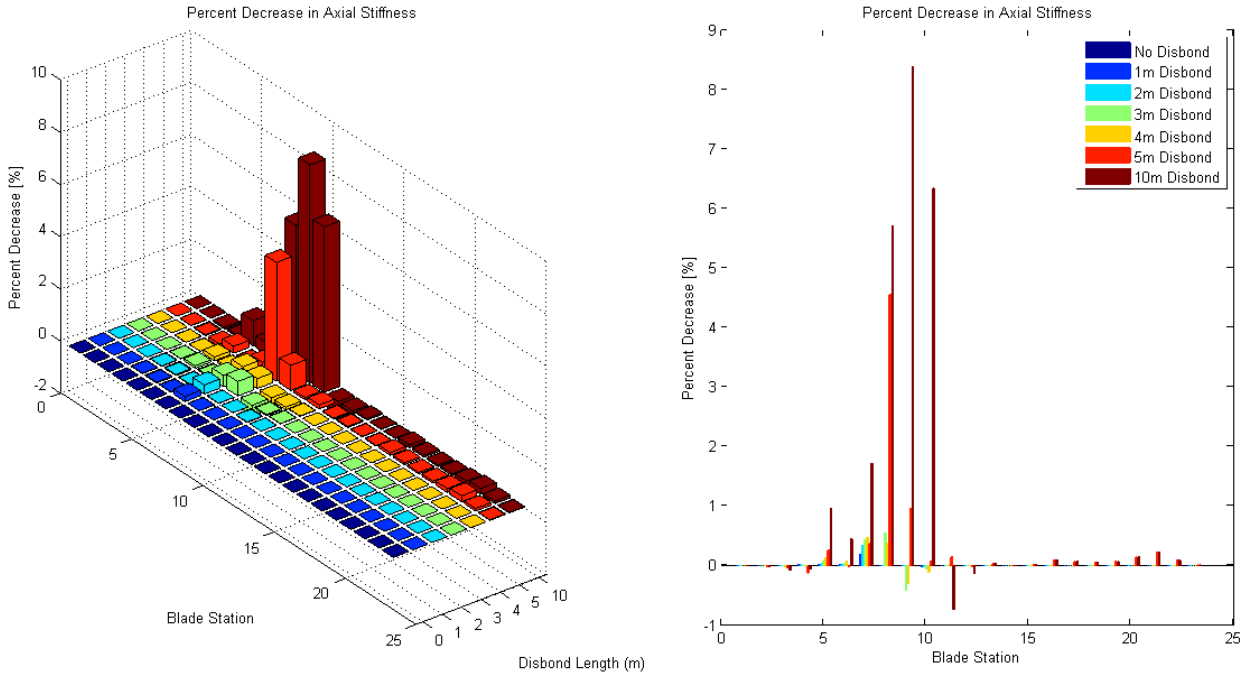

Figure 22. The percent decreases of the axial stiffness value for varying length disbonds for segments spaced along the length of the blade

5.4. Analysis of Measurements Used for Detection Strategy

Analysis was once again applied to blade and non-blade sensors to compare the effectiveness and robustness of the shear web disbond detection strategy described in the FY12 report. All measurements outlined in FY12 were examined to determine if any non-bladed sensors could be used for a refined detection strategy. From the variables analyzed from the FAST simulation outputs, those which displayed significant percentage changes in their RMS value or frequency response magnitude at the operating speed given a blade shear web disbond were identified as key measurement channels. The rotor azimuth position output from FAST was used as the reference signal for time synchronous averaging. The rotational resampling was performed in the same way as described in the FY12 report. The azimuth signal was converted to radians, unwrapped and then the measurement signal was interpolated so that each revolution contained the same number of data samples with each sample corresponding to the same azimuth position of the rotor's rotation. Three revolutions of data blocks were averaged together. By using more than one revolution in the block size, the length of the block's time history could be increased which in turn increases the frequency resolution of the DFT of the time-averaged signal. The shear web disbond detection algorithms for the selected measurements all functioned in a similar way: detecting changes from baseline measurements either in the RMS response or 1p power spectral density magnitude.

5.4.1. *Shear Web Disbond Analysis Results*

The following sections summarize the trends in the results for shear web disbond, as measured in the generator power output and magnitude of the nacelle inertial sensors, blade tip inertial sensors, blade root strain sensors, and blade root inertial sensors.

5.4.1.1. Generator Power

Overall, the generator power did not change significantly in the presence of a shear web disbond when varying the wind speed, horizontal shear, and turbulence wind profiles. The power output experienced a few transients between the cut-in and rated speeds during the turbulent simulations, although all of the power output changes after the turbine reached the rated speed were negligible. Figure 23 shows the RMS percent change in power output for the laminar wind profile in the presence of a shear web disbond.

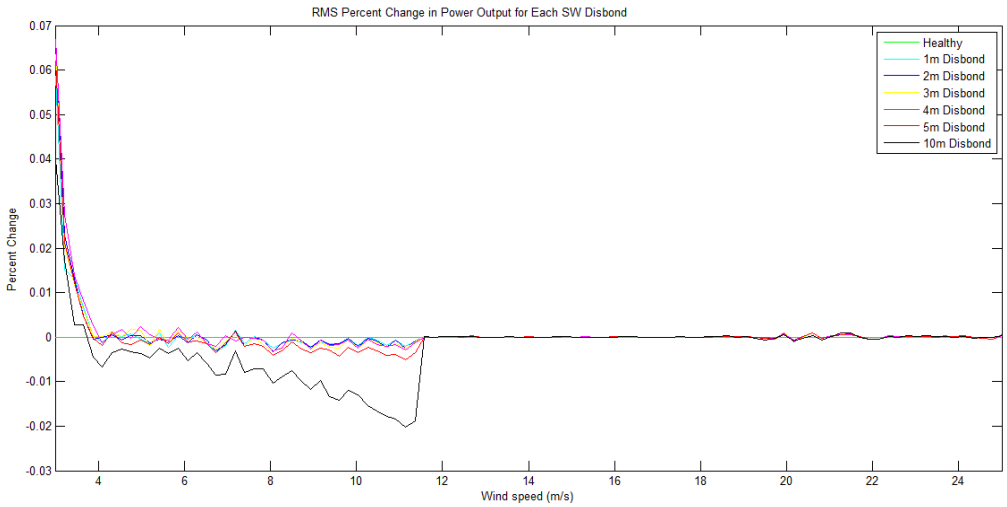

Figure 23. RMS percent change of power output for shear web disbond in varying wind speeds.

5.4.1.2. Nacelle Inertial Measurements

For all wind profiles and damage cases, the RMS value of the nacelle acceleration in all three directions increased at the turbine's rated wind speed (11.4 m/s) or higher. As was seen in the pilot study, the transverse nacelle acceleration showed a clear RMS increase for all aerodynamic cases between the rated speed and approximately 20 m/s (shown in Figure 25). In addition, the nacelle accelerations increased as the shear web disbond length was increased. Figures 24 - 26 show the RMS percent change in nacelle acceleration in the axial, transverse, and vertical directions respectively. The 1p response magnitude was analyzed as well, but the trends of an increasing magnitude were not as apparent for all of the wind loading cases. Because these measurements were made at the nacelle hub, it is not possible to determine the problematic blade if one of the three blades has the shear web disbond. However, these measurements can be used to indicate that a shear web disbond is present and then trigger more sophisticated measurements to be used to determine which blade has the disbond and the severity of the damage.

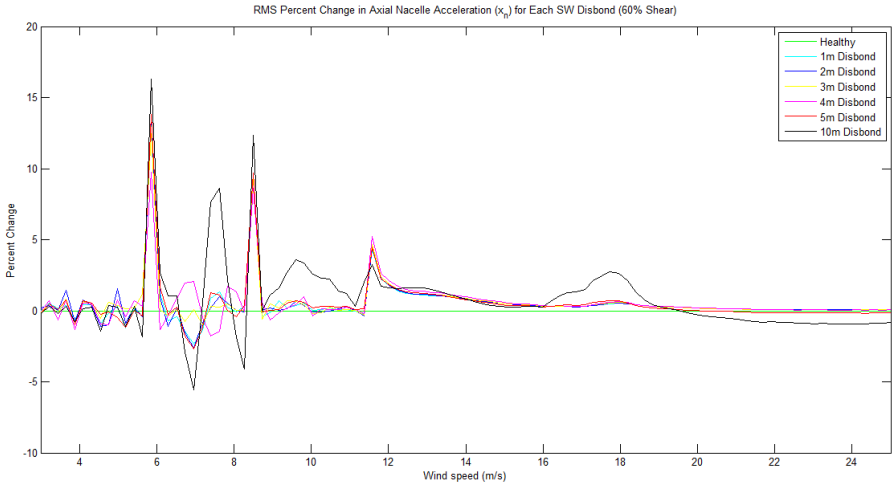

Figure 24. RMS percent change of axial nacelle acceleration for shear web disbond in 60% horizontal shear.

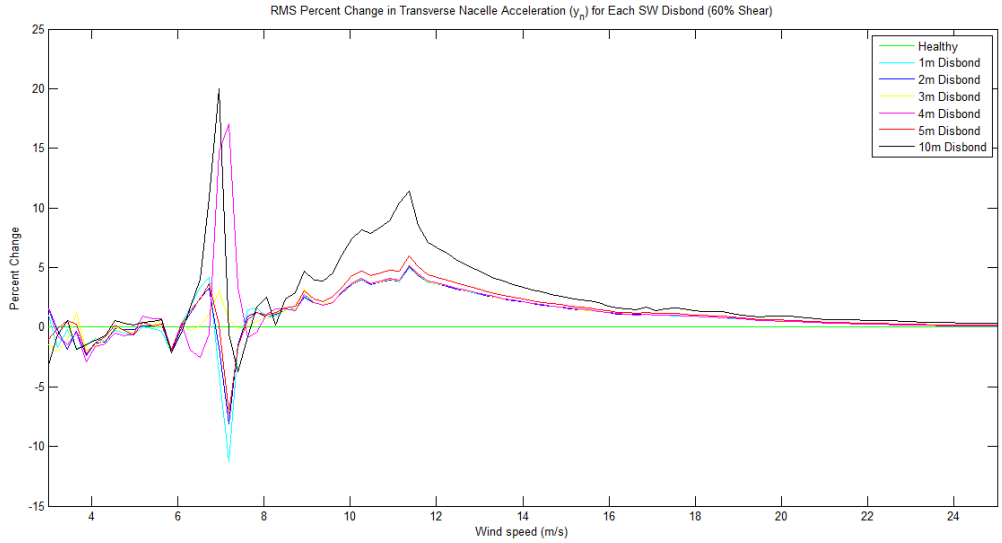

Figure 25. RMS percent change of transverse nacelle acceleration for shear web disbond in 60% horizontal shear.

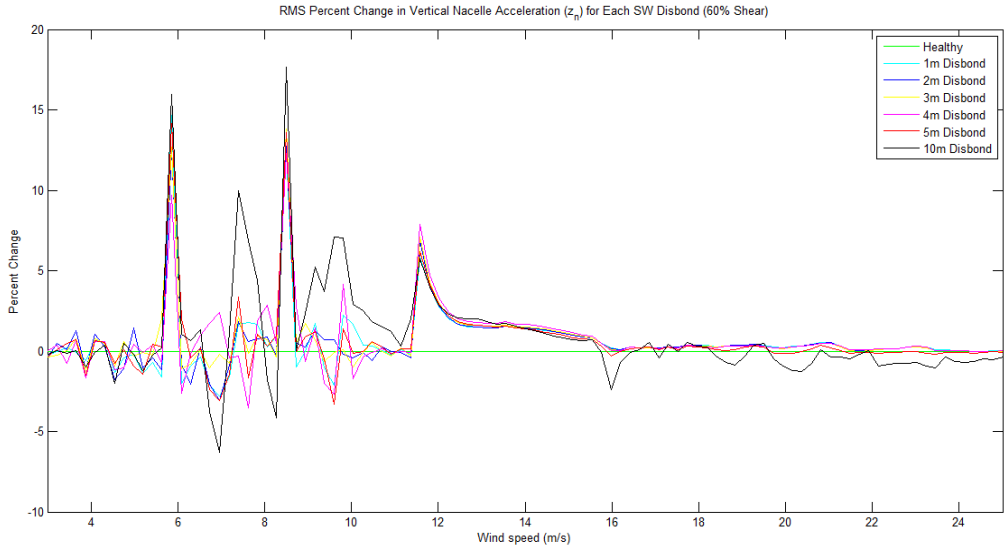

Figure 26. RMS percent change of vertical nacelle acceleration for shear web disbond in 60% horizontal shear.

5.4.1.3. Blade Tip Acceleration Response

The percent change in the RMS response magnitude of the edge-wise blade tip acceleration for shear web disbond at different wind speeds is shown in Figure 27. Although the edge-wise blade tip acceleration was affected by the presence of a shear web disbond, these algorithms did not present a trend that could be correlated to an increase in disbond length.

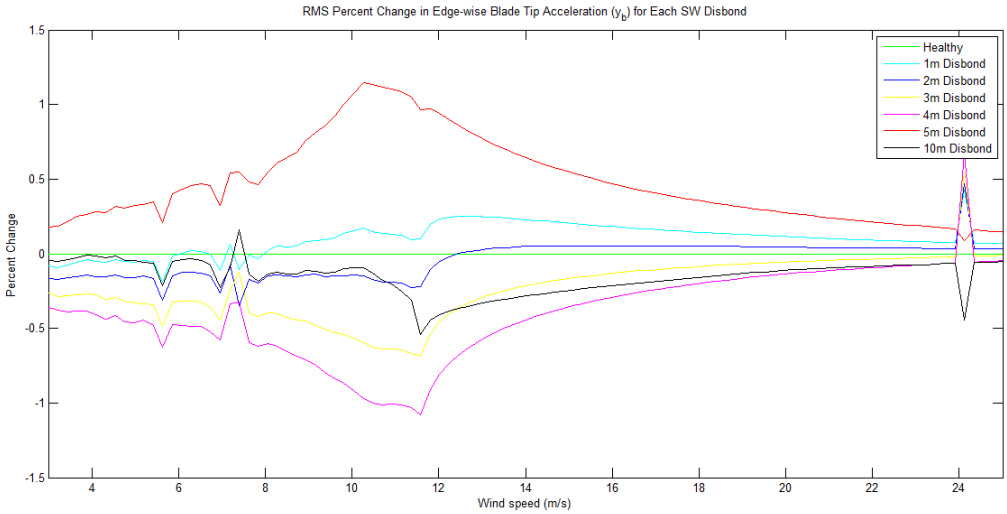

Figure 27. RMS percent change of edge-wise blade tip acceleration for shear web disbond in varying wind speeds.

The span-wise blade tip acceleration 1p response differences are shown in Figures 28 and 29. The plots show that when a shear web disbond was present, the 1p power spectrum response difference was always positive up to 18 m/s for all wind loading cases. Although there doesn't appear to be a trend that shows the severity of the damage, this measurement can serve as a good indicator that a shear web disbond is present.

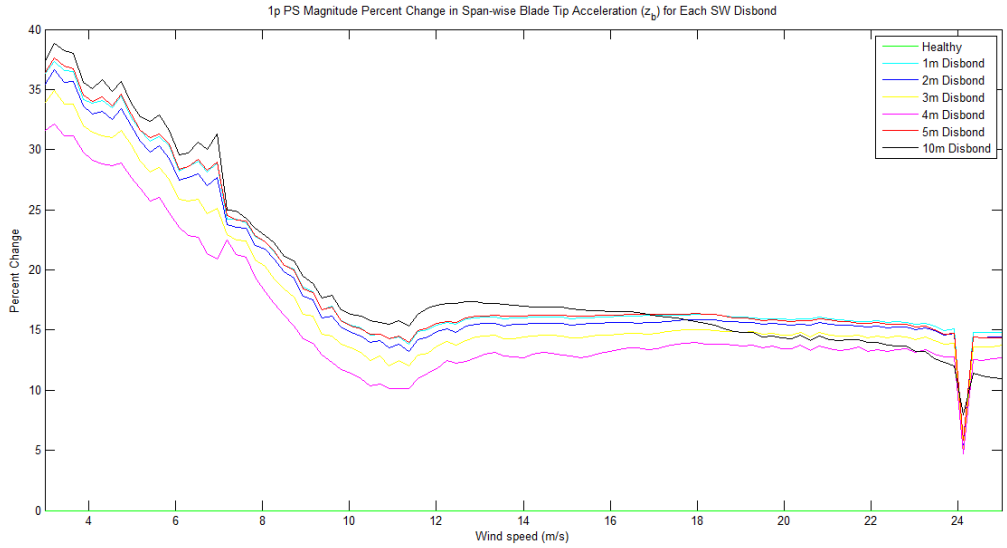

Figure 28. 1p magnitude percent change of span-wise blade tip acceleration for shear web disbond in varying wind speeds.

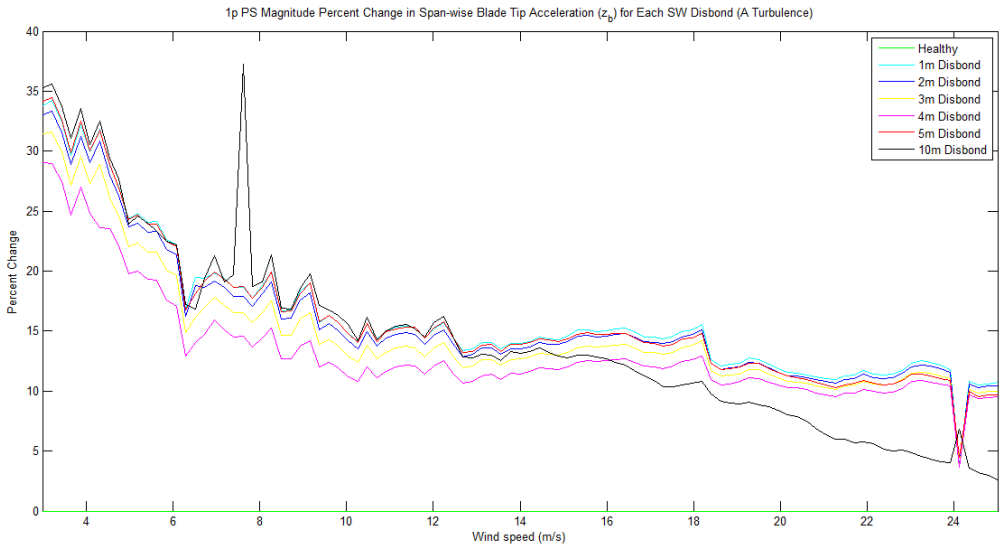

Figure 29. 1p magnitude percent change of span-wise blade tip acceleration for shear web disbond in A turbulence.

The flap-wise blade tip acceleration RMS response differences are shown in Figures 30 and 31. For all wind loading cases, there was a clear decrease in the RMS response at the turbine's rated speed (11/4 m/s) for shear web disbond lengths of 2 meters or greater. The trend of a decreased flap-wise blade tip acceleration RMS response was apparent at rated speed for all of the FAST simulations conducted in this study. In addition, the RMS response decreased as the shear web disbond length was increased. Therefore, this measurement can serve as a feature to indicate shear web disbond severity.

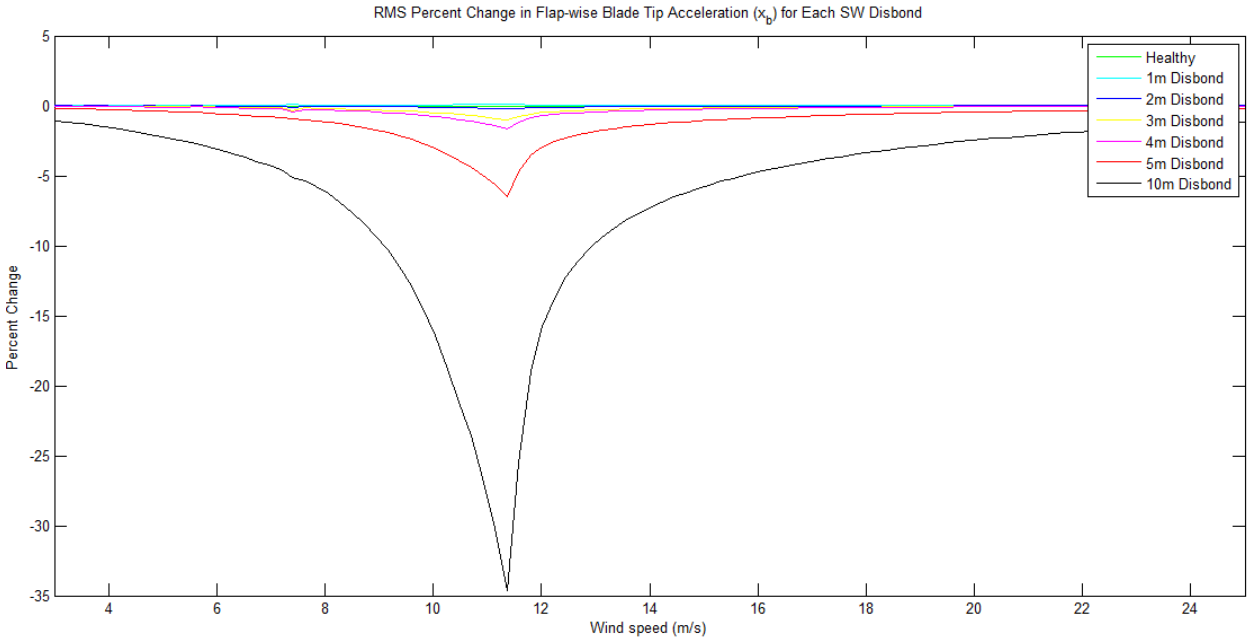

Figure 30. RMS percent change of flap-wise blade tip acceleration for shear web disbond in varying wind speeds.

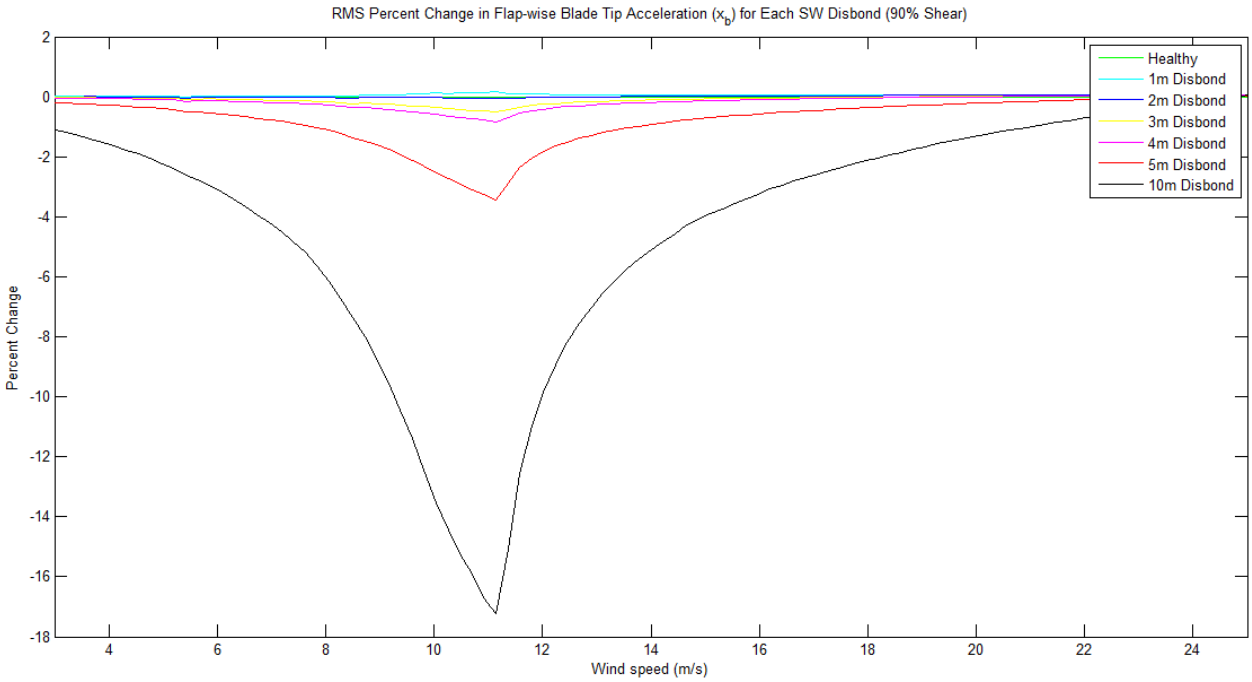

Figure 31. RMS percent change of flap-wise blade tip acceleration for shear web disbond in 90% horizontal shear.

5.4.1.4. Blade Root Pitching Moments

Figures 32 and 33 show the blade root pitching moment 1p response differences for the laminar and B turbulence wind loading cases. For all of the wind cases up to a wind speed of 16 m/s, the 1p response increased for a 4 meter, 5 meter, and 10 meter shear web disbond. This measurement can be used as another indicator that a severe shear web disbond is present in one of the blades. The blade root pitching moment can be measured with strain gages located at the root of each blade.

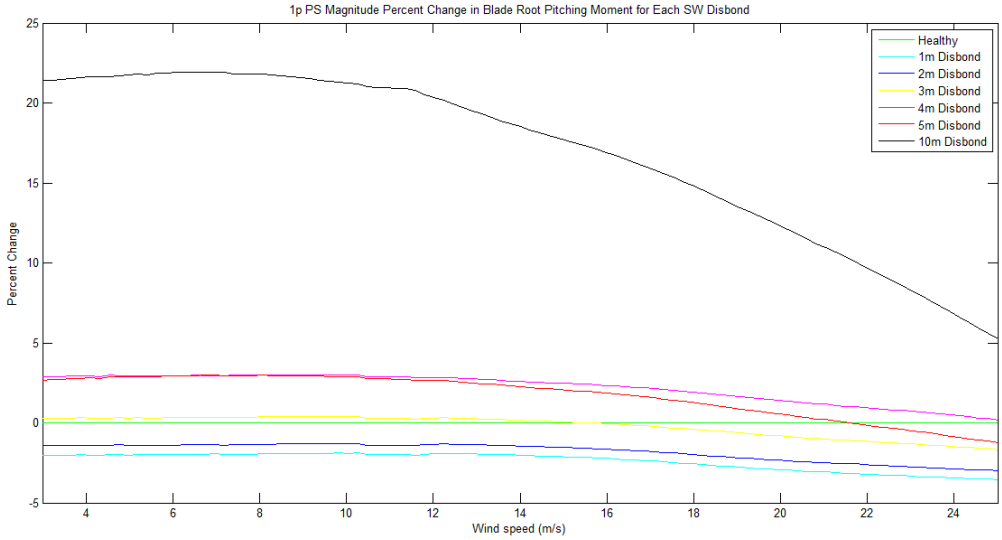

Figure 32. 1p magnitude change of blade root pitching moment for shear web disbond in varying wind speeds.

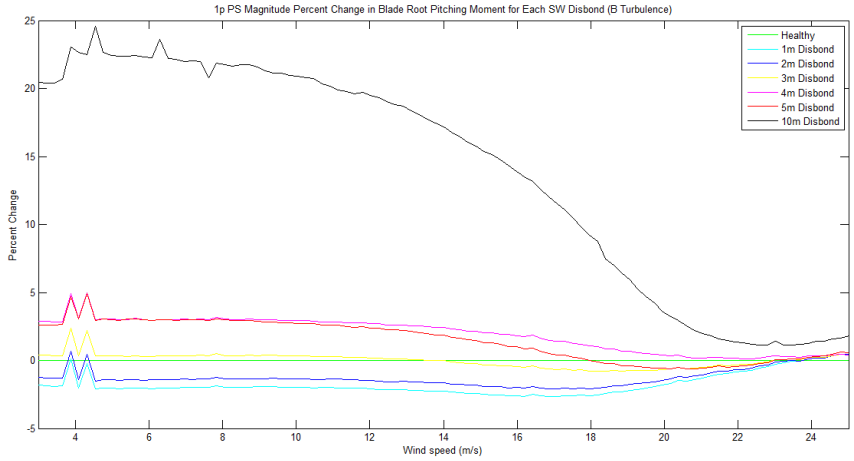

Figure 33. 1p magnitude change of blade root pitching moment for shear web disbond in B turbulence.

5.4.1.5. Blade Root Acceleration Response

The edge-wise and flap-wise blade root acceleration responses did not present any clear features when the RMS and 1p power spectrum responses were analyzed. The flap-wise blade root acceleration 1p response magnitude increased for all shear web disbonds after the rated speed of the turbine, but this trend did not continue for the horizontal shear and turbulent wind loading cases. Figures 34 and 35 shows the blade root acceleration 1p response differences for varying wind speeds and 60% horizontal shear, respectively. Other than the 10 meter shear web disbond, the span-wise blade root acceleration 1p response increased for all damage types for all wind loading cases and most of the wind speed distribution. This measurement could be used as another indicator that a shear web disbond is present at max chord. However, this feature will likely be less sensitive to a shear web disbond located further along the span of the blade because the blade root has such a high stiffness.

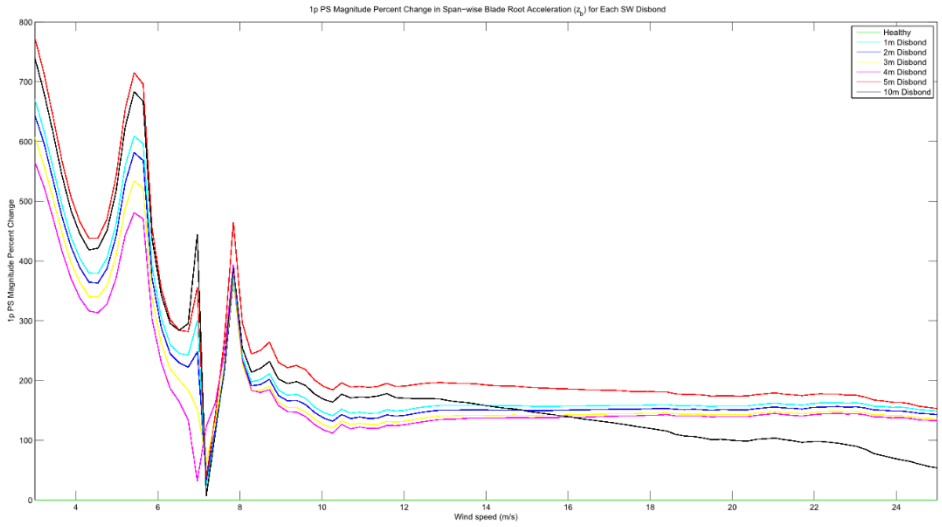

Figure 34. 1p magnitude change of span-wise blade root acceleration for shear web disbond in varying wind speeds.

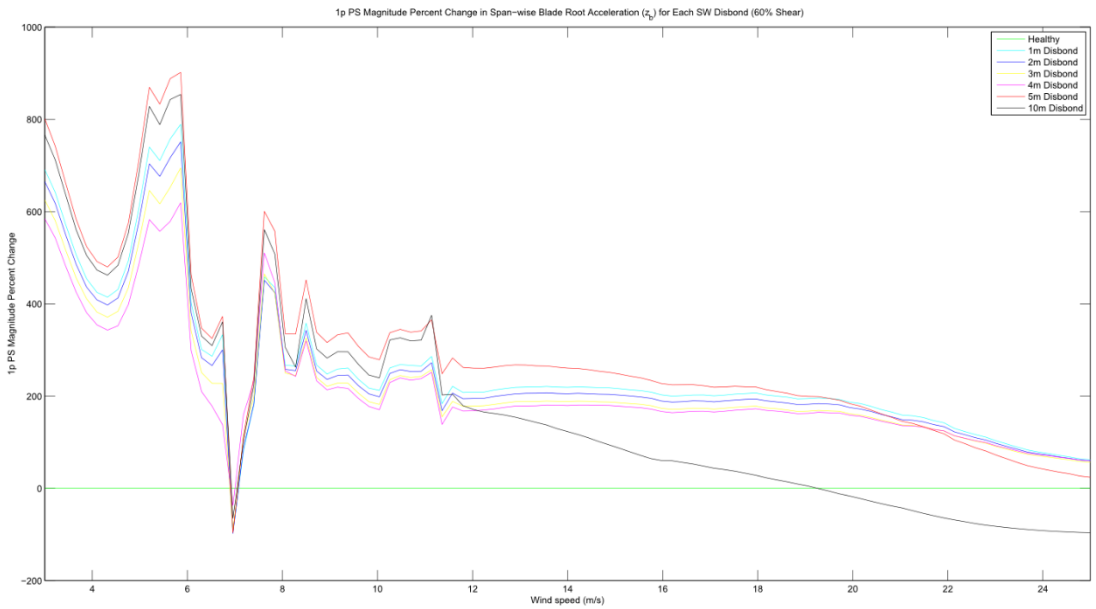

Figure 35. 1p magnitude change of span-wise blade root acceleration for shear web disbond in 60% horizontal shear.

5.5 Summary of Shear Web Disbond Detection Strategy Refinements

The results of the sensitivity analysis and key measurements have been used to refine the shear web disbond detection strategy flowchart originally shown in Figure 36. This strategy employs both blade and non-blade sensor measurements. Specifically, non-blade sensor measurements are used as the first indicator that a shear web disbond may be present and the blade sensors are used to confirm that the damage is present and its level of severity. Using a single sensor measurement to first identify potential damage will drastically reduce the necessary amount of processing and data flow *in situ*. The same action strategy will be used, as shown:

(1) Detect if a shear web disbond exists in one of the blades
(2) Determine the severity of the shear web disbond
(3) Notify turbine operator of the disbond and severity so that a repair can be scheduled or coordinated with other maintenance

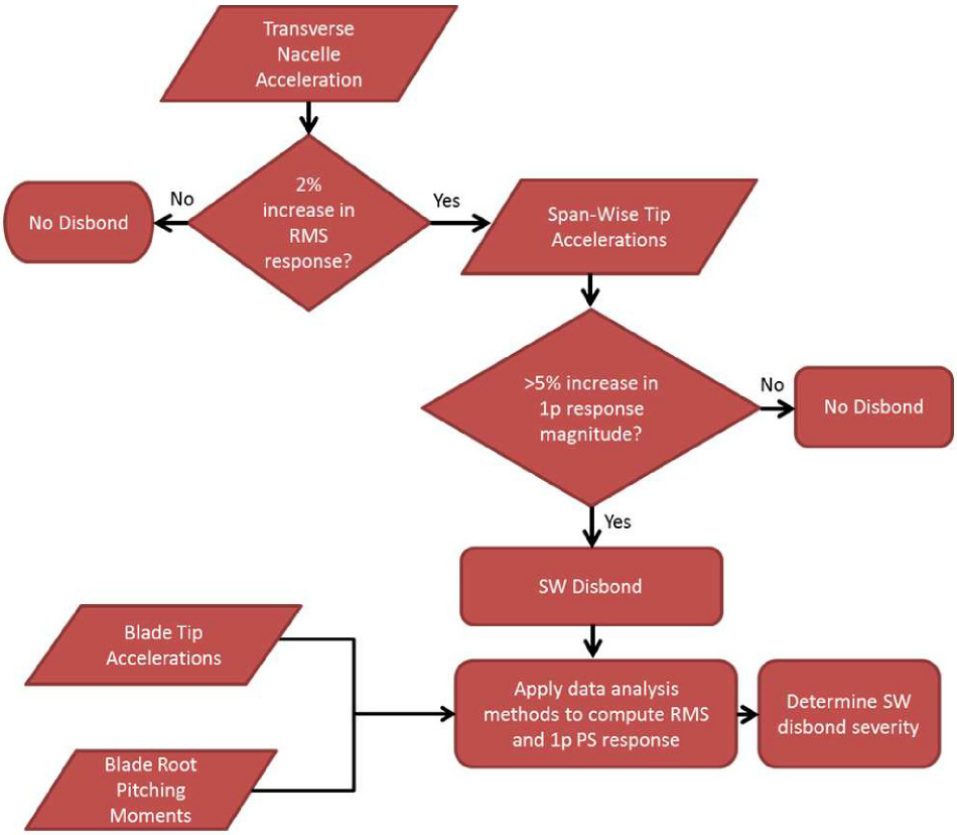

Figure 36. Refined shear web disbond detection flow chart.

The results of the sensitivity analysis and key measurements have been used to refine the shear web disbond detection strategy. This strategy employs both blade and non-blade sensor measurements. Specifically, non-blade sensor measurements are used as the indicator for a shear web disbond and the blade sensors (strain gages at the blade root) are used to detect the problematic blade and assess the level of severity. Each shear web disbond has been assigned thresholds corresponding to the severity of the damage, as shown below in Table 9.

Table 9. Shear web disbond damage state and corresponding feature used for classification

State 1 (Healthy, no disbond)	**1% increase in measured RMS transverse nacelle acceleration versus expected healthy RMS transverse nacelle acceleration**
State 2 (1, 2 meter disbond)	**1% increase in measured RMS transverse nacelle acceleration, less than 0.5% increase in 1p blade root pitching moment**
State 3 (3, 4, 5 meter disbond)	**Greater than 0.5% and less than 5% increase in 1p blade root pitching moment**
State 4 (10 meter disbond or longer)	**Greater than 5% increase in 1p blade root pitching moment**

Probability of detection values were calculated for detecting the presence of a shear web disbond in addition to detecting three different damage states which vary by severity. See Table 9 above for the damage state classifications of shear web disbond. State 2 refers to a 1-2 meter disbond, state 3 is a 3-5 meter disbond, and state 4 is a disbond of 10 meters or more. The POD values

were calculated as described in Section 4.4. If the measurement at a given wind speed, profile, and damage state met the criteria described in the tables above, then it was deemed a success. Otherwise, it was deemed a failure. For example, the blade root pitching moment is extracted from the simulation for the 3.88 m/s laminar wind profile and for a turbine with a blade which has a 4-meter shear web disbond. If there is an increase in the blade root pitching moment 1p and that increase is greater than 0.5% the healthy response and less than 5% greater than the healthy response, then the detection is a success and given a "1" value at that data point. If it does not meet the criteria, it is given a "0" value. The number of successes are then added up and that total is divided by the total number of simulations in that wind profile (101 simulations). The resultant percentage is the probability of detection for that damage state and wind profile. Table 10 shows the POD values for detecting the presence of a disbond and then categorizing the damage into each damage case, respectively. The PODs were calculated over the entire wind speed range in addition to an enhanced wind speed range which optimizes the resulting POD value for accurate damage detection for all wind loading cases. The optimized wind speed range and corresponding POD values are highlighted in green in the table. In addition, each POD value was also weighted by the Weibull distribution to incorporate the frequency of each wind speed used within the analyzed range. The POD results show that the developed algorithms are 100% successful for all of the laminar, 30% horizontal shear, and 60% horizontal shear FAST simulations. The POD values are also ~75% or greater for all but the 90% horizontal shear simulations. There is a large decrease in that probability of detection because the aerodynamic loading greatly influences the transverse nacelle acceleration response and this feature becomes the dominating feature at that measurement location rather than a shear web disbond in one of the three blades. In the real world, however, a 90% horizontal shear wind profile does not occur nearly as often as the laminar and other shear wind profiles.

Table 10. Probabilities of detection for shear web disbond

		PRESENCE OF DAMAGE		STATE 2 (1-2 m DISBOND)		STATE 3 (3-5 m DISBOND)		STATE 4 (>= 10 m DISBOND)	
		3 - 25 m/s	8.5 - 17.08 m/s	3 - 25 m/s	8.5 - 17.08 m/s	3 - 25 m/s	8.5 - 17.08 m/s	3 - 25 m/s	8.5 - 17.08 m/s
LAMINAR	Raw	84.16%	100.00%	84.16%	100.00%	83.33%	100.00%	84.16%	100.00%
	Weibull Weighted	77.24%	100.00%	77.24%	100.00%	77.16%	100.00%	77.24%	100.00%
30% SHEAR	Raw	74.26%	100.00%	72.79%	100.00%	69.11%	100.00%	72.79%	100.00%
	Weibull Weighted	78.07%	100.00%	77.95%	100.00%	77.55%	100.00%	77.95%	100.00%
60% SHEAR	Raw	44.55%	100.00%	35.73%	100.00%	36.61%	100.00%	36.17%	100.00%
	Weibull Weighted	60.18%	100.00%	58.30%	100.00%	58.61%	100.00%	58.46%	100.00%
90% SHEAR	Raw	15.84%	32.50%	10.82%	32.50%	11.29%	32.50%	10.98%	32.50%
	Weibull Weighted	25.19%	39.18%	23.21%	39.18%	23.58%	39.18%	23.34%	39.18%
A TURBULENCE	Raw	37.62%	75.00%	34.27%	75.00%	29.80%	75.00%	27.94%	75.00%
	Weibull Weighted	50.49%	74.99%	50.03%	74.99%	48.31%	74.99%	47.91%	74.99%
B TURBULENCE	Raw	45.54%	85.00%	42.39%	85.00%	36.07%	85.00%	33.82%	85.00%
	Weibull Weighted	62.86%	84.98%	61.73%	84.98%	59.38%	84.98%	59.65%	84.98%
KHTEST TURBULENCE	Raw	45.54%	80.00%	33.82%	80.00%	34.72%	80.00%	28.41%	76.00%
	Weibull Weighted	68.43%	88.06%	64.93%	88.06%	65.41%	88.06%	60.51%	85.76%

6. OPERATIONS AND MAINTENANCE COST MODEL DEVELOPMENT

This section describes the updates to the operations and maintenance cost model that was presented in Reference 17. The cost model is a state-based model that is based upon 4 states of health that decline from new blade or small damage (state 1) to failed or requiring blade replacement (state 4). There are two cases evaluated here in the model: with a SHPM system and without a SHPM system. Both cases assume the same wind conditions with the only difference being the different probabilities of detection (i.e. knowledge of state of health) for each case. The objective is to make a connection between the performance of the SHPM system with the overall economics (see Figure 7 for a flowchart describing this approach). Although more work remains, this section describes an update to our approach to demonstrate and better understand the impacts of the SHPM system performance (namely POD values for the system) to O&M costs and how these costs vary with POD value and wind speed.

In this state-based approach, the O&M costs are added up for the year for all repairs to restore the states that require repair (i.e. state 2 through state 4) back to state 1. The annual energy production is also calculated using the average wind speed that is modeled as a Weibull distribution with downtime included for those states requiring repair. The yearly operations and maintenance cost is divided by the annual energy production to determine the levelized cost of energy for operations and maintenance for each scenario. Finally, the cost benefit is determined by comparing the situations of with and without an SHPM system.

6.1. Introduction

The cost model has been revised in the following ways (since Reference [17]) to incorporate the wind turbine numerical simulation of damage results:

1. The probabilities of detection for the SHPM system have been revised to accept inputs from the variable inflow conditions or sensitivity analysis presented above in the aero-elastic simulations.
2. The model has been revised to consider a stochastic instead of a deterministic detection strategy.
3. The model has been created using @Risk.

6.1.1. *Model Assumptions*

The revised model accounts for the cost-benefit of increased energy production, which is an important element envisioned for these SHPM systems. The present results are focused on analysis of trends in O&M costs versus absolute O&M cost estimates. A limitation of the current model is that it does not consider unscheduled maintenance which may account for a much greater portion of the O&M costs as the literature describes that unscheduled maintenance can cost as much as five times that of scheduled maintenance. In addition, the model does not consider the benefits that may come with increased safety and possible job efficiencies associated with knowing where the defect is located on the blade before repair. Finally, there may be cost synergies between parts that have not been calculated. For instance, a gearbox may

encounter less wear if the blades are kept in balance, but additional research needs to be conducted to determine if there are any benefits due to these component interdependencies.

As such, these results should be viewed simply as a trends or sensitivity analysis -- although, they are intended to also illustrate our approach for combining SHPM system performance information into an economics analysis. Use of this model to produce absolute estimates for O&M costs in a comprehensive sense would require further refinement and inclusion of other costs such as unscheduled maintenance and actual repair costs, vessels costs, etc.

6.1.2. *Probability of Detection (POD) Revisions*

The probabilities of detection have been revised for the SHPM system to evaluate the effects of POD from the variable inflow wind turbine analysis presented above. In the original model, the probabilities of detection were assumed and were ranged from low to high values to determine the effect of varying detection probabilities. The revised probabilities have been incorporated into the current model and change with different wind speeds and wind conditions as seen in Table 11. This has caused a revision in the model to accommodate a POD that changes based upon wind speed. The PODs were arranged into six categories according to the results of the blade defect detection analysis. The PODs are shown in Table 12 showing the higher POD values with a SHPM system and lower POD values without a SHPM system. Similar to the original model, the PODs for the shear web disbond, mass imbalance, and pitch error have been aggregated and weighted according to likelihood of defect occurrence and likelihood of wind condition as noted in wind turbine blade literature. The updated cost model is still a state-based model using a Monte Carlo Markov chain although this current change adds to the randomness due to the PODs being dependent upon the wind speed which is still being modeled as a Weibull distribution where $k = 2$, $c = 11.4$, and $\beta = 1$.

Table 11. Probabilities of detection for SHPM system.

	Wind Type		
Wind Speed	Laminar	A Turb	B Turb
3	24%	12%	18%
6.74	82%	76%	94%
10.48	100%	59%	77%
14.22	100%	71%	82%
17.96	100%	0%	0%
21.7	100%	6%	0%

Table 12. Weighted Probabilities of detection for SHPM and non-SHPM systems.

	With SHPM	Without SHPM		
Wind Speed	All states	State 2	State 3	State 4
3	21%	5%	10%	16%
6.74	83%	21%	41%	62%
10.48	89%	22%	44%	67%
14.22	92%	23%	46%	69%
17.96	66%	17%	33%	50%
21.7	67%	17%	34%	50%

6.1.3. *Stochastic Detection Strategy*

The model has also been revised to use a stochastic detection strategy. This detection strategy has been modeled as a binomial distribution with the mean set to the POD. In order to incorporate this strategy, the Markov Chain has been changed from an ergodic chain to a terminating chain. The ergodic chain was modeled to only allow the blade to transition from a degraded step to a "new/repaired" state when repaired or from a less degraded state to a more degraded step to imitate the blade deteriorating. The detection process was actually part of the Markov chain (the probability that a blade in states 2, 3, or 4 will return to 1) instead of a separate step. In the revised model, the Markov Chain is terminating which means if the model runs long enough, the model will always continue to degrade until it is in a failed state and once in this failed state it will remain in that state permanently. The main difference between the two model types is that the original model can be run continuously since it can return to state 1 from other states and go through the cycle again, whereas the current model will remain in the absorbing state 4 once a sufficient amount of iterations has been reached. In the current model, the blade is only repaired if it is detected by the POD that is modeled as a binomial distribution. This change has two benefits: it is more realistic as a separate process that checks for defects and it can incorporate multiple PODs since a model can get unstable if multiple Markov Chains are used. Although the PODs have changed, the top level probabilities have remained unchanged. The assumption that the blade is repaired once the defect is detected is still valid for the current model.

6.1.4. *@Risk Model*

The model is now in the software tool @Risk. @Risk is Excel based software that is used for many commercial financial applications and cost benefit analysis. @Risk automatically incorporates multiple iterations which facilitates the Monte Carlo process and allows for inputs to easily be entered as a probability distribution. @Risk was chosen since it was designed for applications such as this cost model and allows for easy input and scenario variation. The model was shortened to one year to improve model run times in @Risk. A simulation was run changing the initial state to determine how the shortened model may impact the results since a longer model usually has years that do not start out at state 1. The results through ANOVA showed that there were no statistically significant differences between the different initial states.

6.2. Economic Sensitivity Analysis

An economic sensitivity analysis involves changing input parameters to see what influence the change has on the cost (or the cost savings in this case). The previous economic sensitivity analysis altered the operations & maintenance cost, probability of detection/repair rate, and performance coefficient to see their effects on the cost savings. The previous results showed that there were more cost savings as the disparity between the large crack repair and small crack repair increased, as the repair rate decreased, and to a lesser effect when the performance coefficient decreased. This year, the mean wind speed and the POD difference were changed between the baseline and SHPM system in addition to the changes considered last year. Altering the wind speed is useful since the current PODs change with wind speed. The other parameter that was altered was the percent difference between the baseline and the SHPM system. Since each baseline system will have a different level of detection based upon the instrumentation installed and how the collected data is used, this parameter was changed to determine how much of a change can be seen as the difference increases.

6.2.1. *Changing Mean Wind Speed*

The mean wind speed for the Weibull distribution was altered from 3 m/s to 25 m/s in increments of 2 m/s. The resulting annual energy production and levelized operations and maintenance costs were evaluated.

6.2.2. *Changing Baseline POD*

The baseline PODs were determined as a percentage of the PODs for the SHPM system for each state. The percentages were ranged from 0% to 100% for each state. They were varied one at a time with the remaining states containing the baseline values.

6.3. Simulation Results

The trends were the same as before for the parameters changed during the initial phase of the cost model. The results for the changing mean wind speed can be seen in Figures 37 and 38. The difference in annual energy production due to the SHPM system is a result of assumed decreased downtime based on the damage mechanisms (rotor imbalance, shear web disbond) and developed detection strategies shown in Sections 4 and 5. Without SHPM, the severity of damage due to rotor imbalance and/or shear web disbond is assumed to progress over time within the cost model until the blade is in a failed state.

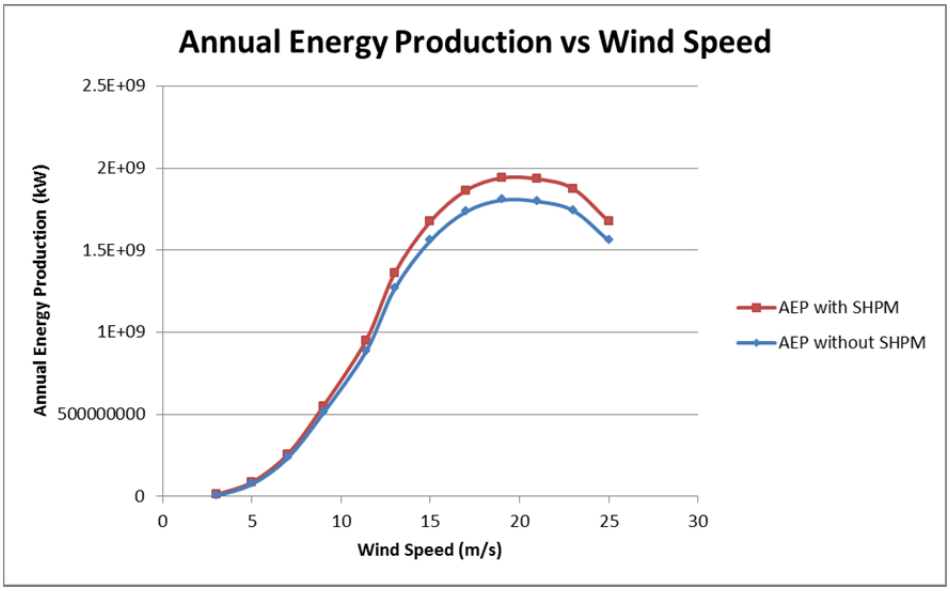

Figure 37. Annual Energy Production versus Wind Speed

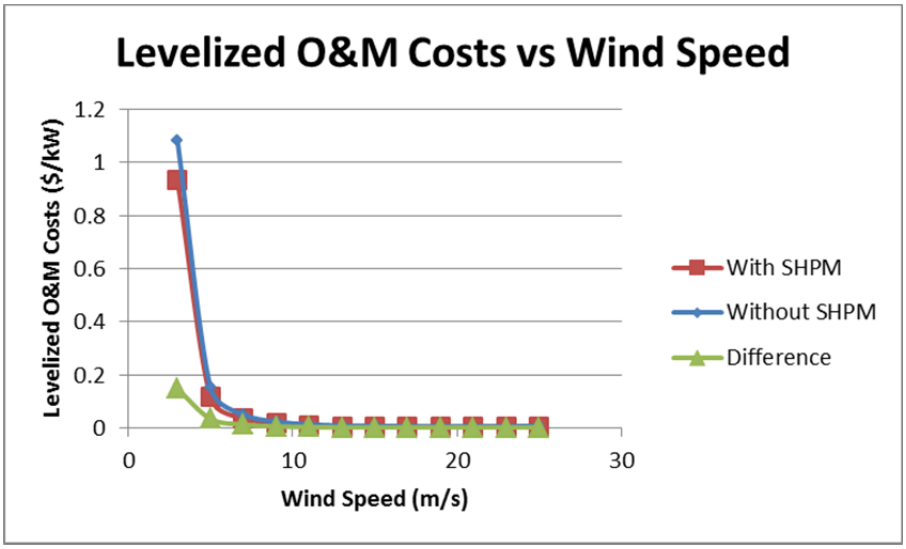

Figure 38. Levelized O&M Costs versus Wind Speed

Figure 38 shows how the levelized O&M Costs in the current model are affected by wind speeds. There is not much difference in the levelized costs for these assumptions once the wind speed surpasses 7 m/s. The SHPM blade system has either equal or slightly lower costs for most of the wind speeds.

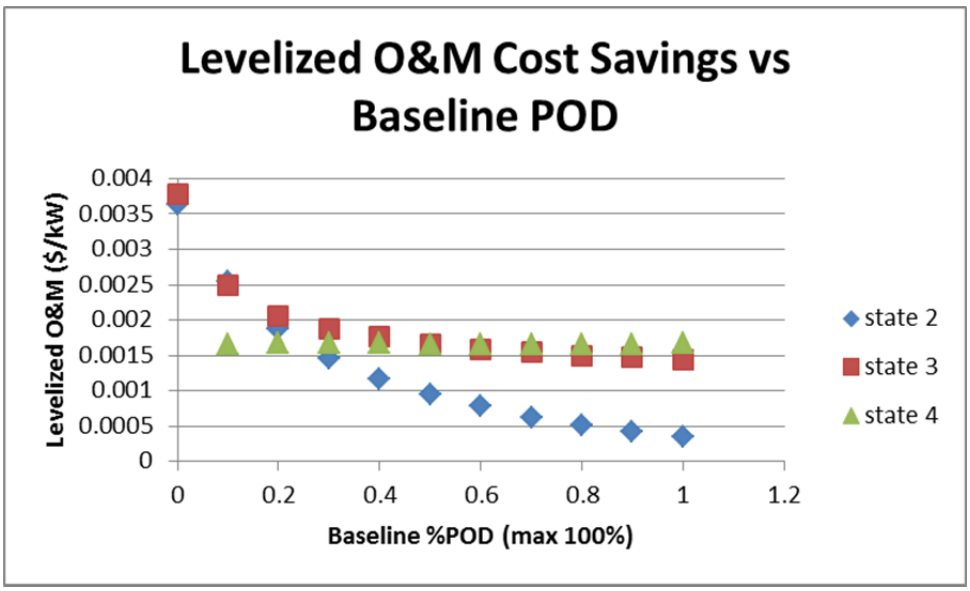

Figure 39. Levelized O&M Cost Savings versus Change in Baseline POD

Figure 39 shows the results of varying the Baseline POD based upon the SHPM POD. The POD for state 2 impacts the levelized O&M more than the POD for states 3 and 4. Although the absolute values for this current model are very small in comparison to actual O&M costs of today, the trends show the relative benefit of higher probability of detection (POD) for reducing O&M costs.

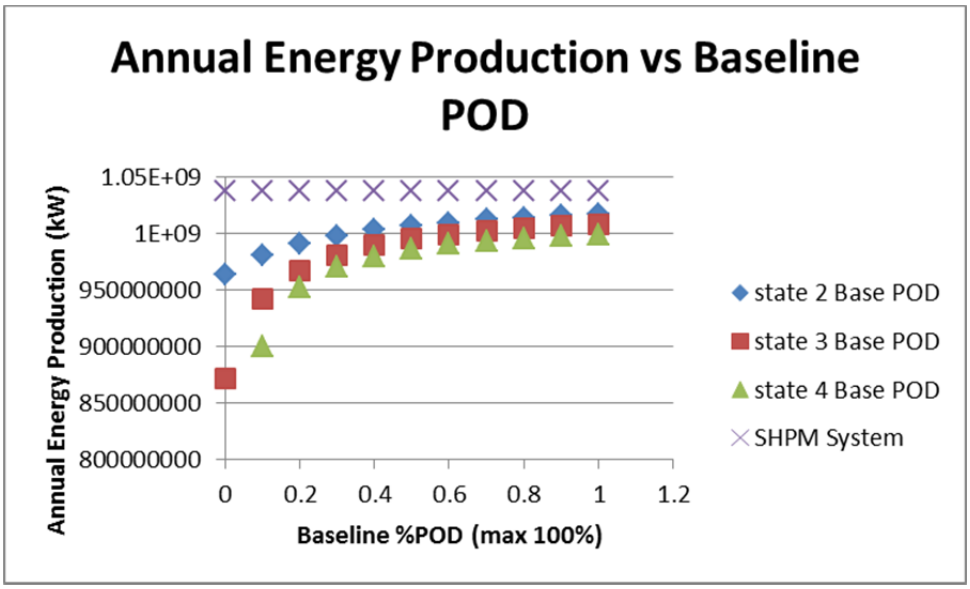

Figure 40. Annual Energy Production vs Change in Baseline POD.

Figure 40 shows the annual energy production when the baseline POD is changed. The PODs that had the highest levelized O&M have the lowest annual energy production. This is caused by the baseline POD at 0% where not being able to the detect damage early results in lower annual energy production. As the PODs improve, the energy production increases.

The cost savings seen in this economic sensitivity analysis are small in an absolute sense. Although refinement is needed, this model has been useful to identify some of the key parameters from the SHPM system that affect cost. These limitations can be addressed in future work by including refined/actual O&M costs data such as comparing planned and unplanned maintenance costs for an offshore wind farm.

7. CONCLUSIONS

A multiscale methodology[12] has been expanded for the investigation and development of structural health and prognostics management (SHPM) methods for offshore wind turbines. The method utilizes the propagation of damage from a high fidelity component level model up to a reduced order model of a full turbine so that the changes in the turbine's operational responses can be examined. Furthermore, these full turbine simulations can be used to replicate fault mechanisms such as pitch error and estimate the loads on the turbine blades which can then be propagated back to the high fidelity model to allow for further local analyses to be conducted. By investigating the effects of damage on multiple scales, the developed methodology takes advantage of available software to investigate the underlying physical changes that occur as a result of damage/faults on both a local and global level which leads to the identification of operational responses that are most sensitive to these physical changes. In turn, fault detection strategies have been developed to help optimize operations and maintenance schemes.

This report has described the application of the developed methodology to investigate rotor imbalance and shear web disbond and their sensitivities to inflow conditions on an offshore 5-MW wind turbine. The 61.5 meter blade model was developed in SNL's NuMAD software and exported to ANSYS where the shear web disbond was simulated by separating the nodes of the shear web from the blade at the location of the disbond. The reduced order blade models with varying levels of damage were included into a model of an offshore turbine on a fixed monopile in 20 meters of water. The response of these offshore turbine models with varying levels of damage/imbalance was then simulated in FAST over a wide range of wind speed, horizontal shear, and turbulence. From these simulations the detection strategies developed in the pilot study could be updated and robust probabilities of detection were derived as an algorithm success metric. For all three fault mechanisms, the probability of detection was 96% or higher for the optimized wind speed ranges including the laminar, 30% horizontal shear, and 60% horizontal shear conditions.

To examine how the structural health of each turbine could be used to optimize the operation and maintenance practices of an offshore wind plant, a state-based cost model was developed to investigate the operations and maintenance costs due to the fault/damage. The cost model compared the cost advantages of employing a SHPM system through the probability of detection values derived in the FAST sensitivity analysis. Although the model contains several assumptions, the results showed a foreseeable benefit to owning such a SHPM system; the SHPM system produced an increase in the annual energy production as well as a decrease in the levelized operations and maintenance costs. The combination of the repair cost information and the structural health of each turbine could be utilized in the optimization of damage mitigating

control strategies and maintenance schedules to reduce the operations and maintenance costs associated with running an offshore wind energy plant. The hope is that combining the SHPM system performance information with an economics analysis of the O&M process will be useful not only to motivate the greater usage of SHPM systems in wind turbine systems, but to also aid in the holistic design of such monitoring systems and the associated best maintenance practices.

8. FUTURE WORK

In future work, the algorithms developed for the 5-MW offshore turbine model could be experimentally validated on a small horizontal-axis wind turbine or utility-scale machine. The pitch error, mass imbalance, and blade damage can be introduced in order to assess the turbine's power performance, loads at the blades and nacelle, and detection of those fault mechanisms. In addition, rotor imbalance and blade damage can be detected in the presence of disturbances such as yaw error and pitch error in addition to other inflow variability from laminar to horizontal shear inflow conditions including a sweep across all operating wind speeds.

9. REFERENCES

[1] A.C. Levitt, W. Kempton, A.P. Smith, W. Musial and J. Firestone, "Pricing offshore wind power." *Energy Policy* (In Press) 2011.

[2] W. Musial and B. Ram, *Large-Scale Offshore Wind Energy for the United State: Assessment of Opportunities and Barriers*, NREL Report No. TP-500-49229, Golden, CO, September 2010.

[3] U.S. Department of Energy, *A National Offshore Wind Strategy: Creating an Offshore Wind Energy Industry in the United States,* Washington: Wind & Hydropower Technologies Program Report No. 5040, February 2011.

[4] R. Wiser and M. Bolinger, *2010 Wind Technologies Market Report*, Lawrence Berkeley National Laboratory: Lawrence Berkeley National Laboratory. LBNL Paper LBNL 4820E, June 2011.

[5] B. Snyder and M.J. Kaiser, "Ecological and economic cost-benefit analysis of offshore wind energy." *Renewable Energy* 34(6), pp. 1567-1578, 2009.

[6] G. van Bussel, A.R. Henderson, C.A. Morgan, B. Smith, R. Barthelmie, K. Argyriadis, A. Arena, G. Niklasson, and E. Peltola, "State of the Art and Technology Trends for Offshore Wind Energy: Operation and Maintenance Issues," *Offshore Wind Energy EWEA Special Topic Conference*, Brussels, Belgium, December 2001.

[7] L.W.M.M. Rademakers, H. Braam, M.B. Zaaiger, and G.J.W. van Bussel, "Assessment and optimisation of operation and maintenance of offshore wind turbines," in *Proceedings of the European Wind Energy Conference*, Madrid, Span, June 2003.

[8] Y. Amirat, M.E.H Benbouzid, B. Bensaker, and R. Wamkeue, "Condition monitoring and fault diagnosis in wind energy conversion systems: a review." In *Proceedings 2007 IEEE International Electric Machines and Drives Conference*, Vol 2., pp. 1434-1439, 2007.

[9] J. Nilsson and L. Bertling, "Maintenance management of wind power systems using condition monitoring systems – Life cycle cost analaysis for two case studies," *IEEE Transactions on Energy Conversion* 22(1), pp. 223-229, 2007.

[10] C.C. Ciang, J.R. Lee, and H.J. Bang, "Structural health monitoring for a wind turbine system: a review of damage detection methods." *Measurement Science and Technology* 19(12), pp. 1-20, 2008.

[11] F. Besnard, K. Fischer, and L. Bertling, "Reliability-centred asset maintenance – A step towards enhanced reliability availability and profitability of wind power plants" in *2010 IEEE PES Innovative Smart Grid Technologies Conference Europe (ISGT Europe)*, 2010.

[12] Z. Hameed, S.H. Ahn, and Y.M. Cho, "Practical aspects of a condition monitoring system for a wind turbine with emphasis on its design, system architecture, testing and installation," *Renewable Energy*, 35(5), pp. 879-894, May 2010.

[13] NWTC Design Codes (FAST by Jason Jonkman, Ph.D.). http://wind.nrel.gov/designcodes/simulators/fast/. Last modified 05-November-2010; accessed 05-November-2010.

[14] R.R. Ryan, ADAMS – Multibody System Analysis Software, Multibody Systems Handbook. Berlin: Springer-Verlag, 1990.

[15] J. Jonkman, S. Butterfield, W. Musial, and G. Scott, "Definition of a 5-MW Reference Wind Turbine for Offshore System Development," NREL/TP-500-38060, Golden, CO: National Renewable Energy Laboratory, February 2009.

[16] D.T. Griffith, N. Yoder, B. Resor, J. White, and J. Paquette, "Structural Health and Prognostics Management for Offshore Wind Turbines: An Initial Roadmap," Sandia National Laboratories Technical Report, SAND2012-10109, Sandia National Laboratories; Albuquerque, NM, Printed December 2012.

[17] N. Myrent, J. Kusnick, N. Barrett, D. Adams, and D.T. Griffith, "Structural Health and Prognostics Management for Offshore Wind Turbines: Case Studies of Rotor Fault and Blade Damage with Initial O&M Cost Modeling," Sandia National Laboratories Technical Report, SAND2013-2735, Sandia National Laboratories; Albuquerque, NM, Printed April 2013.
[18] J. Jonkman and L. Buhl, "FAST User's Guide," NREL/EL-500-38230, Golden, CO: National Renewable Energy Laboratory, August 2005.
[19] J. Giebhardt and WP7 Partners, "Condition Monitoring for Wind Turbines 'State of the Art' Report," Kassel, Germany: European Commission, 2007.
[20] IEC 61400-1, "Wind turbine generator systems-Part 1: Safety requirements," 2nd edition, Geneva, Switzerland: International Electrotechnical Commission, 1999.
[21] B.J. Jonkman and L. Kilcher, "TurbSim User's Guide: Version 1.06.00," NREL/TP-xxx-xxxx (Draft Version), Golden, CO: National Renewable Energy Laboratory, September 2012.
[22] C. A. Walford, Wind turbine reliability: understanding and minimizing wind turbine operation and maintenance costs: United States. Department of Energy, 2006.

(this page intentionally left blank)

CHAPTER 7. DAMAGE MITIGATION: SMART LOADS MANAGEMENT AND DAMAGE TOLERANT DESIGN – FY14

This chapter presents results on two topics within the Operations Decisions thrust area of the SHPM technology roadmap (see Chapter 3): damage mitigation via derating (controls or smart loads management) and damage mitigation via design approaches (damage tolerant design). Damage mitigation can be approached in the operations phase and the design phase. Research has been performed in both areas; however, the optimal solution from an LCOE point of view is to include design, monitoring, and operational considerations together in the *system-level* design and project planning phases.

Highlights of this chapter include:

- A framework for high-fidelity analysis of damaged blades is presented (Section 7.1)
    - A progressive damage model is applied and validated for blade disbonds in the trailing edge and shear web
    - The impact of derating (both power and loads management) on reducing potential for damage initiation and damage growth, as quantified through strain energy release rates (SERRs), is assessed for the damaged blade models by comparing SERRs for normal operation and reduced loads (derated operation)
- The high-fidelity damaged blade analysis is applied in the blade design phase (Section 7.2)
    - Damage tolerant design approaches are applied to a large wind turbine blade to illustrate how the high-fidelity analysis approach can be used in the blade design phase

7.1 High-fidelity Modeling of Local Effects of Damage for Derated Offshore Wind Turbines[5]

7.1.1 ABSTRACT

Offshore wind power production is an attractive clean energy option, but the difficulty of access can lead to expensive and rare opportunities for maintenance. As part of the Structural Health and Prognostics Management (SHPM) project at Sandia National Laboratories, smart loads management (controls) are investigated for their potential to increase the fatigue life of offshore wind turbine rotor blades. Derating refers to altering the rotor angular speed and blade pitch to limit power production and loads on the rotor blades. High-fidelity analysis techniques like 3D finite element modeling (FEM) should be used alongside beam models of wind turbine blades to characterize these control strategies in terms of their effect to mitigate fatigue damage and extend life of turbine blades. This study will consider a commonly encountered damage type for wind turbine blades, the trailing edge disbond, and show how FEM can be used to quantify the effect of operations and control strategies designed to extend the fatigue life of damaged blades. The Virtual Crack Closure Technique (VCCT) will be used to post-process the displacement and stress results to provide estimates of damage severity/criticality and provide a means to estimate the fatigue life under a given operations and control strategy.

7.1.2 INTRODUCTION

Offshore wind power production is an attractive clean energy option, but the difficulty of access can lead to expensive and rare opportunities for maintenance. The Structural Health and Prognostics Management (SHPM) project at Sandia National Laboratories (see [1], [2]) has developed a roadmap to address these issues, in particular technology development to reduce operations and maintenance (O&M) costs and increase energy capture. In one element of this roadmap, smart loads management (controls) are investigated as simple fatigue considerations (under this project as well as in other works) and the potential has been identified to derate a damaged turbine via smart loads management to significantly increase its fatigue life. Derating refers to altering the rotor angular speed and blade pitch to limit power production and loads on the rotor blades. These studies typically have utilized simplified beam models to evaluate new operations and controls strategies and point to a reduction in tower or blade section loading to show the success of the strategy.

High-fidelity analysis techniques such as finite element modeling should be used alongside these beam models to quantitatively and accurately characterize each strategy in terms of its effect to mitigate fatigue damage and extend life of turbine blades. High-fidelity analysis is critical in the case of damaged blades due to local effects in the damaged area of the blade. This study will consider a commonly encountered damage type for wind turbine blades, the trailing edge disbond, and show how finite element modeling can be used to quantify the effect of operations and control strategies designed to extend the fatigue life of damaged blades. The finite element modeling strategy will use a multiscale procedure, with a "global" shell model analysis for behavior of most of the blade, and a "local" model to analyze the behavior in the vicinity of the

[5] Richards, Griffith, Hodges, "High-fidelity Modeling of Local Effects of Damage for Derated Offshore Wind Turbines," Science of Making Torque from Wind Conference, June 18-20, 2014, Lyngby, Denmark.

damage. Both models will represent the damage using nonlinear contact elements that accurately capture opening and closing behavior of the disbonds. The Virtual Crack Closure Technique (VCCT) [3] will then be used to post-process the displacement and stress results from the finite element analyses to provide estimates of damage severity and damage growth rates. The results of this process will indicate the criticality of common damage features with respect to damage location and type of loading, as well as provide a means to estimate the fatigue life or growth of damage under a given operations and control strategy.

7.1.3 BACKGROUND

A general cost-benefit analysis of offshore wind energy is presented by Snyder and Kaiser [4]. This analysis identifies the relative cost and risk of offshore turbines (compared with onshore) as a main barrier for acceptance of offshore wind, and highlights the larger percentage of operational and maintenance costs of the total offshore cost of energy (compared with onshore). A major goal of the SHPM project is to present operational and control strategies for offshore wind farms that will minimize the total cost of energy, by avoiding blade damage or mitigating blade damage growth with smart loads management.

The purpose of the smart loads management system is to (a) avoid a catastrophic failure through advance warning, (b) plan cheaper maintenance and (c) increase energy capture by avoiding shutdown. The resulting strategies will consist of decisions to shut down, operate the turbine normally, or operate potentially damaged turbines in a safe way. The recommendation to operate damaged turbines must justify the risk of further damage to the turbine based on the local sensitivity analysis results and the potential to increase the annual energy production (AEP). An effective prognostic control strategy will therefore reduce the total cost of energy by reducing O&M costs as well as increasing power production for offshore wind farms where inspection and maintenance can be difficult.

7.1.3.1 Operation and Maintenance Strategies

Decisions of how to operate a turbine should be made in conjunction with an inspection and maintenance scheduling strategy. An overview of maintenance management is given by [5]. Rangel-Ramirez and Sorensen [6] applied a risk-based inspection strategy from offshore oil industry to offshore wind farms, showing that operational decisions regarding inspections should consider turbulent wake effects of the farm as a whole. Zhang et al. [7] use a wake-loss model and historical data to define an inspection model that accounts for the wake of each turbine. This inspection model would use weather reports when available and historical data when necessary to make up-to-date decisions. This way wind turbines heavily affected by the wake(s) of one or more other turbines or whose wake affects other turbines would be shut down in favor of turbines operating optimally. This model in particular would be an ideal starting point for an operational strategy that includes damage tolerance considerations. A damaged turbine that is forecasted to be partially within the wake of another, for example, would likely remain shut down, while a damaged turbine that is forecasted to be within a clear inflow would then operate under a prognostic control system. Wenjin et al. [8] proposed a predictive maintenance strategy based on modeling the blade deterioration with Monte Carlo simulations. This is again similar to the proposed operations strategy, except that the damage detection efforts of the SHPM project are intended to augment or replace blade deterioration models [9, 10].

7.1.3.2 Control System Considerations

Under "normal" operation, a wind farm is operated to maximize power production. Modern wind turbines of 5 MW or larger are typically controlled in yaw, pitch, and rotor angular speed to optimize their power production capability. The yaw control is used to align the rotor with the wind direction, while pitch and speed controls are primarily used to control aerodynamic loads and generator performance. The rotational speed of the turbine is controlled via torque control of the generator. The pitch and speed controls of each turbine can either be used individually to maximize the power output of each individual turbine, or in a collective sense to maximize the power output of the wind farm as a whole [11, 12, 13]. For this research, the NREL 5 MW baseline design [14] will be considered as a representative offshore turbine design with yaw, pitch, and rotor speed controls.

Under "damaged" operation, the control strategies will be used to produce power production while alleviating loads on damaged blades. Bossanyi has studied the blade load reduction problem extensively [15, 16, 17, 18]. One example of individual blade control design using sliding-mode control is given by Xiao et al. [19]. Pitch control is often used to mitigate vibrations of offshore platforms, including the use of individual blade pitch control as in [20, 21, 22, 23, 24], and structural control methods as in [25]. These vibrations create fatigue damage of the foundation [26], so are often the focus of offshore wind turbine control design efforts. Accurate platform fatigue analysis requires nonlinear modeling of the wave conditions [27]. In general, the structural health monitoring systems should be integrated with the operation and controls of the wind turbine as demonstrated by Frost et al. [28]. A good prognostic control strategy would address all of these issues in addition to possible blade damage, but these considerations are beyond the scope of the current research. It is enough to say that pitch control techniques have been shown to have a wide variety of applications to blade-load reduction.

The simplest example of a load-reducing, pitch-control method is to utilize the available pitch-control system to control blade RPM and pitch to limit the power production to a lower level [9, 28]. For this research, the derating was accomplished by holding the RPM constant above the wind speed when the power production exceeds its derated level at a 0° pitch setting, and then using the pitch controller to maintain the power production as the wind speed increases. For the NREL 5 MW baseline turbine, a 50% derating strategy, and a Rayleigh wind profile with average wind speed of 10 m/s, the annual energy production (AEP) is reduced from $\approx 2.5 \times 10^7$ kWh to $\approx 1.5 \times 10^7$ kWh. The power production and control scheduling required to achieve this derating is shown in Fig. 1 as well as the root bending moment. The reduction in AEP is less than the reduction in maximum power level because at low wind speed the power production is not changed; the power production is only limited in this case at 9 m/s and above. The loads in terms of maximum bending moments at the root of the blade were reduced by approximately 50%. The advantage to using a simple "derating" method is that it would only involve a change in the software of currently operating offshore turbine control systems, and therefore could be easily retrofitted into pre-existing designs.

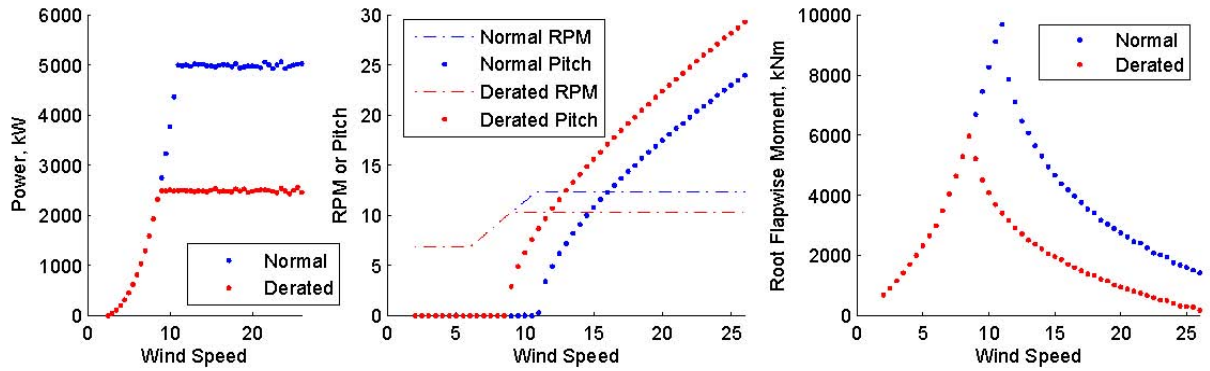

Figure 1: Derated (50% power level) power production control scheduling, and root bending moment compared with normal/baseline operation.

7.1.3.3 Damage Tolerance Analysis within a Prognostic Control Framework

The study of damage tolerance is a field in and of itself, with the damage tolerance of composites being currently quite active. A good review of the subject is given by Fan et al. [29]. Damage tolerance predictions may be divided into two categories: stress-based approaches and energy-based approaches. Stress-based approaches are quite useful for isotropic, ductile materials; but the anisotropic, brittle nature of composites leads to singular stress fields and damage mechanisms that are very different from those in metallic materials. Therefore, energy-based methods are often preferred for prediction of damage initiation and growth in composites. These energy-based methods involve calculation of the Strain Energy Release Rate (SERR), which is an estimate of the strain energy released when a crack opens from length a to a + da and is commonly referred to by the symbol G. Regardless of the material, the field of damage tolerance typically recognizes three distinct modes of crack propagation, referred to as Mode I, II, and III. Therefore, the energy-based prediction method will typically provide three values of G for each mode, denoted G_I, G_{II}, and G_{III}. Fracture is assumed to occur with energy-based methods when some combination of the G values for each mode reaches a material-dependent parameter known as the critical energy release rate G_c. The way in which the G values are combined depends on mode-mixity models, which are typically extracted from experimental data.

One popular energy-based method is the Virtual Crack Closure Technique (VCCT), which is reviewed by Krueger [3]. The VCCT essentially operates on the assumption that as the crack opens from size a to a+da, the internal forces at the crack tip do not change significantly. When attempting to close a crack from length a+da to length a, the energy required will be the opened displacements multiplied by the internal forces that resist the closure. The main assumption of the VCCT allows the forces at the crack tip to be used in this calculation. Therefore, the resulting formulas for the SERR in modes I, II, and III are, respectively,

$$G_I = \frac{1}{2\Delta a} F_y(u_y - \bar{u}_y) \qquad G_{II} = \frac{1}{2\Delta a} F_z(u_z - \bar{u}_z) \qquad G_{III} = \frac{1}{2\Delta a} F_x(u_x - \bar{u}_x) \qquad (1)$$

where u_i are the displacements of the upper surface and $\overline{u_i}$ are the displacements of the lower surface. Here, y refers to the direction perpendicular to the line of the crack in the "opening" direction, z refers to the direction along the line of the crack, and x refers to the direction

perpendicular to the opening direction and the line of the crack. This method has been recently applied to the problem of trailing edge disbonds by Eder et al. [30] to predict damage onset location and assess the effect of loading directions on the blade. They concluded that Mode III is the governing Mode of fracture for this type of damage and that flapwise shear and torsion are the most important load cases.

The VCCT method is valid for linear problems, and does not account for some typical damage phenomena such as fiber bridging. For this study, it is assumed that the damage lies within the adhesive and therefore the linear nature of the VCCT is acceptable. Because the crack is assumed to lie within the adhesive, any issue with the VCCT due to a bimaterial interface was avoided.

7.1.4 APPROACH AND RESULTS

This research will take a multiscale analysis approach to the problem. The Sandia National Laboratories Numerical Modeling and Design (NuMAD) tool is an open-source tool for analyzing realistic composite wind turbine blades [31]. This tool has the capability of transforming a traditional beam and section definition of a wind turbine model into a high-fidelity ANSYS shell model. Since this capability is readily available to interested academic and industry parties and it produces a high-fidelity model of the blade as a whole, this shell modeling capability was utilized for this study as the "global" analysis. The shell model does not have a sufficiently refined mesh near the trailing edge, which is the area of interest of this research, so the global analysis needs to be supplemented with a "local" analysis as well. After the VCCT is verified with a simple example and the mesh dependency of the technique is established, the criticality of trailing edge disbonds with respect to damage location and size is examined for both the normal operational strategy and the derated strategy. The comparisons will be made at the rated wind speed, where there is a significant difference in loading between the two operational strategies. To demonstrate the method, only the "global" analyses are shown here, so that the qualitative nature of the trends can be established.

7.1.4.1 Validation for Isotropic Section

To validate the VCCT method, a classic example was set up with isotropic materials. The example consists of a horizontal crack in a thin, square plate, with a vertical displacement condition applied to the upper and lower boundaries. The example has a known analytical solution for the SERR, which can be compared to the VCCT results to validate the method. The analytical solution is:

$$G_I = \frac{\pi \sigma^2 a}{E} \tag{2}$$

Figure 2 compares the grid convergence of this simple example. The general trend of the behavior is captured with the smallest mesh density, which lends credence to the following trends recovered using only the "global" shell model. For this study the shell model was used to examine the qualitative behavior of the SERRs, and further work will refine the analyses quantitatively.

7.1.4.2 Global NuMAD Shell Model

The damage location on the wind turbine blade, the coordinate system and the possible directions of damage propagation are depicted in Fig. 3. The NuMAD tool was used to generate an ANSYS model from a description of the NREL 5MW blade geometry and materials. The ANSYS shell model was modified by removing the connectivity of elements adjacent to the trailing edge, adding coincident nodes along the trailing edge, and reconnecting the upper elements to the new coincident nodes. Then, COMBIN elements, which are essentially nonlinear springs, were used to connect the coincident nodes. The stiffness behavior of the COMBIN elements was modified to have zero stiffnesses in the "X" (chordwise) and "Z" (spanwise) directions and in the positive "Y" (flapwise) directions, but a very high stiffness in the negative "Y" direction. This approach was verified to model the opening/closing behavior of the disbonds. The loading at rated wind speed during normal or derated operation was calculated using WT_Perf, which is a blade-element/momentum theory solver for wind turbines provided by the National Renewable Energy Laboratory (NREL). The distributed loading from the WT_Perf model was then applied to the ANSYS model via the application of point loads at each external node in the ANSYS model. The value of the point loads was obtained by performing a least-squares regression to determine a value of forces at each node to produce the desired distributed forces and twisting moments. The capability to map distributed loads to the ANSYS model is included in the NuMAD functionality [32].

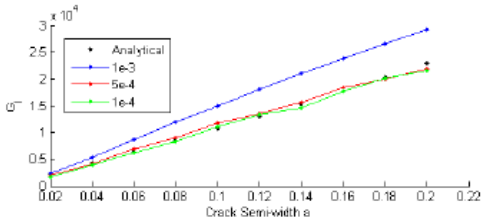

Figure 2: VCCT results for rectangular sample with horizontal mid-plane crack.

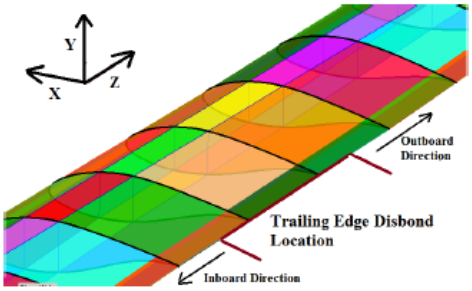

Figure 3: Depiction of trailing edge disbond location on blade, and possible directions of damage propagation.

<u>Healthy Blade Stress Results</u>

The healthy baseline stress values σ_{yy}, σ_{zz}, σ_{yz}, and σ_{xz} are shown along the bond line in Figs. 4 – 7, respectively. The stress components σ_{yy} and σ_{yz} are related to opening of the crack due to Mode I, and σ_{zz} and σ_{zx} are related to opening of the crack in modes II and III. Note that these healthy stress components show major perturbations in the vicinity of R = 10 m and R = 40 m locations. These locations happen to coincide with the locations where the ANSYS model blends from circular cross sections to blunt trailing edges (≈10 m span) and from blunt trailing edges to sharp trailing edges (≈ 40 m span). These transition points are shown in Fig. 8. These regions of high stress in the undamaged blade are therefore of interest when it comes to analysis of damage criticality.

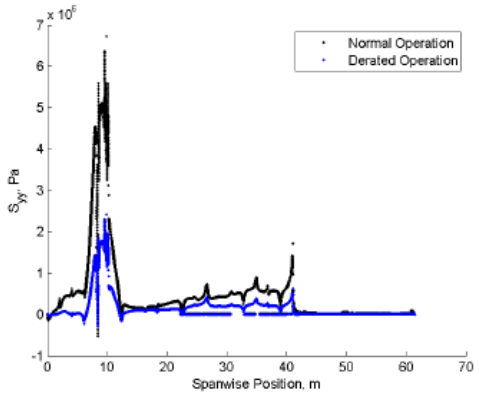

Figure 4: Stress results for σ_{yy} along the bond line for the baseline model during normal operation and derated to 50% power level.

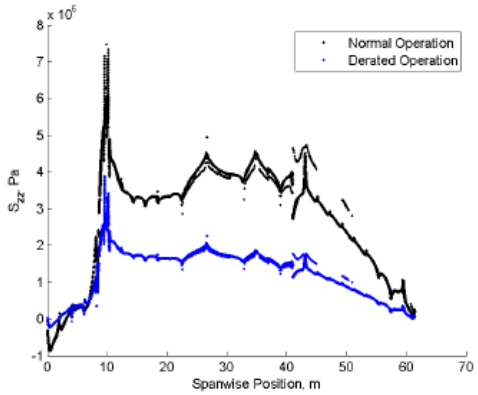

Figure 5: Stress results for σ_{zz} along the bond line for the baseline model during normal operation and derated to 50% power level.

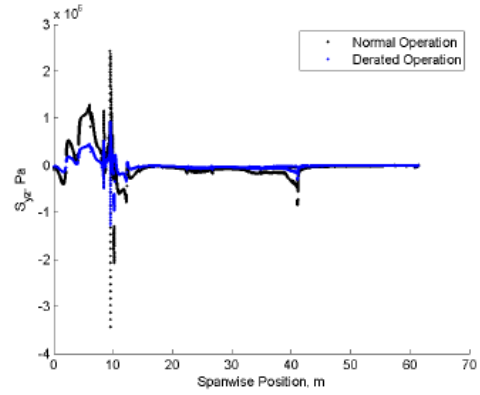

Figure 6: Stress results for σ_{yz} along the bond line for the baseline model during normal operation and derated to 50% power level.

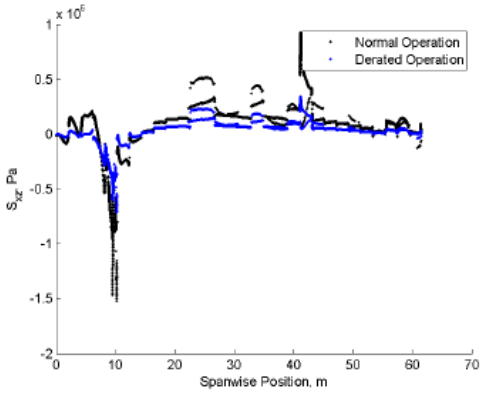

Figure 7: Stress results for σ_{xz} along the bond line for the baseline model during normal operation and derated to 50% power level.

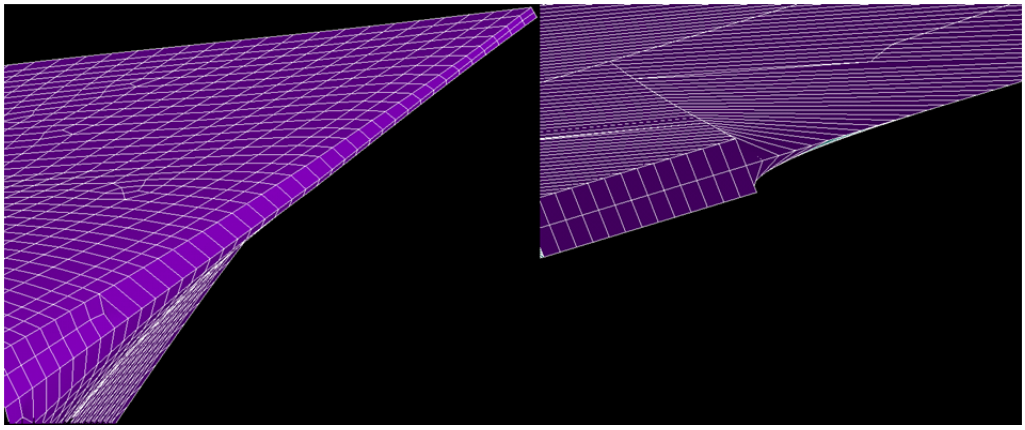

Figure 8: Geometry transitions from circular cross sections to airfoil sections with blunt trailing edges (left) and transition from blunt trailing edges to sharp trailing edges (right).

SERR Calculations Under Normal Operation

The SERR was calculated from the "global" ANSYS shell model by using the resulting nodal forces at the crack tip and the opened displacements of the nodes just within the crack tip. At this time, the "global" results are not fully trusted to be numerically accurate to the actual SERRs within the propagation, but it is assumed that these results are sufficient for demonstrating general trends. The results for SERRs of the healthy model are then shown in Figs. 9 – 14. Note that the results labeled "inboard" would represent the SERR for propagating the crack towards the hub, while results labeled "outboard" represent SERRs for crack propagation towards the tip of the blade. These show that the G_I values for the inner and outer crack tip are very high when the crack begins around the 10 m span location, and then drop suddenly as the start of the crack moves from 11 m to 12 m. After this the G_I values increase with the starting position of the crack. The G_{II} and G_{III} values generally increase both with increasing a and also with increasing starting position.

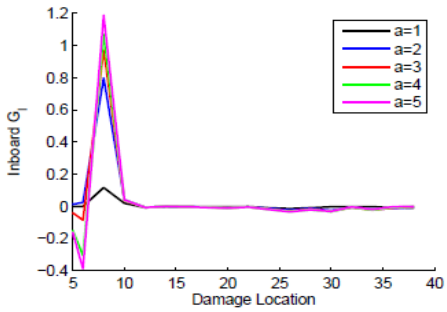

Figure 9: SERR (J/m^2) for Mode I fracture of the inner crack tip for various starting positions (11 – 20 m) and crack lengths (0.5 – 5 m), normal operation, rated wind speed.

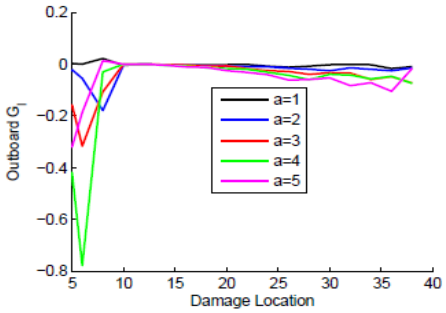

Figure 10: SERR (J/m^2) for Mode I fracture of the outer crack tip for various starting positions (11 – 20 m) and crack lengths (0.5 – 5 m), normal operation, rated wind speed.

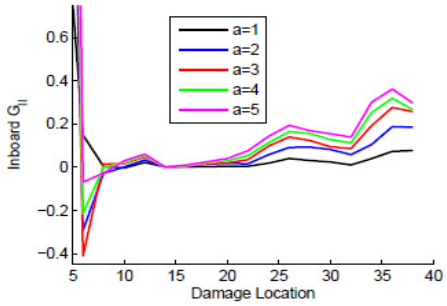

Figure 11: SERR (J/m^2) for Mode II fracture of the inner crack tip for various starting positions (11 – 20 m) and crack lengths (0.5 – 5 m), normal operation, rated wind speed.

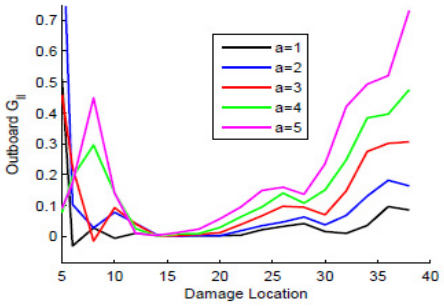

Figure 12: SERR (J/m^2) for Mode II fracture of the outer crack tip for various starting positions (11 – 20 m) and crack lengths (0.5 – 5 m), normal operation, rated wind speed.

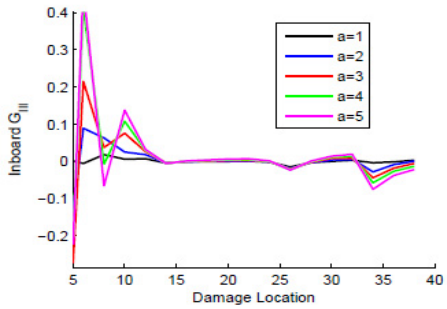

Figure 13: SERR (J/m^2) for Mode III fracture of the inner crack tip for various starting positions (11 – 20 m) and crack lengths (0.5 – 5 m), normal operation, rated wind speed.

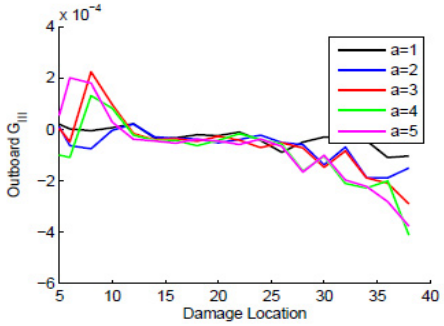

Figure 14: SERR (J/m^2) for Mode III fracture of the outer crack tip for various starting positions (11 – 20 m) and crack lengths (0.5 – 5 m), normal operation, rated wind speed.

SERR Calculations under Derated Operation

The loading at the rated wind speed during derated operation was calculated using WT_Perf and again mapped to the ANSYS model via nodal point loads. The derating involved setting the maximum power level to 2.5 MW and allowing the turbine controls to behave as if this were the rating of the wind turbine. The result was a slight adjustment to the RPM and pitch scheduling of the wind turbine (vs. wind speed). Figures 15 and 16 show selected SERR results for the turbine under this type of derating, at the rated wind speed, where the root bending moment has been reduced by a factor of 2.8.

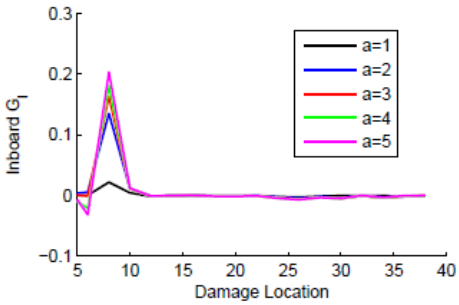

Figure 15: SERR (J/m^2) for Mode I fracture of the inner crack tip for various starting positions (11 – 20 m) and crack lengths (0.5 – 5 m), derated operation, rated wind speed.

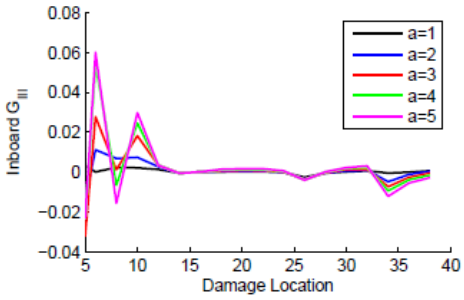

Figure 16: SERR (J/m^2) for Mode III fracture of the inner crack tip for various starting positions (11 – 20 m) and crack lengths (0.5 – 5 m), derated operation, rated wind speed.

These figures demonstrate that the derated values followed trends similar to those under normal operation but with reduced magnitude. This was true for each of the outputs shown in the previous section. For G_I, the calculated SERRs were reduced by around a factor of 7 by the derating process, and the SERR values for G_{II} and G_{III} were reduced by factors of around 5 by the derating process for this wind speed.

7.1.5 CONCLUSIONS – DAMAGE MITIGATION VIA SMART LOADS MANAGEMENT

A framework has been established for high-fidelity analysis of damage severity and demonstrated for the common damage type of trailing-edge disbonding. These efforts demonstrated that the most critical area in terms of damage onset is in the vicinity of the 10 m span location, which happens to be where the cross-sectional shape transitions from circular to airfoil-shaped. Therefore, this transition point is a key area of interest in damage tolerance analysis or designs that account for damage tolerance. Of course, the sharp corner in Fig. 8 may be due to mesh coarseness, but in general if this transition area can be smoothed out or reinforced, it may produce a more damage tolerant blade. In this research, the area of stress concentration in the baseline (healthy) bond line also had the highest SERR values. This implies that designing the blade considering the healthy stress results only may also be a strategy for producing damage tolerant designs.

This research also demonstrated the application of a derating controls strategy to reduce the SERRs of this common damage type. Although values of G_I were reduced significantly, a smaller reduction was found in G_{II} and G_{III}. Eder et al. [30] identified Mode III as the dominant failure mode for damage of this type. A more advanced derating strategy that also targets G_{II} and G_{III} will likely be more effective.

This high-fidelity analysis framework will be used to evaluate new control strategies or potentially damage tolerant designs. In order to provide accurate predictions of damage onset and growth using this model, it must first be supplemented by a local analysis procedure in order to

enhance the accuracy of the results. The SERR results will be used as inputs to a damage onset or growth model. The analysis will be conducted for each operating wind speed, and a probability law will be used to combine the growth rates into a meaningful result; also, dynamic analysis of extreme events will be performed. Then, the framework will be suitable to provide operations and maintenance guidelines for wind turbines under different types of operational strategies. These guidelines will help operators avoid catastrophic failure of turbine blades through advance warning, plan efficient maintenance operations and increase energy capture by avoiding shutdown. The smart loads management system, if possible, will utilize control architectures of modern offshore wind turbines and will therefore be useful for operators of existing state-of-the-art wind plants.

7.1.6 REFERENCES

[1] Griffith D T, Yoder N, Resor B, White J and Paquette J 2012 Structural health and prognostics management for offshore wind turbines: An initial roadmap Tech. Rep. SAND2012-10109 Sandia National Laboratories

[2] Griffith D T, Yoder N C, Resor B, White J and Paquette J 2013 Wind Energy

[3] Krueger R 2004 Applied Mechanics Review 57

[4] Snyder B and Kaiser M J 2009 Renewable Energy 34 1567–1578

[5] Frangopol D M, Saydam D and Kim S 2012 Structure and Infrastructure Engineering 8 1–25

[6] Rangel-Ramirez J G and Sorensen J D 2012 Structure and Infrastructure Engineering 8 473–481

[7] Zhang J, Chowdhury S, Zhang J, Tong W and Messac A 2012 12th AIAA Aviation Technology, Integration, and Operations (ATIO) Conference and 14th AIAA/ISSM. Indianapolis, Indiana

[8] Wenjin Z, Fouladirad M, Berenguer C et al. 2013 Annual Reliability and Maintainability Symposium-RAMS 2013

[9] Myrent N, Kusnick J, Barrett N, Adams D and Griffith D 2013 Structural health and prognostics management for offshore wind turbines: Case studies of rotor fault and blade damage with initial om cost modeling Tech. Rep. SAND2013-2735 Sandia National Laboratories

[10] Myrent N J, Adams D E and Griffith D T 2014 32nd ASME Wind Energy Symposium. National Harbor, Maryland

[11] Marden J R, Ruben S D and Pao L Y 2012 Proceedings of the 50th AIAA Aerospace Sciences Meeting, Nashville, TN.

[12] Gonzalez J S, Payan M B and Santos J R 2013 Eurocon, 2013 IEEE (IEEE) pp 1129–1134

[13] Kusiak A and Song Z 2010 Renewable Energy 35 685–694

[14] Jonkman J, Butterfield S, Musial W and Scott G 2009 Definition of a 5-mw reference wind turbine for offshore system development. Tech. Rep. NREL/TP-500-38060

[15] Bossanyi E 2000 Wind Energy 3 149–163

[16] Bossanyi E 2003 Wind Energy 6 119–128

[17] Bossanyi E 2003 Wind Energy 6 229–244

[18] Bossanyi E 2005 Wind Energy 8 481–485

[19] Xiao S, Yang G and Geng H 2013 ECCE Asia Downunder (ECCE Asia), 2013 IEEE (IEEE) pp 227–232

[20] Wang L, Wang B, Song Y and Zeng Q 2013 Advances in Vibration Engineering 12 377–390

[21] Larsen T J and Hanson T D 2007 Journal of Physics: Conference Series 75
[22] Jonkman J M 2008 2008 ASME Wind Energy Symposium, Reno, Nevada.
[23] Christiansen S, Bak T and Knudsen T 2013 IEEE Transactions on Control Systems Technology 6 4097–4016
[24] Namik H and Stol K 2010 Wind Energy 13 74–85
[25] Rotea M, Lackner M and Saheba R 2010 48th AIAA Aerospace Sciences Meeting and Exhibit, Orlando, Florida
[26] Yamashita A and Sekita K 2004 Proceeding of the 14th International Offshore and Polar Engineering Conference pp 166–171
[27] Trumars J M, Tarp-Johansen N J and Krogh T 2005 24th International Conference on Offshore Mechanics and Arctic Engineering (ASME)
[28] Frost S A, Goebel K, Balas M J and Henderson M T 2013 51st AIAA Aerospace Sciences Meeting Including the New Horizons Forum and Aerospace Exposition. Grapevine, TX, USA
[29] Fan X, Sun Q and Kikuchi M 2010 Journal of Solid Mechanics Vol 2 275–289
[30] Eder M, Bitsche R, Nielsen M and Branner K 2013 Wind Energy 17
[31] Berg J C and Resor B R 2012 Numerical manufacturing and design tool (numad v2.0) for wind turbine blades: Users guide Tech. Rep. SAND2012-7028 Sandia National Laboratories
[32] Berg J, Paquette J and Resor B 2011 52nd AIAA/ASME/ASCE/AHS/ASC Structures, Structural Dynamics, and Materials Conference. Denver, Colorado

7.2 Operating Strategies and Design Recommendations for Mitigating Local Damage Effects in Offshore Turbine Blades[6]

7.2.1 ABSTRACT

Two major barriers to widespread US acceptance of offshore wind energy is reliability of rotor blades and the difficulty to access for inspection and maintenance. This work presents operation and design strategies aimed to increase blade reliability and maximize power production. Operating strategies that prolong blade life while optimizing energy output allow for smarter maintenance planning and lower maintenance costs. Offshore plants require significant balance of station costs associated with each turbine, leading to large rotor diameters to capture the most energy per turbine. Rotor diameters have already approached 130 m, so this work extends that trend to 100 m blade (205 m diameter) designs. A combined aero/structural optimization process was used to produce new 100 m blade designs. A high-fidelity analysis method is presented to assess the local damage effects of a common damage type. The operation and design strategies are then compared for their effect to mitigate the local damage effects.

7.2.2 INTRODUCTION

Offshore wind power production is an attractive clean energy option, but there are several challenges to overcome if offshore wind is to be a viable energy source. Offshore plants require significant balance of station costs associated with each turbine, leading to large rotor diameters to capture the most energy per turbine. To investigate issues that arise with large blades, Sandia National Laboratories produced an all-glass design for a 100 m blade (Ref. 1) and a design utilizing carbon fiber (Ref. 2). An overview of the 100 m blade design project is given by Griffith et al. (Ref. 3). More conventional large turbine designs are in the neighborhood of 125 m diameter (63 m blade length), which is exemplified by the NREL 5 MW baseline turbine (Ref. 4).

The distance from shore creates significant operations and maintenance issues, sometimes leading to long periods between maintenance or inspection opportunities. The Structural Health and Prognostic Management (SHPM) project at Sandia National Laboratories attempts to address these issues by proposing a structural health and prognostic management system (Ref. 5). The overall flow chart for the SHPM project is shown below in Fig. 17. So far, it is has successfully shown that blade sensor measurements have the capability to estimate the size, nature, and location of blade damage (Refs. 6, 7). Simple fatigue considerations have identified the potential to derate the damaged turbine and significantly increase its fatigue life. Initial operating and maintenance cost models have been developed to predict the reduction in operating and maintenance costs that can be achieved using a prognostic control strategy, based on probabilities of progression from one damage state to another (Ref. 6). Here derating refers to altering the speed/pitch controller to limit the power production to a level lower than the normal rating of the turbine. This work concerns the "local" effects of damage, in terms of the

[6] Richards, Griffith, Hodges, "Structural Health and Prognostics Management: Operating Strategies and Design Recommendations for Mitigating Local Damage Effects in Offshore Turbine Blades," 70th American Helicopter Society Annual Forum & Technology Display, May 20-22, 2014, Montreal, Quebec, Canada.

opening/closing behavior of discrete damage features, early onset of buckling due to disbonded surfaces, etc. High-fidelity analysis techniques such as finite element analysis (FEM) should be used to evaluate these local effects of damage in order to characterize and quantify the risk of operating at a derated level when damage is known to exist. Understanding the local behavior of common damage types will then lead to development of operating and design strategies for more reliable offshore wind turbine blades.

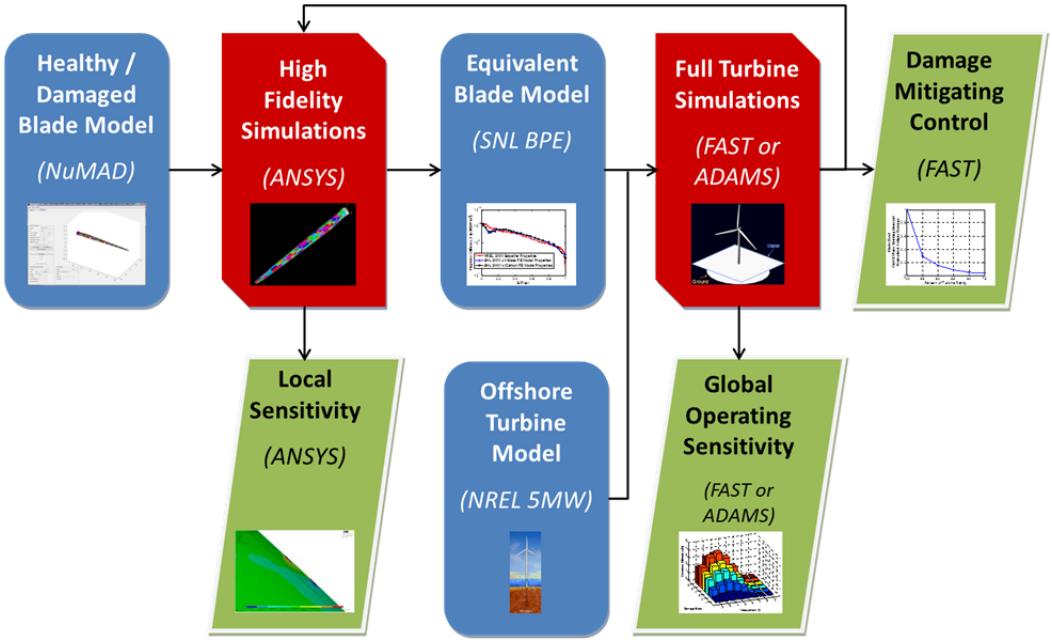

Fig 17: The SHPM multi-scale damage modeling and simulation methodology.

7.2.3 BACKGROUND

7.2.3.1 Damage Tolerance Analysis

See Section 7.1.3.3 for a description of the damage tolerance analysis approach.

7.2.3.2 Design Strategies for Damage Tolerance

The design of damage tolerant composite structures typically involves avoiding delamination by introducing "dispersion" into laminates and analyzing the adhesion of various types of bonded joints. The concept of dispersion is described by Lopes et al. (Ref. 8) and involves avoiding placing adjacent layers at the same layup angle so that cracks will be arrested at the interface between layers. Damage tolerance is also of primary concern in the design of adhesive joints, as illustrated by Kim, Kwon, and Keune (Ref. 9) in their study of adhesively bonded fuselage skins.

Damage tolerant design efforts for wind turbine blades need to consider the loading environment as well as common damage types. For example, Schaumann et al. (Ref. 10) use a time domain approach to consider fatigue loading from wind and waves in the design process of offshore platform support structures. Wetzel (Ref. 11) showed that spar caps embedded in the skin are less susceptible to spar bond failures, another example of damage tolerant structural design. Skin buckling is a primary design factor in large rotor blade design. Disbonded surfaces

typically worsen the skin buckling performance, whether due to changing the boundary conditions (in the case of a trailing edge disbond) or increasing the effective panel size (in the case of a spar/skin disbond). Therefore, a blade with a higher skin buckling capacity can be thought of as more damage tolerant in general. Concerning disbonding of adhesively bonded fuselage skins Kim, Kwon, and Keune (Ref. 9) state "the driving force for disbond growth following buckling initiation is the postbuckling deformations," so the panel buckling performance can be tied to damage tolerance for some damage types.

7.2.4 APPROACH AND RESULTS

This research will take a multi-scale analysis approach to the problem. The Sandia National Laboratories Numerical Modeling and Design (NuMAD) tool is an open-source tool for analyzing realistic composite wind turbine blades (Ref. 12). This tool has the capability of transforming a traditional beam and section definition of a wind turbine model into a high-fidelity ANSYS shell model. *See Section 7.1.4 for more information on blade modeling.* The criticality of trailing edge disbonds with respect to damage location was examined for both the NREL 5 MW (63 m radius) and the SNL 100-02 (102.5 m radius, Ref. 13) blade designs. Two simple derating strategies were explored using beam analysis tools such as WT_Perf and FAST/AeroDyn as well as using the "global" shell model to determine the capability of the strategy to mitigate local damage effects. Then, a combined aero/structural optimization was used to produce several new design candidates for the 100 m blade. These candidates are compared in terms of conventional measures such as geometry, AEP, blade weight, and stress-based fatigue damage as well as in terms of the damage tolerance of each design in the case of a trailing edge disbond.

7.2.4.1 ANSYS Analysis of Strain Energy Release Rates (SERRs)

The global NuMAD shell model was modified by removing the connectivity of elements adjacent to the trailing edge, adding coincident nodes along the trailing edge, and reconnecting the upper elements to the new coincident nodes. Then, COMBIN elements, which are essentially nonlinear springs, were used to connect the coincident nodes. The stiffness behavior of the COMBIN elements was modified to have zero stiffnesses in the "X" (chordwise) and "Z" (spanwise) directions and in the positive "Y" (flapwise) directions, but a very high stiffness in the negative "Y" direction. This approach was verified to model the opening/closing behavior of the disbonds. The loading at rated wind speed during normal or derated operation was calculated using WT_Perf, which is a blade-element/momentum theory solver for wind turbines provided by the National Renewable Energy Laboratory (NREL). The distributed loading from the WT Perf model was then applied to the ANSYS model via the application of point loads at each external node in the ANSYS model. The value of the point loads was obtained by performing a least-squares regression to determine a value of forces at each node to produce the desired distributed forces and twisting moments. The capability to map distributed loads to the ANSYS model is included in the NuMAD functionality (Ref. 14).

The values of G_I, G_{II}, and G_{III} were calculated for a 2 m disbond initiating at various points along the inner portion of the blade and are shown in Figs. 18 – 20. In these figures and onward, "Inboard" refers to the inboard crack tip and "Outboard" refers to the outboard crack tip. These show that for G_I and G_{III}, there seem to be critical areas for each blade. For the NREL 5 MW blade, the areas of 6 m and 8 m were chosen as areas of interest for G_{III} and G_I, respectively.

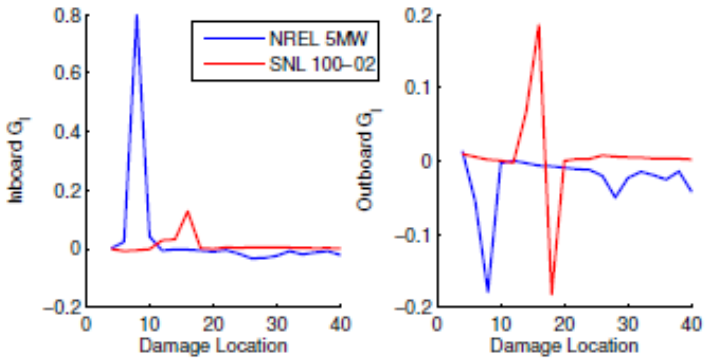

Fig 18: Damage criticality trends for G_I for the NREL 5 MW and SNL100-02 blade at the rated wind speed.

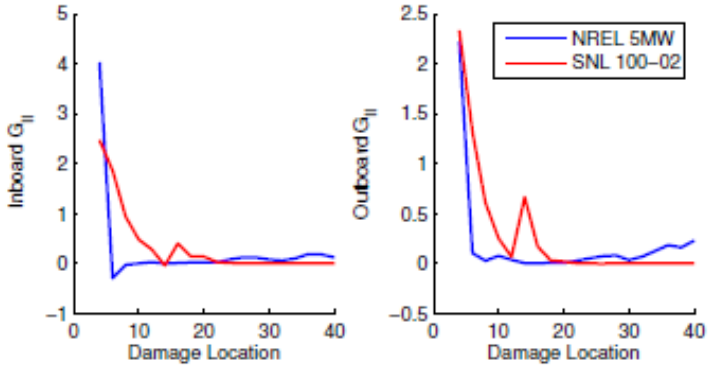

Fig 19: Damage criticality trends for G_{II} for the NREL 5 MW and SNL100-02 blade at the rated wind speed.

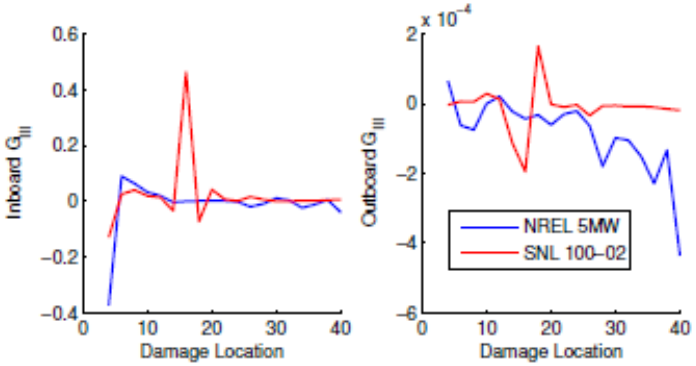

Fig 20: Damage criticality trends for G_{III} for the NREL 5 MW and SNL100-02 blade at the rated wind speed.

7.2.4.2 Potential SHPM Operation and Control Strategies

As discussed in Section 7.1.3.2, the simplest example of a load-reducing, pitch-control method is to utilize the available pitch-control system to control blade RPM and pitch to limit the power production to a lower level (Refs. 6, 15). For this research, the derating was accomplished by holding the RPM constant above the wind speed when the power production exceeds its derated

level at a 0° pitch setting, and then using the pitch controller to maintain the power production as the wind speed increases. For the NREL 5 MW baseline turbine, a 50% derating strategy, and a Rayleigh wind profile with average wind speed of 10 m/s, the AEP is reduced from $\approx 2.5 \times 10^7$ kWh to $\approx 1.5 \times 10^7$ kWh. The advantage to using a simple "derating" method is that it would only involve a change in the software of currently operating offshore turbine control systems, and therefore could be easily retrofitted into pre-existing designs.

To evaluate the realism of such a derating strategy, derating strategy "B" was analyzed using a FAST/AeroDyn wind speed sweep and compared to the baseline performance. Figures 21 – 22 show the speed controller and root bending moment predictions from the two analyses. These figures show the FAST/AeroDyn implementation varies slightly from intended, as the rotor speed was not intended to change. However, the power prediction and pitch controller performance were similar to predicted and the strategy successfully lowers the maximum bending moment by around 25%. The difference between these results and WT_Perf predicted reduction of 50% is due to a slight difference in the way the two loads are defined. Therefore, the WT_Perf loads were used in this report to calculate the SERRs for the normal and derated case.

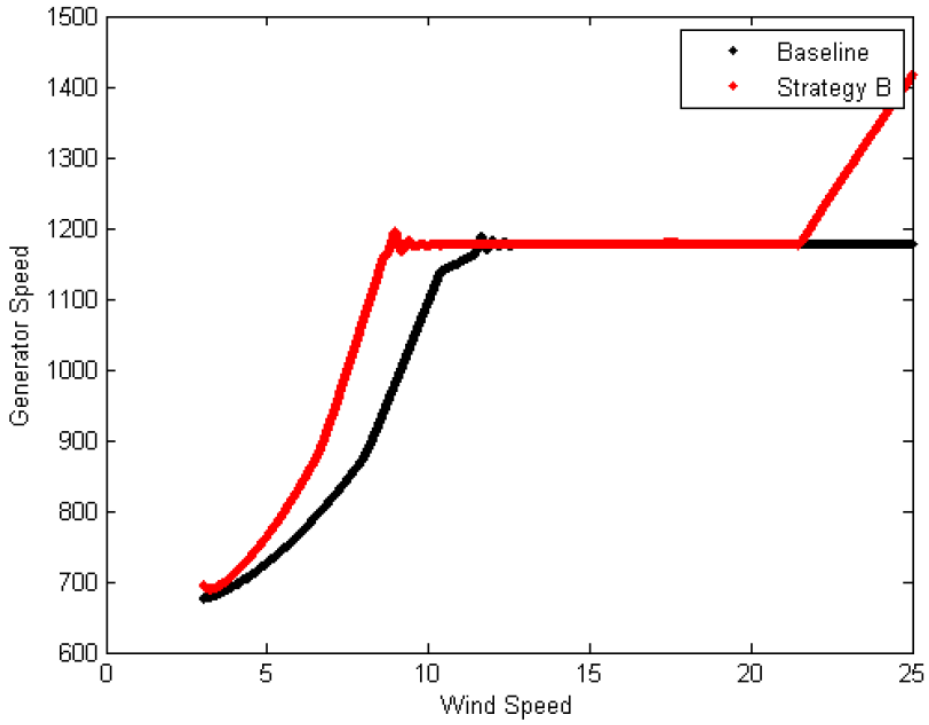

Fig 21: Rotor speed controller performance for NREL 5 MW baseline turbine for normal and derated operation.

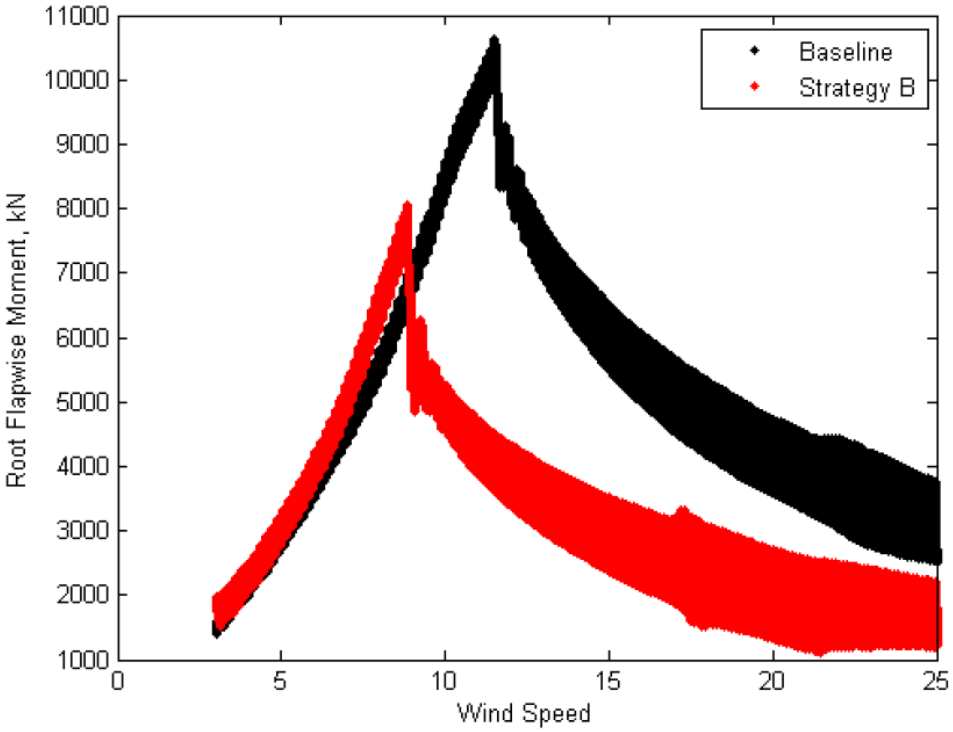

Fig 22: Flapwise bending moment predictions for NREL 5 MW baseline turbine for normal and derated operation.

The effect of these strategies in reducing the SERRs was also evaluated. The criticality analysis identified the 6 m and 8 m locations as areas of interest. Therefore, these areas were analyzed for G_I and G_{III} under the derating strategies "A" and "B." Figure 23 and 24 show how the SERRs at the areas of interest change with wind speed under normal and derated operation. These figures show a behavior similar to the thrust/moment vs. wind speed behavior (See Chapter 8, Fig. 1). The SERRs were then summed using a probability-weighted sum (similar to the way AEP is calculated), producing a weighted average SERR for each operating strategy. A Rayleigh wind speed distribution with an average wind speed of 10 m/s was used. This allowed calculation of an effective reduction in SERR due to the derating, which is shown for the 8 m disbond location in Table 1. These effective reductions could be thought of an effective decrease in damage growth rate while operating under the derated strategy. When results are refined with multi-scale analysis techniques and a growth law is applied, then effective reduction in damage growth rate can be predicted. These predictions will then be used to design a more comprehensive operations strategy to maximize power output while also maintaining blade reliability.

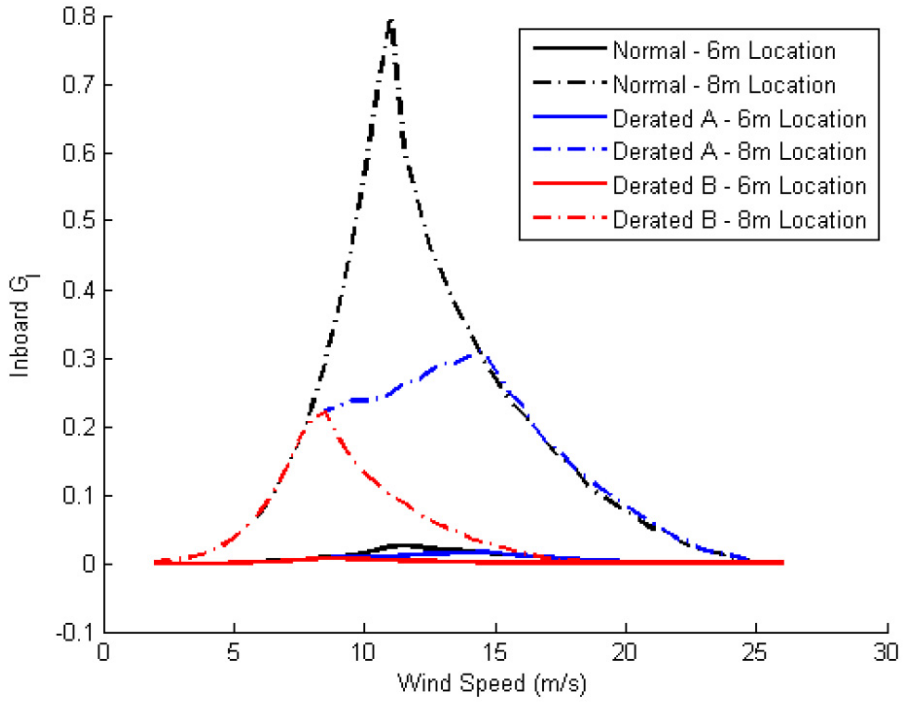

Fig. 23: G_I with respect to wind speed for NREL 5 MW turbine in normal/derated operation.

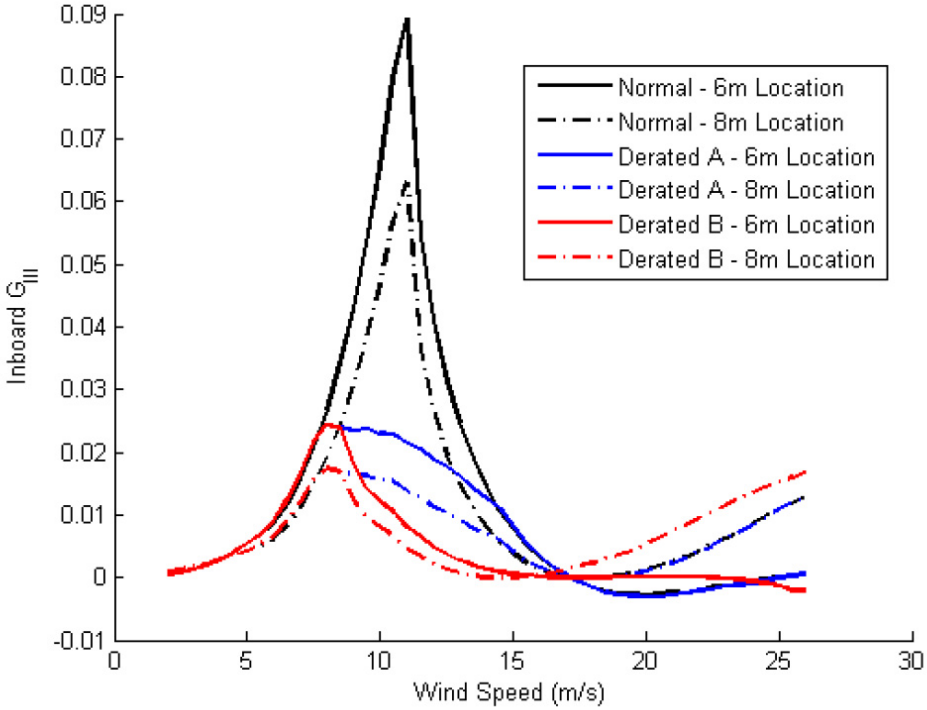

Fig. 24: G_{III} with respect to wind speed for NREL 5 MW turbine in normal/derated operation.

Table 1: Reduction in averaged SERRs for 8m disbond location under derated operation, weighted by a Rayleigh wind distribution with average wind speed of 10 m/s.

Derating Strategy	A	B
Reduction in G_I	35%	70%
Reduction in G_{II}	33%	70%
Reduction in G_{III}	47%	63%

7.2.4.3 Design Strategies for Damage Tolerance

The Sandia 100 m carbon blade design is used as a baseline for the reliable blade design process, as it represents a trend in future blade designs. A significant issue in the 100 m blade design precess was panel buckling, and these buckling issues can worsen in the presence of damage. The buckling performance can be improved by reducing the skin panel size, which provides an incentive for low solidity blade designs. The solidity of the blade can be decreased by increasing the operating tip speed ratio and implementing higher lift airfoils. So-called flat-back (FB) airfoils have high-lift properties, and the flat trailing edge provides an ideal location for trailing edge reinforcement. Trailing edge disbonding is a commonly encountered damage type and such reinforcement would improve the tolerance of blade designs to this type of damage.

So that "apples-to-apples" comparisons can be made between the new airfoils and the baseline airfoils, an optimized design was also produced with the baseline set of airfoils as well. The optimization process resulted in a Pareto front of candidates, which were then analyzed for their performance in terms of damage tolerance.

The process indicated that weight reduction and annual energy output (AEP) increases can be achieved by increasing the optimum (design) tip speed ratio and rotor solidity, but that damage tolerance considerations may place a limit on how high the design tip speed ratio should be raised. This is demonstrated by comparing two optimized designs with the DU series airfoils with two optimized designs with FB airfoils.

Combined Aero/Structural Optimization with Damage Tolerance Analysis

A multi-objective optimization process was conducted using the optimization tool HARP Opt, integrated with Sandia National Laboratories NuMAD toolbox and an open source code for composite wind turbine blade structural analysis, CoBlade (Refs. 16–18). The MATLAB Genetic Algorithm is used for the optimization process, with the objective functions being AEP and blade mass. After an optimization run, a Pareto front of candidates is produced. The selection of one particular candidate along the Pareto front should be based on economic decisions, so the increased costs associated with blade weight, including material and manufacturing costs, should be weighed against the potential for increased power output. However, such a detailed economic model is often based on prior experience and in this case difficult to apply. Therefore, the two candidates on the Pareto front were investigated in terms of blade weight, AEP, and damage tolerance: one candidate with the same AEP as the baseline, and another at an increased level of AEP. Therefore four candidates in total resulted from the optimization process, two with DU airfoils and two with flat-back (FB) airfoils. The candidates with the same AEP as the baseline will be referred to as DU #1 and FB #1, and the increased AEP candidates are DU #2 and FB#2.

The damage tolerance analyses included a stress-based fatigue analysis based on the S-N law

and Miner's rule. Representative material properties for the carbon fiber, unidirectional glass, and bidirectional skin material were used in the S-N analysis. The number of cycles and loading magnitudes are obtained from FAST/AeroDyn analysis of turbulent operation at each wind speed. Then, Miner's rule was used to sum the fatigue damage at each winds peed using the design wind speed profile, and the fatigue life was calculated. An ANSYS model of each design was created and used to calculate the buckling capacity at the maximum service loading condition. This ANSYS model was then used to perform a damage criticality analysis (SERRs) of each design.

An overview of each design including the analysis results is given in Tables 2 – 3. The twist, chord, and spar layers distributions of each design are summarized in Figs. 25 – 26. Figures 27 – 29 show some details about the aerodynamic performance of the different designs compared with the baseline. The optimized designs each feature an increased optimal tip speed ratio (TSR), which is demonstrated in Fig. 29 and results in a shift of the power production to lower wind speeds. These results highlight the tradeoff between design TSR, blade solidity, blade weight and AEP.

While the "damage tolerance" of the blade design in terms of the fatigue life calculation decreases with increasing TSR (decreasing solidity), the buckling margin increases as the solidity decreases. Therefore, the "damage tolerance" criterion would seem to suggest a moderate increase in the design TSR with respect to the SNL 100-02 design. *The fatigue life of the FB airfoils was generally improved with respect to the DU airfoils, especially considering that a lower number of spar layers are used in the FB designs.*

Table 2: 100 m blade design details, DU series airfoils.

Design	SNL 100-02	DU #1	DU #2
AEP (GWh)	66.7	66.7	67.3
Weight (kg)	59,043	52,765	55,588
Max Chord (m)	7.59	6.58	7.37
Design TSR	7.35	9.55	8.45
ECD Tip Δ (m)	10.97	10.62	11.28
Spar Life (yr)	15.3	1.9	14.7
TE Life (yr)	72	16.9	70.9
Buckling	2.19	2.02	1.92

Table 3: 100 m blade design details, FB airfoils.

Design	SNL 100-02	FB #1	FB #2
AEP (GWh)	66.7	66.7	67.3
Weight (kg)	59,043	52,876	55,375
Max Chord (m)	7.59	6.87	7.11
Design TSR	7.35	9.4	8.4
ECD Tip Δ (m)	10.97	10.47	11.67
Spar Life (yr)	15.3	33.7	8.3
TE Life (yr)	72	130	50
Buckling	2.19	2.63	2.57

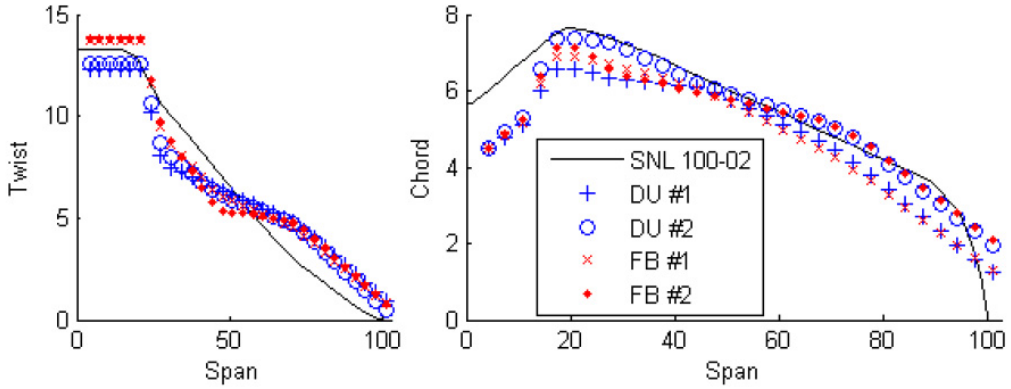

Fig. 25: Chord and twist distributions for two 100 m designs utilizing either DU series or FB airfoils.

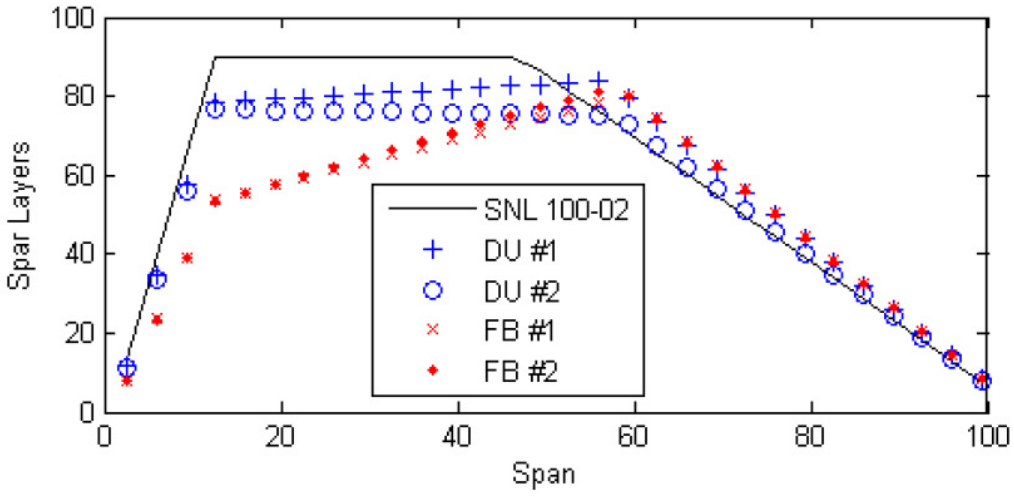

Fig. 26: Spar layer distributions for two 100 m blade designs.

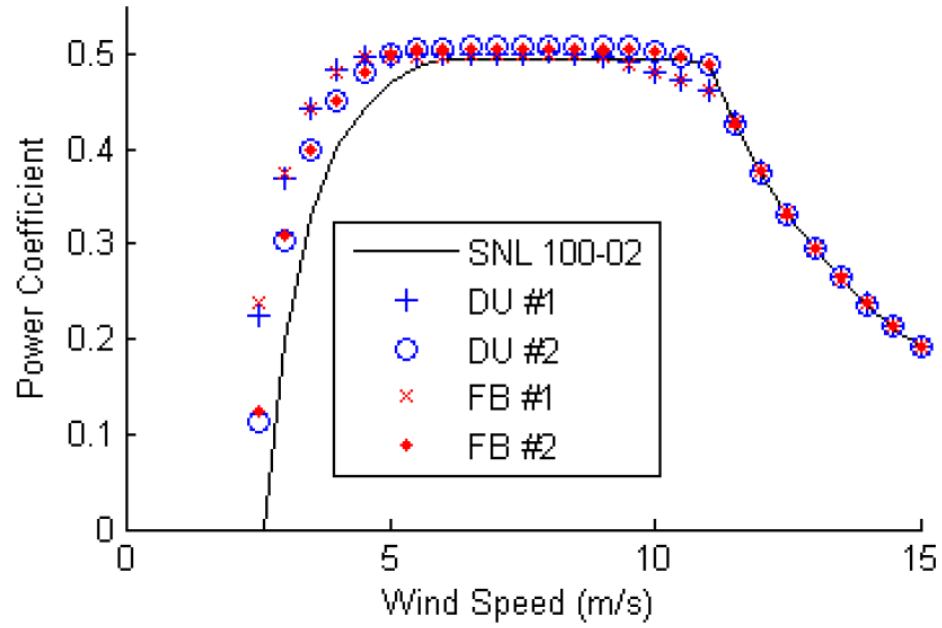

Fig. 27: Predicted power output in terms of C_p from the four different designs.

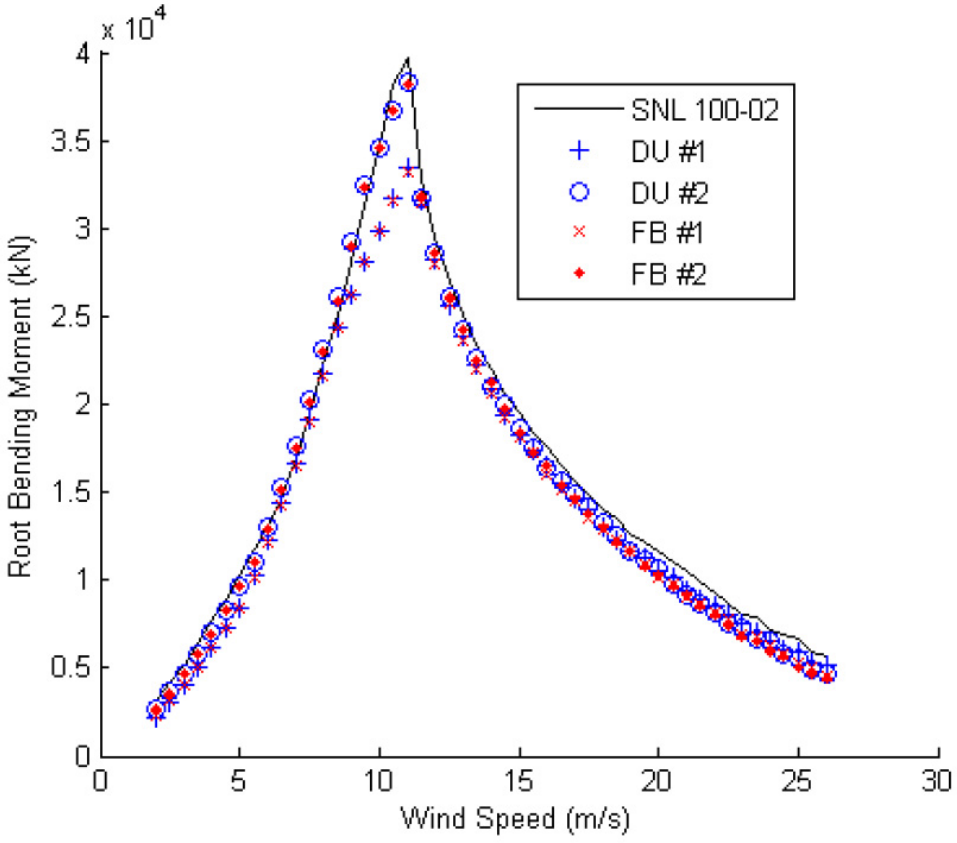

Fig. 28: Root bending moment predictions in kN for 100 m blade designs.

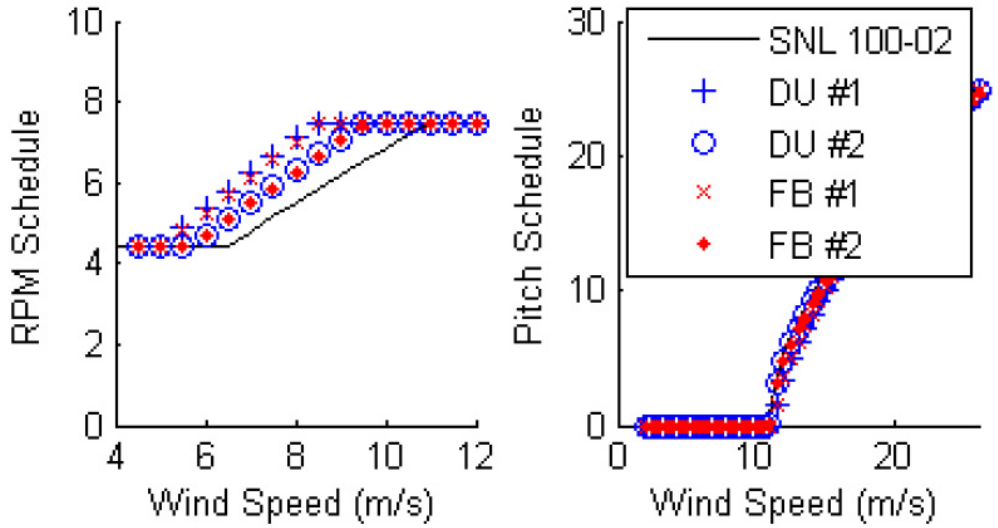

Fig. 29: Design control scheduling for 100 m blade designs. Pitch schedule is nearly identical for the three designs.

The damage criticality analysis was performed for each design for a trailing edge disbond length of 2 m. The resulting SERR values are given in Figs. 30 – 35. The optimized design DU #1, which had the same AEP and airfoil selection as the baseline design, but a greatly increased design TSR and reduced blade solidity, was found to have a higher peak in G_I , but generally decreased values in G_{II} and G_{III} . The DU #2 design, which has a moderately increased TSR, generally has lower SERR values. This suggests that the DU #2 design is the most damage tolerant design with respect to this damage type (TE disbond). The FB designs have lower G_{III} values, but G_I and G_{II} are higher for most of the damage onset locations. The SERR values for the FB designs are lower than the DU designs over the 10 – 20 m span location, which suggests that the FB airfoils could be used over this location to improve the damage tolerance of the baseline design.

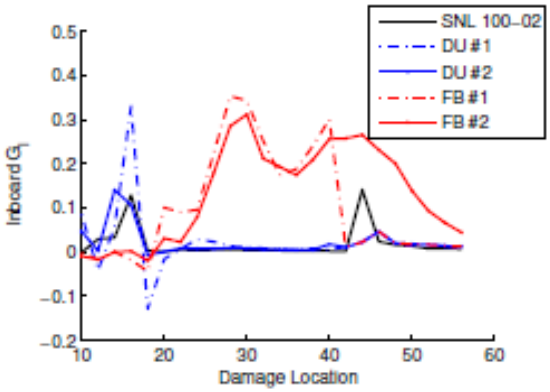

Fig. 30: Inboard G_I comparative measures for 100 m blade designs.

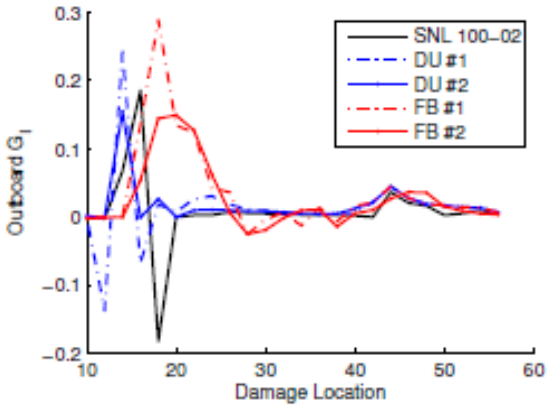

Fig. 31: Outboard G_I comparative measures for 100 m blade designs.

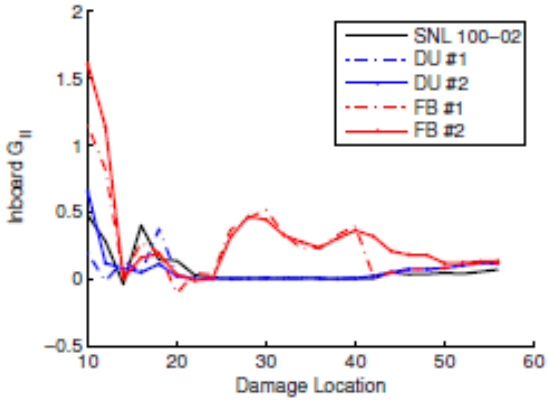

Fig. 32: Inboard G_{II} comparative measures for 100 m blade designs.

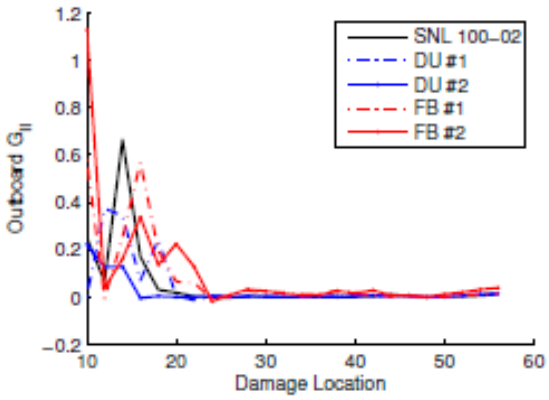

Fig. 33: Outboard G_{II} comparative measures for 100 m blade designs.

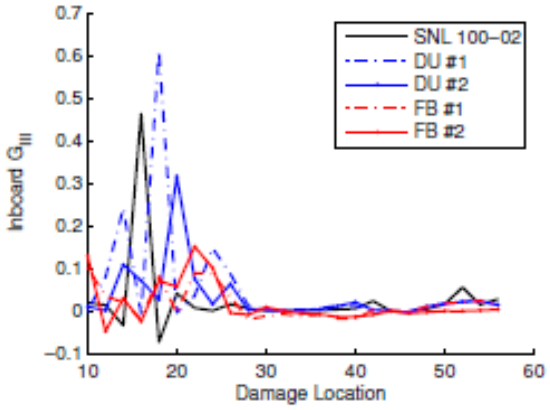

Fig. 34: Inboard G_{III} comparative measures for 100 m blade designs.

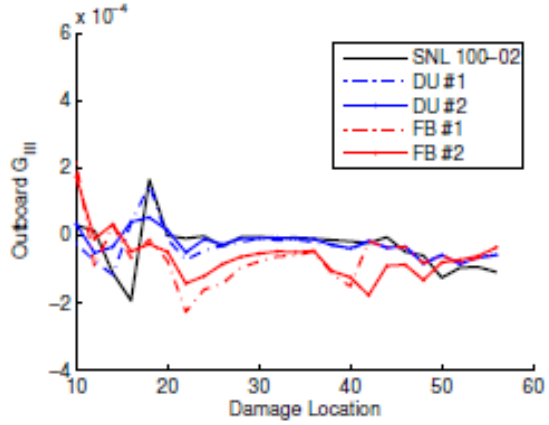

Fig. 35: Outboard G_{III} comparative measures for 100 m blade designs.

The designs were then analyzed in FAST/AeroDyn with a "static" analysis, a simple wind speed sweep, as well as a dynamic load case, the standard "extreme gust with direction change" design load case. The "static" results from the wind sweep analysis for the baseline and optimized designs are shown in Figs. 36 – 37. The dynamic analysis wind profile is shown in Fig. 38 and the performance is shown in Figs. 39 and 40. These show a general reduction in blade loads for the #1 designs, but a possible increase in loads with the #2 designs. However, the SERR calculations effectively replace these measures when evaluating the damage tolerance of each design, and the higher loads shown in Fig. 28 for DU #2 compared with DU #1 actually corresponded with lower SERRs. Therefore, the increased loads in Fig. 39 of the DU #2 design with respect to the baseline or DU #1 designs do not translate to reduced damage tolerance, and similarly the reduced loads of DU #1 do not translate to increased damage tolerance. Dynamic analysis of the SERRs will be required to obtain a more accurate characterization of the damage tolerance of each design.

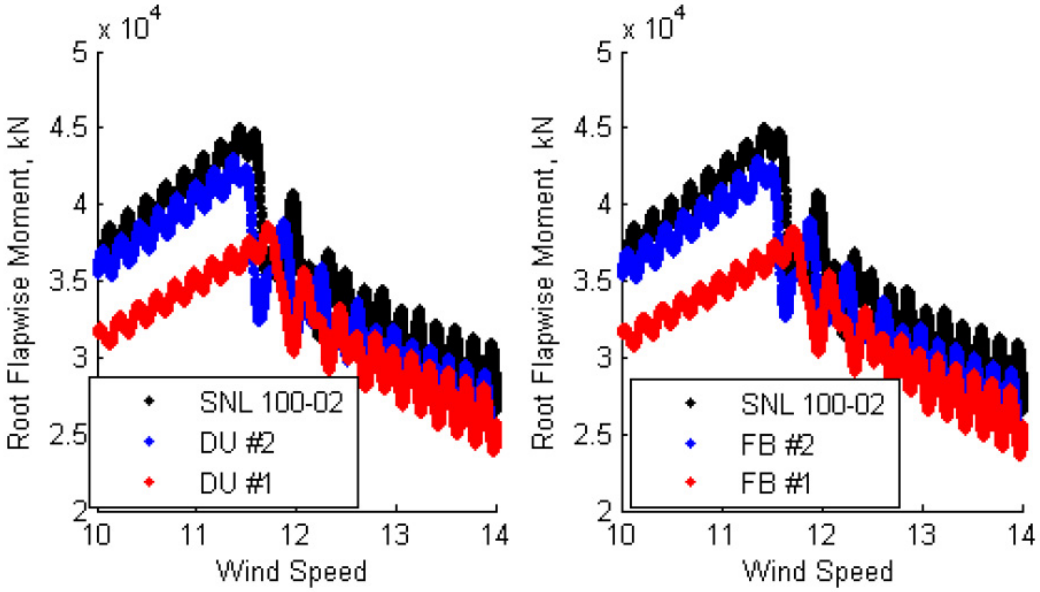

Fig. 36: Flapping moment predictions for 100m blade designs from wind sweep FAST/AeroDyn analysis.

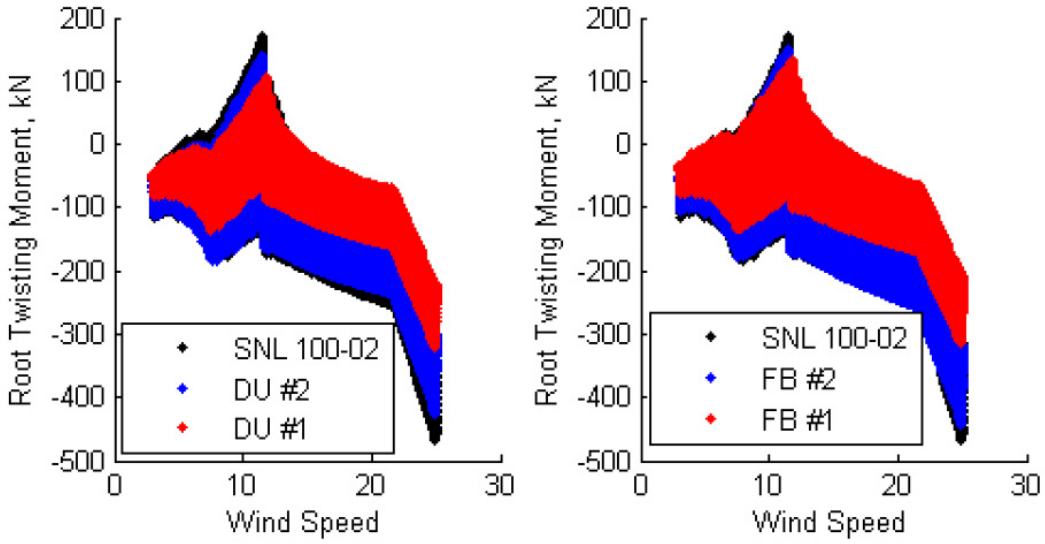

Fig. 37: Twisting moment predictions for 100m blade designs from wind sweep FAST/AeroDyn analysis.

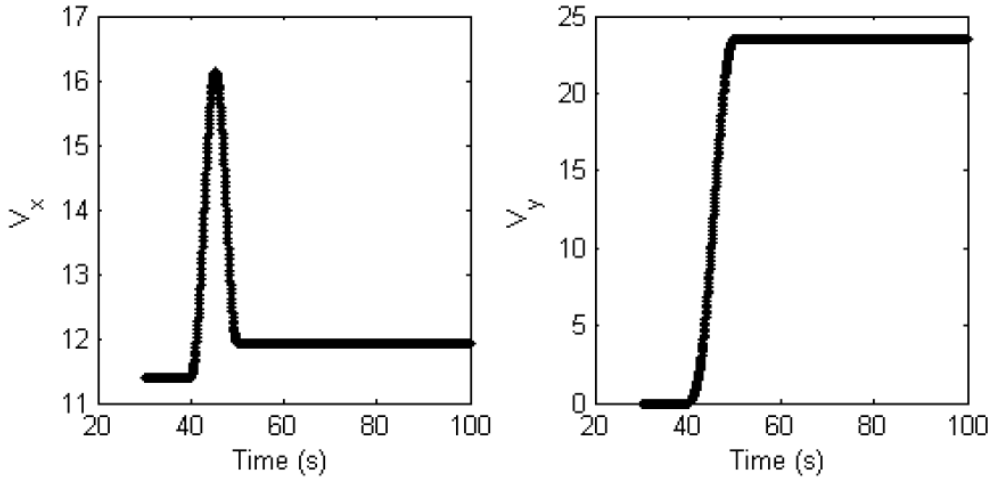

Fig. 38: Wind profile for "extreme coherent gust with direction change" analysis. V_x is aligned with the shaft axis and V_y is perpendicular to the shaft direction (but not vertical).

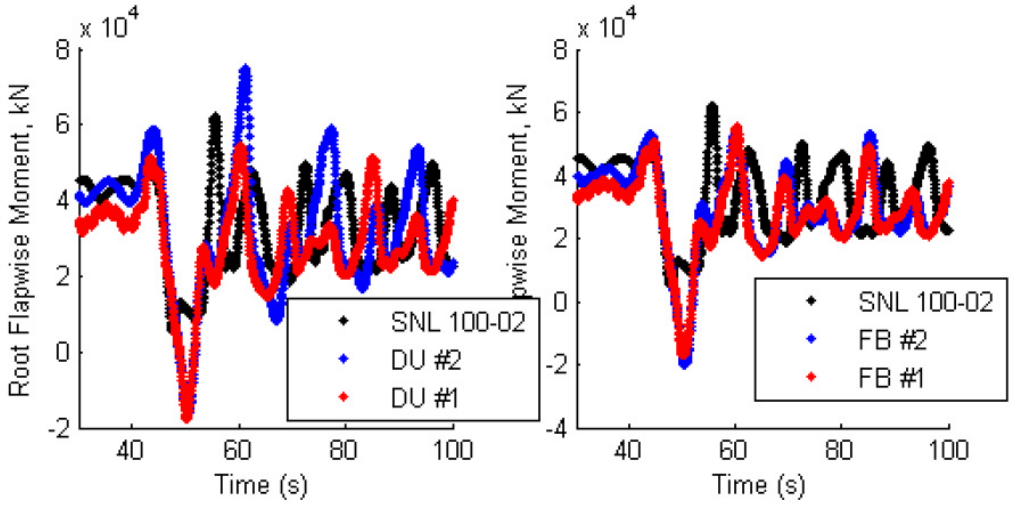

Fig. 39: Root bending moment (kN) time histories from ECD analysis of competing designs.

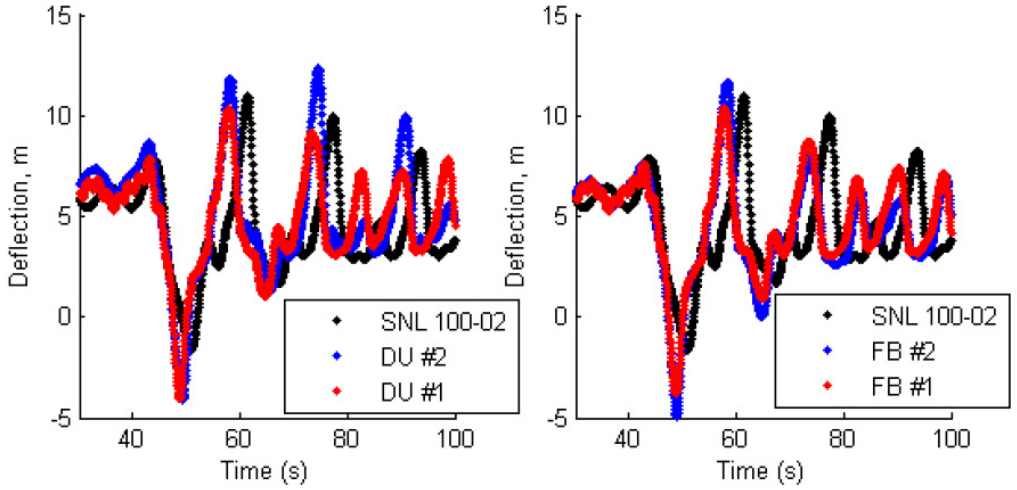

Fig. 40: Tip deflection time histories from ECD analysis of competing designs.

7.2.5 CONCLUSIONS – DAMAGE TOLERANT DESIGN

One of the primary barriers to wider acceptance of wind energy in the US is the reliability of offshore wind systems. This work attempts to increase the reliability for offshore wind turbine blades by introducing operating and design strategies designed to mitigate the effects of damage while continuing to produce power. Two simple derating strategies were evaluated with their potential to increase annual energy output (AEP), compared with shutdown, while reducing the effects of damage in terms of strain energy release rates. These derating strategies utilize available control systems for modern wind turbines, such as the NREL 5 MW representative model, as a "software" change, with no changes to the "hardware" required for implementation.

To demonstrate a damage tolerant design process for a wind turbine blade, a combined aero/structural optimization process was used to produce several candidates for a 100 m blade. The baseline DU series airfoils were compared with a new set of flat-back (FB) airfoils to investigate their potential to introduce damage tolerance. These candidates revealed that a moderate increase in design TSR allows for a reduction in blade weight and increase in AEP, but stress-based as well as SERR-based fatigue considerations place an upper limit on how much the design TSR should be increased. The FB airfoils seemed to perform better than the DU airfoils in terms of stress-based fatigue, but generally worse in terms of the trailing edge disbond SERRs.

However, the SERRs were lower for the FB airfoils over the 10 – 20 m location, and the flat trailing edge is an ideal location for additional reinforcement. If trailing edge reinforcement can be used to mitigate the SERR results for the FB #1 design, it would satisfy all design requirements and would be a good candidate for a new 100 m FB design. The focus of this work was the damage tolerant design method; however, a specific observation regarding slender (low-solidity) designs is made in that more slender blade designs can suffer from damage tolerance point of view; however, this can be addressed with additional layers applied to trailing edge. This design iteration was not pursued in this work; although, it would be worth considering as the addition of these trailing edge layers is easier from a manufacturing perspective for the flatback airfoil case.

Additional future work includes continuing efforts to explore damage tolerant operations and design strategies. The next step in this process would be to refine the accuracy of the SERR results as well as consider other types of common damage, such as a spar/skin disbond. Dynamic analysis of the SERR results will give a more accurate characterization of the damage tolerance of each design. Also, more advanced control strategies may be more effective in reducing the SERRs, especially in dynamic events like the "extreme gust with direction change" load case.

7.2.6 REFERENCES

[1] Griffith, D. and Ashwill, T., "The Sandia 100-meter All-glass Baseline Wind Turbine Blade: SNL100-00." Technical Report SAND2011-3779, Sandia National Laboratories, 2011.

[2] Griffith, D., "The SNL100-01 Blade: Carbon Design Studies for the Sandia 100-meter Blade." Technical Report SAND2013-1178, Sandia National Laboratories, 2013.

[3] Griffith, D. T., Resor, B. R., and Ashwill, T. D., "Challenges and Opportunities in Large Offshore Rotor Development: Sandia 100-meter Blade Research," AWEA WINDPOWER 2012 Conference and Exhibition. Atlanta, GA, USA, 2012.

[4] Jonkman, J., Butterfield, S., Musial, W., and Scott, G., "Definition of a 5-MW Reference Wind Turbine for Offshore System Development." Technical Report NREL/TP-500-38060, 2009.

[5] Griffith, D. T., Yoder, N., Resor, B., White, J., and Paquette, J., "Structural Health and Prognostics Management for Offshore Wind Turbines: An Initial Roadmap," Technical Report SAND2012-10109, Sandia National Laboratories, 2012.

[6] Myrent, N., Kusnick, J., Barrett, N., Adams, D., and Griffith, D., "Structural Health and Prognostics Management for Offshore Wind Turbines: Case Studies of Rotor Fault and Blade Damage with Initial OM Cost Modeling," Technical Report SAND2013-2735, Sandia National Laboratories, 2013.

[7] Myrent, N. J., Adams, D. E., and Griffith, D. T., "Aerodynamic Sensitivity Analysis of Rotor Imbalance and Shear Web Disbond Detection Strategies for Offshore Structural Health Prognostics Management of Wind Turbine Blades," 32nd ASME Wind Energy Symposium. National Harbor, Maryland, 2014.

[8] Lopes, C., Seresta, O., Abdalla, M., G¨urdal, Z., Thuis, B., and Camanho, P., "Stacking sequence dispersion and tow-placement for improved damage tolerance," Proceedings of the 49th Structures, Structural Dynamics, and Materials Conference, Schaumburg, Illinois, Paper AIAA 2008-1735, April 7 – 10, 2008.

[9] Kim, H., Kwon, H., and Keune, J., "Buckling Initiation and Disbond Growth in Adhesively Bonded Composite Flanges." 44th AIAA/ASME/ASCE/AHS/ASC Structures, Structural Dynamics, and Materials Conference. Norfolk, VA., 2003.

[10] Schaumann, P. and Wilke, F., "Enhanced Structural Design for Offshore Wind Turbines," XICAT 2006, Xi'an International Conference of Architecture and Technology, 2006.

[11] Wetzel, K., "Defect-Tolerant Structural Design of Wind Turbine Blades." 50th AIAA/ASME/ASCE/AHS/ASC Structures, Structural Dynamics, and Materials Conference. Palm Beach, FL., 2009.

[12] Berg, J. C. and Resor, B. R., "Numerical Manufacturing And Design Tool (NuMAD v2.0) for Wind Turbine Blades: User's Guide," Technical Report SAND2012-7028, Sandia National Laboratories, 2012.

[13] Griffith, D.T., "The SNL100-02 Blade: Advanced Core Material Design Studies for the Sandia 100-meter Blade," Sandia National Laboratories Technical Report, November 2013, SAND2013-10162.

[14] Berg, J., Paquette, J., and Resor, B., "Mapping of 1D Beam Loads to the 3D Wind Blade for Buckling Analysis," 52nd AIAA/ASME/ASCE/AHS/ASC Structures, Structural Dynamics, and Materials Conference. Denver, Colorado, 2011.

[15] Frost, S. A., Goebel, K., Balas, M. J., and Henderson, M. T., "Integrating Systems Health Management with Adaptive Contingency Control for Wind Turbines," 51st AIAA Aerospace Sciences Meeting Including the New Horizons Forum and Aerospace Exposition. Grapevine, TX, USA, 2013.

[16] Sale, D., "HARP Opt, Horizontal Axis Rotor Performance Optimization," National Renewable Energy Laboratory. http://wind.nrel.gov/designcodes/simulators/HARP_Opt/, Accessed: July 2013.

[17] "Numerical Manufacturing And Design Tool (NuMAD)," Sandia National Laboratories. http://energy.sandia.gov/?page_id=2238, Accessed: July 2013.

[18] Sale, D., "CoBlade, Open Source Software for Composite Wind Turbine Blades," https://code.google.com/p/co-blade/, Accessed: July 2013.

(this page intentionally left blank)

CHAPTER 8. IMPACTS OF SHPM-BASED DERATING ON AEP AND REVENUE

In this chapter, economic implications of SHPM are considered. The focus is on the potential increase in energy capture based on implementing a smart loads management (derating) strategy as discussed in Chapter 7. Highlights of this chapter include:

- The economic payback of derating versus a shutdown is quantified (for an assumed value of electricity).
- A parameter study is performed to quantify the effects of the following variables on SHPM economics (i.e. AEP):
  - derating type (Strategy A or Strategy B)
  - derating level (e.g. percent derating in maximum power)
  - seasonal variation effects (i.e. monthly variation)
  - impacts of the quality of the wind resource (e.g. low versus high wind site).

Additional cost analysis for O&M is addressed in the earlier chapters (see Chapters 4 and 6) for the initial modeling of the O&M costs impacts of SHPM.

As noted in Chapter 7, two different ways (derating types) to reduce service bending moments by derating were evaluated: (a) limiting the value of the bending moment or thrust without limiting the power rating (derating strategy "A"), or (b) limiting the power rating (derating strategy "B"). Figure 1 shows an example of the two derating strategies for the case of limiting the bending moment to 50% of its maximum value.

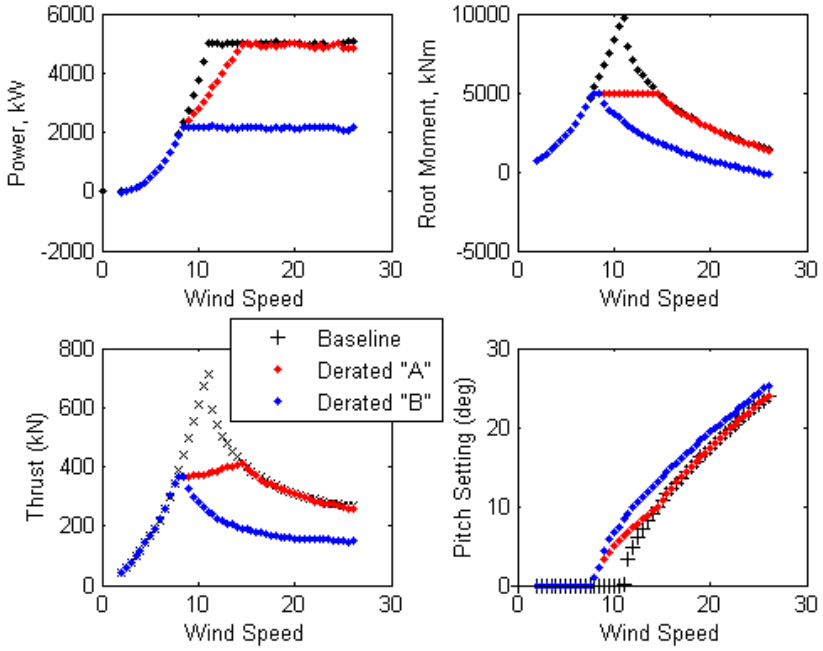

Figure 1: Power Production, Root Bending Moment, Rotor Thrust Predictions for Two Derating Strategies "A" and "B" and Derating Level of 50%. The Derating Strategies Are Achieved by Modifying the Pitch Control Settings as Shown in Lower Right.

The NREL 5 MW baseline design is used for the operations and control strategy evaluations as a representative of "current" offshore blade technology. The AEP of the NREL 5 MW baseline turbine for a possible Alaska location with a one-month shutdown, using wind data from Pryor et al. (Ref 1), is then shown in Table 1. The location was chosen as a realistic representative site with an average wind speed of ≈ 10 m/s. The additional revenue for operating at a derated level for the 12th month instead of shutting down is also given in Table 1.

Consider if the value of electricity was assumed to be 20 cent/kW-hr, which is closer to current offshore wind prices. Then, the additional revenues shown in the tables would be the same monetary values for an assumed derating period of only 1 week (approximating 1 week at 0.25 of a month).

Table 1: Annual Revenue and Revenue Increases (using 5 cent/kW-hr) for Operating at Derated Level for 1 Month Instead of Shutdown

	Alaska Site (9.9 m/s)
Annual Revenue	$1,210,000
Derating Level	Additional Revenue
75% (A)	+$108,000 (+8.9%)
75% (B)	+$81,600 (+6.8%)
50% (A)	+$96,000 (+8.0%)
50% (B)	+$64,000 (+5.3%)
25% (A)	+$60,400 (+5.0%)
25% (B)	+$22,900 (+1.9%)

Figure 2 shows the wind speed monthly variation as measured at a Baltic offshore site which has an approximate average wind speed of 11 m/s, and Table 2 shows how the additional revenue could vary over the course of the year with derating in calm month of 7 m/s in Month 6 versus derating in a windy month of 16.5 m/s average wind speed.

If a turbine must be shutdown (for example for inspection or maintenance), there is an incentive to derate during the high wind speed months to avoid the larger revenue losses of a shutdown in these periods versus a shutdown during the calm months. Further, maintenance actions can be postponed until a calm period so that plant revenues can be increased. In addition, it is during the calm period when offshore turbine accessibility (i.e. ability to get to the turbine) is greater, which provides additional motivation for the timing of such derating actions together with maintenance actions.

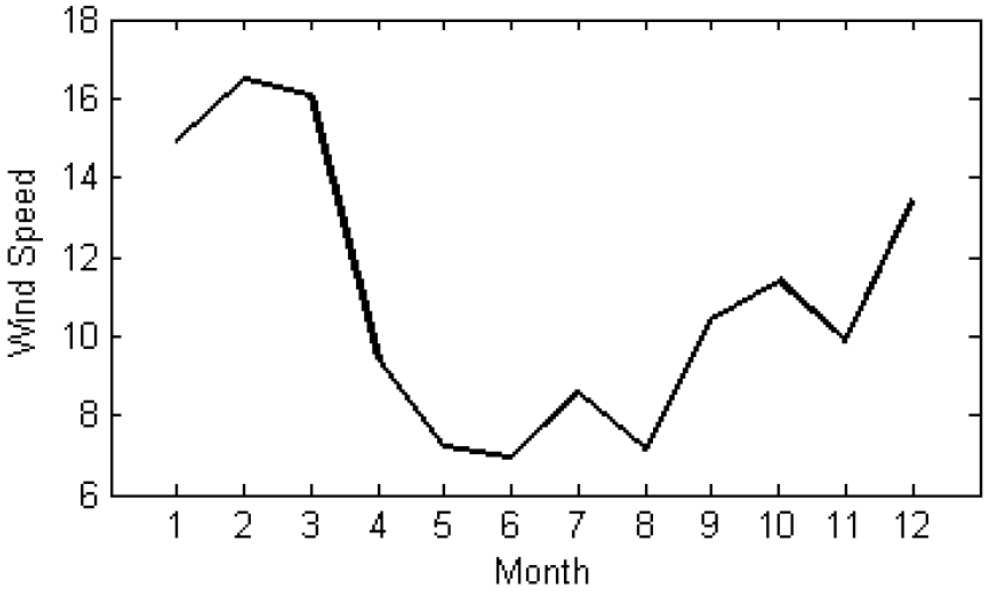

Figure 2: Monthly Variation in Winds peed for a Baltic Offshore Site with a Wind Speed Average of 11 m/s (Ref. 2)

Table 2: Variations due to Monthly Wind Speed Variation in Possible Revenue Increases (using 5 cent/kW-hr) when Derating for 1 Month Instead of Shutdown

Level	Calm (7 m/s)	Windy (16.5 m/s)
75% (A)	+$63,800 (+4.9%)	+$140,000 (+10.7%)
75% (B)	+$53,400 (+4.1%)	+$99,100 (+7.6%)
50% (A)	+$55,800 (+4.3%)	+$131,000 (+10.0%)
50% (B)	+$44,500 (+3.4%)	+$73,800 (+5.6%)
25% (A)	+$35,300 (+2.7%)	+$96,800 (+7.4%)
25% (B)	+$19,200 (+1.5%)	+$23,900 (+1.8%)

REFERENCES

[1] Pryor, S., Nielson, M., Barthelmie, R., and Mann, J., "Can Satellite Sampling of Offshore Wind Speeds Realistically Represent Wind Speed Distributions? Part II: Quantifying Uncertainties Associated with Distribution Fitting Methods." *American Meteorological Society*, Vol. 43, (5), May 2004, pp. 739–750.

[2] Palutikof, J., Halliday, J., Watson, G., Holt, T., Barthelmie, R., Coelingh, J., Folkerts, L., and Cleijne, J., "Predicting the Wind Energy resource in the Offshore seas of Europe," Symposium on Environmental Applications; American Meteorological Society 82.

(this page intentionally left blank)

CHAPTER 9. SUMMARY OF MAJOR FINDINGS, STATUS OF SHPM TECHNOLOGY ROADMAP, AND RECOMMENDATIONS FOR FUTURE WORK

In summary, this report is a compilation of the research performed in the Sandia Structural Health and Prognostics Management (SHPM) program from 2011 to 2015. The SHPM program focused on research to develop and evaluate technical innovations showing promise for maximizing plant revenues and reducing LCOE for offshore wind plants. More specifically the goals of the SHPM program were to reduce O&M costs and increase energy capture through use of SHPM-based technologies.

This research addresses one of the key challenges facing the industry, that is, to develop reliable methods to detect damage in the rotor blades and to detect them early enough to impact operations and repair/maintenance decisions leading to reduced costs and increased revenues. The principal motivations of this research are to reduce operations and maintenance (O&M) costs, improve wind-plant reliability, and reduce downtime. A particular focus, when considering offshore siting, is to mitigate the large rise in costs for offshore O&M due to access difficulty, weather, high sea states, etc. using structural health monitoring and prognostics management (as illustrated in Figure 1).

Figure 1. Illustration of Offshore Wind Accessibility Challenges (Weather, High Sea States, and Remote Access) that Motivate the Need for Structural Health and Prognostics Management

With the overall goals to significantly reduce O&M costs and increase energy capture, the motivations behind this research were to develop and evaluate new strategies – robust and cost-effective SHPM strategies that can provide the following features (of varying complexity):

1. ensure operations in a desired (designed) safe state of health,
2. aid in planning of maintenance processes versus more costly unplanned servicing,
3. avoid catastrophic failures through advance warning, and/or
4. improve energy capture by avoiding unnecessary shutdown and increasing overall plant availability.

LCOE is affected in 3 principal ways through implementation of an SHPM monitoring system:

1. Increased capital costs for sensing and prognostics. These additional costs must be offset by the benefits of SHPM (in the following two areas, O&M and AEP) for cost-effectiveness:
2. Reduced operations and maintenance (O&M) costs via improved maintenance processes and improved maintenance planning, and also the benefit of
3. Increased energy capture (AEP) by minimization of downtime or planning of downtime when the wind resource (and revenue loss) is at a minimum,

as illustrated in Figure 2.

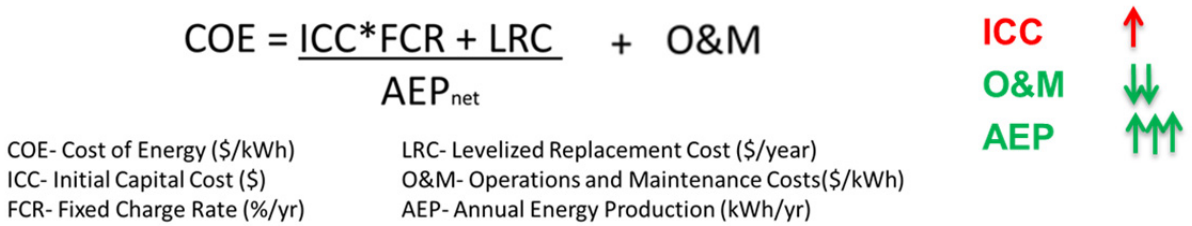

Figure 2. Illustration of SHPM Impacts on LCOE (Higher Capital Costs with Potential for Improvements in AEP and O&M Cost Reductions)

This concluding chapter is organized as follows:

- First, the major findings of the research program are summarized (Section 9.1).
- In the next section (Section 9.2), the SHPM Technology Roadmap is reviewed. The current status is summarized. Recommendations for near-term and longer-term follow-on activities in each of the roadmap Thrust Areas are suggested.
- In the final section (Section 9.3), additional recommendations for future work are made. Whereas Section 9.2 provides specific recommendations associated with each Thrust Area of the technology roadmap, in Section 9.3 overall recommendations on SHPM technology integration and an SHPM decision making process are suggested.

9.1 Summary of Major Findings of the Sandia SHPM Program

Here, the major findings and contributions of the Sandia Structural Health and Prognostics Management (SHPM) program are summarized:

[1] A Roadmap for SHPM Technology. A comprehensive technology roadmap for SHPM was developed bringing together structural health monitoring and prognostics management. This roadmap outlined the individual technical research blocks, their maturation paths and the integration needed across the research blocks to *develop a cost-effective SHPM system for wind turbine rotors* for maximizing revenue and reducing LCOE in wind plants.

[2] A Multi-scale Damage Modeling and Simulation Methodology. A multi-scale damage modeling and simulation method was developed and demonstrated (See Figure 3). This methodology provided a new capability that is computationally efficient and broadly applicable to all blade damage types. This methodology aids in the design and evaluation of new sensing & damage detection strategies and in development of new prognostic management strategies (e.g. smart loads management, damage mitigating controls) for wind turbine blades; and by extension is applicable to other structural components as well.

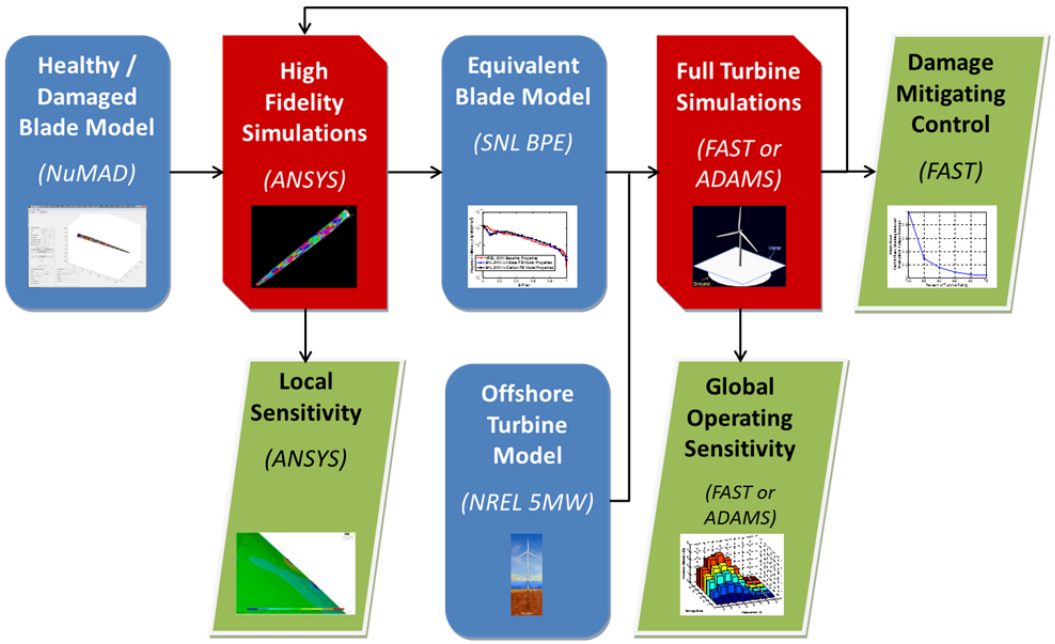

Figure 3. The multi-scale damage modeling and simulation methodology designed to aid in the development and optimization of health monitoring systems for wind turbine blades.

[3] Damage Detection Strategies for Common Damage Types (Global Operating Sensitivity). Damage detection is possible in wind turbine rotors. In these studies, the operational response of the rotor (i.e. moments, accelerations) was found to be sensitive to the presence of damage; indicating that damage can be detected with common sensors such as strain sensors or accelerometers and demonstrating which locations in the blade are most suitable for

sensor placement. This was demonstrated for several important case studies of blade damage or rotor faults:

a. Trailing edge (TE) disbonding (See Figure 4 for an operational response analysis)
b. Shear web (SW) to spar disbonding (See Figure 5 for a detection strategy using blade and non-blade sensors)
c. Rotor imbalance (mass and aerodynamic imbalance)

These were the three case studies that were analyzed in this research program; however, the multi-scale modeling and simulation approach has broad applicability for additional damage and fault cases of interest.

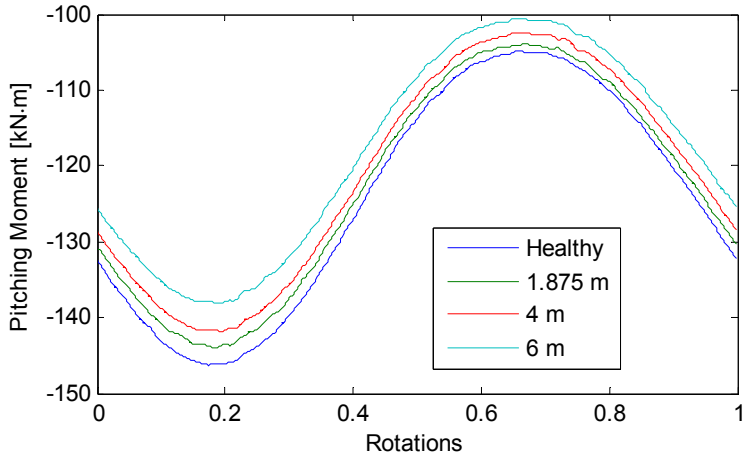

Figure 4. An operational response of the rotor, here the local pitching moment, illustrates sensitivity to trailing edge disbond damage (1.875, 4 or 6 meters in length).

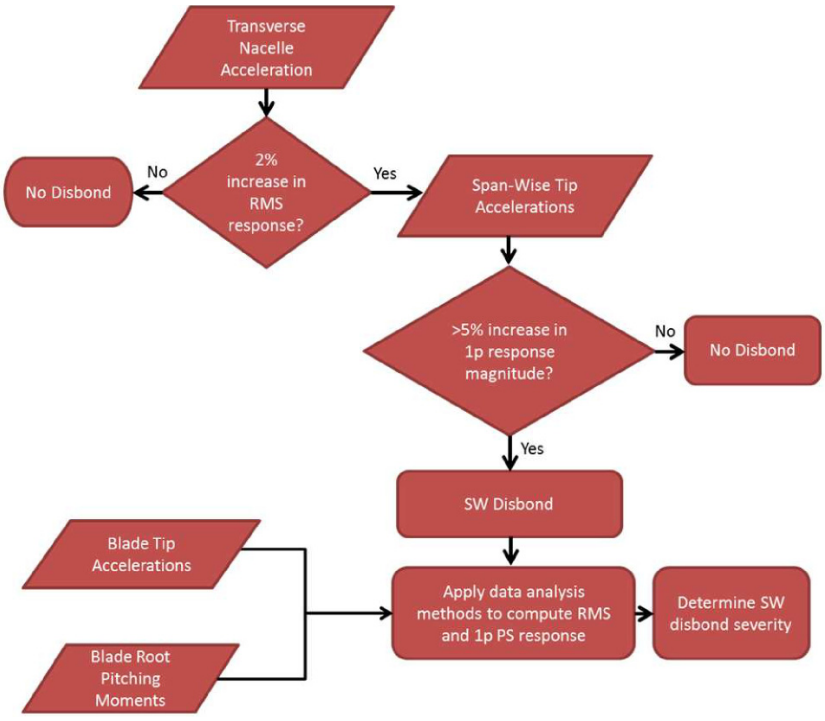

Figure 5. Refined shear web disbond detection strategy.

[4] State of Health of Damaged Turbines Assessment (Local Sensitivity). Loads analysis of damaged turbines was demonstrated for damaged blade models. A design standards-based approach was proposed for remaining life estimation in which design loads (operating and extreme loads) are applied to damaged blade models in order to evaluate if positive design margins are in place for the damaged blades. This was demonstrated by structural analysis in this work to; for example, quantify the impact of damage on blade design requirements (e.g. deflection, localized strain (See Figure 6), buckling, fatigue life). This information is used in decision making (e.g. shutdown, normal operations, derating, etc).

As noted in the next section ([5] on the following page), the blade damage models were matured over the course of the research program in order to reduce uncertainty in damaged blade structural calculations and as a result increase confidence in decision-making based on these improved structural calculations.

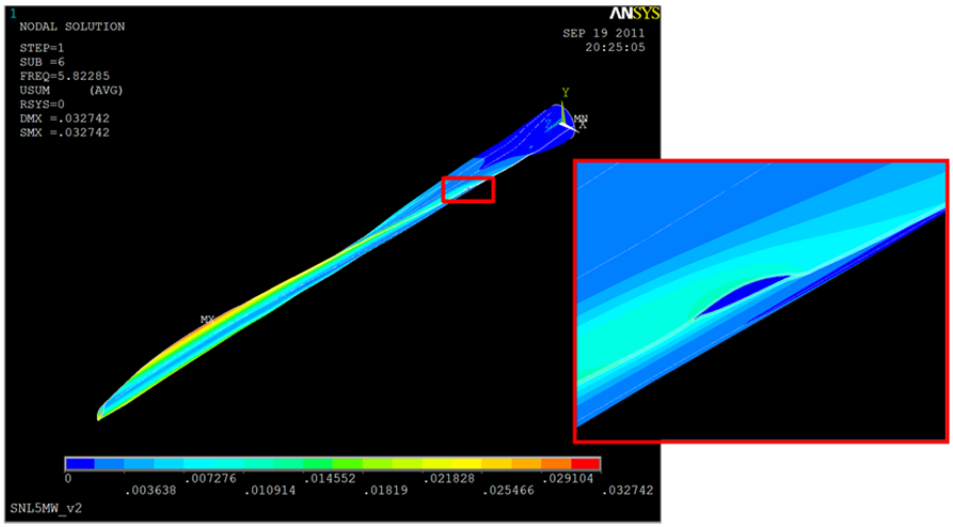

Figure 6. Loads analysis and localized strain increase in a damaged blade.

[5] Maturation of Damage Models for Wind Turbine Blade Analysis. Damage modeling methods for wind turbine blades were matured in several ways over the course of the research program:

a. Detailed models of damage were implemented in a blade modeling code (the Sandia NuMAD code). This enabled inclusion of detailed damage effects in high-fidelity loads analysis of damaged blades (See Local Sensitivity in Figure 3) and calculation of degraded blade cross-sectional properties of the damaged blade (See Equivalent Blade Model in Figure 3) for use in turbine aero-elastic simulations.
b. Progressed from the initial linear damage models in NuMAD to nonlinear models of contact in high-fidelity models of blade damage for blade disbonds (See Figure 7).
c. Implemented and validated progressive damage models in blades. Trailing edge and shear web disbond damage cases were analyzed.
d. Progressed from linear to nonlinear methods for estimating beam properties of damaged blades for use in turbine aero-elastic simulations. Implemented a nonlinear approach in the SNL BPE "Beam Property Extraction" code (again, see Equivalent Blade Model in Figure 3) for estimating beam properties for nonlinear models of contact in high-fidelity models of blade damage. This was an extension of [5]b.

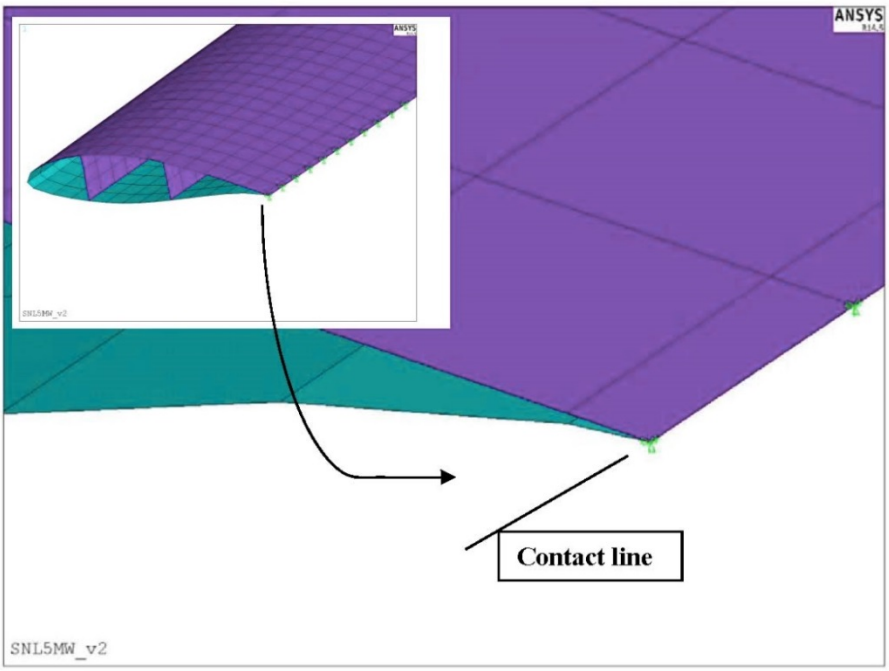

Figure 7. Nonlinear contact elements implemented in SNL/NuMAD blade modeling software. In this case, applied at trailing edge to improve modeling of trailing edge disbond type damage.

[6] Smart Loads Management (or Derating, Damage-mitigating Controls, Prognostic Controls) for Wind Turbine Rotors. Several smart loads management concepts were proposed and demonstrated for rotor loads management by derating the turbine through changes to blade pitch and RPM schedules. The impacts of smart loads management were quantified on reducing aggregate turbine loads such as blade root bending moment and rotor thrust (See Figure 8). In addition, localized effects of loads management were demonstrated in reduction of strain energy release rates (SERRs) in blade bondline damage (See Table 1).

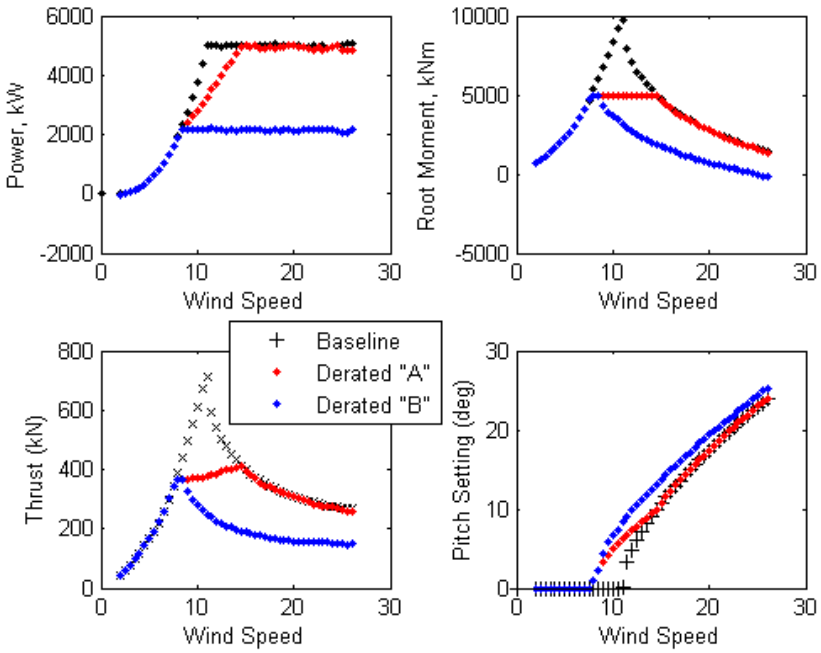

Figure 8: Power Production, Root Bending Moment, Rotor Thrust Predictions for Two Derating Strategies "A" and "B" and Derating Level of 50%. The Derating Strategies are Achieved by Modifying the Pitch Control Settings as Shown in Lower Right.

Table 1: Reduction in averaged SERRs for 8m disbond location under derated operation, weighted by a Rayleigh wind distribution with average wind speed of 10 m/s.

Derating Strategy	A	B
Reduction in G_I	35%	70%
Reduction in G_{II}	33%	70%
Reduction in G_{III}	47%	63%

[7] Optimized Maintenance Processes. Concepts were proposed and outlined for optimizing O&M strategies through use of an SHPM monitoring system. A key objective of the SHPM monitoring system is to detect damage early enough so that low-cost repairs (up-tower repairs) can be performed versus more costly ground repair or blade replacement – Figure 9 illustrates this concept. Monetary values for repair costs could be used to quantify new and optimized O&M processes enabled by early SHPM-based damage detection and state of health estimation. In addition, as noted in Chapter 8, derating actions can be timed within an overall maintenance strategy to avoid shutdown in high wind speed (high revenue months) by derating and then perform maintenance in the lower wind speed (lower revenue months) when revenue loss is reduced and accessibility (e.g. by offshore vessel) is easier.

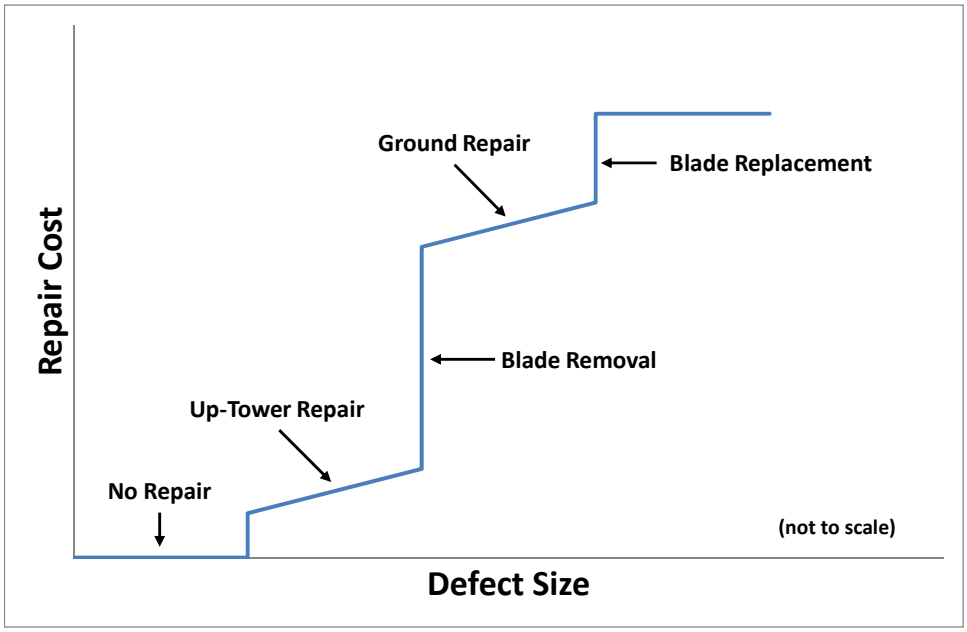

Figure 9. States of Health Concept and Cost Dependence (Four States: No Repair, Up-Tower Repair, Ground Repair, and Blade Replacement).

[8] SHPM Economic Calculations. Economics impacts of SHPM on O&M costs and increased energy capture (via smart loads management) were quantified to demonstrate good potential for economic return on investment:

a. A framework for O&M cost analysis was developed with initial calculations to illustrate the initial modeling approach.
b. Economics of derating was analyzed. Revenue increases enabled by SHPM by operating damaged turbines instead of a shutdown were quantified. A parameter study was performed to examine the effects of the following:
    i. different derating types (See Figure 8, Strategy A or B),
    ii. different levels of derating (e.g. 50%, 75% derated),
    iii. seasonal variation in wind resource (i.e. monthly variation), See Figure 10 and Table 2 for an example comparing derating in Month 2 versus Month 6, and
    iv. site characteristics (high versus low resource sites) were considered.

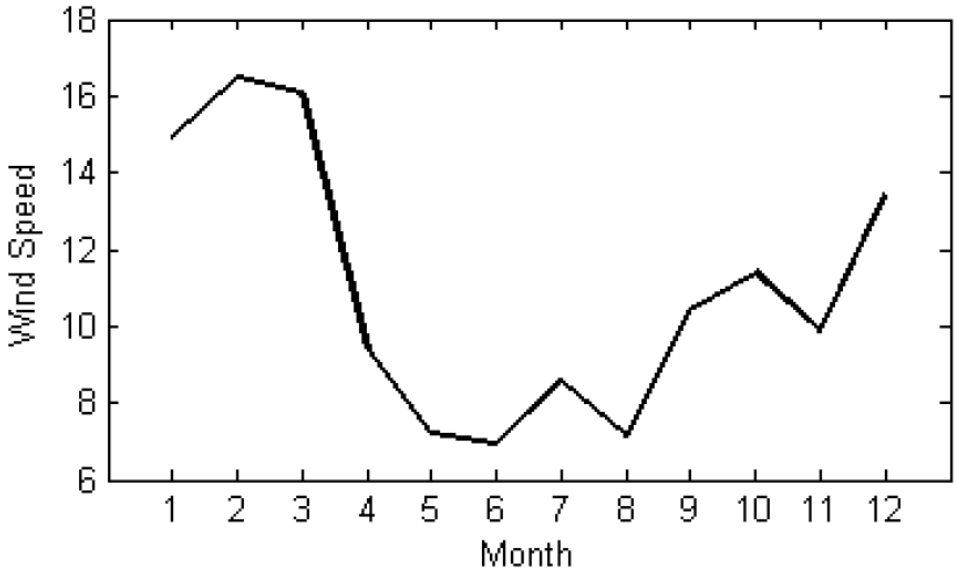

Figure 10: Monthly Variation in Winds peed for a Baltic Offshore Site with a Wind Speed Average of 11 m/s

Table 2: Variations due to MonthlyWind speed Variation in Possible Revenue Increases (using 5 cent/kW-hr) when Derating for 1 Month Instead of Shutdown

Level	Calm (7 m/s)	Windy (16.5 m/s)
75% (A)	+$63,800 (+4.9%)	+$140,000 (+10.7%)
75% (B)	+$53,400 (+4.1%)	+$99,100 (+7.6%)
50% (A)	+$55,800 (+4.3%)	+$131,000 (+10.0%)
50% (B)	+$44,500 (+3.4%)	+$73,800 (+5.6%)
25% (A)	+$35,300 (+2.7%)	+$96,800 (+7.4%)
25% (B)	+$19,200 (+1.5%)	+$23,900 (+1.8%)

[9] Damage Detection Strategies Tested under Realistic and Variable Inflow Conditions. In order to test the damage detection strategies (e.g. See Figure 5), an inflow variability study was performed. The robustness of the damage detection strategies was tested under realistic and variable inflow conditions: wind speeds were varied from cut-in to cut-out with varying levels of turbulence and varying levels of horizontal shear. (See Table 3). One key result is that the damage detection strategies performed well under these inflow conditions. Another key result is that wind speed ranges optimized ranges for detection of damage were identified. The performance of the damage detection strategies was quantified through POD (probability of detection) and POC (probability of classification) analyses based on a database of more than 16,000 turbine aero-elastic simulations. These analyses were performed for multiple damage types and for a range of extents of damage.

Table 3: Variables of the Inflow Variability Study (wind inflow characteristics and extent of damage)

	Healthy	1m Dis-bond	2m Dis-bond	3m Dis-bond	4m Dis-bond	5m Dis-bond	10m Dis-bond
Wind Speed (3 - 25 m/s)	101	101	101	101	101	101	101
Horizontal Shear (30%, 60%, 90%)	303	303	303	303	303	303	303
Turbulence (A, B, KHTEST)	303	303	303	303	303	303	303

[10] A Framework for SHPM Decision Making. A statistical framework for decision-making was proposed - within the multi-scale modeling and simulation of damage approach. See Section 9.3 for a description.

9.2 Status of the SHPM Technology Roadmap

As detailed in Chapter 3, a technology roadmap for Structural Health and Prognostics Management (SHPM) was developed early in the research program. The basic research blocks of the roadmap were defined in six (6) thrust areas for the SHPM Technology Roadmap. The status of the roadmap and recommended next steps are presented in this section.

The intent in providing this status update for the roadmap is two-fold. This provides a summary of how the work of this research program has contributed to maturing the technology and/or understanding in each of these thrust areas since this roadmap was defined. In addition, this is intended to outline in what areas and in what ways stakeholders may leverage, connect with, and extent these results.

The stage of maturity for each, at the time of this report and as a result of the work conducted in this research program, is listed here:

Thrust 1:	Identify Relevant Damage Features	Stage 2
Thrust 2:	Model and Characterize the Damage Features	
Thrust 2a:	Effects of damage on operational response (Global Sensitivity)	Stage 4
Thrust 2b:	Effects of damage on blade state of health (Local Sensitivity)	Stage 4
Thrust 3:	SHPM Economics Analysis	Stage 2
Thrust 4:	SHPM Operations Decisions: Controls	Stage 4
Thrust 5:	SHPM Operations Decisions: Maintenance	Stage 1-2

Table 4 provides a graphical summary of the roadmap and current status.

The major focus of the Sandia research efforts was Thrust Area 2a, Thrust Area 2b and Thrust Area 4, in the areas of damage modeling & damage detection (Thrust Area 2) and loads management of damaged turbines (Thrust Area 4). These are the core technology development areas of the roadmap.

Further maturation in Thrust Areas 1, 3, and 5 requires data and information from industry such as component failure rates, repair costs information, accessibility information, and capital costs for sensors & data acquisition. The roadmap outlines how this information can be utilized and integrated with the Thrust Areas.

Here, a description of each Thrust Area is provided with specific recommended next steps for each Area:

Thrust Area 1 -- Identify Relevant Damage Features
The focus of this Thrust Area is to identify common, highly-relevant damage features that must be addressed by SHPM. These damage features are ranked based on impact on revenue loss (consequence of failure, frequency of occurrence, downtime, replacement costs, etc.). Additional maturity is gained through assessment of the collective effects of these damage features on revenue losses.

Recommendations for near-term and longer-term efforts in Thrust Area 1 are:

- Perform a comprehensive accounting of un-reliability for all major sources to ensure the needed breadth of capability and to ensure that cost analysis accounts for all of them
- Identify approaches to simulate damage experimentally for laboratory- and field-scale demonstration
- Expand from component to turbine level health monitoring and prognostics management

Thrust Area 2 -- Model and Characterize the Damage Features

In Thrust Area 2, modeling and characterizing the damage features (e.g. those identified in Thrust Area 1) is done using the developed multi-scale simulation of damage approach. The two key elements of this approach are sensitivity analysis of the operating response for damage detection (Thrust 2a: global sensitivity) and sensitivity analysis of the blade state of health (Thrust 2b: local sensitivity). The maturity plan for each of these modeling efforts involves refining the fidelity of damage modeling and moving toward data collection for validation of these models.

Thrust Area 2a -- Effects of Damage on Operational Response (Global Sensitivity)

This Thrust Area focuses on the effects of damage on the operating response, as changes in the operating response is the indicator of damage and is used for damage detection. In this Area, sensor & condition monitoring systems and algorithms are evaluated (and designed) to detect and characterize a damaged condition.

Recommendations for near-term and longer-term efforts in Thrust Area 2a are:

- Simulate additional damage and fault cases identified as important in Thrust Area 1
- Demonstrate damage detection in experiments; progressing from laboratory to field scale experiments

Thrust Area 2b -- Effects of Damage on Blade State of Health (Local Sensitivity)

This Thrust Area focuses on effects of damage on blade state of health (i.e. blade remaining life). The approach proposed is to use loads analysis defined in blade design standards to evaluate performance margins of the principal design loads requirements (ultimate strains, tip-tower clearance, fatigue life, and buckling capacity) in the presence of damage. This loads analysis will determine if blade remaining life has been diminished from the healthy design state and will lead to a safe, revenue-optimizing decision (e.g. shutdown, smart loads management (derating), or maintenance actions).

Recommendations for near-term and longer-term efforts in Thrust Area 2b are:

- Perform a full scale experimental validation of local effects of damage in damaged blade models
- Perform a statistical analysis to characterize uncertainty in blade state of health (i.e. remaining life) for revenue optimizing decision making (see Section 9.3 for more details on decision making)

Thrust Area 3 -- SHPM Economics Analysis

An economics analysis compatible with the other thrust areas is needed for development, as defined in Thrust Area 3. The maturity plan for this Area includes developing initial cost models

for SHPM, moving to refined cost models and then integrating them with the other Areas (end to end demonstration). The cost analysis should be flexible enough to be useful for design analysis as well as real-time economics decision-making.

Recommendations for near-term and longer-term efforts in Thrust Area 3 are:

- Perform a more comprehensive end to end analysis of the design and operation of the SHPM system; a comprehensive cost-benefit analysis should be performed (potentially with development of a cost-benefit analysis tool)
- Incorporate field validation and cost data into cost analysis in order to assess accuracy and validate SHPM cost and decision tools. Incorporate Thrust Area 1 and Thrust Area 5 data to feed economics analysis; i.e. "to make the business case"

Thrust Area 4 -- SHPM Operations Decisions: Controls

This Thrust Area involves safe, revenue-optimizing control actions based on smart loads management strategies using a SHPM system. These prognostic control actions can include shutdown to prevent catastrophic failure or derating strategies that avoid shutdown so as to produce revenue in a safe manner (even when damaged) until proper maintenance can be executed (based on component availability, weather, sea states, etc.).

Recommendations for near-term and longer-term efforts in Thrust Area 4 are:

- Implement and demonstrate smart loads management in an operating turbine
- Connect smart loads management decisions (in a statistical approach) with the operations decision-making process based on Thrusts 2a and 2b outputs for damage detection and state of health (remaining life), respectively (see Section 9.3 for more details on decision making)

Thrust Area 5 -- SHPM Operations Decisions: Maintenance

This Thrust Area involves new maintenance processes that are enabled by SHPM. One focus is to enable predictive or planned maintenance at lower costs versus conventional unplanned or reactive maintenance when using a cost-effective SHPM system.

Recommendations for near-term and longer-term efforts in Thrust Area 5 are:

- Acquire repair costs data needed for O&M cost analysis and incorporate into economics analysis of Thrust Area 5
- Acquire special equipment costs (e.g. vessels costs) for economics analysis
- Incorporate cost data into scenarios and run simulations to quantify economic impacts of different maintenance strategies (e.g. with and without SHPM or for various levels of SHPM capability)

Table 4. SHPM Technical Maturity Roadmap – Version 1.0
(Key: mature/completed, current, near-term future, longer-term future) As of March 2015

		Stage 1	Stage 2	Stage 3	Stage 4	Stage 5
Thrust Area 1	**Identify Relevant Damage Features**	• Identify single damage feature #1 • Define criterion for selection: rank based on impact on revenue	• Identify additional important rotor damage features	• Quantify and validate collective effects of these features on revenue loss	• Implement approach for experimental simulation of damage	• Identify and demonstrate the method for non-blade components (e.g. tower)
Thrust Area 2(a)	**Model and Characterize Damage Features: *Global Operating Sensitivity***	• Develop methodology to model and simulate damage globally • Identify sensor needs for blade and non-blade sensing for feature #1 • Identify detection strategy for feature #1	• ID sensor needs for multiple features (blade and non-blade) • ID detection strategies for additional features (blade and non-blade) • Comprehensive survey of industry sensor products (turbine and general)	• Mature detection robustness to uncertainties and multiple simultaneous damage features • Mature the damage model (linear versus nonlinear models) of operating sensitivity	• Mature the damage model (progressive damage model) for operating sensitivity • Laboratory demonstration of detection strategies	• Demonstrate detection in field tests on utility-scale rotor
Thrust Area 2(b)	**Model and Characterize Damage Features: *Local Damage Effects***	• Develop methodology to model and simulate damage locally • Develop a plan to quantify the blade state of health • Perform targeted load case analysis	• Perform complete set of load case analyses to quantify damage effects on state of health tied to IEC/GL blade design standards	• Mature the damage modeling (linear versus nonlinear models) for buckling and strain calculations	• Mature the damage model (progressive damage model) for effect on local sensitivity	• Demonstrate localized damage effects and their progression in full-scale blade test
Thrust Area 3	**SHPM Economics Analysis**	• Initial cost model defined for SHPM system assessment (ID inputs/outputs)	• Refine the fidelity of the SHPM cost model • Perform input/output sensitivity studies	• Integrate with simulations in Thrust Areas 2(a) and 2(b) in end to end case study of SHPM system cost and performance	• Field demonstration project to validate SHPM system model performance and economics	• Distribute validated SHPM cost and decision tools to industry
Thrust Area 4	**SHPM Operations Decisions: Controls**	• Define conceptual prognostic (damage mitigating) control modes	• Refined loads management strategy to avoid catastrophic failure/total loss	• Refined loads management strategy to maximize revenue; to mitigate damage growth	• Model and test/validate the impact of upstream turbine(s) wake on downstream SHPM	• Field demo of prognostic control in utility-scale rotor
Thrust Area 5	**SHPM Operations Decisions: Maintenance**	• Define conceptual maintenance states for blade SHPM • ID the information needed from sensor/SHM system for maintenance decisions	• Refine/expand model to include other information (vessels, weather, etc.) • Refine the blade repair/replacement cost information • Exercise SHPM cost model with new inputs	• Review loads management strategies in the context of optimal maintenance planning	• End to end simulations that demonstrate the effect of SHPM system on maintenance process economics	• Field test validation of SHPM-based maintenance operations for utility-scale wind farm

Technology Integration

Technology Thrust Maturation Path

9.3 Recommendations for Future Work

In summary, a few additional recommendations for future work are made. Whereas Section 9.2 lists specific recommendations associated with each Thrust Area, here in Section 9.3 overall recommendations on SHPM technology integration and an SHPM decision-making process are suggested.

I. **Health Monitoring & Inspection:** Coordination of the SHPM monitoring system with component inspection protocols is suggested. The extent to which the SHPM monitoring system can coordinate with and reduce inspection needs/costs or potentially replace inspection should be considered in the design and development of a SHPM system.

II. **System/Plant Life-cycle Design Improvements:** A turbine and/or wind plant should be "designed for inspection and monitoring" to ensure reliability and reduce costs over the lifetime.

III. **Loads Monitoring:** Loads monitoring and loads forecasting should be incorporated into the SHPM system as it has potential to improve the SHPM system performance and reduce costs.

IV. **SHPM Validation by Modeling and Simulation:** A "blind" damage detection study to test damage detection strategies would be beneficial. This should be approached first with a comprehensive modeling and simulation-based campaign and later through experimental validation.

V. **SHPM Validation in the Field:** Following validation by modeling and simulation, validation of SHPM and its various elements (e.g. damage detection, remaining life estimation, smart loads management (derating), optimized O&M processes, economics analysis) with experimental validation at laboratory then field scale (utility scale) is needed to reduce uncertainty and reduce risk (of deploying new sensors & implementing new processes or corrective actions)

With regards to SHPM-based decision making, it is important to consider integration of information based on statistics or statistical methods, uncertainty, and how these tie to decision-making. In this framework, the following SHPM decision-making process is envisioned, starting with identified damage scenario case studies:

(1) Damage scenario case studies of relevant damage types (either single damage case or multiple possible cases) are defined;
(2) The selected damage scenario feeds or initiates the multi-scale damage modeling and simulation process including aero-elastic simulations (global sensitivity of damage) and high-fidelity loads analysis (local sensitivity of damage) of damaged turbines;
(3) A probabilistic framework is applied within this multi-scale simulation approach of both global and local sensitivity:
    1. Global sensitivity (damage detection): statistics (probability estimation) are estimated for the identified damage and its characteristics (i.e. damage type, damage

location, and extent of damage) using the operational response based damage detection strategy, then

2. Local sensitivity (state of health): based on the statistics of the damage state estimated in global sensitivity (i.e. "probability estimation"), statistics associated with the state of health (remaining life) are computed, thus connecting the statistics and uncertainty of the estimated damage state with a statistical estimate and uncertainty estimate of remaining life (e.g. fatigue life, ultimate strain, tower strike, buckling, etc.).

(4) The statistical (uncertainty) estimate of remaining life (as a function of loads or inflow conditions) will be used for SHPM-based decision-making. A conservative approach would be to assume the largest possible damage conditions (e.g. +3 sigma damage state) and apply control actions and maintenance actions accordingly based on the allowed loading conditions;

(5) The effects of these control actions on damage growth and remaining life are to be confirmed via aero-elastic simulation (either real-time computation or pre-computed look-up values) through loads analysis. This will provide information to ensure safe, revenue-optimizing control actions or maintenance decisions such as normal operation, shutdown, or smart loads management (derating).

DISTRIBUTION

5	MS1124	D. Todd Griffith	06121
1	MS0899	Technical Library	9536 (electronic copy)


Sandia National Laboratories